

Contents

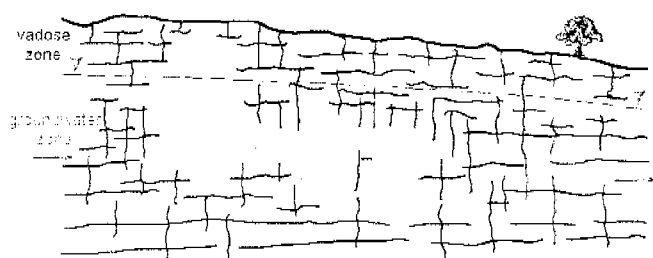
Volume I

1.0	Introduction	1-1
1.1	Facility Description and History	1-1
1.2	Problem Overview and Solution Approach.....	1-2
1.3	Information Sources Used to Develop the Conceptual Model.....	1-3
2.0	Overview of Conceptual Site Model.....	2-1
3.0	Geology	3-1
3.1	Regional Geologic Setting	3-1
3.2	Depositional Environment.....	3-1
3.3	Stratigraphy.....	3-2
3.4	Structures	3-3
3.5	Preliminary Assessment of Geologic Features on Groundwater Flow	3-4
4.0	Hydrogeology	4-1
4.1	Historical Summary	4-1
4.2	Estimate of Site Bulk Hydraulic Conductivity from Water Balance	4-1
4.3	Hydraulic Conductivity Testing	4-2
4.4	Vadose Zone Water Content	4-2
4.5	Influence of Stratigraphy and Geologic Structure on Hydraulic Conductivity.....	4-3
4.6	Delineation of Groundwater Units	4-4
4.7	Interconnected Nature of Chatsworth Formation Fracture Network	4-5
4.8	Groundwater Units	4-5
4.9	Hydraulic Apertures, Fracture Porosity and Average Linear Groundwater Velocity.....	4-6
4.10	Summary of Hydrogeology at the SSFL	4-7
5.0	TCE Occurrence at the SSFL.....	5-1
5.1	TCE Input Locations.....	5-1
5.2	Historical and Preliminary RFI Finding	5-1
5.3	TCE in Chatsworth Formation Groundwater.....	5-2

Stage 4: *Complete DNAPL disappearance and TCE plume expansion (Figure 6.4)*. At some point the DNAPL completely disappeared from the fracture network due to diffusion, dissolution and sorption. The timeframes for complete DNAPL disappearance are expected to range from 2 to 50 years due to the variability in fracture apertures and matrix porosity.

The solute plume will continue to expand as the groundwater flows through the fracture network, but the rate of expansion will be very slow because the mass of fractured bedrock available for diffusion greatly increases with plume expansion. The timeframe over which the plume will continue to migrate relative to a concentration limit is expected to range from tens to hundreds of years depending on the duration and mass loading of a DNAPL source.

Figure 6.4



Stage 4: No DNAPL Remains, Plume Has Expanded and Migrates Very Slowly

6.1 DNAPL Flow and Distribution in the Vadose Zone

Four characteristics affect the flow of DNAPL in the Chatsworth Formation vadose zone. These four characteristics are: vadose zone water pressure, water content, fluid wettability and effective permeability. Each of these characteristics and their influence on DNAPL flow is described below. Detailed discussions on the flow and distribution of TCE in the vadose zone are provided in Appendix D.

- **Water Pressure:** By definition, the water pressure within the vadose zone is less than the atmospheric pressure (i.e. negative gage pressure). Negative gage pressures develop in the sandstone matrix because of capillary forces. Water at negative gage pressure preferentially resides in small pore spaces of the bedrock. Smaller and smaller pore spaces will retain water against the force of gravity as the negative gage pressure increases. Since fractures represent the largest openings (or pore spaces) in the rock, they will not be water-filled unless water is available to the fracture at

positive gage pressure. Positive gage pressures are likely to arise during infiltration events and below surface water storage ponds. The distribution of water pressure in the vadose zone is shown conceptually in Figure 6.5. Once TCE is released into the bedrock, TCE DNAPL will preferentially and spontaneously flow within the fracture network since the fractures are air-filled except at locations or times noted above.

- **Water Content:** As discussed in section 4.4, the average water content of the vadose zone matrix blocks is determined by the ratio of average recharge flux to the average saturated hydraulic conductivity of the matrix blocks. This ratio is less than unity and represents the mean relative permeability of the sandstone matrix to water. The water content of the matrix adjusts until it is in equilibrium with this ratio. At the SSFL, the mean water content is estimated to be about 0.7 (i.e., the matrix pore space is filled with about 70% water and 30% air, on average). However, the local water content is expected to be highly variable due to variations in rock properties, which is conceptually depicted in Figure 6.5.

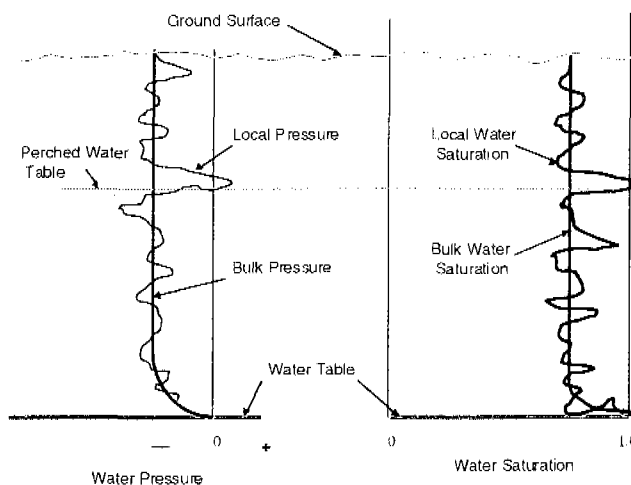


Figure 6.5 Conceptual Distribution of Water Pressure and Content in the Vadose Zone

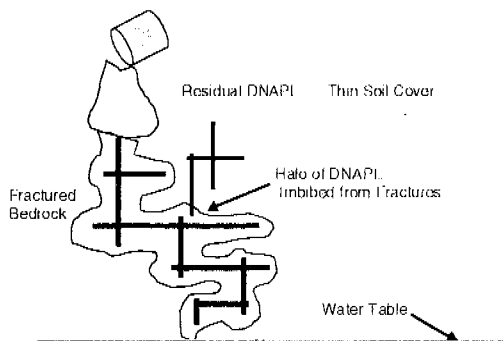
- **Wettability:** Once DNAPL is released into the bedrock, its distribution and flow will be governed by the wettability of the three fluids (air, water and TCE) resident within the Chatsworth Formation. TCE is the wetting fluid with respect to air. This phenomena will cause the TCE DNAPL within the fractures to be soaked up (or imbibed) into the sandstone matrix adjacent to the walls of the fractures, since the matrix pores contain about 30% air. Imbibition of the TCE, shown conceptually in Figure 6.6, will create a halo of DNAPL around the fractures. TCE DNAPL will not displace the water that is resident within 70% of the sandstone matrix because water is the wetting fluid with respect to TCE.

- **Effective Permeability:** The effective permeability of the matrix to the DNAPL is determined by the intrinsic permeability of the matrix and the pore volume available for DNAPL flow. Since DNAPL can only occupy a small portion of the pores of the rock matrix because of the presence of water and air, the maximum effective permeability of the matrix to DNAPL is a factor of 14 lower than the saturated permeability. Additional calculations show that the reduced permeability limits the penetration of DNAPL into the matrix to only a few centimeters from the fracture wall. The halo of imbibed DNAPL is expected to be quite irregular owing to the local variations in water content. DNAPL imbibition will be prevented at locations where the water content of the matrix is near or at saturation. At these locations, the DNAPL will continue to flow within the fracture network to areas of lower water content and become imbibed, or will flow to the water table. DNAPL is expected to migrate to the water table through the otherwise air-filled fractures within hours to days.

Figure 6.6

Conceptual Distribution of DNAPL in the Vadose Zone

Conceptual Distribution of DNAPL In Vadose Zone



TCE Distribution in the Vadose Zone as a Result of Inter-Phase Partitioning

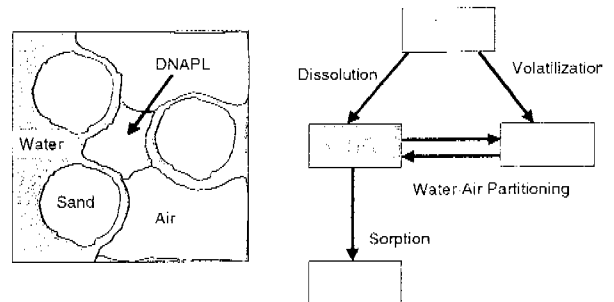
Inter-phase partitioning (Figure 6.7) will control the distribution of TCE that is imbibed into the sandstone matrix or present within vadose zone fractures. Detailed discussions of inter-phase partitioning in the vadose zone can be found in *Dense Chlorinated Solvents and other DNAPLs in Groundwater* (Pankow and Cherry, 1996). At equilibrium, the inter-phase partitioning includes:

- dissolution of DNAPL into the aqueous phase as characterized by the effective solubility of TCE in water,
- volatilization into the air phase as characterized by the vapor pressure of TCE at the prevailing temperature,

- mass transfer of TCE between the aqueous and gaseous phases, governed by Henry's law and characterized by the dimensionless Henry's constant, and
- sorption of TCE dissolved in the aqueous phase to the solid phase in accordance with the organic carbon partition coefficient and the fraction of organic carbon in the bedrock.

Figure 6.7

Inter-Phase Partitioning of TCE In Unsaturated Matrix Blocks



TCE will be distributed by diffusion in all directions from the DNAPL. Its distribution and migration is dominated by gaseous phase diffusion and will produce significant lateral spreading. This is because the gaseous phase diffusion coefficient is approximately 1000 times greater than the aqueous phase diffusion coefficient, even though the air content (which represents the gas) is smaller (30%) than the water content (70%). As TCE spreads in the gaseous phase, it partitions into the aqueous phase. Once in the aqueous phase, TCE is transported primarily downward by advection in the recharge waters. Aqueous phase TCE migration due to advection is affected by partitioning to the rock matrix through sorption.

The result of these mutually-dependent partitioning and transport processes is the creation of a "cloud" of aqueous and gaseous phase TCE around the portion of the fracture system beneath the DNAPL input locations. The lateral spreading that occurs in the vadose zone causes the areal extent of the TCE source zone as observed at the water table to be significantly larger than that observed at the ground surface or at the bedrock contact.

The gaseous phase in the vadose zone is expected to be continuous with atmospheric air, at least through the fractures and possibly through the rock matrix that is not completely saturated with water. These connections provide a pathway for TCE to diffuse to the atmosphere. A substantial portion of the total mass of TCE that has

By definition, water pressures in the saturated zone are positive. Therefore, all interconnected openings, both fracture and rock matrix, are water-filled below the water table. Since TCE DNAPL is the non-wetting fluid with respect to water, it requires positive pressure to enter any water-filled openings.

DNAPL will enter a water-filled opening only if its pressure exceeds the water pressure by some threshold value. This threshold is called the entry capillary pressure or simply the entry pressure. The entry pressure is dependent upon the:

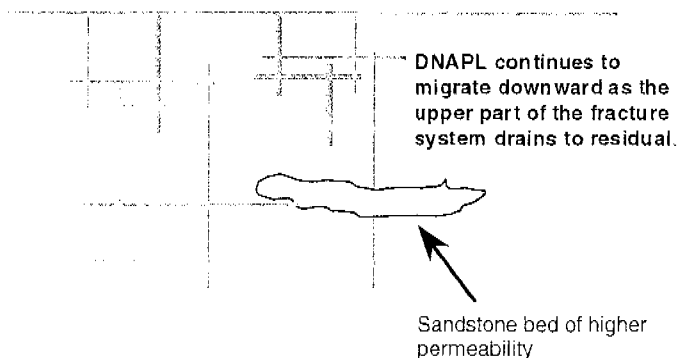
- interfacial tension between liquid-phase TCE and water,
- contact angle, and
- size of the opening across which the two-fluid interface is positioned.

Entry pressures generally increase as the size of the opening across the two-fluid interface decreases, assuming that the geometry, interfacial tension and fluid wettability remain constant.

The entry pressure of the fracture system at the SSFL is much smaller than matrix block entry pressures since fracture openings are much larger than openings in the matrix. DNAPL is expected to migrate and reside primarily in fractures below the water table. Once the DNAPL source is exhausted, DNAPL in the fracture system drains. However, drainage is not complete, and a residual remains after the fracture drains (Figure 6.10). The formation of the trail of residual consumes the mobile DNAPL and limits the depth of DNAPL migration.

Figure 6.10

Redistribution of DNAPL Below the Water Table After a Release Has Ceased

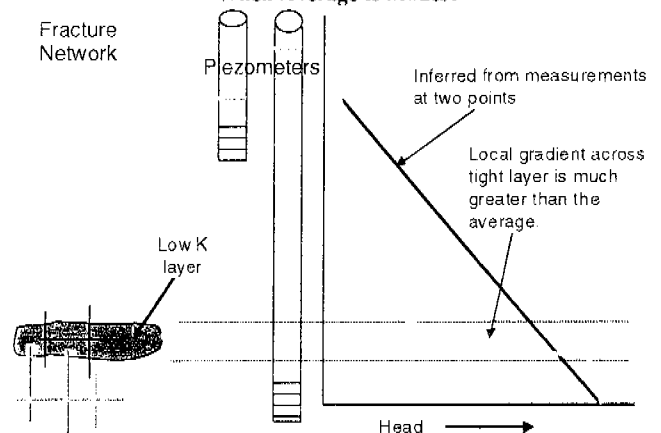


The depth of DNAPL penetration below the water table is also effected by a number of physical characteristics at the site

- The presence of strong local upward hydraulic gradients. Local upward gradients can be large, even when the average upward gradient indicated by piezometer measurements is small as shown in Figure 6.11. Strong local upward gradients were present at RD-46 as shown by groundwater monitoring results using a multi-level monitoring device.

Figure 6.11

Local Hydraulic Gradient May Be Large, Even When Average Is Modest



- Entry and retention of the TCE DNAPL within coarse sandstone beds where entry pressures are lower. Entry pressures are reduced within coarse sandstone beds due to an increase in the pore space openings. These increased pore space openings result in increased hydraulic conductivity. TCE rock pore water results indicate that coarse sandstone beds likely present a significant area for TCE storage.
- Partitioning and retention of the TCE DNAPL within the vadose zone. As presented in section 6.1, TCE DNAPL partitions into and becomes retained within the vadose zone as solute and vapor.
- Retention of the TCE DNAPL within fractures. The porosity of the fracture system provides storage capacity for DNAPL within the fracture network.
- Increasing entry pressures with depth due to lithostatic loading. Lithostatic loading likely results in smaller fracture apertures with increasing depth.
- Loss of DNAPL mass due to matrix diffusion. DNAPL dissolves into the rock matrix through diffusion and loses its mass resulting in disconnected segments of DNAPL. These effects are more fully discussed in the following section.

- Shunting of DNAPL flow through vertical fractures by bedding plane fractures. A discussion was presented in section 3.5 stating that the vertical fractures at the SSFL are typically confined within single sandstone beds, where they terminate at the bedding plane. These points-of-termination force the DNAPL to flow along the bedding plane and shunt its vertical penetration.
- The presence of shale or other low permeability beds. These features limit DNAPL penetration because the fracture apertures within the beds are significantly smaller than within the sandstone, thus increasing the entry pressure.

6.4 Effects of Matrix Diffusion on TCE DNAPL Below the Water Table

Once DNAPL is present in the fracture network below the water table, it diffuses into the sandstone matrix according to Fick's Law and dissolves in the groundwater as controlled by its aqueous solubility. This process is conceptually shown on Figure 6.12. Detailed descriptions of this process are provided in section 3.0 of Appendix E.

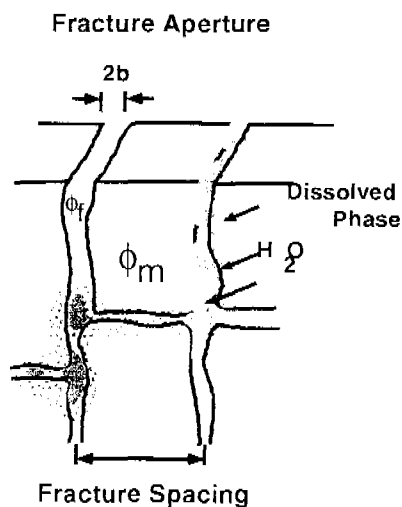
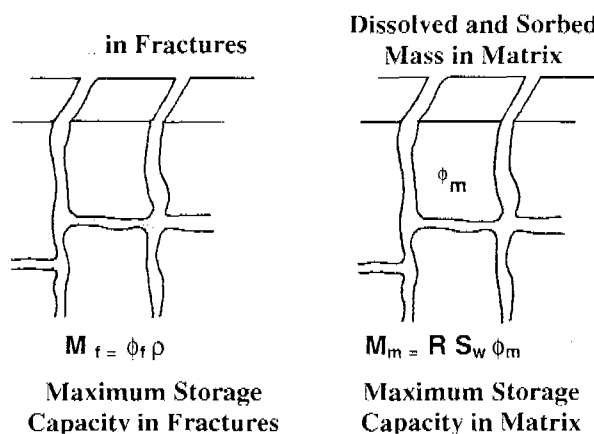


Figure 6.12 Conceptual diagram of TCE DNAPL dissolving away from fractures and into the sandstone matrix.

DNAPL disappearance through matrix diffusion in fractured bedrock results when the mass storage capacity of the rock matrix exceeds the mass storage capacity of the fracture network (Figure 6.13). Calculations were made using Chatsworth Formation data to estimate the ratio of the matrix storage capacity to the fracture storage capacity.

These results showed that the Chatsworth Formation sandstone can store between 5 and 100 times the mass of DNAPL within the matrix than within the fracture and that DNAPL disappearance through matrix diffusion is expected.



When $M_m/M_f > 1$, DNAPL Disappearance is Likely

Figure 6.13 DNAPL mass storage capacities in fracture network and matrix

The effect that matrix diffusion has on DNAPL dissolution can be quantified using a solution to Fick's second law. The time for DNAPL to disappear from Chatsworth Formation fractures can be calculated by solving Fick's second law and results in the following equation for a single parallel-plate fracture:

$$t_D = \frac{\pi \rho^2 (2b)^2}{16 S_w \phi_m^2 D_c R_m}$$

where:

- t_D = DNAPL disappearance time
- ρ = density of TCE
- $2b$ = fracture aperture
- S_w = aqueous solubility of TCE
- ϕ_m = matrix porosity
- D_c = diffusion coefficient
- R_m = retardation in the matrix due to sorption, calculated by

$$R_m = 1 + (\rho_b / \phi_m) (K_{oc} \times f_{oc})$$

where:

- ρ_b = dry bulk density
- ϕ_m = matrix porosity
- K_{oc} = octanol-water partition coefficient for TCE
- f_{oc} = fraction of organic carbon

Site-specific data were used to quantify average values for matrix porosity, the diffusion coefficient and organic carbon. Values are shown on Table 6.1. DNAPL disappearance times were calculated using these average values along with estimates of the size of fracture apertures that were determined from pumping tests and advanced downhole geophysical tests at RD-35B and RD-46B. The calculations show that matrix diffusion causes DNAPL to disappear from fractures in timeframes ranging from 2 to 50 years.

Property	No. of Measurements	Minimum	Maximum	Mean
Porosity (%)	59	1.0	21.60	12.86
Diffusion Coefficient (cm ² /sec)	10	7.5x10 ⁻⁷	2.2x10 ⁻⁶	1.5x10 ⁻⁶
Fraction Organic Carbon (%)	8	0.02	0.15	0.10
Hydraulic Fracture Apertures (microns)	Not applicable	10	300	100

Table 6.1 Values of Input Parameters for DNAPL Disappearance Calculations

These DNAPL disappearance calculations do not consider the additive effect on DNAPL dissolution that results from bulk groundwater flow (advection). DNAPL dissolution associated with groundwater flow through the fracture network was qualitatively evaluated through the use of a fate and transport model that was developed for fractured porous media (VanderKwaak and Sudicky, 1996). Simulations were made using the model to quantify DNAPL.

disappearance times associated with matrix diffusion with and without the effects of advection. The simulation results for a single fracture having an aperture of 100 microns showed a reduction in the DNAPL disappearance times from 5.4 years without advection to 0.16 years with advection, which is about 30 times shorter. It is expected that a similar reduction in the DNAPL disappearance times that were calculated for RD-35B and RD-46B (where advection was not included) would result.

Site-Specific Data Indicating the Disappearance of DNAPL

Two boreholes (RD-35B and RD-46B) were the focus of intensive studies to determine the effects of matrix diffusion on TCE in Chatsworth Formation groundwater (Sterling, 1999). These boreholes were located immediately adjacent to or near suspected TCE input locations. As mentioned in section 6.1, RD-46B was located adjacent to a pond at CTL-III and RD-35B was located near suspected sources at IEL where TCE concentrations in groundwater were high (in the tens of mg/L range). Over 277 samples of rock core were collected and analyzed for the presence and concentration of VOCs from these two locations. One hundred twelve (112) of the 277 samples contained TCE above the method detection limit of about 0.5 mg/L. (See Figure 6.14). The highest concentration of TCE detected in the rock pore water from either location was 164 mg/L. This value is approximately one order-of-magnitude lower than the aqueous solubility of TCE (1420 mg/L) and provides supporting evidence that almost all of the DNAPL that may have entered the Chatsworth Formation groundwater has disappeared.

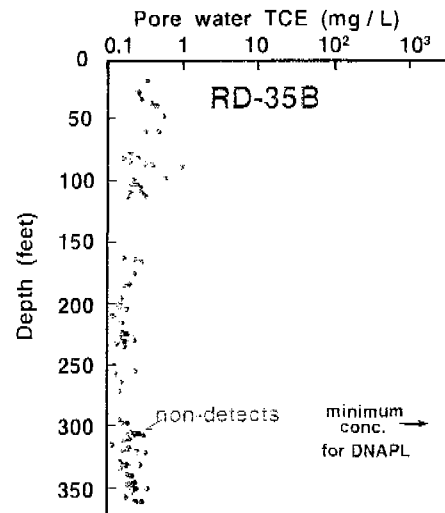
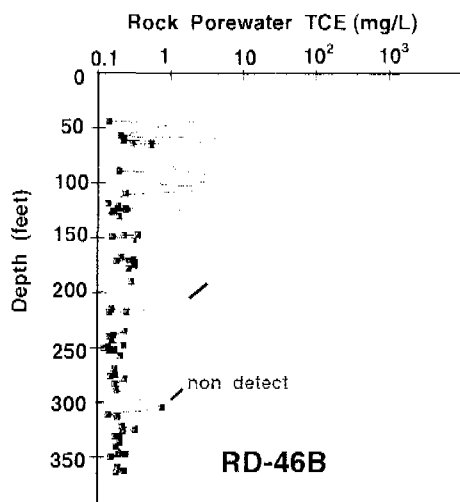


Figure 6.14
Results of rock core analyses from RD-35B and RD-46B. Maximum concentrations detected are one order-of-magnitude below the aqueous solubility.

6.5 Summary of Flow, Distribution and Fate of TCE DNAPL in Source Zones

TCE as a DNAPL flowed through the fractures in the vadose zone bedrock and spontaneously imbibed into the matrix a distance of a few centimeters. Once in the matrix, TCE partitioned into the gaseous and aqueous phases and sorbed onto the matrix grains from the aqueous phase. TCE was transported to the ground surface in the gaseous phase and volatilized to the atmosphere or was transported to the groundwater by advection in the flowing recharge waters. Dissolution rates from the vadose zone to the groundwater zone at source areas are expected to be fairly small (few tenths of a kilogram to a few kilograms per year).

TCE DNAPL that is transported through the vadose zone and to the saturated zone must establish a certain head to overcome the relatively small entry pressures of the fractures to penetrate below the water table. The migration of TCE into the fracture network can be stopped due to a number of processes. Once TCE is within the fracture network, the DNAPL begins to dissolve due to molecular diffusion into the sandstone matrix, sorption onto the matrix grains and dissolution into the groundwater flowing in the fracture network. DNAPL is expected to be present in the Chatsworth Formation fracture network for periods ranging from 2 to 50 years.

7.0 Transport and Fate of TCE Solute

The porous sandstone matrix of the Chatsworth Formation has a strong influence on the migration rate of dissolved-phase TCE flowing through the fracture network. This section of the technical memorandum describes and quantifies the effects that matrix diffusion and sorption have on migration rates of the TCE solute. Additional descriptions and supporting documentation are provided in Appendices E and F. The retardation process is shown conceptually in Figure 7.1.

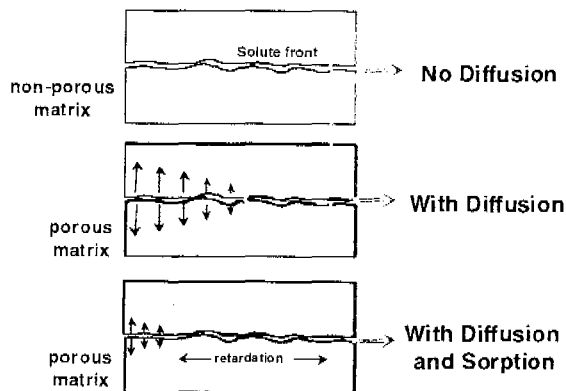


Figure 7.1 Conceptual Effect of Retardation of TCE due to Matrix Diffusion and Sorption

The approaches taken to assess the migration rates of the TCE solute include:

- Applying a numerical model (FRACSTRAN, Sudicky and McLaren, 1992) to simulate groundwater flow and TCE transport a single fracture, and to evaluate and quantify the retardation effects of matrix diffusion on TCE migration. A full description and details of the modeling are provided in Appendix F. The numerical model is also used to evaluate the sensitivity of migration rates to changes in geologic and hydrogeologic properties including:

- ✓ matrix porosity,
- ✓ retardation in the matrix due to sorption,
- ✓ the diffusion coefficient,
- ✓ hydraulic conductivity,
- ✓ fracture apertures, and
- ✓ hydraulic gradient.

The timeframe over which a DNAPL source is present is also varied to assess the effect on TCE plume migration rates. Varying the duration of the DNAPL source reflects the expectation that DNAPL dissolves away from the fracture network due to matrix diffusion and advection as was discussed in section 6.4.

- Applying FRACSTRAN to a two-dimensional fracture network that more closely simulates migration of TCE

solute through the Chatsworth Formation. The two-dimensional model is also used to predict plume characteristics and to demonstrate the effects of retardation in an interconnected fracture network.

- Comparing model results to field data to assess the current stage of plume migration at the SSFL.

The evaluation of the retardation rates of the TCE solute is presented in the context of the average linear groundwater velocity in a fracture network. As presented in section 4.9, the average linear groundwater velocity at SSFL is expected to range from 500 to 10,000 feet per year. Actual groundwater velocities will be faster than the calculated average linear velocity due to the tortuous pathway in the fracture network through which the groundwater must travel. Diffusion of the TCE solute into the sandstone matrix is expected to cause TCE to migrate at rates much slower than the average linear groundwater velocity.

Definitions

The time required for the front of a TCE plume to migrate a specific distance downgradient can be compared to the time for groundwater to travel the same distance. The comparison of the TCE arrival time to the groundwater arrival time is defined as the "apparent retardation". The plume front can be defined as the ratio of a specific concentration "C" (e.g., 1.42 mg/L) relative to a source concentration C_0 (e.g., 1420 mg/L, the aqueous solubility of TCE). In this example, the ratio, C/C_0 , is equal to $1.42/1420$, or 1×10^{-3} . Further discussions on the TCE solute migration will frequently reference these two terms.

7.1 TCE Solute Transport and Retardation in a Single Fracture

Two different model domains were established for the single-fracture simulations on the transport of TCE solute. A model domain of 5 meters (m) in the vertical dimension (or "z") by 200 m in the horizontal dimension (or "x") was established for the initial simulations (Figure 7.2). Input parameters for the initial simulation (i.e., the base case) included the following:

- matrix porosity, $\phi_m = 10\%$
- retardation factor associated with sorption, $R_m = 1.0$
- diffusion coefficient, $D_a = 10^{-6} \text{ cm}^2/\text{sec}$
- hydraulic gradient, $i = 1\%$
- fracture aperture, $2b = 100 \mu\text{m}$

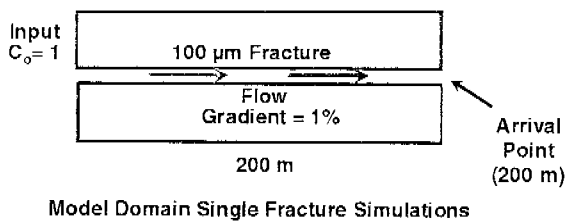


Figure 7.2

The objective of these simulations was to evaluate the effects of matrix diffusion on the migration of the TCE solute by quantifying the time of arrival for the TCE plume front relative to the groundwater arrival time at a C/C_0 of 10^{-3} . A constant source input function representing TCE DNAPL was placed at the upgradient boundary of the model at $x = 0$ m. This model was also used to quantify the effects that variations of the input parameters have on the arrival time of the TCE plume front relative to the base case. Results are presented in Table 7.1.

	Parameter Value	Arrival Time at 200 m	Apparent Retardation
groundwater	NA	28 days	1
TCE Solute Sorption	$R_m = 1$	4 yrs. (Base Case)	52
	$R_m = 3$	11.5 yrs.	150
Porosity (%)	5	1.6 yrs.	21
	10	4.0 yrs. (Base Case)	52
	15	8.6 yrs.	112
Diffusion Coefficient (cm^2/sec)	1×10^{-9}	4.0 yrs. (Base Case)	52
	2×10^{-6}	7.5 yrs.	98
Fracture Aperture (μm)	100	4.0 yrs. (Base Case)	52
	200	0.2 yrs.	3

Table 7.1 This table summarizes the affects that changing parameters have on the apparent retardation of the TCE plume front at a C/C_0 of 10^{-3} . Other parameters shown in the base case are held constant while each individual parameter is varied to determine its affect on the arrival time.

In summary, the simulations show that matrix diffusion causes TCE to arrive at a distance 200 m downgradient of the DNAPL input location, which also represents the end of the model domain, in 4 years, while groundwater arrives at this same location in 28 days. Comparing the TCE arrival time to the groundwater arrival time results in an apparent retardation factor of 52 for the base case. When the base case is altered to include sorption, TCE arrives at the end of the model domain in 11.5 years. These simulations show the strong retardation effect that matrix diffusion has on the migration of TCE solute along a single fracture.

The same model domain was used to evaluate the effects on the arrival time of the TCE solute that result from varying the relative concentration or C/C_0 . These simulations were also used to evaluate what changes hydraulic gradient has on the arrival time of TCE solute. The input parameters for this second set of simulations (base case) were changed to be more representative of the Chatsworth Formation and were as follows:

- matrix porosity, $\phi_m = 13\%$
- retardation factor associated with sorption, $R_m = 3.0$
- diffusion coefficient, $D_c = 10^{-6} cm^2/sec$
- hydraulic gradient, $i = 2\%$
- fracture aperture, $2b = 70 \mu m$

Results from these simulations show that it takes longer for the TCE plume front to arrive as the C/C_0 increases (i.e., the higher concentration portions of the plume arrive at a specified location at a much later time than the lower concentration portions of the plume). The results also show that the apparent retardation factor increases as the distance from the source input increases. This decreasing rate-of-change or deceleration of plume front arrival is the result of the plume invading an ever-increasing volume of Chatsworth Formation sandstone, which provides increased TCE storage capacity. Decreasing the hydraulic gradient from 2% to 1% results in a reduction in the arrival time of the TCE plume front at the end of the model domain by a factor of about 4, from 21 years to 86 years.

A slightly larger model domain of the single fracture case was used to evaluate the effects on arrival time of the TCE solute that result from varying the timeframe over which a DNAPL source is present. This larger model domain was also used to evaluate what changes in TCE concentrations within the plume would result after very long periods of time (e.g., 500 years) when the source has a finite life. The model domain used in these simulations was expanded to 10 m in the z-direction and to 500 m in the x-direction. Input parameters to the model were as follows:

- matrix porosity, $\phi_m = 13\%$
- retardation factor associated with sorption, $R_m = 3.0$
- diffusion coefficient, $D_c = 10^{-6} cm^2/sec$
- hydraulic gradient, $i = 1\%$
- fracture aperture, $2b = 70 \mu m$

Simulations were made using two types of sources:

- A constant source throughout the entire simulation to represent persistent DNAPL, and
- A 10-year finite term to represent DNAPL dissolution. Although the DNAPL phase has disappeared, the TCE mass from the DNAPL remains in the source area for a long time continuing to contribute mass to the plume, but at diminishing concentrations.

The 10-year finite case is believed to more accurately reflect conditions at the SSFL where TCE DNAPL disappears due to matrix diffusion and advective dissolution.

The simulation results show that the maximum concentrations of TCE solute in the plume are greatly reduced when a source of TCE DNAPL is present over a finite period. This effect is graphically presented on Figure 7.3.

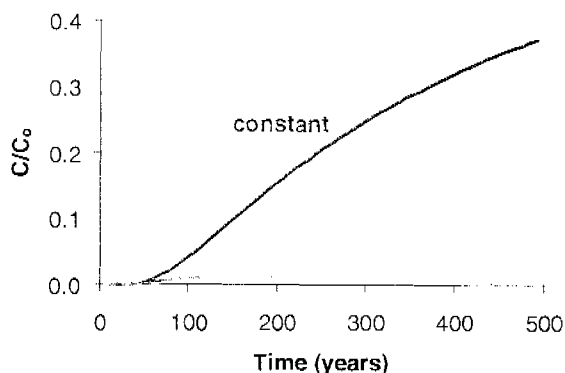


Figure 7.3 Graph of relative TCE concentrations over time for constant and 10-year sources at $x=200$ m. Concentrations in the constant source condition continually increase while the concentrations in the 10-year source condition peak and then gradually decrease. The maximum concentration in the 10-year source condition is also much lower than the constant source condition.

The model results also show that TCE concentrations within the plume naturally attenuate or reduce over time. After several decades, the plume front is essentially stable as its rate of migration has slowed to less than 2 m/year and will continue to migrate at ever-decreasing rates relative to a defined concentration. This effect on plume migration is shown on Figure 7.4

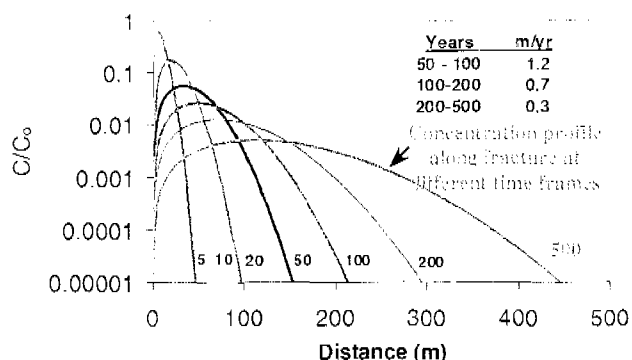


Figure 7.4 Relative TCE concentration profiles along the fracture under the 10-year source condition. Migration rates of the plume front at a C/C_0 of 10^{-5} are also shown for three different time frames.

The results of the simulations presented in this section show the ultimate effects of matrix diffusion and sorption on the fate of TCE. The eventual dissolution of the DNAPL phase indicates the end of the source condition as solute-free groundwater from upgradient of the source zone begins to flush the fractures and reverse the concentration gradient causing diffusion from the matrix blocks back into the fractures (reverse diffusion). The process of reverse diffusion is shown conceptually in Figure 7.5.

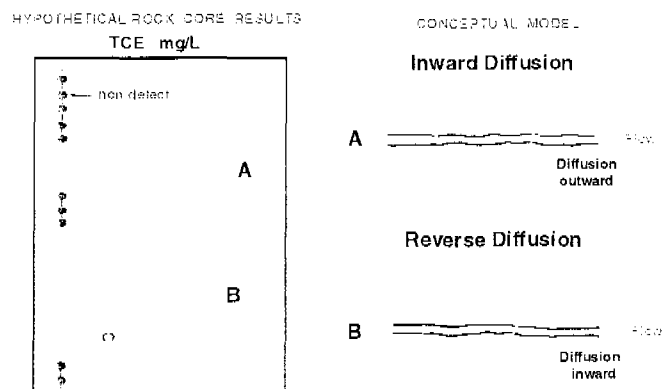


Figure 7.5 Conceptual depiction of diffusion from the matrix bedrock into the groundwater flowing through the fractures (shown as condition 'B'). Note the change in the concentration profile in the hypothetical rock core results. As groundwater passes through the fractures, the pore water concentration in the matrix adjacent to the fracture decrease first, while those deeper into the matrix remain elevated.

The process of flushing the source zone is initiated as the mass is transported downgradient in a much more dilute form, which is also susceptible to matrix diffusion and sorption as it migrates in the plume. This concept gives rise to a fifth stage of the TCE plume development, the first four of which were presented in section 6.0. This stage is characterized as follows:

- **Stage 5: Source Zone is Clean and Plume Front is Stable or Retreating (Figure 7.6).** Groundwater at the original source zone where DNAPL was present no longer contains concentrations exceeding a threshold value. The continually diminishing concentrations in the plume cause the rate of migration of the TCE solute at the plume front to slow considerably or stop. As lower and lower concentrations of TCE continue to diffuse out of the matrix blocks into the clean groundwater flowing in the fracture network from upgradient, the plume will appear to retreat by moving upgradient relative to a defined concentration value (e.g., 0.005 mg/l.). Eventually all areas of the former source zone and plume will contain concentrations of TCE below a defined concentration limit.

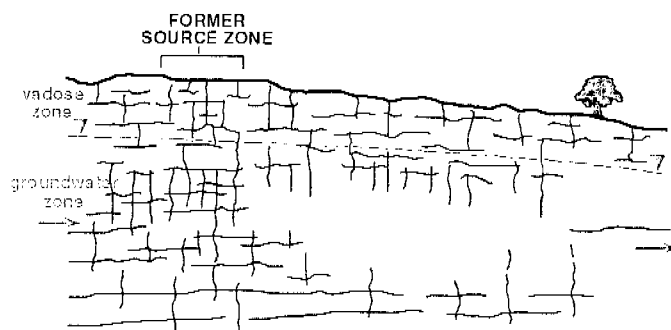


Figure 7.6

Stage 5 Source Zone is Clean and Plume Front is Stable or Retreating

7.2 TCE Solute Transport and Retardation in a Two-Dimensional Fracture Network

The same numerical model was used to simulate the migration of TCE solute in a two-dimensional fracture network. The objective of these simulations was to develop an understanding of the transport and fate of TCE over long periods of time (e.g. 500 years) in an interconnected fracture network of sandstone while using input parameters similar to the Chatsworth Formation. Model properties and input parameters were as follows:

- orthogonal fracture network with variable fracture apertures shown in Figure 7-7, mean aperture, $2b = 70 \mu\text{m}$, minimum aperture less than $30 \mu\text{m}$ and maximum aperture of greater than $250 \mu\text{m}$.
- retardation factor associated with sorption, $R_m = 3.0$
- steady state groundwater flow,
- source constant for 10 years at TCE solubility,
- matrix porosity, $\phi_m = 13\%$
- hydraulic gradient,
 - ✓ horizontal 2%,
 - ✓ vertical = 1%
- diffusion coefficient, $D_e = 10^6 \text{ cm}^2/\text{sec}$,
- bulk hydraulic conductivity,
 - ✓ horizontal: $K_x = 1.5 \times 10^{-5} \text{ cm/sec}$
 - ✓ vertical: $K_z = 3.0 \times 10^{-6} \text{ cm/sec}$ (anisotropy ratio of ~5)
- fracture porosity, $\phi_f = 5.9 \times 10^{-5}$
- average linear groundwater velocity, $v_l = 1.6 \text{ km/yr}$ (1 mile per year)

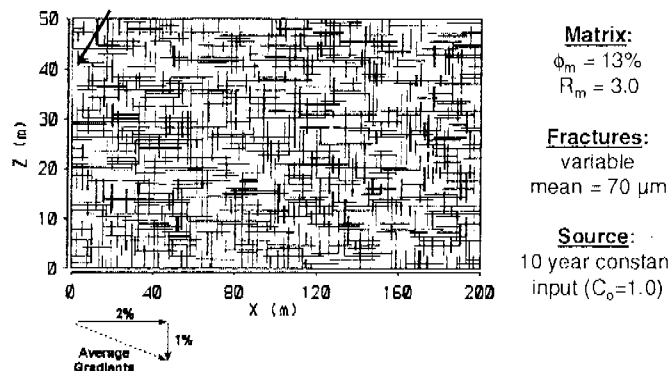


Figure 7.7 Variable aperture network used for two-dimensional vertical simulation of TCE transport.

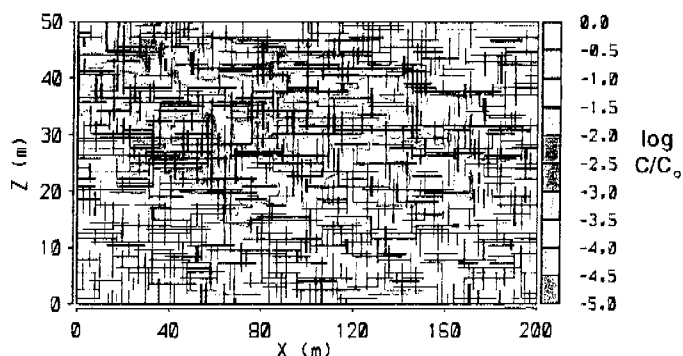


Figure 7.8 TCE plume at 50 years

Simulations were performed for durations extending to 500 years. The graphic output of the model results of the TCE plume at 50 years is shown on Figure 7.8.

Results of the simulations were consistent with those of the single-fracture simulations and revealed the following:

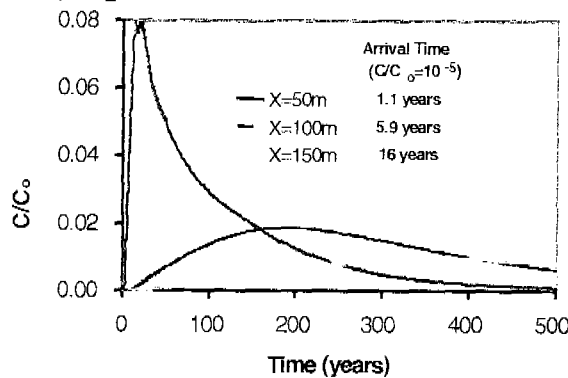
- The maximum concentration of TCE in the plume decreases over time as shown on Table 7.1.

Time (years)	Maximum Relative Concentration in Plume (C/C_0)
20	0.66
50	0.51
100	0.2
500	0.03

Table 7.1 Changes in the maximum relative concentration over time from the two-dimensional modeling simulation.

- The time of arrival of the plume front becomes longer as the distance from the source input increases. Arrival times for fractures containing the highest concentrations of TCE were 1.1, 5.9 and 16 years at distances of 50 m, 100 m and 200 m from the source, respectively. The increasing time of arrival with distances is shown on Figure 7.9.

Figure 7.9 TCE arrival over time for the highest



concentration fracture in the network at a distance of 50m, 100m and 150m from the source. Note that the time when TCE first arrives at each of these locations increases with distance from the source. Note also the shape of the concentration curve at each location where concentration increases, peaks and slowly decreases.

- The concentration at a specified distance from the source decreases over time. As an example, the relative concentration in the fracture containing the highest concentration of TCE at a location 100 m from the source over time is summarized in Table 7.2.

Time (years)	Maximum Relative Concentration (C/C_0) at $x = 100m$
100	0.014
200	0.018
300	0.015
400	0.01
500	0.006

Table 7.2 Changes in the relative concentration of TCE over time in the highest concentration fracture at $x = 100m$

- The area where the TCE source was located no longer contains concentrations above a C/C_0 of 10^{-5} within 500 years indicating the source and plume will naturally attenuate. The results also show that approximately 75% of the mass that entered the system during the 10-year source period remains within the 200 meter model domain after 500 years, which provides supporting evidence that the mass of TCE remains near the input location.

7.3 Comparison of Model Results with Field Data

Vertical TCE concentration profiles are one of the output files that are produced from the modeling simulations. Vertical profiles produced from the simulations were compared to the vertical profiles produced from sampling and analysis of the rock core from RD-35B and RD-46B. These comparisons were made to qualitatively assess whether the model forecasts conditions similar to those observed in the field. Comparison of the vertical TCE profiles from the model with those from the field shows the profiles to be similar in their shape and peak concentrations, as shown on Figure 7.10.

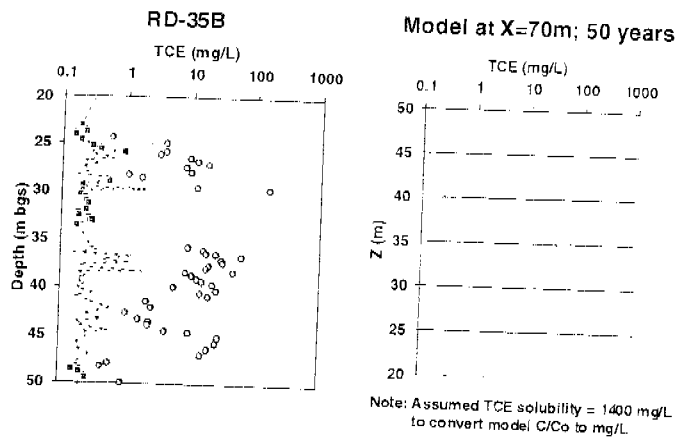


Figure 7.10 Rock core results from RD-35B are compared to hypothetical rock core results from the modeling simulations at a projected distance and time believed to be representative of the conditions at RD-35B. The shape and peak concentrations of TCE in rock pore water between field data and model output are similar.

The rock core results from RD-35B and RD-46B were inspected to determine the current stage of plume migration in Chatsworth Formation groundwater. Inspection of the vertical TCE profiles and fractures at RD-46B indicates that the matrix is releasing TCE back into the groundwater flowing within the fracture network. Rock core concentrations and fracture locations from the core log are shown on Figure 7.11. This "reverse diffusion" process occurs when the concentration gradient between groundwater retained within the sandstone matrix and the groundwater flowing through the fractures is reversed (i.e. water flowing through the fracture network is cleaner than the pore water within the sandstone matrix blocks).

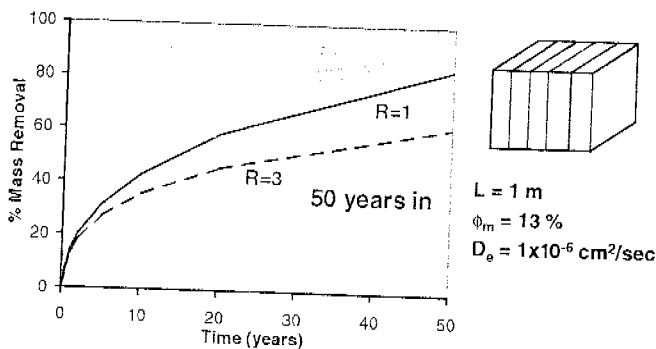


Figure 7.12 Graph of TCE mass removal from tabular matrix blocks over time. Mass removal rates are plotted for two finite-term source conditions, 5 and 50 years. The effects of sorption on the rate of mass removal through reverse diffusion are also plotted on the figure. Note that under the 5 year source condition that approximately 20% of the mass remains in the matrix blocks after 50 years of flushing.

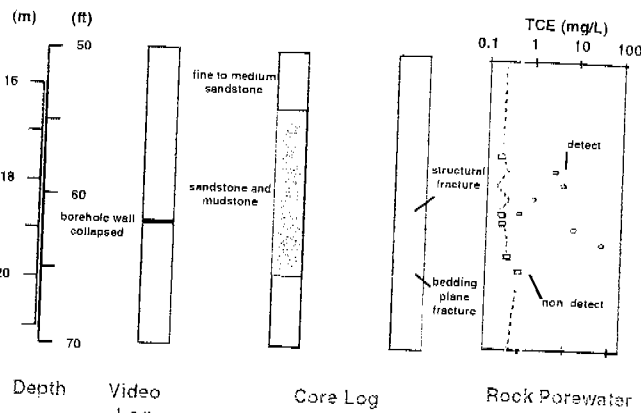


Figure 7.11 Fracture and TCE rock pore water data from RD-46B. Note that the TCE concentrations in rock core immediately adjacent to the fracture are lower than the concentrations deeper into the matrix. These conditions, which were conceptually presented in Figure 7.5, indicate that TCE is diffusing from the matrix into the groundwater flowing through the fractures and are indicative of stage 4 of plume evolution.

Reverse diffusion is characteristic of stage 4 of plume development when no DNAPL remains in the fracture network and plume migration is very slow. Calculations were made using an analytical solution to Fick's second law to evaluate the rate of TCE mass removal from the matrix blocks to groundwater flowing through the fracture network (Parker, McWhorter and Cherry, 1997). A graph of the mass removal rate of TCE from tabular matrix blocks is presented on Figure 7.12. As can be seen from the graph, the rate of diffusion out of the matrix is very slow and the mass removal rate becomes asymptotic with time. This indicates that long time frames are needed for reverse matrix diffusion to transfer the TCE back out of the matrix.

7.4 Summary

Diffusion, sorption and dispersion of TCE solute into the sandstone matrix of the Chatsworth Formation cause the rate of migration of TCE to be orders of magnitude lower than the average linear groundwater velocity within distances of hundreds of feet from the source zone. The rate of migration is very slow (<2 m/yr) or nearly stationary within decades after releases have stopped. Elevated concentrations remain near the input locations. The concentrations in the source zone and plume continue to decline over time (hundreds of years) as mass is transferred back out of the matrix and into groundwater flowing through the fracture network. Rock core data indicates that the plumes at the SSFL are likely in Stage 4. The stages of plume front advancement are conceptually shown on Figure 7.13.

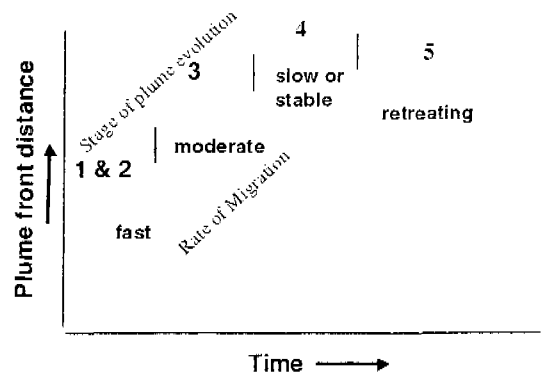


Figure 7.13 Graph of conceptual migration rates of each plume stage over time and distance.

8.0 Monitoring Chatsworth Formation Groundwater

Three characteristics of the Chatsworth Formation are believed to distribute TCE throughout the groundwater system in an orderly and predictable manner. These characteristics produce plumes that can be detected, characterized and monitored and include:

- An interconnected fracture network,
- Strong retardation of the plume as a result of matrix diffusion and sorption and,
- Distributory influence of dispersion on solute behavior.

Additional descriptions on the applicability of groundwater monitoring are provided in Appendix G.

8.1 Interconnected Fracture Network

Several different lines of evidence of an interconnected fracture network were previously presented in section 4.7. Additional information on the interconnected fracture network of the Chatsworth Formation has been developed from the sampling and analysis of rock core. All data that were collected during the rock coring program were reviewed to determine whether the TCE identified in the rock core was associated with transport of the TCE through the fracture network or through sandstone beds having higher permeability due to coarser grain sizes. Data that were assimilated to make this determination included: inspection and description of the rock core to identify fractures, advanced downhole geophysical methods that provided data as to whether fractures were open, their orientation and groundwater flow characteristics (rate and direction) within fracture zones.

In summary, as shown in Figure 8.1, these data show transport of TCE in many fractures in both boreholes, along with transport through a number of more permeable sandstone beds. TCE transport through many fracture indicates that the fracture network is interconnected.

8.2 Plume Retardation

The effects that matrix diffusion and sorption have on retarding the migration rate of TCE solute relative to the average linear groundwater velocity were presented in section 7.0 and are fully discussed in Appendix E. Strong retardation primarily effects the ability to monitor the groundwater because the highest concentrations remain near the input location and the plume front will have migrated only short distances from the input location relative to the average linear groundwater velocity. The large capacity of the rock matrix to store TCE results in the broad, three-dimensional distribution of TCE solute within the fracture network as well as within the rock matrix as shown in Figure 8.2. The large spatial distribution results in a "plume" of TCE that can be located, characterized and, if necessary, delineated. Placement of an appropriately designed monitoring device within the "plume" would provide useful and reproducible information as to the presence and concentration of TCE solute migrating at any location within the fracture network.

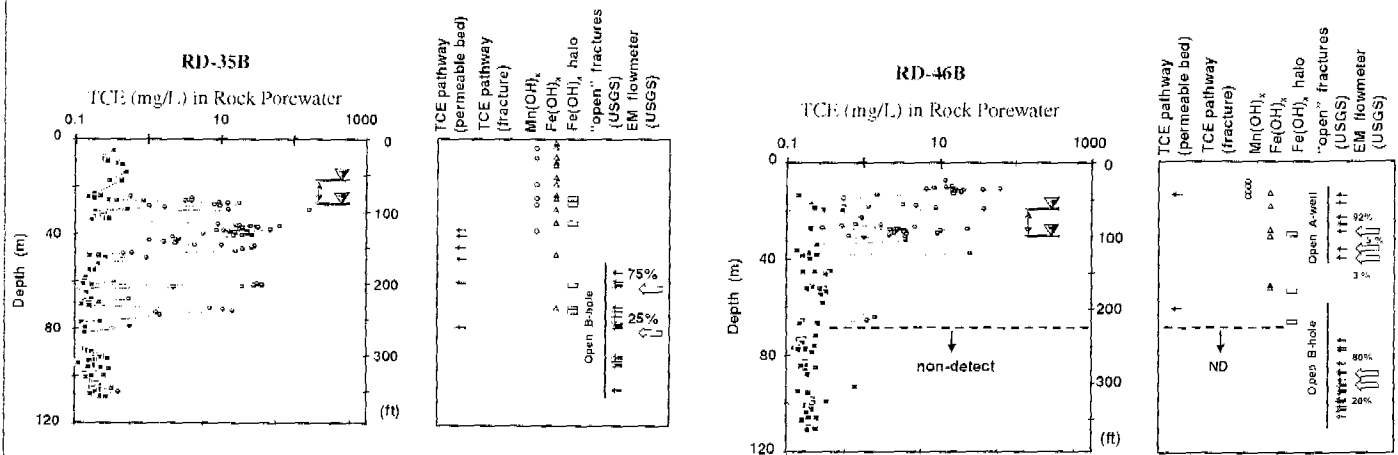


Figure 8.1 Evidence of Migration Pathways in RD-35B and RD-46B

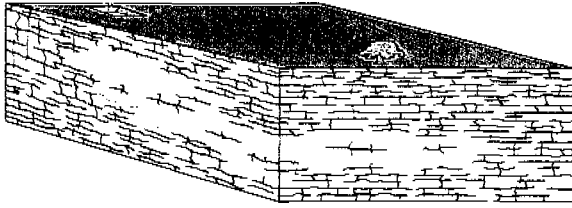


Figure 8.2 Schematic of Plume in Fractured Sandstone

This concept of a "plume" that results from the broad spatial distribution of TCE due to the interconnected fracture network and matrix diffusion was further explored using the discrete-fracture numerical model discussed in section 7.0. Additional simulations of the transport of TCE solute were performed in plan view. These simulations were performed to evaluate the pattern and extent of TCE distribution that would result in a fracture network consisting of a single plane through a "plume" in the fractured sandstone. The model domain in this simulation was 200 meters by 200 meters in the "x" and "y" directions. Other input parameters are as follows.

- uniform fracture apertures of 100 microns,
- constant source input,
- matrix porosity $\phi_m = 13\%$,
- diffusion coefficient $D_c = 1 \times 10^{-6} \text{ cm}^2/\text{sec}$,
- retardation factor associated with sorption $R_m = 3$,
- hydraulic gradient, 1%
- bulk hydraulic conductivity, $K_b = 1 \times 10^{-5} \text{ cm/sec}$

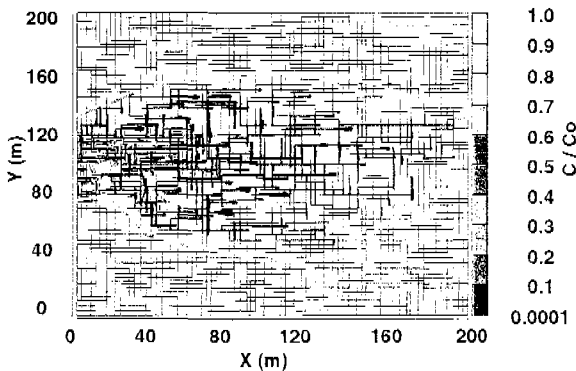


Figure 8.3 Plan View Simulation Results of Plume in Sandstone at 50 Years

The results of the modeling simulations are shown in Figure 8.3 and reveal that matrix diffusion and sorption causes the TCE solute to migrate slowly through the fracture network,

thus allowing ample time to locate the downgradient extent of the plume and monitor its further migration.

The results presented in these simulations need to be considered within the context of the vertical section simulations discussed in section 7.2 (See Figure 7.8). The vertical and horizontal simulations can be considered within the context of three-dimensional space where numerous horizontal and vertical simulations represent planes or unique slices that would collectively comprise a plume. Output from the vertical simulations showing the TCE distribution in rock pore water was used to demonstrate that a monitoring device intercepting the plume would detect the TCE solute in the groundwater (Figure 8.4) These demonstrations confirm that TCE migrating through the fracture network can be located and monitored.

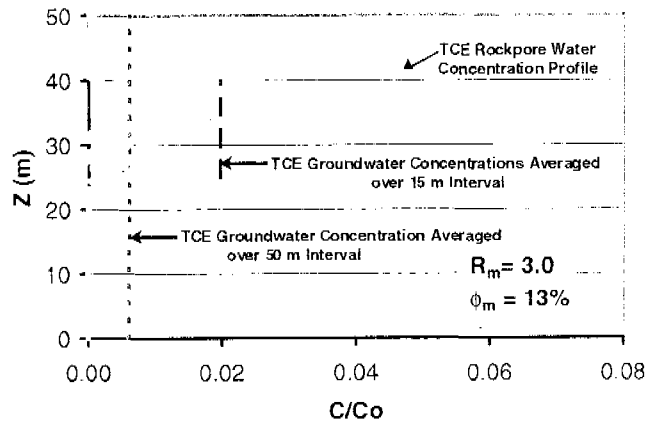
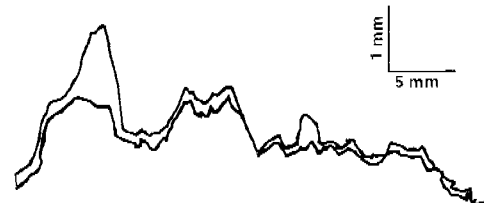


Figure 8.4 Vertical TCE Profile at X=50m after 50 years in rock porewater and in hypothetical monitoring wells with 15 and 50 m open intervals

8.3 Dispersion

Dispersion of TCE in the groundwater flowing through the fracture network has a distributory effect, i.e. the TCE becomes more broadly distributed throughout the fracture network. Dispersion is a result of molecular diffusion and



Source: NRC 1986

Figure 8.5 Variability of Fracture Aperture (Distance Between Opposing Surfaces)

hydraulic mixing. Dispersion causes the solute concentration to decline and expand into a larger volume of groundwater than would occur only by flow (or advection). Dispersion occurs within the fracture network at two different locations: within the fracture plane and at fracture plane junctions.

Conceptually, dispersion occurs within the fracture plane due to the variability in the aperture opening (see Figure 8.5). This varying opening causes groundwater to travel on a molecular scale through different flow paths that are separated by closed contacts within the fracture plane thus creating a channeling effect. As TCE is dissolved into the groundwater flowing at different rates through the channels in the fracture plane, plume "segments" are created that have varying lateral concentration gradients as shown in Figure 8.6. The lateral concentration gradients produce dispersion within the fracture plane transverse to the direction of groundwater flow.

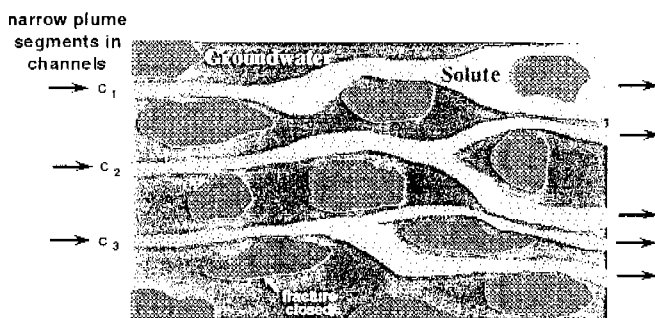


Figure 8.6 Conceptualization of Dispersion Due to Channeling in Single Fracture Plane

A field experiment was performed to evaluate the extent of dispersion within a single fracture plane at a site in Canada (Lapcevic, Novakowski and Sudicky, 1999). The experiment was initiated by injecting a tracer into groundwater flowing within the fracture plane and showed

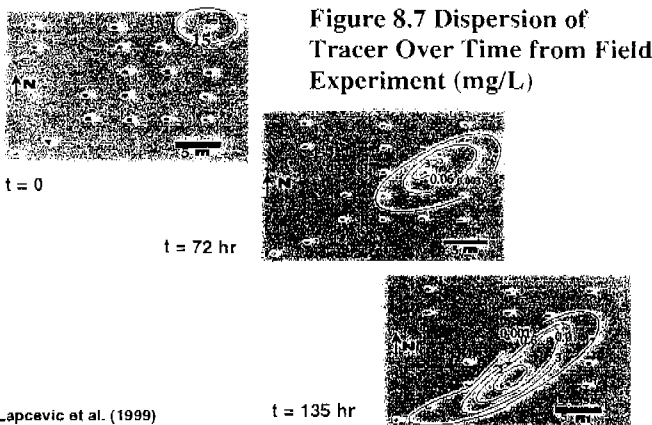


Figure 8.7 Dispersion of Tracer Over Time from Field Experiment (mg/L)

that the tracer spread both laterally and longitudinally in the mean groundwater flow direction (Figure 8.7). Transverse dispersion caused the plume to widen two to three times the source diameter and was attributed to groundwater velocity variations and closure of the fracture surfaces, which created tortuous flow paths.

Dispersion is also expected to occur at the intersection of two fracture planes due to mixing of groundwater as shown in Figure 8.8. Laboratory experiments show that complete mixing at the intersection of fracture planes is instantaneous even under laminar flow conditions (Krizek, Karadi and Socias, 1972 and Castillo, Krizek and Karadi, 1972). Instantaneous mixing is attributed to diffusion caused by waters containing different concentrations of the solute at the intersection.

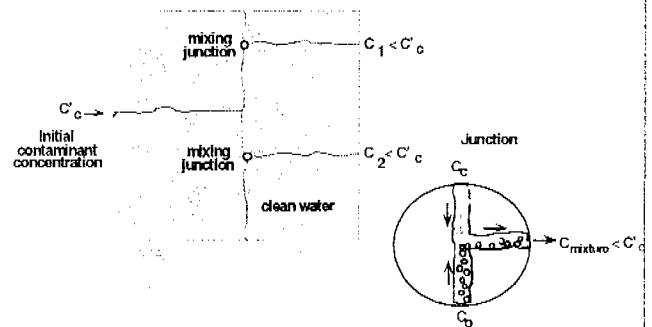


Figure 8.8 Conceptualization of Dispersion Due to Mixing at Fracture Junctions

This phenomenon causes the solute to spread orthogonal to the general direction of groundwater flow (transverse dispersion). The effects of transverse dispersion can be seen in the plan view simulations of the transport of TCE solute as shown on Figure 8.3. As TCE migrates downgradient, the width of the plume expands when compared to the plume width at the source.

The combined effects of dispersion within the fracture plane and at fracture plane junctions result in distributing TCE broadly throughout the fracture network, thereby increasing the ability to detect the plume as it migrates from the source.

8.4 Temporal and Spatial Monitoring

The effects on the transport of the TCE solute that are produced by matrix diffusion, sorption and dispersion, indicate that variations in dissolved TCE concentrations

over time are expected to be small. This is particularly true at the SSFL where the releases occurred decades ago and the TCE migration rates likely are in the range of a few feet per year. Variations in TCE concentrations over time (years to decades) will be small (less than an order of magnitude) because of diffusion of the TCE from the matrix back into the groundwater system. Figure 8.9 and 8.10 are concentration plots over time from the numerical simulations of the transport of TCE solute that reflect the slight variations in concentrations over long time frames (100 years).

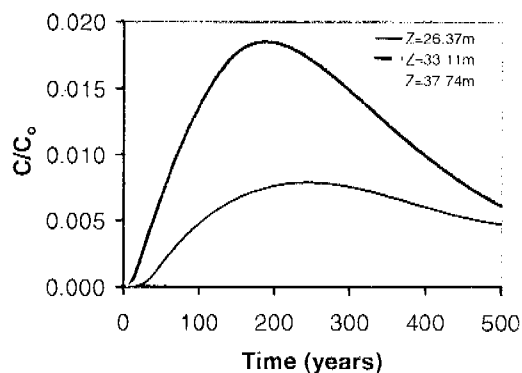


Figure 8.9 Plots of relative TCE concentrations over time in individual fractures at $x=100$ meters from 2-dimensional vertical modeling simulations. Note the simulations predict little variation in concentrations over a 100 year period.

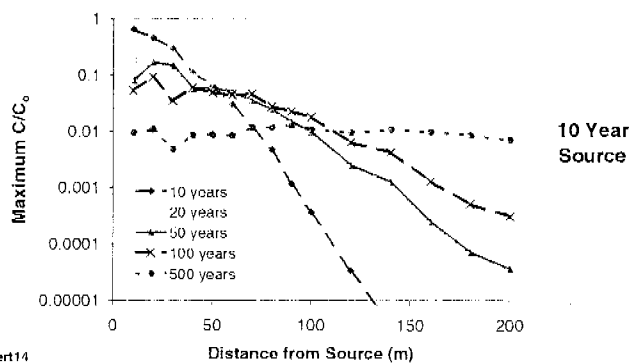


Figure 8.10 Maximum concentration over time and distance plots of TCE from single fracture modeling simulation. After 20 years, note the small variations in concentrations over long time frames at almost any distance from the source.

This understanding of the TCE migration rate indicates that periods between groundwater sampling and analysis events could be much longer than the current quarterly or even annual monitoring schedule. Variations in TCE concentrations produced by samples collected from existing monitoring wells are likely the result of several different factors that include:

- Differences in the volume of rock from which the sample was drawn based on variations in the well purge volumes between sampling events (see Figure 8.11) and,
- Changes in the groundwater flow system (e.g., changes in the groundwater extraction program) that effect the static water levels in the wells.

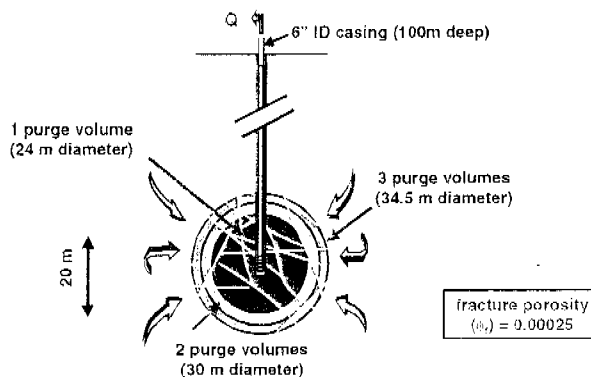


Figure 8.11 Estimated Volumes of Rock Influenced by Changes in 1 to 3 Purge Volumes

Data produced from conventional groundwater monitoring methods are difficult to interpret with regards to the spatial distribution of TCE in the groundwater. In light of the conceptual model presented in this technical memorandum, more mass is likely present in the groundwater system and sandstone matrix than can be accounted for by the dissolved concentrations in the groundwater produced by the existing monitoring well network. Efforts on groundwater characterization and monitoring in the future need to utilize new sampling and monitoring technologies which are currently available, most of which were applied at RD-35B and RD-46B.

9.0 Summary of Conceptual Site Model

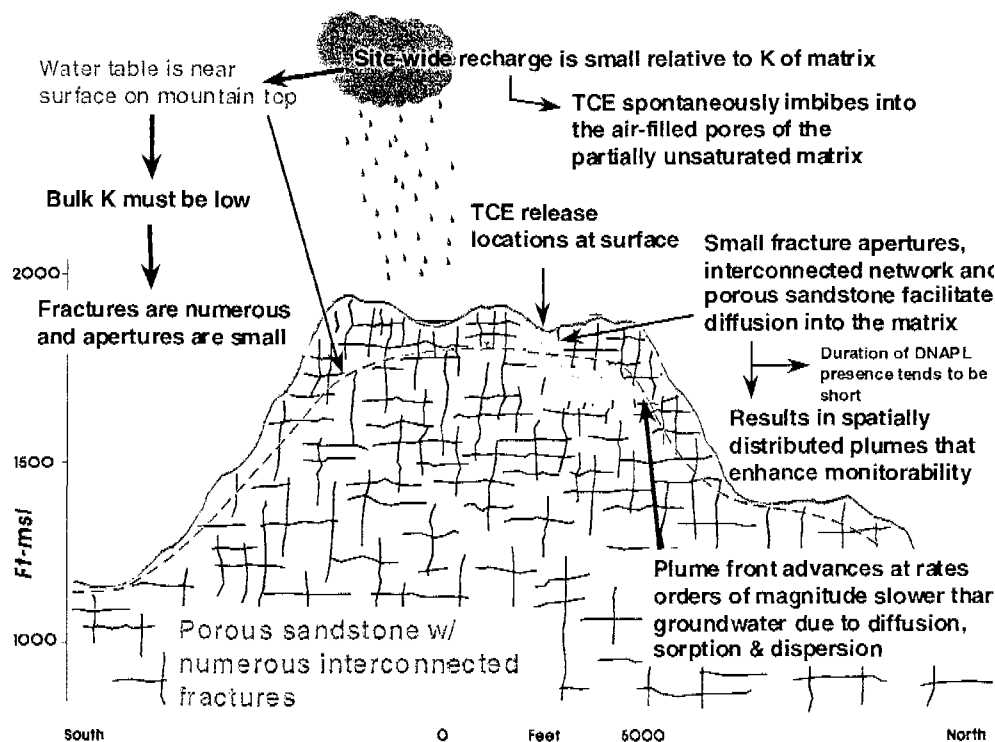
This technical memorandum has presented a conceptual model of the movement of TCE at the SSFL. The effects of the geology, hydrogeology and TCE diffusion, sorption and dispersion were considered. A summary is provided below.

1. *The fractures at the SSFL are small, systematic and interconnected.*

- Calculations of the hydraulic fracture apertures were made using site values for hydraulic conductivity and fracture spacing. Hydraulic apertures ranged from 10 to 300 microns, with a mean value of about 100 microns.
- Frequent and systematic fractures are present as evidenced by inspections of outcrops and rock core, downhole geophysics tests and the distribution of TCE in rock pore water adjacent to fractures.
- Fracture systems are interconnected as indicated by pumping test analyses, a hydraulic communication study, groundwater elevation correlations and the presence of TCE in rock pore water at numerous depths throughout the vertical profile of two test boreholes.
- Analysis of pumping test data indicated a lack of any high hydraulic conductivity zones along lineaments, suggesting that extensive open fractures do not exist.

2. *The small, systematic and interconnected fractures, coupled with the porous sandstone matrix, facilitates diffusion of TCE into the matrix.*

- Diffusion into the sandstone matrix at the SSFL has been documented by chemical analysis of 277 samples of rock core for VOCs. Samples were collected from two boreholes placed near TCE input locations. All TCE concentrations detected in rock pore water were no more than 10% of the aqueous solubility limit for TCE. These data support the conclusion that little to no DNAPL is present in fractures below the water table.
- 3. *TCE plume fronts are strongly retarded due to matrix diffusion and the presence of organic carbon, and advance at rates that are orders-of-magnitude slower than the average linear groundwater velocity.*
- Inspection of 15 years of groundwater chemistry data shows that TCE has not migrated far from the input locations. Maximum concentrations are also near the input locations.
- Numerical modeling simulations for TCE migration through fracture networks using properties representative of the conditions at the SSFL, predict strong retardation of the TCE plume front as it migrates downgradient from the input location. The simulations also predict an overall decline in concentrations throughout the source zones and plumes.
- Inspection of the distribution of TCE in the rock core at RD-46B indicates that the plumes at the SSFL are most likely in stage 4, which is characterized by the plumes migrating very slowly and becoming stable.



The conceptual model describing the evolution of the TCE source zone and plume, developed in this document and applied to the Chatsworth Formation at the SSFL, is supported by the mathematical modeling and field data. However, some parts of the model will require additional support. Additional field data will be acquired and mathematical modeling performed to substantiate this conceptual site model.

Figure 9.1
Graphic Depiction of
Conceptual Site Model

10.0 References

- Dibblee, T. W., 1992. Geologic Map of the Calabassas Quadrangle, Los Angeles and Ventura Counties. Dibblee Geologic Foundation Map DF-37
- DOE, 1989. U.S. Department of Energy, *Environmental Survey Preliminary Report*. DOE Activities at the Santa Susana Field Laboratories, Ventura County, California, February 1989
- EPA, 1993. U.S. Environmental Protection Agency, *Guidance for Evaluating the Technical Impracticability of Ground-Water Restoration, Interim Final*, EPA Directive 9234.2-25, September 1993
- Freeze, R. Allen and John A. Cherry, 1979. *Groundwater* (a textbook). Prentice-Hall, Englewood Cliffs, NJ 604 pp
- Foster, S.S.D. 1975. The Chalk groundwater tritium anomaly-A possible explanation. *Journal of Hydrology*, v. 25, pp 159-165
- Groundwater Resources Consultants, Inc. 1993. *Soil Sampling, Area I/Thermal Treatment Unit, June 1993*. Santa Susana Field Laboratory, Rocketdyne Division, Rockwell International Corporation, Ventura County, California, August 16, 1993.
- ICF Kaiser Engineers. 1993a. *Current Conditions Report and Draft RCRA Facility Investigation Work Plan, Areas I and III*, Santa Susana Field Laboratory, Ventura County, California, October 1993.
- ICF Kaiser Engineers. 1993b. *Current Conditions Report and Draft RCRA Facility Investigation Work Plan, Area II and Area I LOX plant*, Santa Susana Field Laboratory, Ventura County, California, October 1993.
- ICF Kaiser Engineers. 1993c. *Current Conditions Report and Draft RCRA Facility Investigation Work Plan, Area IV*, Santa Susana Field Laboratory, Ventura County, California, October 1993.
- Kirkpatrick, Glen A. 1998. Infiltration, Migration and Phase Transfer of Common DNAPLs in Naturally Fractured Clayey Aquitard: Field Experiments. M.Sc. Thesis, Department of Earth Sciences, University of Waterloo, Waterloo, Ontario, Canada
- Lapevic, P.A., K.S. Novakowski and E.A. Sudicky, 1999. The interpretation of a tracer experiment conducted in a single fracture under conditions of natural groundwater flow. *Water Resources Research*, Vol. 35, No. 8, pp. 2301-2312.
- Link, M. H., Squires, R. L., Colburn, I. P., 1981. Simi Hills Cretaceous Turbidites, Southern California, Field Trip Guide published by the Pacific Section of the Society of Economic Paleontologists and Mineralogists.
- National Research Council Committee on Fracture Characterization and Fluid Flow, 1996. *Rock Fractures and Fluid Flow. Contemporary Understanding and Applications*, National Academy Press
- Ogden Environmental and Energy Services Co., Inc., 1996. *RCRA Facility Investigation Workplan Addendum*, Santa Susana Field Laboratory, Ventura County, California, Volume II, Appendix C RFI Field Sampling Plans, September 1996
- Ogden Environmental and Energy Services Co., Inc., 1999. *RCRA Facility Investigation, Preliminary Soil Sampling Results*, Santa Susana Field Laboratory, Ventura County, California, December 1999
- O'Hara S.K., B.L. Parker, J.A. Cherry and P.R. Jorgensen, 2000. Trichloroethene DNAPL flow and mass distribution in naturally fractured clay: Evidence of aperture variability. *Water Resources Research*, Volume 36, Number 1, pp 135-147
- Pankow, J.F. and J.A. Cherry, 1996. *Dense Chlorinated Solvents and other DNAPLs in Groundwater*, Waterloo Press, 1996
- Parker, Beth L., Robert W. Gillham and John A. Cherry, 1994. *Diffusive Disappearance of Immiscible Phase Liquids in Fractured Geologic Media*, *Ground Water*, Volume 32, Number 5, September-October 1994
- Parker, Beth L., David B. McWhorter and John A. Cherry, 1997. *Diffusive Loss of Non-Aqueous Phase Organic Solvents from Idealized Fractured Networks in Geologic Media*, *Ground Water*, Volume 35, Number 6, November-December 1997
- Rocketdyne, undated. *Water Supply and Usage for Rocketdyne Propulsion Field Laboratory*, BCI 63-224 (Likely 1963)
- Sage, O.G., Jr. 1971. Geology of the Eastern Portion of the "Chico" Formation, Simi Hills, California (M.A. thesis); University of California at Santa Barbara
- Snow, David T., 1968. Rock fracture spacings, openings and porosities. In *Proceedings of the American Society of Civil Engineers, Journal of the Soil Mechanics and Foundations Division*, Volume 94:73-91
- Sterling, S.N., 1999. Comparison of Discrete Depth Sampling Using Rock Core and a Removable Multilevel System in a TCE Contaminated Fractured Sandstone. M.Sc. Thesis, Department of Earth Sciences, University of Waterloo, Waterloo, Ontario, Canada
- Sudicky, E.A. and R.G. McLaren, 1992. The Laplace Transform Galerkin Technique for large-scale simulation of mass transport in discretely fractured porous formations. *Water Resources Research*, 28(2): 499-514
- VanderKwaak, J.E. and E.A. Sudicky, 1996. *Dissolution of non-aqueous phase liquids and aqueous-phase contaminant transport in discretely-fractured porous media*. *Journal of Contaminant Hydrogeology*, 23: 45-68.

TECHNICAL MEMORANDUM

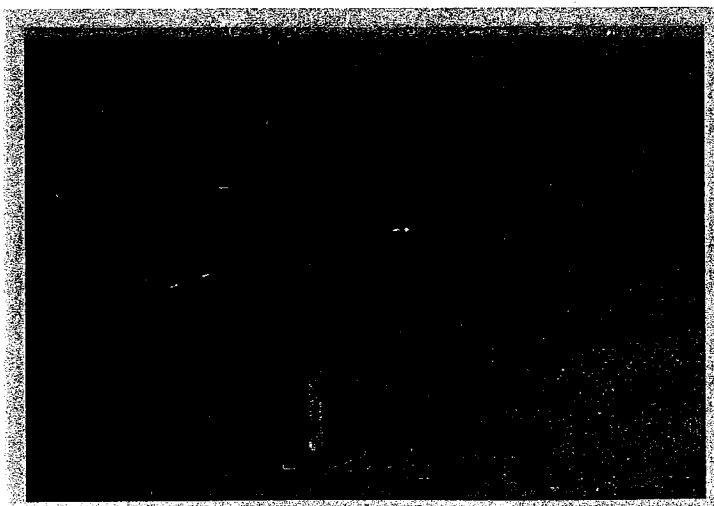
Conceptual Site Model Movement of TCE in the Chatsworth Formation

Volume II of III



April 2000

Prepared by
Montgomery Watson for
The Boeing Company
Santa Susana Field Laboratory
Ventura County, CA



Appendix A

Geologic Characterization Santa Susana Field Laboratory Ventura County, California

April 2000

Prepared for
The Boeing Company
Rocketdyne Propulsion and Power
6633 Canoga Avenue
Canoga Park, CA 91309-7922

Prepared by
Montgomery Watson
1340 Treat Boulevard
Suite 300
Walnut Creek, CA 94596

CONTENTS

1.0	GEOLOGIC CHARACTERIZATION.....	1
1.1	Regional Geologic Setting	1
1.2	Depositional Environment of the Chatsworth Formation	1
1.3	Stratigraphy of the Chatsworth Formation.....	3
1.3.1	Lower Chatsworth Formation	3
1.3.2	Upper Chatsworth Formation.....	4
1.3.3	Shales of the Upper Chatsworth Formation	5
1.3.4	Definition of Sandstone 1 and Sandstone 2	6
1.4	Faults.....	6
1.4.1	Geologic Characteristics of the Shear Zone	6
1.4.2	The Skyline Fault	8
1.4.3	The North Fault	8
1.4.4	The Happy Valley Fault	9
1.4.5	The Tank Fault	9
1.4.6	The Coca Fault	10
1.4.7	The Burro Flats Fault	11
1.5	Joints	11
1.5.1	Joint Spacing	13
1.5.2	Joint Orientation.....	13
1.5.3	Joint Continuity and Inferred Groundwater Flow Patterns	13
1.5.4	Joint Characteristics of Sandstones and Shales.....	15

Figures

1. Regional Geologic Setting
2. Depositional Environment
3. Geologic Map of SSFL
4. SSFL Stratigraphic Column
5. Measured Stratigraphic Sections at SSFL
6. Cross Section through Coca Shale
7. Observations of Joint Spacing at SSFL
8. Rose Diagrams of Joint Orientation
9. Site Wide Rose Diagram of Joint Orientation from Aerial Photos and Outcrops
10. Rose Diagrams of Stratigraphic Units at SSFL

1.0 GEOLOGIC CHARACTERIZATION

The geologic setting of the Santa Susana Field Laboratory (SSFL) was characterized by completing the following tasks:

- Reviewing existing geologic literature,
- Developing a geologic map of the SSFL by field examination of rock exposures and other geologic features such faults and joints and a review of boring logs, rock core and other subsurface geologic information,
- Viewing aerial photographs of the site to evaluate large-scale geologic features and to verify the areal extent of the geologic features that were identified during performance of the fieldwork.

1.1 Regional Geologic Setting

The SSFL is located in the Transverse Ranges of Southern California, a geologic province that is in north-south compression and in which geologic structures, such as faults and folds, strike in an approximately east-west direction. Most of the site is underlain by late Cretaceous Chatsworth Formation. The Chatsworth consists of interbedded sandstone and shale that are interpreted to have been deposited by marine turbidites (Link, Squires and Colburn, 1981; Dibblee, 1992). As shown in Figure 1, the Chatsworth Formation is conformably or disconformably overlain by the Simi Conglomerate Member of the Paleocene Santa Susana Formation in the northern part of the site, and is faulted against the Santa Susana Formation in the western part of the site. To the south the Chatsworth is unconformably overlain by southward dipping late Tertiary Formations.

Structurally, the facility is located on the south flank of an east-west striking and westward plunging syncline which passes through the central part of Simi Valley. Bedding at the site typically strikes approximately N70E and dips 25 to 35 degrees to the northwest. Faults within the facility typically strike either in a generally east-west direction, or in a northeast-southwest direction (Figure 1). Information derived from published literature and measurements taken in the field indicate that all of these structures dip steeply, typically more than 70 degrees.

1.2 Depositional Environment of the Chatsworth Formation

Existing interpretations of the depositional environment of the Chatsworth Formation suggest that it was deposited on the surface of a sand-rich, submarine fan at water depths between approximately 600 and 3,000 feet below sea level (Link et al, 1981). In a

1.3 Stratigraphy of the Chatsworth Formation

A field evaluation of the stratigraphy of the Chatsworth Formation was conducted in late February and early March of 1999. This effort was followed by several short, focused field visits to provide detailed information on some of the stratigraphic units at the site. The goal of this effort was to define stratigraphic units that might influence groundwater flow and contaminant distribution at the SSFL.

1.3.1 Lower Chatsworth Formation

The lower Chatsworth Formation is found stratigraphically below the upper Chatsworth, in the southern and eastern part of the SSFL (Figure 3). The lower Chatsworth is distinctly finer-grained than the upper Chatsworth. It typically underlies a gentler topography than does the upper Chatsworth, and outcrops are normally rarer in the lower than the upper Chatsworth (Photograph A-1 and Figure 4).

The contact between the upper and lower Chatsworth Formation is gradational with interbedding between the thick relatively coarse grained sandstones of the upper Chatsworth Formation and the relatively fine grained sediments of the lower Chatsworth. In the area to the east of the Shear Zone (Figure 3), the contact is interpreted to lie at the lowermost of the coarser grained upper Chatsworth sandstones. The sandstones of the upper Chatsworth Formation are, however, lenticular, and the contact shown on Figure 3 does not follow a single stratigraphic horizon, but it is a line that defines an envelope around the lowermost of the coarser grained upper Chatsworth sandstones.

Scattered outcrops of the lower Chatsworth Formation show it to consist of two kinds of lithologies. Part of the formation consists of relatively thin, medium to coarse grained, and locally pebbly sandstones similar to those found in the upper Chatsworth. These coarser-grained sandstone beds are typically less than 20 feet thick and lenticular. The sandstones typically cannot be traced more than a few hundred feet laterally. Although sandstones similar to those of the upper Chatsworth Formation are present, the predominant lithology in the lower Chatsworth consists of interbedded fine grained sandstone, siltstone and shale. Within these finer grained parts of the lower Chatsworth, individual beds typically range from 1 to 6 feet thick, and about half of the rock are composed of siltstone and shale (Photograph A-2).

Two stratigraphic sections have been measured from exposures in Woolsey Canyon, and both of these sections show significant fine-grained material in the lower Chatsworth Formation (Figure 5). The section of Colburn, Saul, and Almgren (presented in Link et

1.3.3 Shales of the Upper Chatsworth Formation

Although most of the shales in the upper Chatsworth Formation are lenticular, several show significant lateral continuity. These shales are important both because hydrologic evidence (see Appendix B) suggests that they are aquitards because some of the shales provide stratigraphic markers which separate sandstones with different hydrologic properties. Five relatively continuous shale units are currently recognized at the SSFL. Shales 1, 2 and 3 are located in a relatively unfaulted stratigraphic sequence in the northcentral part of the site, and the stratigraphic position of these three shales can be established. Two other shales (The Happy Valley and Coca Shale) are separated from Shales 1, 2 and 3 by faults, and their relative stratigraphic position is currently unknown.

Shale 1 is located in the south-central part of the SSFL (Photograph A-4). As shown in Figure 3, it can be traced for approximately 4,000 feet to the northeast of the Coca Fault, and, although exposures are poor, apparently pinches out in the vicinity of well RD-47. Shale 1 can be subdivided into two separate shale beds shown as Shales 1A and 1B on Figure 3. Shale 1B bifurcates near its easternmost end, passing stratigraphically above and below a sandstone unit. It is likely that the southwestward pinch-out of the sandstone bed occurs at the western edge of a sand-filled, submarine channel that is located to the east of the pinch-out.

Shale 2 passes through the central part of the site, and is well exposed along Black Canyon Road (Photograph A-4). Shale 2 locally consists of at least two individual shale beds that are separated by sandstone. Although exposures are poor, field relationships suggest that Shale 2 is never less than 50 to 100 feet thick even though individual shale beds pinch out.

Shale 3 is located at the top of the Chatsworth Formation, stratigraphically below the Simi Conglomerate Member of the Santa Susana Formation. Like Shale 2, Shale 3 consists of multiple shale beds, some of which pinch out along strike. Field observations and the review of aerial photographs suggest that Shale 3 is never less than 50 to 100 feet thick even though individual shale beds pinch out. Although not shown on Figure 3, ground traverses to the northeast and an evaluation of the aerial photographs show that Shale 3 extends at least as far to the northeast as Black Canyon Road.

The Happy Valley Shale is located in the eastern part of the SSFL, just east of the Shear Zone and south of the Happy Valley Fault (Figure 3). Limited outcrops show the shale to consist of interbedded clay shale and sandstone. Clay shale makes up approximately half of the unit, and bedding is typically less than approximately 1 foot thick (Photograph A-

Exposures of the Shear Zone are present at four widely separated locations. These locations are:

- Black Canyon Road, southwest of the RD-39 well cluster,
- Immediately east of well WS-14,
- Immediately north of the well RD-45 cluster and,
- Immediately north of well RD-3.

All of these exposures show a 25- to 50-foot wide zone of intense fracturing. The fractures are typically spaced less than one inch apart, and commonly have a preferred orientation that is approximately parallel to the mapped trace of the fault. Caliche is common along fracture surfaces locally being as much as 1-2 feet thick near the ground surface. Gouge is also present along some of the fractures. Locally, gouge zones reach a thickness of more than one foot (Photograph A-6). In the vicinity of the well RD-45 cluster, good exposures show that to the east of the closely fractured rock, there is a zone at least 50 feet wide with well developed fractures running nearly parallel to the Shear Zone boundary. These well developed fractures are spaced from 1 to 3 feet apart, are near vertical, and have a well developed iron oxide stain that is typically present adjacent to the fractures.

The magnitude and direction of displacement on the Shear Zone is not known due to a lack of identifiable stratigraphic units that have been displaced. Although the total displacement on the Shear Zone is unknown, the lack of displacement (or very small displacement) on Shale 2 along the northeastward projection of the structure (Dibblee, 1992) suggests that the total displacement is relatively small (i.e. less than 100 feet). Field observations suggest that there is an apparent left lateral displacement of the Shear Zone. The observations that lead to this suggestion are the offsets of pebbly sandstones on either side of the failure surfaces within the Shear Zone.

The lateral extent of the Shear Zone is inferred from both geomorphic and geologic features. Geomorphically, the outcrops of the Shear Zone are all located in the bottom of a valley, suggesting that the valley was created by erosion of the fractured rocks of the Shear Zone. The valley extends from the vicinity of the RD-39 well cluster in the northeast to the Coca Fault in the southwest. Exposures are poor, but no evidence for the presence of the Shear Zone was found to the south of the Coca Fault, and on that basis the Shear Zone is interpreted to end at the Coca Fault. Dibblee (1992) shows no displacement of Shale 2 to the northeast of the RD-39 well cluster, and a reconnaissance of the same area during this evaluation was consistent with Dibblee's mapping. On this basis, the

The lateral extent of the North Fault is inferred primarily from its geomorphic expression. To the east of the intersection between the North Fault and Shale 2, the fault projects along a very linear drainage that ends in the vicinity of the Shear Zone. On the basis of the end of the linear drainage and the absence of evidence of the North Fault being present to the east of the Shear Zone, the North Fault is interpreted to terminate against the Shear Zone. To the west, the North Fault projects along a linear drainage into the vicinity of well WS-12. The drainage becomes less linear to the west of well WS-12, and the western extent of the North Fault is interpreted to be just west of this well.

1.4.4 The Happy Valley Fault

The Happy Valley Fault is an east-west striking structure located in the eastern part of the SSFL, on the east side of the Shear Zone (Figure 3). The structure creates a well-developed aerial photo lineament and is exposed in both road cut and natural exposures. Road cut exposures show the fault to strike between N80W and N85W and to dip between 70 and 75 degrees to the north (Photograph A-7). The fault zone as exposed in the road cuts ranges from 3 inches to as much as 1.5 feet wide, with the material within the fault zone consisting of a brown, sandy silt gouge. There is no well-developed zone of fractures adjacent to the fault. Poorly developed striae that are parallel to the dip of the fault are present.

The western end of the Happy Valley Fault is interpreted to be at the Shear Zone, because of the absence of an aerial photo lineament along strike of the Happy Valley Fault on the west side of the Shear Zone. The eastward extent of the Happy Valley Fault is not currently known. Displacement on the Happy Valley Fault is currently unknown because mapping of the Happy Valley Shale has not been completed.

1.4.5 The Tank Fault

The Tank Fault is an approximately east-west striking structure that is located north of the Coca fault in the south-central part of the SSFL (Figure 3). The fault creates a well-developed aerial photo lineament, and it is relatively well-exposed in artificial exposures near the intersection of the Tank Fault and the Skyline Fault. These exposures show the Tank Fault to consist of 6 to 8 failure surfaces spread across an approximately 10 foot wide zone (Photograph A-8). The failure surfaces strike approximately N 80 W and dip more than 75 degrees to both the north and south. Striae are present on some of the Tank Fault failure surfaces. All of the observed striae are approximately parallel to the dip of the fault.

the fault, and are spaced less than three inches apart. Elsewhere the zone of fractures is as much as 30 feet wide and fractures are spaced from 5 to 10 feet apart. These fractures are near vertical, closed, and are commonly strongly mineralized with iron oxide.

The southernmost mapped trace of the Coca Fault is exposed in a road cut just a few feet to the south of the previously described trace. The southernmost branch of the fault is approximately parallel to the branch described in the preceding paragraph. There is neither gouge nor significant fracturing adjacent to this trace (Photograph A-12), and near vertical strata are present on the fault surface. This southernmost mapped branch terminates 50 to 100 feet to the east of the road cut.

The contact between the upper and lower Chatsworth Formation shows an apparent right lateral separation across the Coca Fault (Figure 3). The near vertical strata observed on the failure surfaces of the fault, when taken in conjunction with the apparent right lateral separation across the fault, suggest there is a down to the north displacement on the Coca Fault.

The lateral extent of the Coca Fault can be inferred from both published mapping and work completed during this evaluation. To the east (1992) interprets the fault to extend off of the SSFL and perhaps join the Burro Flats Fault to the west of the San Fernando Valley. Exposures are insufficient to clearly define the western extent of the fault. The fault is currently interpreted to end at the western end of the fairly linear drainage near the Coca Stands.

1.4.7 The Burro Flats Fault

The Burro Flats Fault was mapped by Dibblee (1992) and shows the structure striking approximately east-west within the SSFL. The apparent displacement on the Burro Flats Fault as inferred from the juxtaposition of stratigraphic units shown by Dibblee is down to the north, the same as the sense of displacement inferred for the Coca Fault. Further descriptions of the Burro Flats Fault are not provided because no direct observations or measurements were made. The Burro Flats Fault is on the southern perimeter of the area of interest in this study and the area has not been developed, so man-made exposures associated with road cuts are not available for inspection.

1.5 Joints

The nature and orientation of joints in bedrock can influence groundwater flow and contaminant transport. To assess this potential at SSFL, data on joint frequency, spacing

1.5.1 Joint Spacing

The results of the aerial photo evaluation of joint spacing are presented in Figure 7. Estimated joint spacing ranges from as little as 15 feet in the northeastern part of the site (near Woolsey Canyon Road), to more than 1000 feet in the north-central part of the site. Although there is significant variation in joint spacing locally, joints in the northern part of the site are generally spaced more widely than in the southern part of the site. Joint spacing in the northern part of the site generally exceeds 100 feet, and commonly exceeds 200 feet. In much of the southern part of the site, measured joint spacing is less than 50 feet, and in almost all places is less than 100 feet. Within the central part of the site, the boundary between the two spacing domains lies approximately at the contact between Sandstone 1 and Sandstone 2 (Figure 7).

Calculated average joint spacing is consistent with the interpretations shown of Figure 7. Table 1 shows calculated average joint spacing for several different structural blocks within Sandstone 1 and for Sandstone 2. Average joint spacing in Sandstone 1 is generally 1/2 to 1/3 that observed in Sandstone 2.

1.5.2 Joint Orientation

Data derived from aerial photographs, measurements from outcrops, and orientations measured in borcholes indicate that steeply dipping joints preferentially strike in a north-northwesterly and northeasterly direction. Joint orientations derived from aerial photographs, outcrop measurements, and borcholes are shown separately in Figure 8. Figure 9 combines data from 595 joint orientation measurements from outcrop and aerial photo data.

Joint orientations were also plotted by stratigraphic unit to assess whether joint orientation varied with stratigraphy and/or geography. This information is presented in Figure 10. All joint orientations found in Sandstone 1 and Sandstone 2, as well as those in areas bounded by faults, were plotted separately. The relatively large number of northeast striking joints present in the two easternmost rose diagrams of Figure 10 are the result of a relatively large number of joints in small parts of the structural blocks in which the rose diagrams are located.

1.5.3 Joint Continuity and Inferred Groundwater Flow Patterns

Steeply dipping joints exposed in prominent sandstone outcrops at the SSFL typically show discontinuities at their intersection with bedding planes. This is potentially important to groundwater flow in the Chatsworth Formation, because discontinuous joints potentially create circuitous groundwater flowpaths with multiple relatively low

1.5.4 Joint Characteristics of Sandstones and Shales

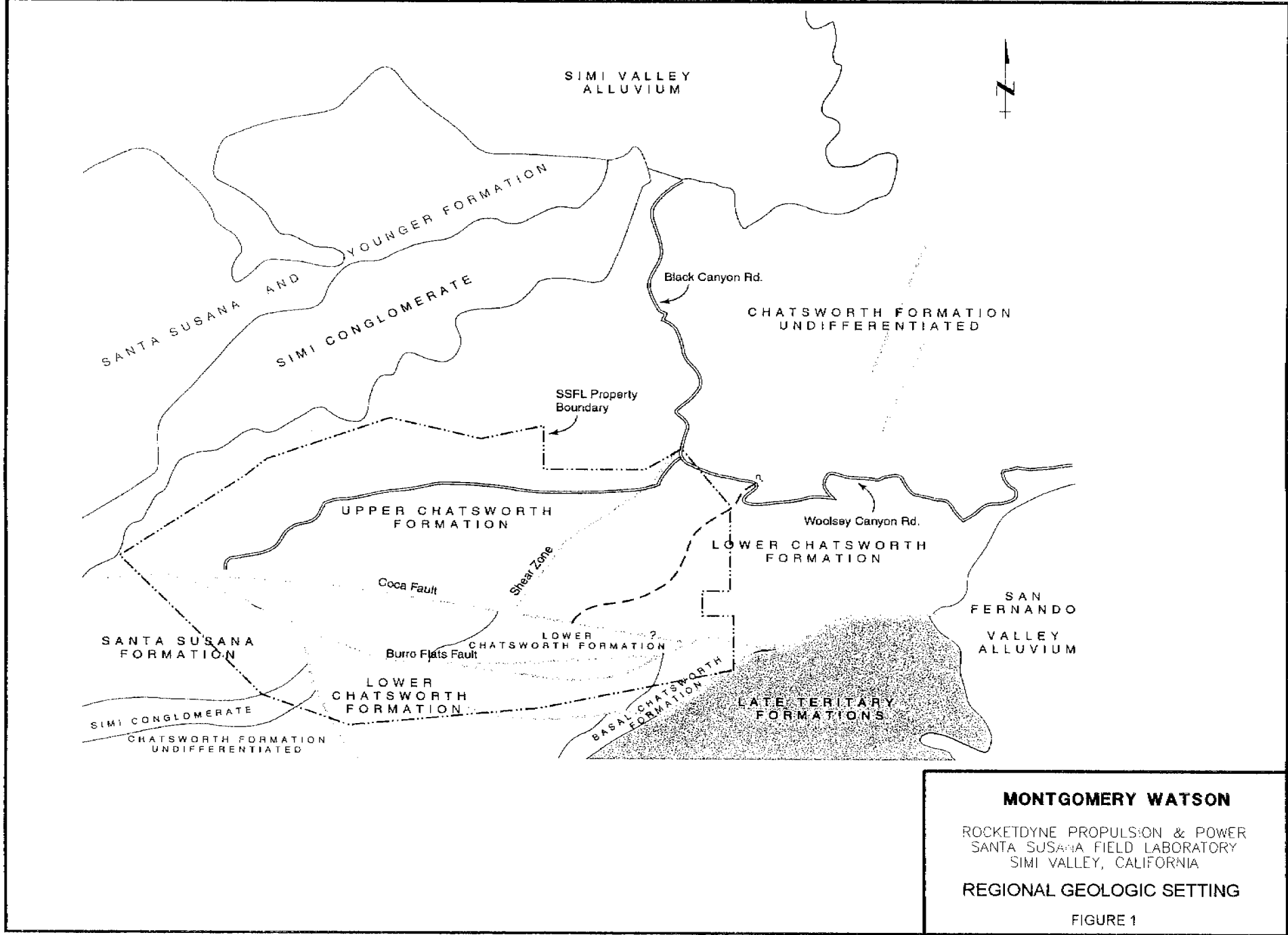
Sandstone and shale typically show distinctly different joint characteristics in outcrops at the SSFL, and the following discussion addresses the question of the kind of influence the fractures in shale might have on groundwater flow. As has been discussed, sandstone normally shows relatively widely spaced joints that show systematic orientation. In contrast, fractures observed in shale outcrops are much more closely spaced, typically being less than an inch apart. Closely spaced fractures in Shales 1 and 2 are shown in Photograph A-4. The closely spaced fractures in the shale beds raise two possibilities: Either the fractures in the shale units are open and deep, and the shales might at as preferred groundwater flowpaths, or the fractures observed in shale outcrops are superficial weathering phenomena, and are closed at depth. Field observations, information from core, and laboratory permeability studies all suggest that the fractures observed in shale outcrops are not major groundwater flowpaths.

Field data concerning the hydraulic characteristics of fractures in shale are derived from the distribution of iron oxide stains in outcrops in which a variety of lithologies are present. Photograph A-18 is a photograph of an outcrop that consists of interbedded sandstone, siltstone, and shale. Iron oxide stains are consistently associated with the coarser-grained siltstone and sandstone beds, but not the fractured shale beds, suggesting that groundwater has preferentially moved through the coarser-grained units, not through the closely fractured shale.

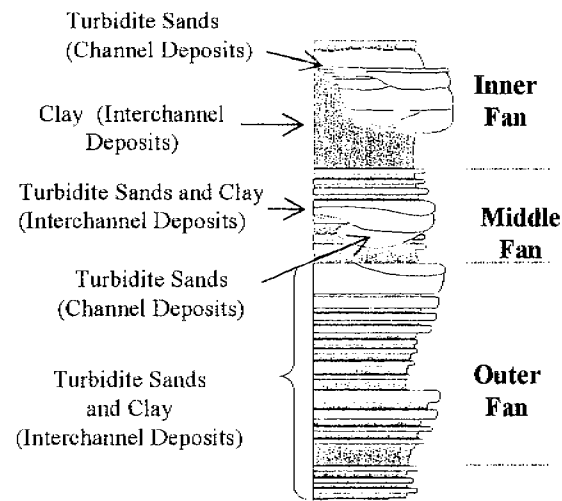
Core from the boring from well RD-46B also suggests that the fractures observed in outcrops of shale are features which are confined to shallow, weathered zones and that they do not act as preferred groundwater flowpaths. Photograph A-19 is a photograph of core from a depth of slightly more than 300 feet. The darker-grey core is composed of clay shale while the lighter gray material is siltstone. Closely spaced fractures are absent in the shale, suggesting that the fractures observed in outcrop are weathering features that do not extend to significant depths.

Photograph A-20 shows core from well RD-46B from a depth of 40 to 50 feet. The brown, iron oxide stained core is composed of medium- to coarse-grained sandstone, while the dark gray, unstained core is composed of shale. As with the core from greater depths, the shale at a depth of 40 to 50 feet does not show the closely spaced fractures that are present in surface outcrops. In addition, the presence of iron oxide staining in the sandstone, but not in the shale, suggests that groundwater flows preferentially through sandstone rather than through shale

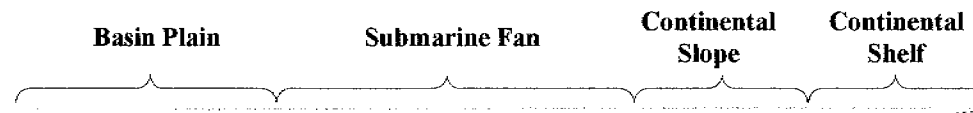
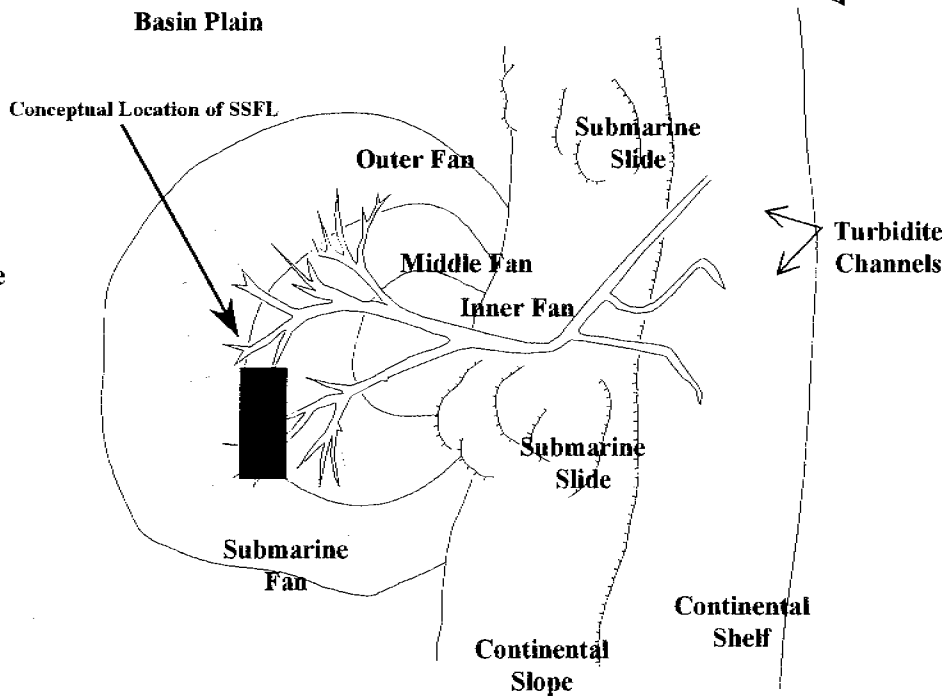
FIGURES



MONTGOMERY WATSON
 ROCKETDYNE PROPULSION & POWER
 SANTA SUSANA FIELD LABORATORY
 SIMI VALLEY, CALIFORNIA
REGIONAL GEOLOGIC SETTING
 FIGURE 1



With Modifications From Mutti and Lucchi (1972)

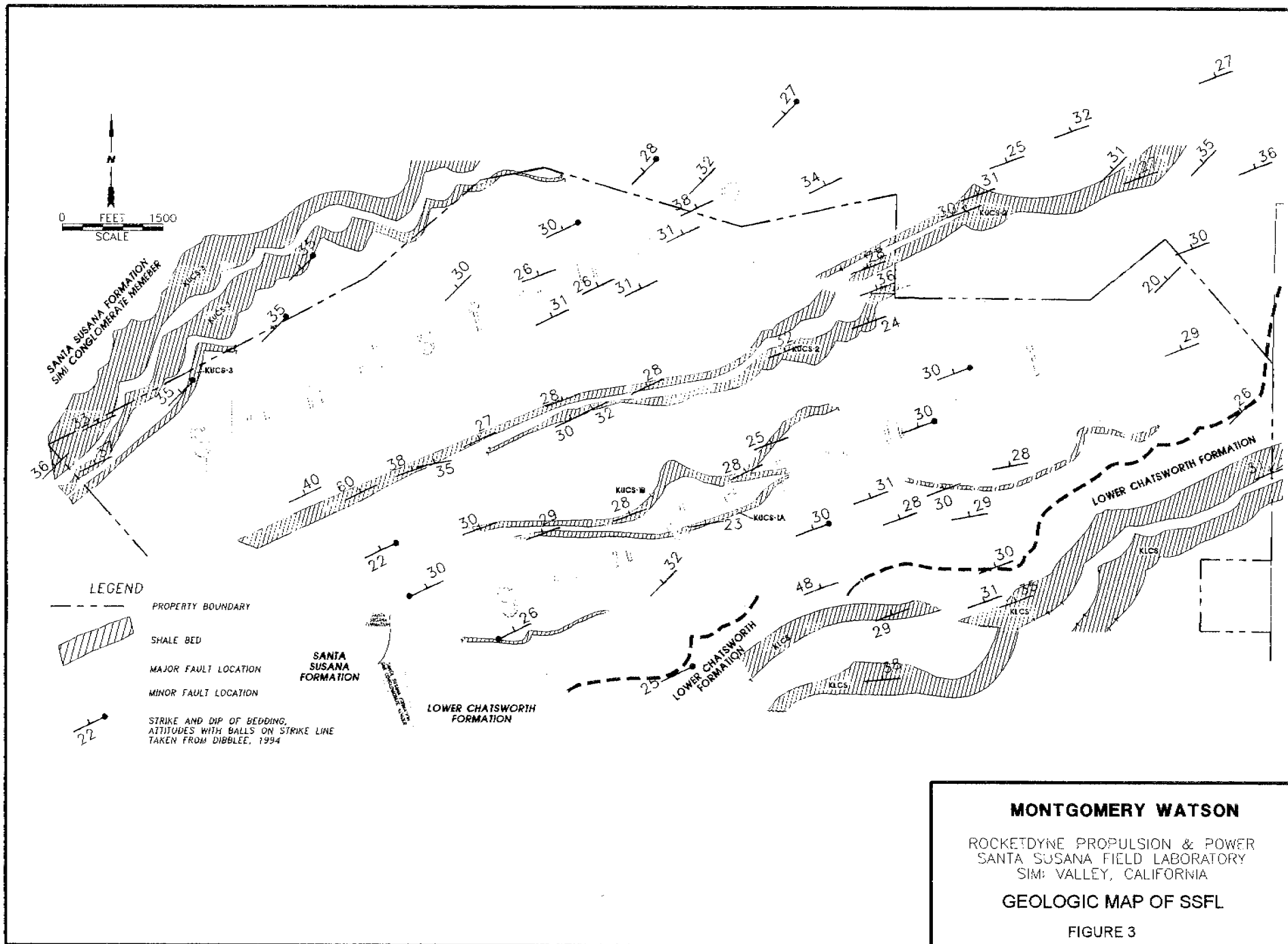


MONTGOMERY WATSON

ROCKETDYNE PROPULSION & POWER
 SANTA SUSANA FIELD LABORATORY
 SIMI VALLEY, CALIFORNIA

DEPOSITIONAL ENVIRONMENT

FIGURE 2

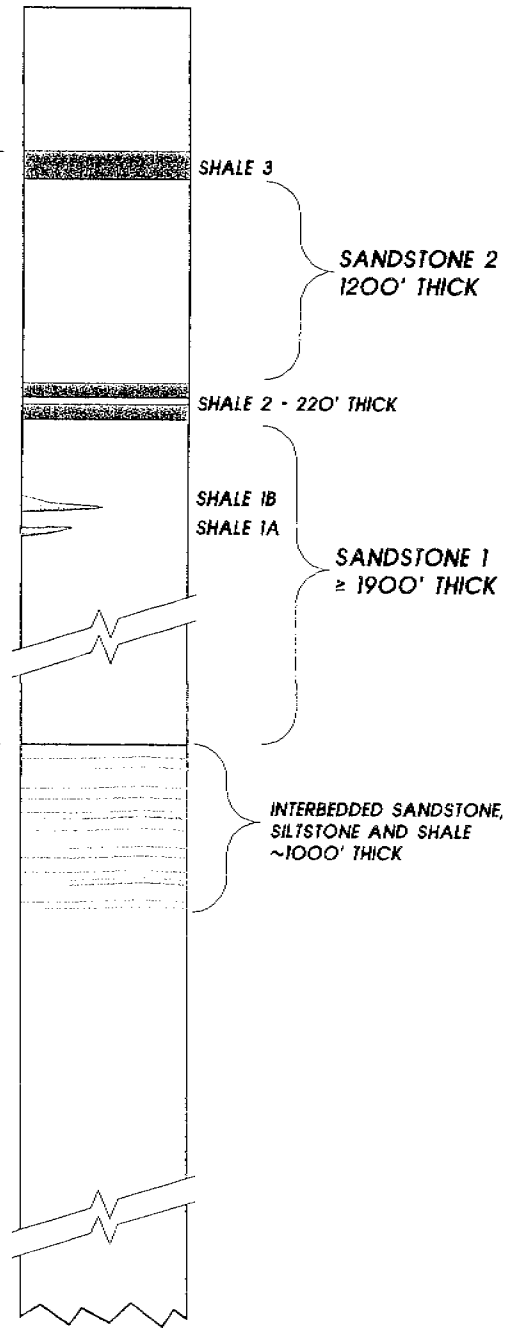


SIMI CONGLOMERATE
MEMBER OF THE
SANTA SUSANA
FORMATION

UPPER
CHATSWORTH
FORMATION

LOWER
CHATSWORTH
FORMATION

BASAL
CHATSWORTH
FORMATION

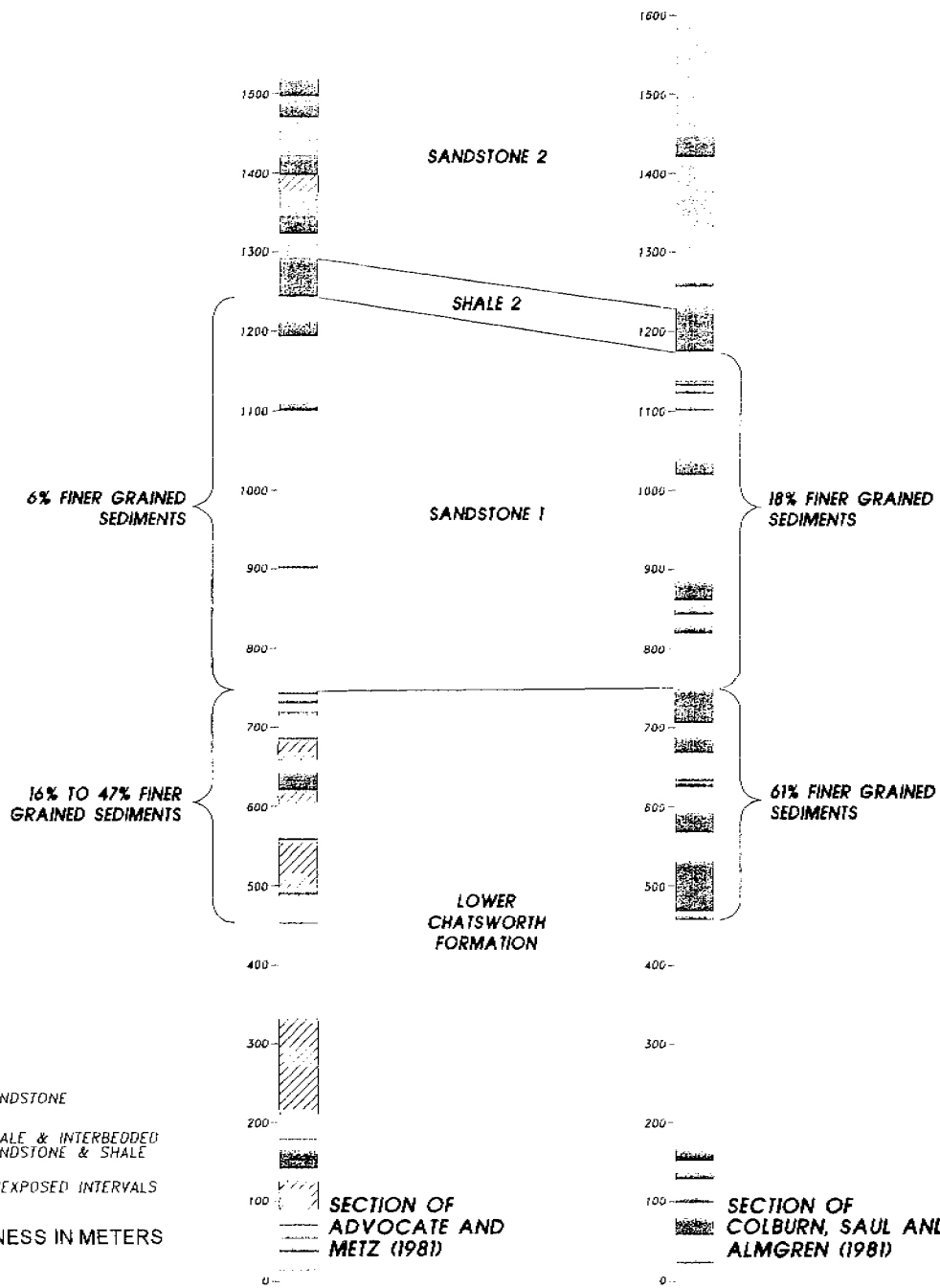


MONTGOMERY WATSON

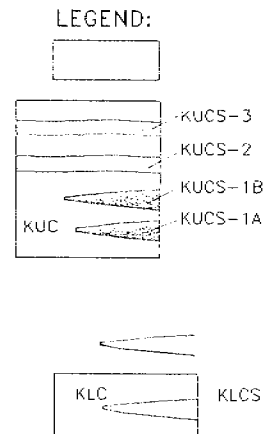
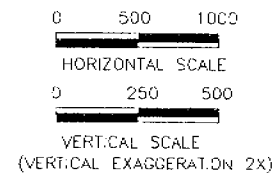
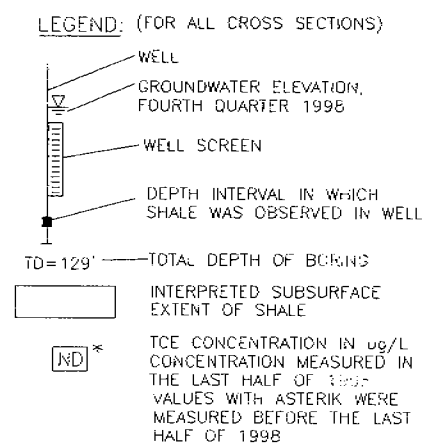
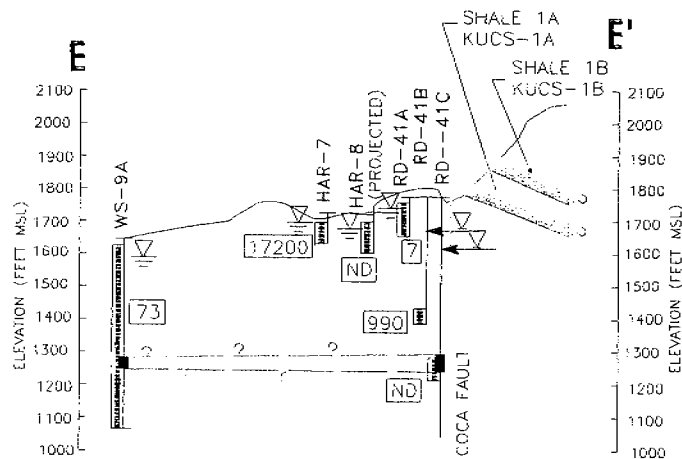
ROCKETDYNE PROPULSION & POWER
SANTA SUSANA FIELD LABORATORY
SIMI VALLEY, CALIFORNIA

SSFL STRATIGRAPHIC COLUMN

FIGURE 4



MONTGOMERY WATSON
 ROCKETDYNE PROPULSION & POWER
 SANTA SUSANA FIELD LABORATORY
 SIMI VALLEY, CALIFORNIA
**MEASURED STRATIGRAPHIC
 SECTIONS AT SSFL**
 FIGURE 5



TIPS-SIMI CONGLOMERATE, INTERBEDDED CLAYE CONGLOMERATE AND SANDSTONE

KUC-UPPER CHATSWORTH FORMATION, PRIMARILY SANDSTONE WITH THIN SHALE AND SILTSTONE BEDS

KUCS-3. PRIMARILY SHALE, WITH LESSER AMOUNTS OF SILTSTONE AND SANDSTONE

KUCS-2. PRIMARILY SHALE, WITH LESSER AMOUNTS OF SILTSTONE AND SANDSTONE

KUCS-1B. PRIMARILY SHALE, WITH LESSER AMOUNTS OF SILTSTONE AND SANDSTONE

KUCS-1A. PRIMARILY SHALE, WITH LESSER AMOUNTS OF SILTSTONE AND SANDSTONE

UNNAMED SHALE BEDS

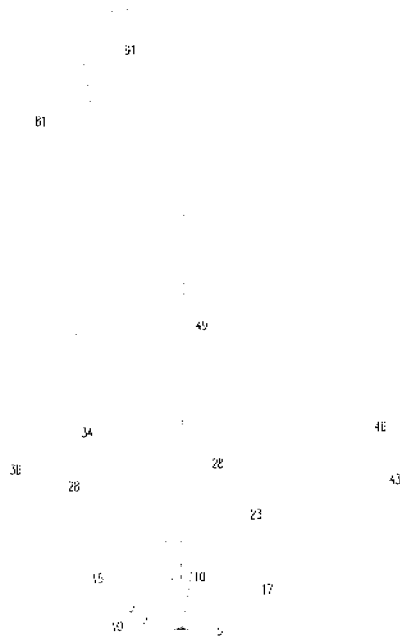
KLC-LOWER CHATSWORTH FORMATION, SANDSTONE INTERBEDDED WITH SANDSTONE/SHALE UNITS

KLCS-INTERBEDDED SANDSTONE AND SHALE

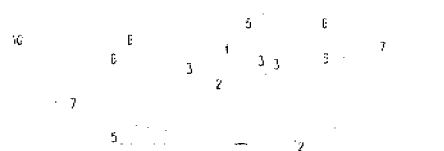
FAULT, QUESTIONED WHERE APPROXIMATELY LOCATED



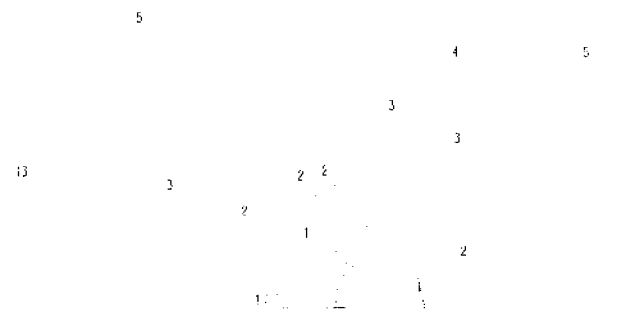
MONTGOMERY WATSON
ROCKETDYNE PROPULSION & POWER
SANTA SUSANA FIELD LABORATORY
SIMI VALLEY, CALIFORNIA
CROSS SECTION
THROUGH COCA SHALE
FIGURE 6



Rose Diagram of Joint Orientations taken from Aerial Photographs



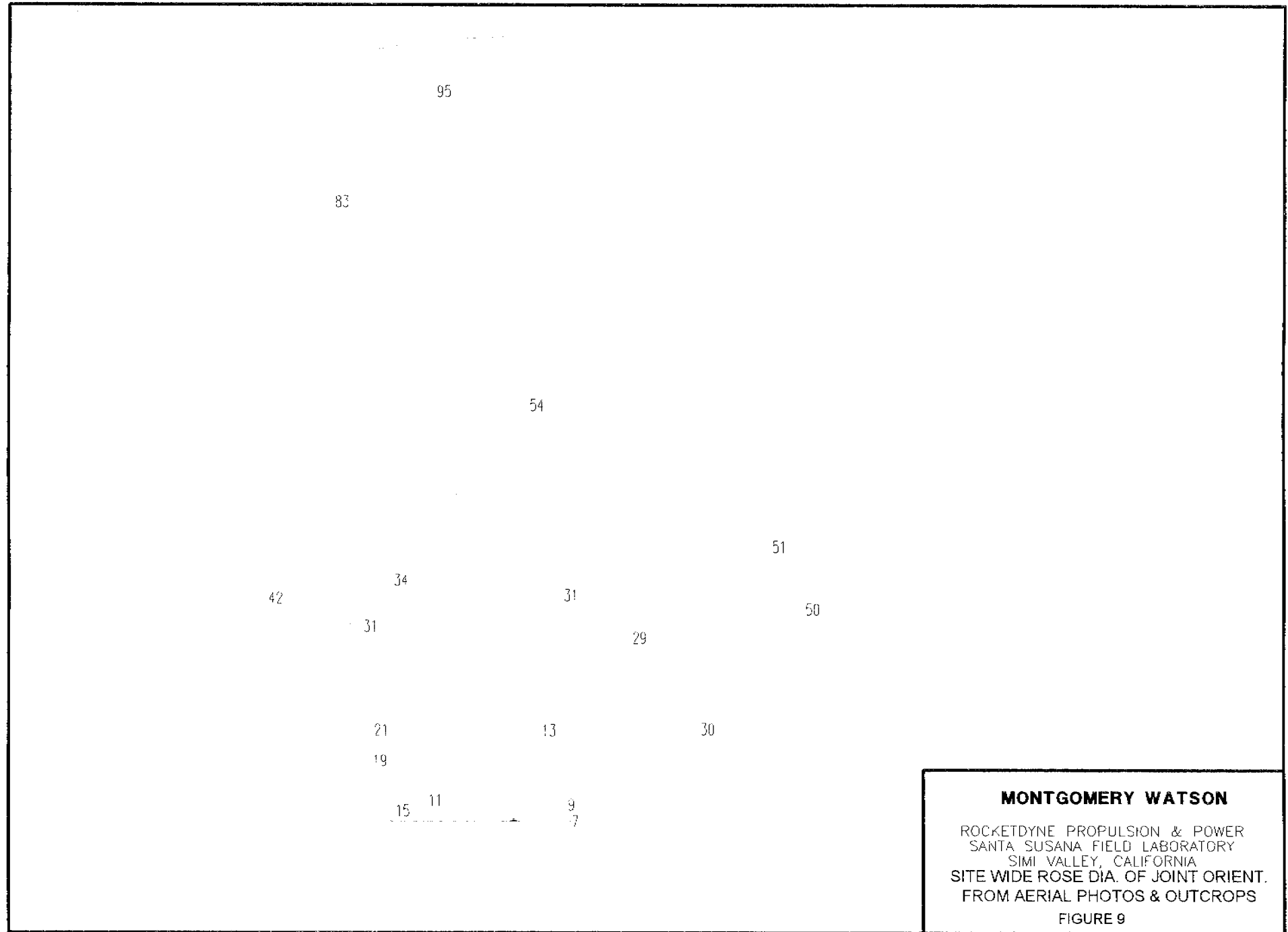
Rose Diagram of Joint Orientations taken from Outcrops



Rose Diagram of Orientations of Steeply Dipping Joints in Wells RD-35B, RD-46A and RD-46-B

MONTGOMERY WATSON

ROCKETDYNE PROPULSION & POWER
 SANTA SUSANA FIELD LABORATORY
 SIMI VALLEY, CALIFORNIA
**ROSE DIAGRAMS OF
 JOINT ORIENTATION**
 FIGURE 8



MONTGOMERY WATSON

ROCKETDYNE PROPULSION & POWER
SANTA SUSANA FIELD LABORATORY
SIMI VALLEY, CALIFORNIA
SITE WIDE ROSE DIA. OF JOINT ORIENT.
FROM AERIAL PHOTOS & OUTCROPS

FIGURE 9

TABLES

Table 1
Mean Joint Spacing
Santa Susana Field Laboratory
Ventura County, CA

Sandstone 1	Spacing	Sandstone 2	Spacing
West of Shear Zone and North of Coca Fault	63 Feet	All of Sandstone 2	124 Feet
South of Coca Fault	60 Feet		
East of Shear Zone	30 Feet		
All of Santstone 1	53 Feet		

Table 2
Hydraulic Conductivity Measurements from Rock Cores

Santa Susana Field Laboratory
Ventura County, CA

SANDSTONE SAMPLES			
Well	Depth (ft)	Porosity %	K (cm/sec)
RD-45A	114.0-115.0	11.9	1.6×10^{-6}
	209.0-210.0	12.5	1.1×10^{-5}
	272.5-274.0	13.1	1.5×10^{-5}
RD-46B	24.0-24.2	21.0	1.1×10^{-4}
	49.1-50.2	13.2	6.0×10^{-5}
	70.0-70.5	11.9	3.6×10^{-6}
	105.2-105.6	15.2	1.7×10^{-6}
	140.5-140.9	13.5	1.6×10^{-5}
	177.9-178.2	13.6	7.2×10^{-6}
	210.2-210.5	12.2	5.6×10^{-6}
	292.4-292.7	15.4	1.2×10^{-4}
	358.3-358.6	15.0	6.3×10^{-6}
304.7- 304.9	13.8	1.9×10^{-6}	
RD-49	62.8-64.0	13.4	2.0×10^{-6}
	68.5-70.0	10.8	1.5×10^{-6}
RD-55	76.4-78.0	15.9	6.8×10^{-6}
	90.0-91.0	13.3	1.1×10^{-5}
RD-54C	28.0-29.1	13.4	1.6×10^{-6}
Geometric Mean			7.4×10^{-6}
SHALE/SILTSTONE SAMPLES			
RD-45A	40.3-41.0	6.6	8.5×10^{-11}
RD-55	26.5-28.0	10.6	6.4×10^{-9}
	46.0-47.0	11.4	2.5×10^{-10}

Photographs

- A-1 Geomorphic Expression of Upper and Lower Chatsworth Formation
- A-2 Lithology of the Lower Chatsworth Formation (a)
- A-3 Outcrop of the Upper Chatsworth Formation
- A-4 Outcrops of Shale 1 and Shale 2
- A-5 Lithology of the Lower Chatsworth Formation (b)
- A-6 Gouge in the Shear Zone
- A-7 Gouge Zone of the Happy Valley Fault
- A-8 Outcrop of the Tank Fault
- A-9 Discontinuous Failure on the Tank Fault
- A-10 Discontinuous Failure Surface on the Tank Fault
- A-11 Outcrop of the Coca Fault
- A-12 Outcrop of the Coca Fault
- A-13 Discontinuous Joints in the Chatsworth Formation
- A-14 Discontinuous Joints in the Chatsworth Formation
- A-15 Influence of Joints and Bedding on Groundwater Flow
- A-16 Influence of Joints and Bedding on Groundwater Flow
- A-17 Influence of Joints and Lithology on Groundwater Flow
- A-18 Influence of Joints and Lithology on Groundwater Flow
- A-19 Relationship Between Lithology and Iron Oxide Stains
- A-20 Shale Characteristics from Rock Core Samples
- A-21 Oxidation of Sandstone in Shallow Core

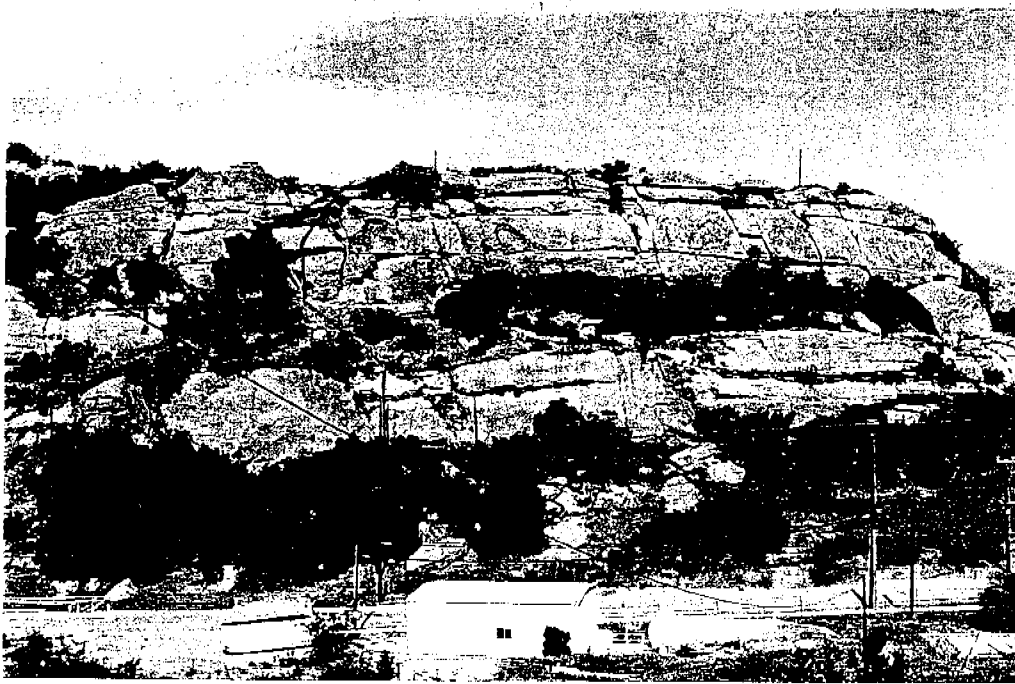
A-1 Geomorphic Expression of Upper and Lower Chatsworth Formation



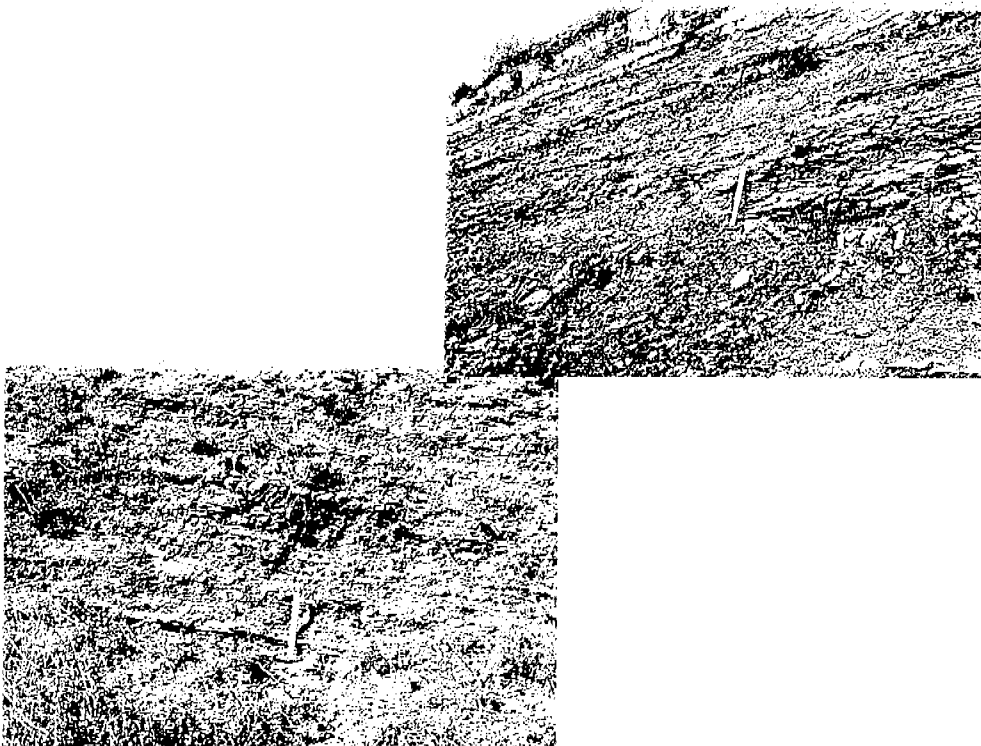
A-2 Lithology of the Lower Chatsworth Formation



A-3 Outcrop of the Upper Chatsworth Formation



A-4 Outcrops of Shale 1 and Shale 2



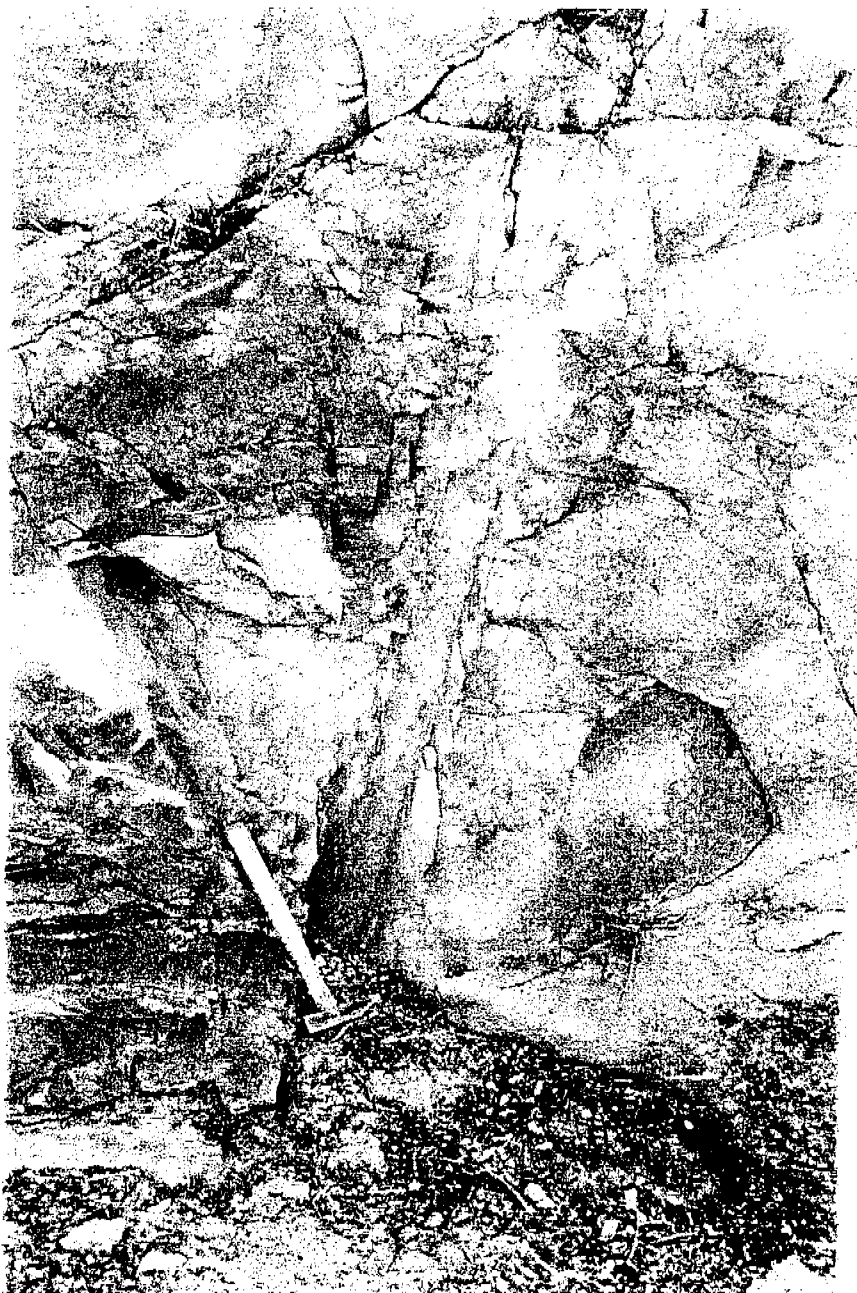
A-5 Lithology of the Chatsworth Formation



A-6 Gouge in the Shear Zone



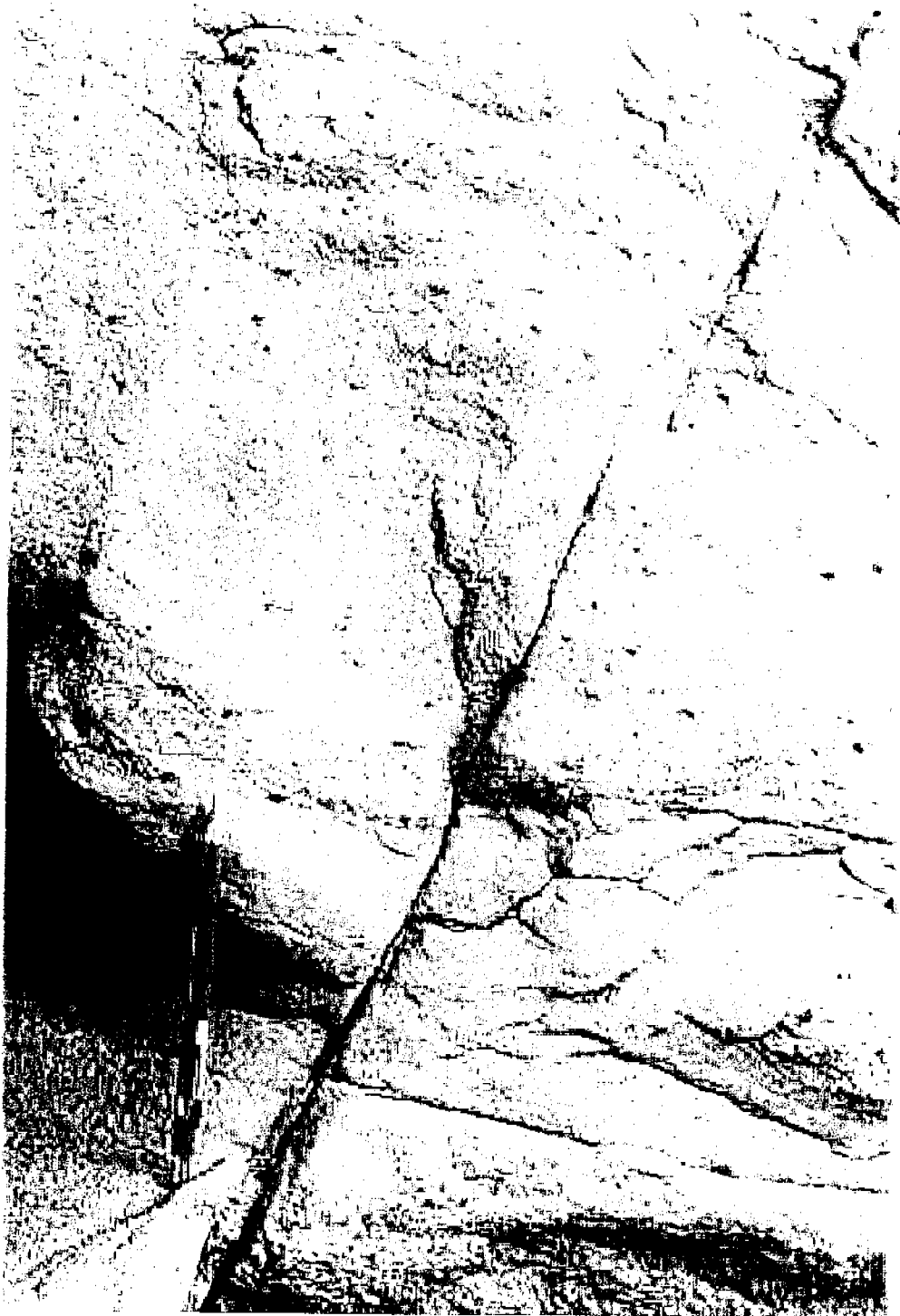
A-7 Gouge Zone of the Happy Valley Fault



A-8 Outcrop of the Tank Fault



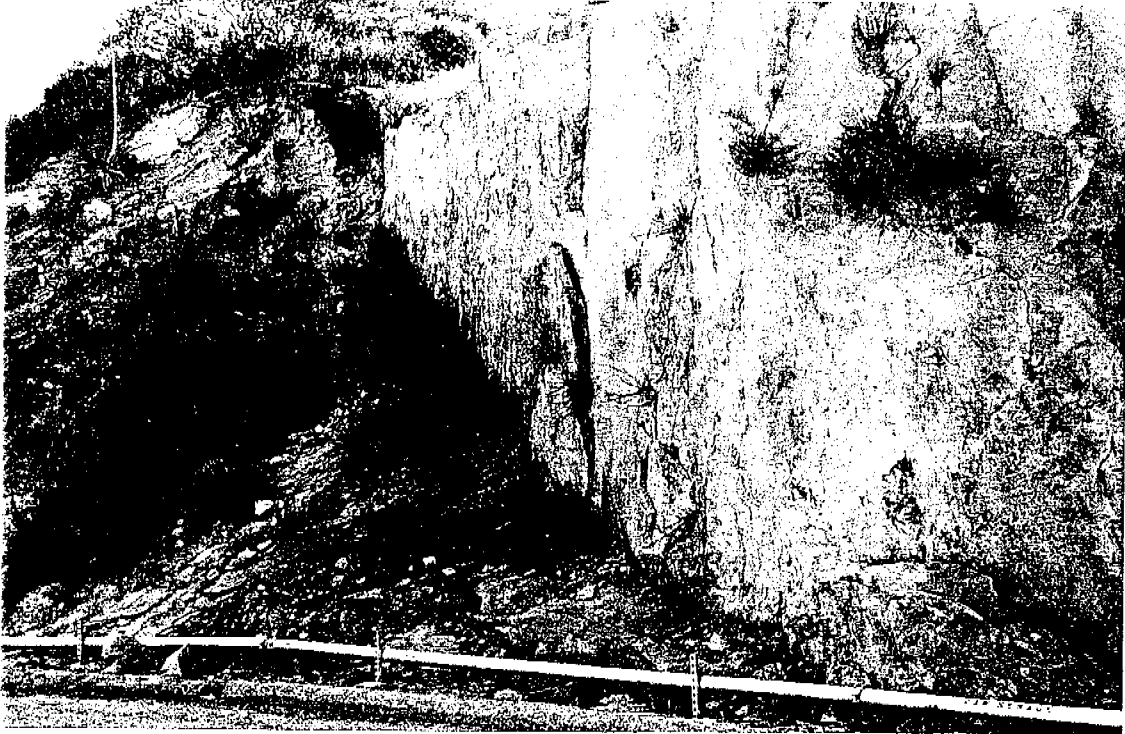
A-9 Discontinuous Failure Surface on the Tank Fault



A-10 Discontinuous Failure Surface on the Tank Fault



A-11 Outcrop of the Coca Fault



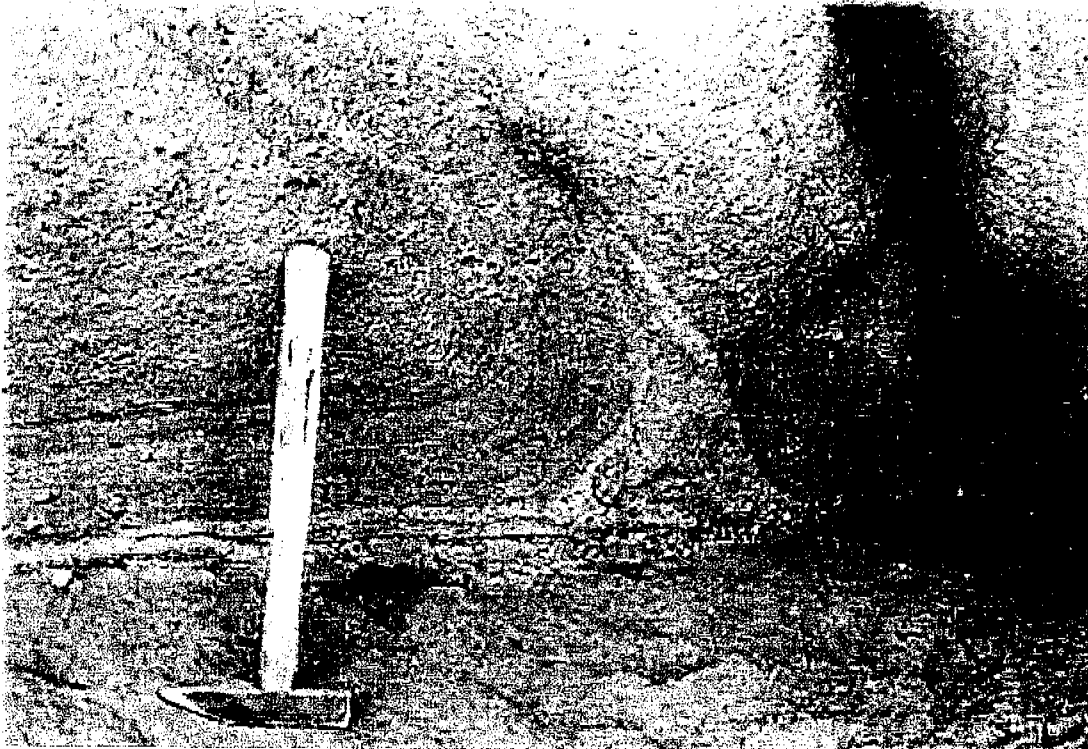
A-12 Outcrop of the Coca Fault



A-13 Discontinuous Joints in the Chatsworth Formation



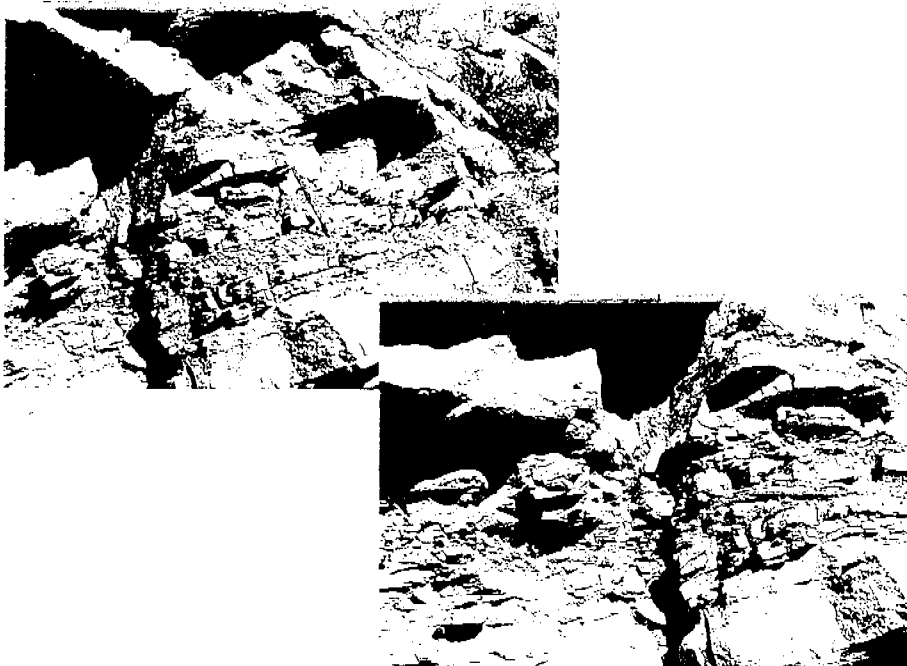
A-14 Influence of Joints and Bedding on Groundwater Flow



A-15 Influence of Joints and Bedding on Groundwater Flow



A-16 Influence of Joints and Lithology on Groundwater Flow



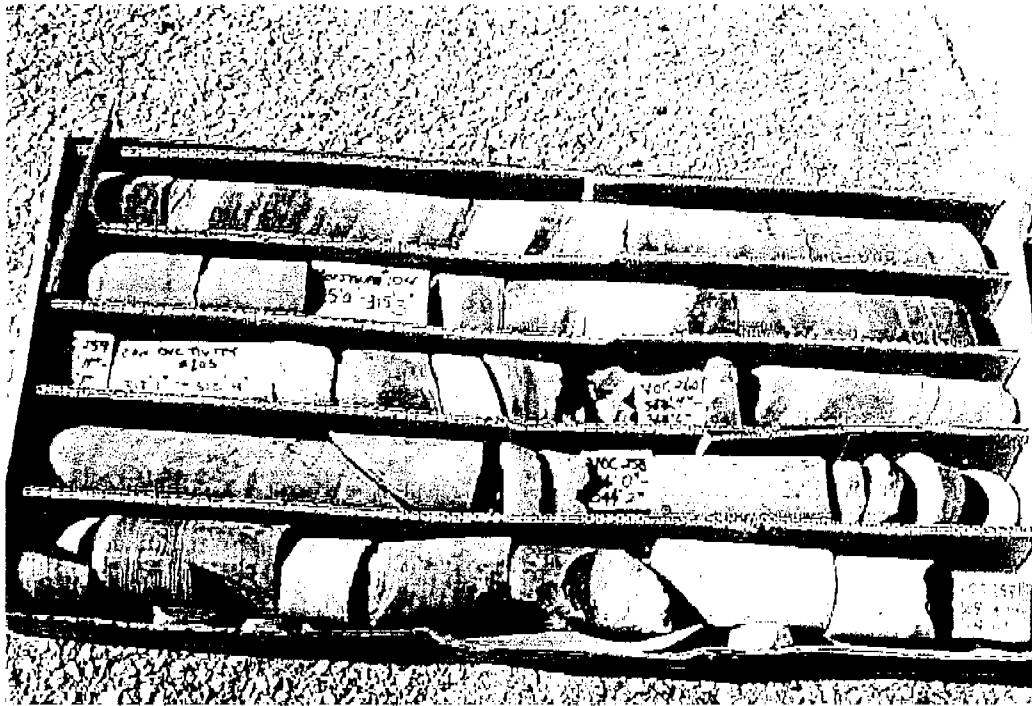
A-17 Influence of Joints and Lithology on Groundwater Flow



A-18 Relationship Between Lithology and Iron Oxide Stains



A-19 Shale Characteristics From Rock Core Samples

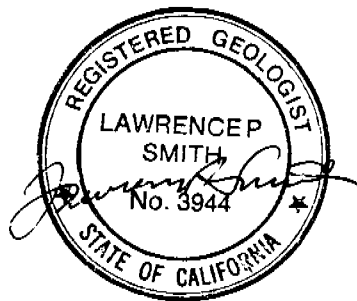


A-20 Oxidation of Sandstone in Shallow Core



**APPENDIX B
SANTA SUSANA FIELD LABORATORY
HYDROGEOLOGY SUMMARY REPORT**

By:



Lawrence P. Smith, R.G., C.H.

**Haley & Aldrich, Inc.
Brea, California**

for

**Montgomery Watson
Walnut Creek, California**

**File No. 86187-014
April 2000**

TABLE OF CONTENTS

	Page
LIST OF TABLES	iii
LIST OF FIGURES	iv
1.0 HISTORICAL BACKGROUND	1
1.1 Water Supply Development	1
1.2 Precipitation	4
1.3 Monitoring Well Installation	5
1.4 Hydrogeologic Significance of Well Construction Methods	7
1.5 Historical Water Levels Changes	7
1.6 Pumping Well Water Level Changes	8
1.7 Seasonal Water Level Fluctuations	10
2.0 EVALUATION OF HYDROGEOLOGIC CONDITIONS	12
2.1 Monitoring Wells and Stratigraphy	12
2.2 Conceptual Estimation of Site Bulk Hydraulic Conductivity	12
2.3 Hydrogeologic Properties of SSFL Rock Core	13
2.3.1 Matrix Hydraulic Conductivity	13
2.3.2 Matrix Porosity	14
2.4 Hydraulic Conductivity from Packer Testing	15
2.5 Hydraulic Conductivity from Pumping Tests	15
2.5.1 Single Well Pumping Tests	16
2.5.2 Multi-Well Pumping Tests	18
2.5.3 Evaluation of Hydraulic Conductivity Data for SSFL	22
2.5.4 Comparison of Matrix and Well Hydraulic Conductivity	24
2.5.5 Influence of Open Interval on Hydraulic Conductivity Estimates	25
2.5.6 Spatial Distribution of Hydraulic Conductivity	25
2.5.7 Impacts of Faults and Major Lineaments on Hydraulic Conductivity	25
2.5.8 Summary of Hydraulic Conductivity	27
2.6 Vertical Distribution of Hydraulic Conductivity and Water Level Impacts	27
2.7 Observed Water Level Response During the 1996 Hydraulic Communication Study	29
2.8 Observed Water Level Offsets at Major Geologic Features	31
2.9 Correlations in Water Levels Between Wells	33
2.10 Summary of SSFL Chatsworth Formation Hydrogeology	35
2.10.1 Stratigraphic Considerations	35
2.10.2 Structural Considerations	36
2.10.3 Inter-connection of the Fracture Network	37

LIST OF TABLES

Table No.	Title	
1.1	Water Supply Well Installation History	1
1.2	Water Usage in 1963	2
2.1	Hydrogeologic Properties of SSFL Rock Core	13
2.2	Hydraulic Conductivity Estimates For Sandstone 1 Wells From Single Pumping Tests	16
2.3	Hydraulic Conductivity Estimates For Wells Completed In Sandstone 2 From Single Well Pumping Tests	17
2.4	Hydraulic Conductivity Estimates For Lower Chatsworth Formation Wells From Single Well Pumping Tests	18
2.5	RD-73 Pumping Test Results	20
2.6	RD-63 Pumping Test Results	22
2.7	Summary of SSFL Pumping Test Results	23
2.8	Hydraulic Conductivity and Open Interval	25
2.9	Hydraulic Conductivities of Wells on Known Faults or Lineaments	26
2.10	Summary of SSFL Hydraulic Conductivity Data	27
2.11	Hydraulic Conductivity and Head Data for Cluster Wells	28
2.12	Restart Dates of Pumping Wells	29
4.1	Summary of SSFL Hydraulic Conductivity Data	48

LIST OF FIGURES

(continued)

Figure No.	Title	
2.20	Water Level Offset Across Shale 3	33
2.21	Water Level Fluctuations in Selected SSFL Wells	34
2.22	Water Level Correlgrams of WS-12 vs WS-13 and RD-10 vs RD-31	34
2.23	Water Level Correlation Between Wells	34a
2.24	Screened Interval of WS-13	35
3.1	Aquitard Locations and Groundwater Units	38
3.2	Water Level Elevations in Wells in Groundwater Unit 1A	38
3.3	Water Levels in Wells in Groundwater Unit 1B	39
3.4	Water Level Elevations in Wells in Groundwater Unit 2	40
3.5	Water Level Decline at SSFL From 1954-1997 (After GWRC, 1998)	40
3.6	Water Level Conditions at Groundwater Unit 2 Contact with Shale 2	41
3.7	Water Level Conditions at Groundwater Unit 2 Contact with the Shear Zone	41
3.8	Water Levels Measured in Wells in Groundwater Unit 3	42
3.9	Water Level Conditions at Shale 2 and Shale 3 Boundaries of Groundwater Unit 3	42
3.10	Water Levels Measured in Wells in Groundwater Unit 4	43
3.11	Water Level Conditions Along the Coca Fault	43
3.12	Water Levels Measured in SSFL Wells	44
4.1	Conceptual View of SSFL Groundwater Flow without Fractures or Aquitards	45
4.2	Conceptual View of SSFL with Fractures and Aquitards	45
4.3	Model Domain for Simulation of Groundwater Flow	45
4.4	Simulated Flow Lines in an Homogeneous Groundwater System	46
4.5	Placement of Lower and Higher Hydraulic Conductivity Beds in the Model Domain	46
4.6	Groundwater Flow Lines in Model Domain with Sloping Beds of Lower and Higher Hydraulic Conductivity	47
4.7	Hydraulic Head Profile at X = 1,800 Meters	47
4.8	Cluster Well Coverage at SSFL	49
4.9	Groundwater Elevations in Groundwater Unit 1A	49
4.10	Drawdown Resulting from RD-73 Pumping Test at 2.7 GPM	50
4.11	Groundwater Elevations in Groundwater Unit 1B	51
4.12	Water Level Elevations in Groundwater Unit 2	51
4.13	Water Level Elevations in Groundwater Unit 3	52
4.14	Water Level Elevations Measured in Groundwater Unit 4	52

1.0 HISTORICAL BACKGROUND

1.1 Water Supply Development

Water supply development activities at the Santa Susana site began in 1948 with the initiation of the Propulsion Field Laboratory (PFL) on 430 acres now known as Area 1. Site Location details are shown in Figure 1.1. Water supply wells were installed to meet the water resource needs for the expanding test facility, which by 1954 had grown to 1,526 acres. By 1963, 17 water supply wells had been installed in the Chatsworth Formation, but only 5 of the wells yielded sufficient water and the remainder were abandoned or not used, as summarized in Table 1.1.

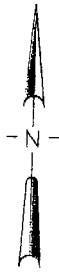
WATER SUPPLY WELLS SANTA SUSANA FIELD LABORATORY ⁽¹⁾					
Year	Well (WS-)	Yield (gpm)	Initial Water Level	Abandoned	Reason Abandoned
1948	1	--	--	1948	Low yield
	2	--	--	1948	Low yield
	3	115	1648	1954	On leased land
1951	4	60	1677	1953	Low yield
	5	165	1680		
1953	4a	110	1659	1957	Low yield
	6	225	1660		
1954	7	40	1776	1963	Low yield
	8	40	1600	1963	Low yield
1955	9	--	--	1955	"Dry hole"
1956	9A	125	1483		
	9B	--	--	1956	"Dry hole"
	10	--	--	1956	"Dry hole"
	11	30	1626	1963	Low yield
	12	450	1567		
1957	13	225	1441		
1958	14	150	1575		Never connected

(1) Data from 10 February 1959 Rocketdyne table "PFL Water Level Data"

Table 1.1 Water Supply Well Installation History

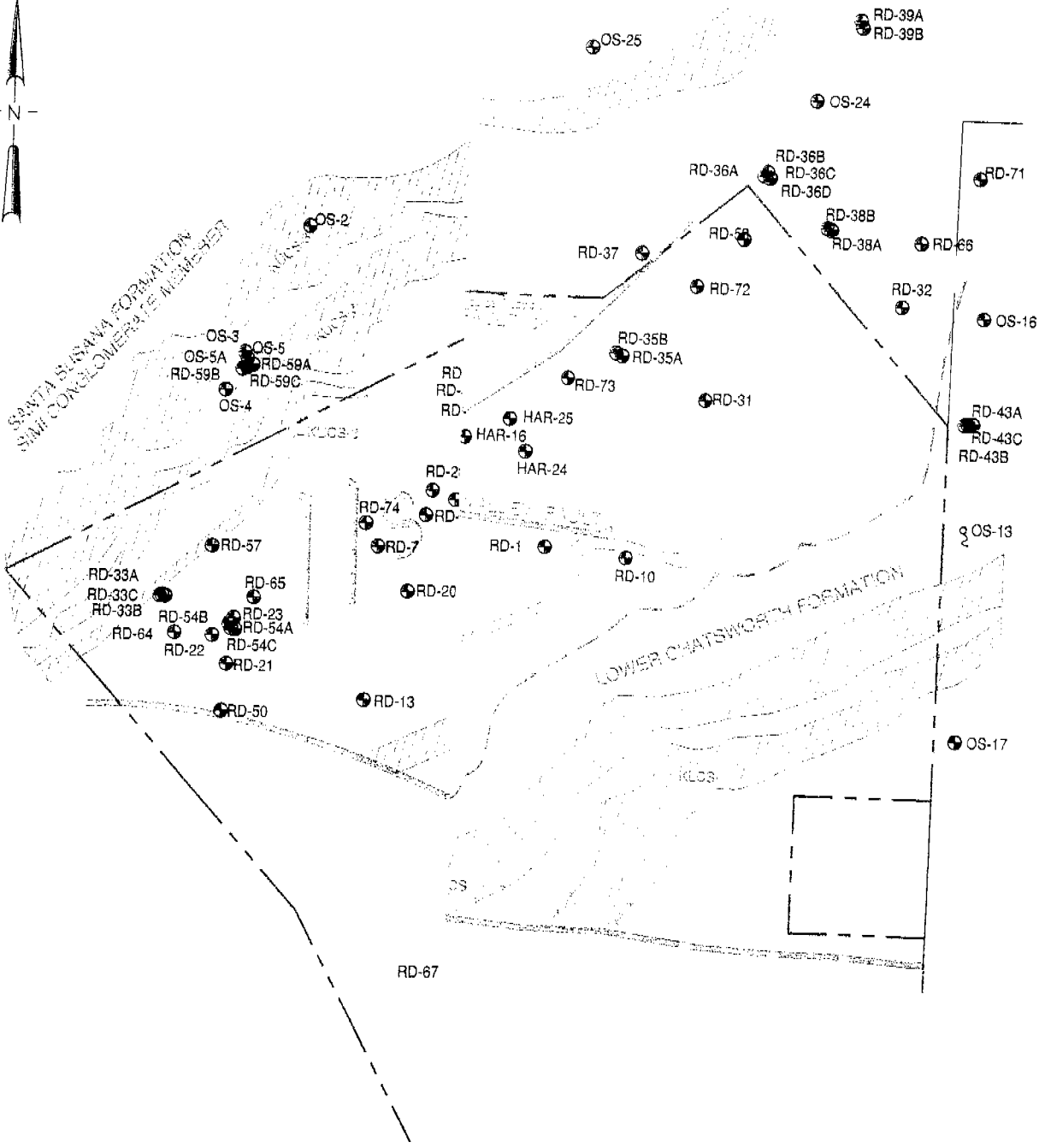
The use of reclaim water was first started on the facility in 1957 with the construction of several surface impoundments as a means of supplementing the available water supply. This stored water was a source of recharge to site groundwater and may have provided baseflow in some of the small streams on the site.

A major facility expansion was completed in 1958 with the installation of the Alfa, Bravo, Canyon, Coca, and Delta test stands, and the construction of Component Test Labs III, IV and V. Accompanying this facility expansion was a substantial increase in groundwater withdrawal, which peaked at about 400 gallons per minute in 1958. Groundwater production from SSFL averaged about 250 gpm between 1956 and 1963, with the bulk of the water being derived from wells WS-5, 6, 9A, 12, and 13.



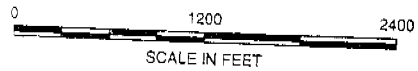
SANTA SUSANA FORMATION
SAND CONGLOMERATE MEMBER

LOWER CHATSWORTH FORMATION



LEGEND:

- RD-29 WATER SUPPLY WELL
- MONITORING WELL
- PROPERTY BOUNDARY
- SHALE UNIT
- FAULT OR SHEAR ZONE



THE BOEING COMPANY
SANTA SUSANA FIELD LABORATORY
SANTA SUSANA, CALIFORNIA

KEY SITE FEATURES AND
WELL LOCATION PLAN

UNDERGROUND
CONSTRUCTION
ENVIRONMENTAL
SOLUTIONS

SCALE: AS SHOWN

APRIL 2000

86187-014 B05

Water usage in 1963 was reported as shown in Table 1.2. Water usage for cooling purposes during rocket testing was largely consumptive. The high rate of groundwater withdrawal and consumptive use resulted in the rapid dewatering of the bedrock aquifer in the central portion of the site, with over 500 feet of water level decline observed in the wells by the early 1960s.

REPORTED WATER USAGE – 1963 SANTA SUSANA FIELD LABORATORY	
Usage	Percentage
Flame bucket coolant	70
Buildings and personnel	5
Safety Showers and Firex	15
Basic Research	10

Table 1.2 Water Usage in 1963

This significant dewatering, coupled with the expanding water demand necessary to support testing for the space program, resulted in the construction of a water supply pipeline to the Calleguas Water District in 1963.

No groundwater withdrawal was recorded from 1964 to 1966. Pumping between 1967 and 1969 averaged less than 20 gpm, and no groundwater withdrawal was reported between 1970 and 1983.

Investigation of groundwater quality in the Chatsworth Formation began at the site in 1984 with the installation of bedrock monitoring wells. The identification of groundwater contamination resulted in the re-activation of two water supply wells in 1984, with pumping from additional water supply and monitoring wells initiated in the late 1980s and early 1990s. Groundwater withdrawal averaged about 100 gpm between 1984 and 1988, and has averaged about 250 gpm since that time. Historical groundwater withdrawals for the SSFL site are summarized in Appendix A and are shown in Figure 1.2.

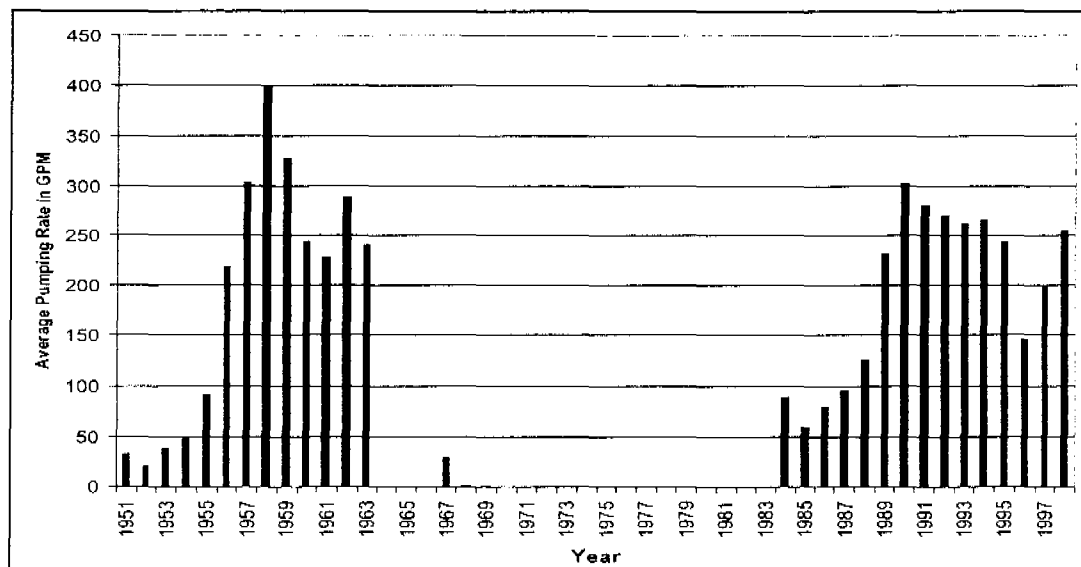


Figure 1.2 Historical Groundwater Withdrawal at SSFL

Pumping rates vary between the water supply wells, with the majority of the historical production being provided by WS-5 and 6. The pumping histories of selected wells are shown in Figure 1.3.

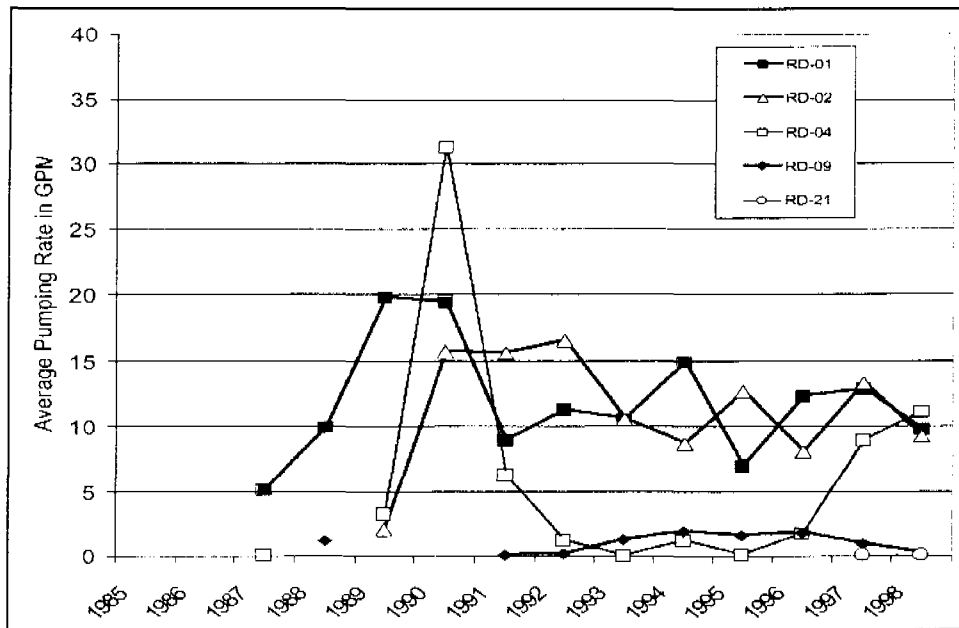


Figure 1.3c. Groundwater Pumping from SSFL Monitoring Wells

In addition to groundwater pumping, the water supply available at SSFL has been augmented by water from the Calleguas Water District since 1964. Water importation from the district has continued to the present at an annualized average rate ranging from about 50 to 130 gpm, providing a total water supply at SSFL of 300 to 350 gpm. The combined water supply at SSFL since 1990 is shown in Figure 1.4.

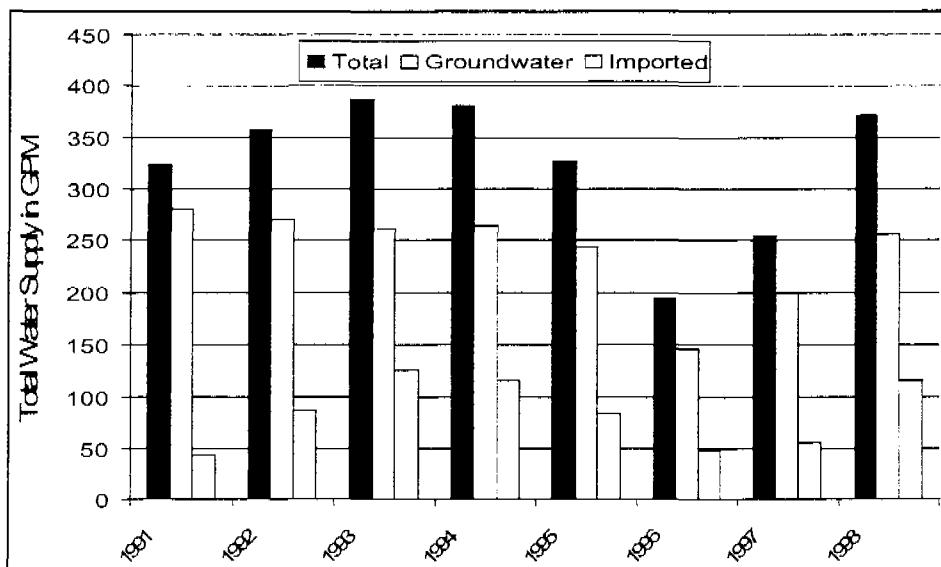


Figure 1.4. Total SSFL Water Supply from Groundwater and Calleguas District

1.2 Precipitation

Precipitation at SSFL has averaged about 19 inches per year since 1960, as shown in Figure 1.5. The low for the period of record was 6.2 inches in 1987, while the high was 41.2 inches in 1998.

Well construction details and specific open intervals of SSFL bedrock wells are shown in Appendix B.

1.4 Hydrogeologic Significance of Well Construction Methods

The bedrock monitoring wells at SSFL were drilled with air-rotary equipment. The method uses air to lift cuttings from the drill hole and requires a minimum submergence of the drill string below the water table in a well in order to lift water out of the borehole. Because of this minimum submergence requirement, low yielding zones are often bypassed during advancement of the borehole. As a result, the "first water" wells are biased to zones of preferentially greater hydraulic conductivity.

For the deeper zone wells installed at cluster locations, well installation was targeted to zones of elevated water production during drilling. As with the "first water" wells, the deeper wells at each of the cluster locations are biased to zones of greater hydraulic conductivity. When considering the "first water" and deeper zone wells together, about 70 of the 104 bedrock monitoring wells installed at SSFL were specifically targeted to zones of elevated hydraulic conductivity. Accordingly, any estimate of "bulk" hydraulic conductivity derived from this data set will be inherently high.

The balance of the bedrock monitoring wells have long open intervals that provide a vertically averaged hydraulic conductivity. This is also true of the water supply wells.

1.5 Historical Water Levels Changes

Water level data from the initial period of site operations in the 1950s and 1960s is limited to infrequent measurements from the water supply wells. A contour plan showing water level elevations in site water supply wells during 1957 and 1958 is shown in Figure 1.8.

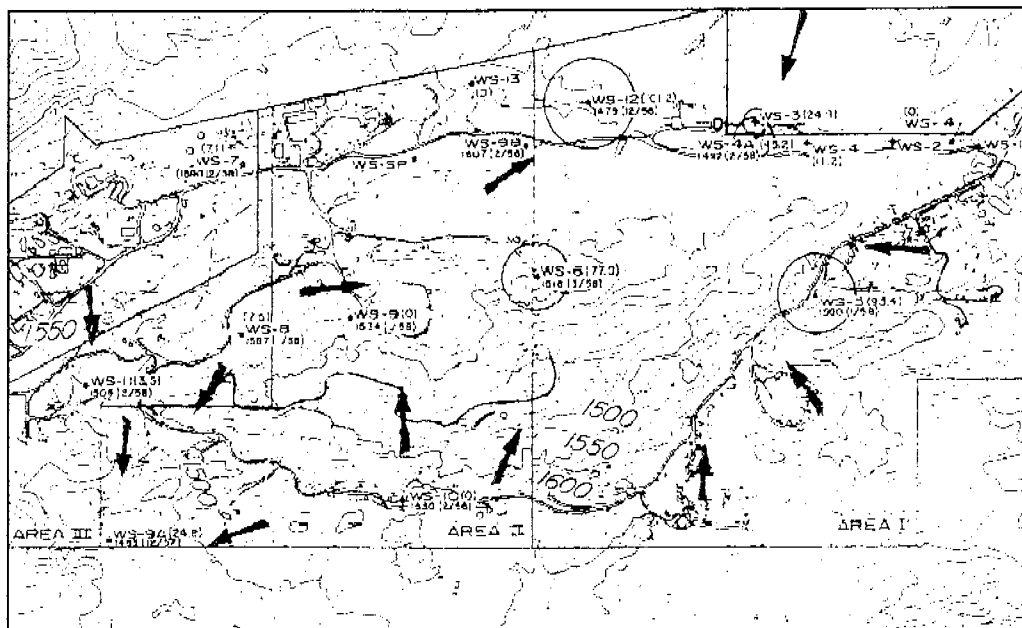


Figure 1.8. SSFL Water Level Elevations, 1957-1958 (GWRC, 1998)

Water level elevations depicted in Figure 9 reflect the early influence of pumping at SSFL, which peaked in 1958. Water level measurements taken from water supply wells in the early 1960s

show water level declines of up to 500 feet near WS-5 and WS-6. A report by GWRC (2000) detailing early water levels and well pumping is included in Appendix C.

Groundwater withdrawal at SSFL ceased in the late 1960s and was not reportedly resumed until 1984. Water levels at the site would have undoubtedly rebounded during the extended period of non-pumping, but consistent water level measurements were not taken until 1986, two years after pumping resumed at WS-5 and WS-13. An estimate of site-wide water level decline between 1954 and 1997 is included as Figure 1.9.

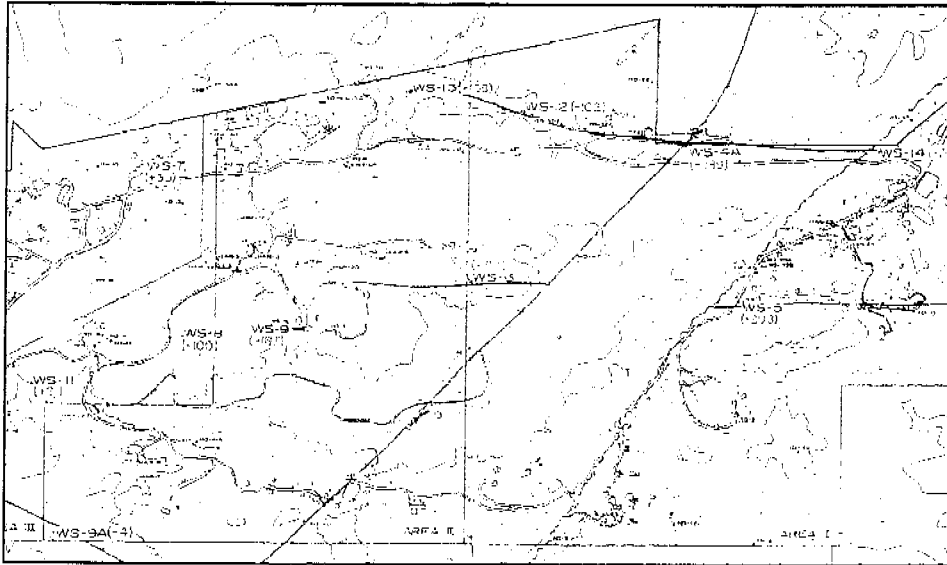


Figure 1.9. Observed water level changes 1954-1997. (GWRC, 1998)

1.6 Pumping Well Water Level Changes

Water levels have been recorded in the water supply wells since the mid-1980s. Water level declines in wells WS-5, 6 and 9a are included as Figures 1.10A-C below.

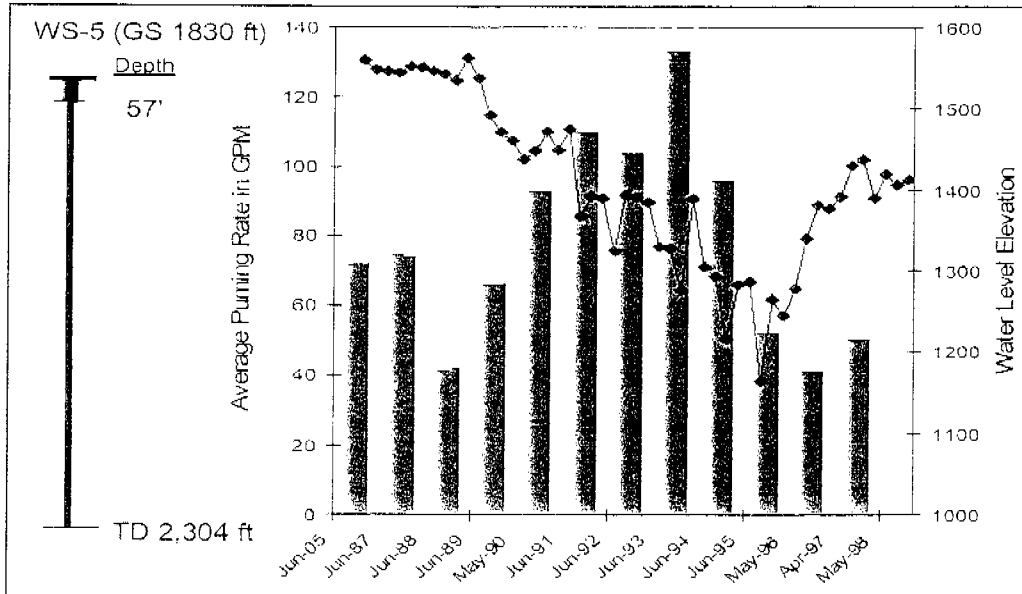


Figure 1.10A WS-5 water levels and pumping rates 1984-1998.

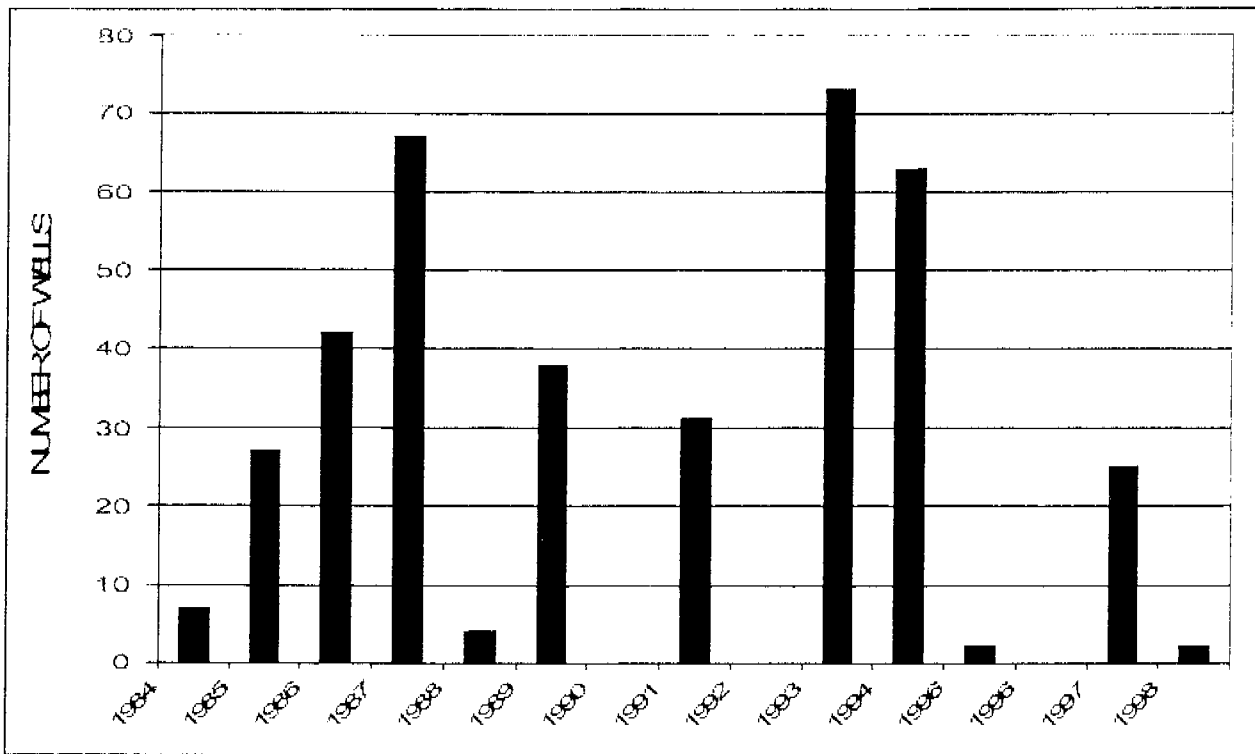


Figure 1.6. Overburden and Bedrock Well Installation at SSFL Since 1984

The majority of the 104 bedrock wells installed at SSFL are single well completions. The open intervals of the wells range from 50 to over 600 feet, as shown in Figure 1.7.

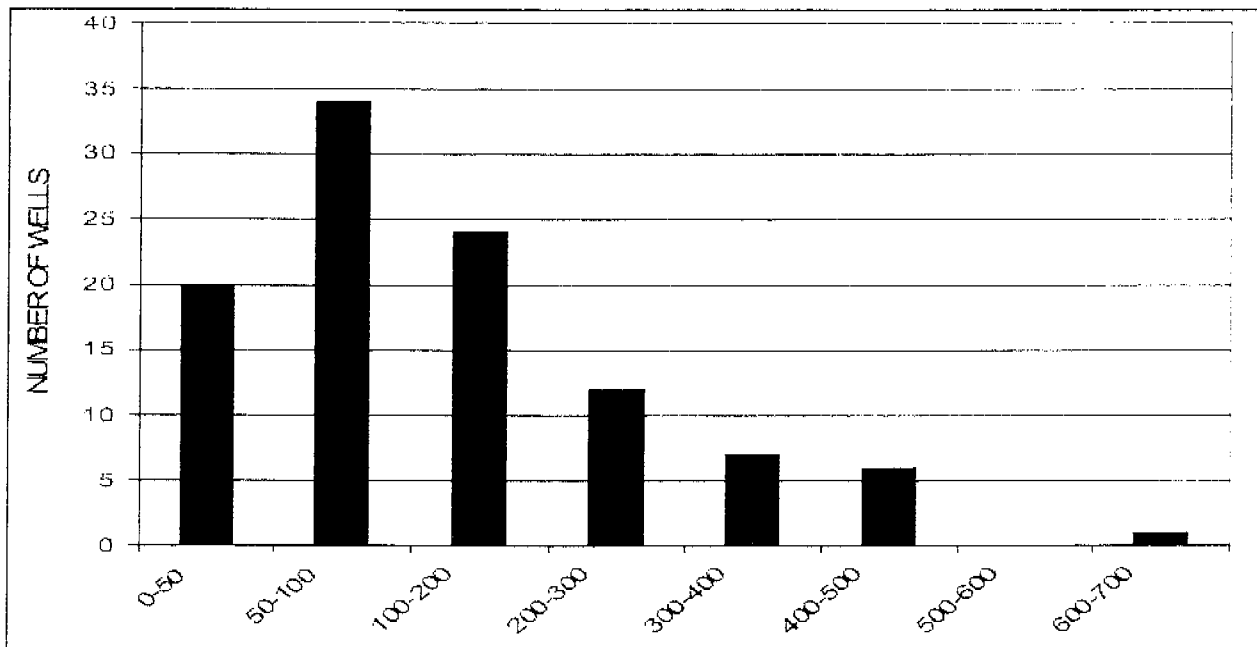
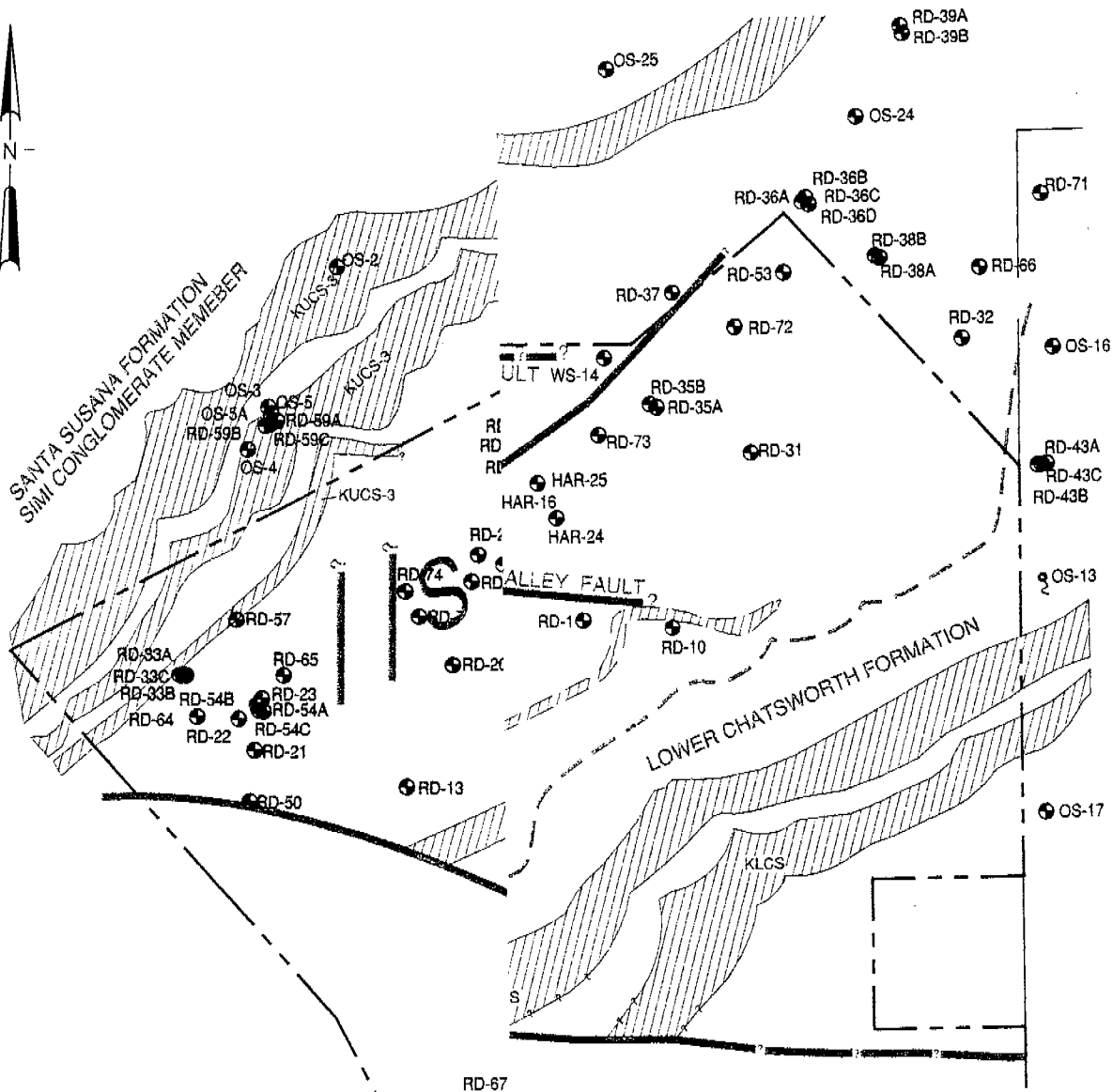
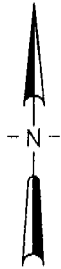






Figure 1.7. Open Intervals of SSFL Bedrock Monitoring Wells in Feet



LEGEND:

-  SANDSTONE 2 WELL
-  SANDSTONE 1 WELL
-  LOWER CHATSWORTH FORMATIC
-  SANTA SUSANA FORMATION WELL



THE BOEING COMPANY
 SANTA SUSANA FIELD LABORATORY
 SANTA SUSANA, CALIFORNIA

**BEDROCK WELL LOCATIONS
 AND STRATIGRAPHY**

SCALE: AS SHOWN

APRIL 2000

UNDERGROUND
 ENGINEERING &
 ENVIRONMENTAL
 SOLUTIONS

86187-014 B07

FIGURE 2.2

2.5×10^{-5} cm/sec for the ridge. Increasing the recharge rate to 20 percent results in bulk hydraulic conductivity estimates of 2.5×10^{-5} cm/sec and 5×10^{-5} cm/sec, respectively.

2.3 Hydrogeologic Properties of SSFL Rock Core

Laboratory testing of rock core obtained from wells installed at SSFL has been performed to determine hydrogeologic properties including matrix hydraulic conductivity, and matrix porosity. Results of these analyses are discussed below.

2.3.1 Matrix Hydraulic Conductivity

Intrinsic permeability data were used to estimate the hydraulic conductivities of the core samples and the results are included with the measured porosity data in Table 2.1. The hydraulic conductivity obtained from laboratory analysis of 21 samples of rock core from wells drilled at SSFL and ranged from 8.5×10^{-11} cm/sec to 1.7×10^{-4} cm/sec. The geometric mean hydraulic conductivity is 1.7×10^{-6} cm/sec, which is about one order of magnitude lower than the bulk hydraulic estimated based on the position of the water table beneath the mountain, as described above.

SANDSTONE SAMPLES			
Well	Depth (ft)	Porosity %	K (cm/sec)
RD-45A	114.0-115.0	11.9	1.6×10^{-6}
	209.0-210.0	12.5	1.1×10^{-5}
	272.5-274.0	13.1	1.5×10^{-5}
RD-46B	24.0-24.2	21.0	1.1×10^{-4}
	49.1-50.2	13.2	6.0×10^{-5}
	70.0-70.5	11.9	3.6×10^{-6}
	105.2-105.6	15.2	1.7×10^{-6}
	140.5-140.9	13.5	1.6×10^{-5}
	177.9-178.2	13.6	7.2×10^{-6}
	210.2-210.5	12.2	5.6×10^{-6}
	292.4-292.7	15.4	1.2×10^{-4}
	358.3-358.6	15.0	6.3×10^{-6}
304.7- 304.9	13.8	1.9×10^{-6}	
RD-49	62.8-64.0	13.4	2.0×10^{-6}
	68.5-70.0	10.8	1.5×10^{-6}
RD-55	76.4-78.0	15.9	6.8×10^{-6}
	90.0-91.0	13.3	1.1×10^{-5}
RD-54C	28.0-29.1	13.4	1.6×10^{-6}
Geometric Mean			7.4×10^{-6}
SHALE/SILTSTONE SAMPLES			
RD-45A	40.3-41.0	6.6	8.5×10^{-11}
RD-55	26.5-28.0	10.6	6.4×10^{-9}
	46.0-47.0	11.4	2.5×10^{-10}

Table 2.1. Hydrogeologic Properties of SSFL Rock Core

A frequency distribution of matrix hydraulic conductivities is shown in Figure 2.3.

2.4 Hydraulic Conductivity from Packer Testing

Packer testing was conducted at the RD-35 and RD-46 locations to aid in the selection of screened intervals. The test intervals were selected based on geophysical logs and well yields during drilling, with the test zones biased to areas of likely or observed water production (and correspondingly elevated hydraulic conductivity). The hydraulic conductivity for the 11 tests ranged from 10^{-7} cm/sec to 10^{-4} cm/sec, with a geometric mean of 4.5×10^{-5} cm/sec, consistent with the estimated bulk hydraulic conductivity for the mountain. This is about one order of magnitude greater than the matrix values shown in Section 2.3, indicating the influence of the fracture network on hydraulic conductivity. A frequency distribution of packer test hydraulic conductivity data is shown in Figure 2.5.

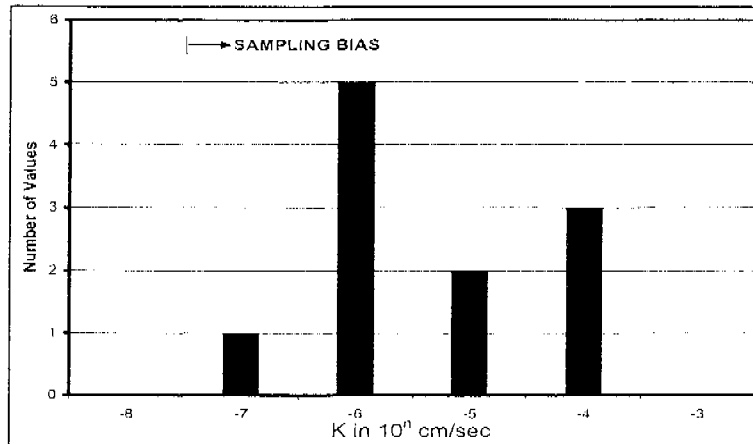


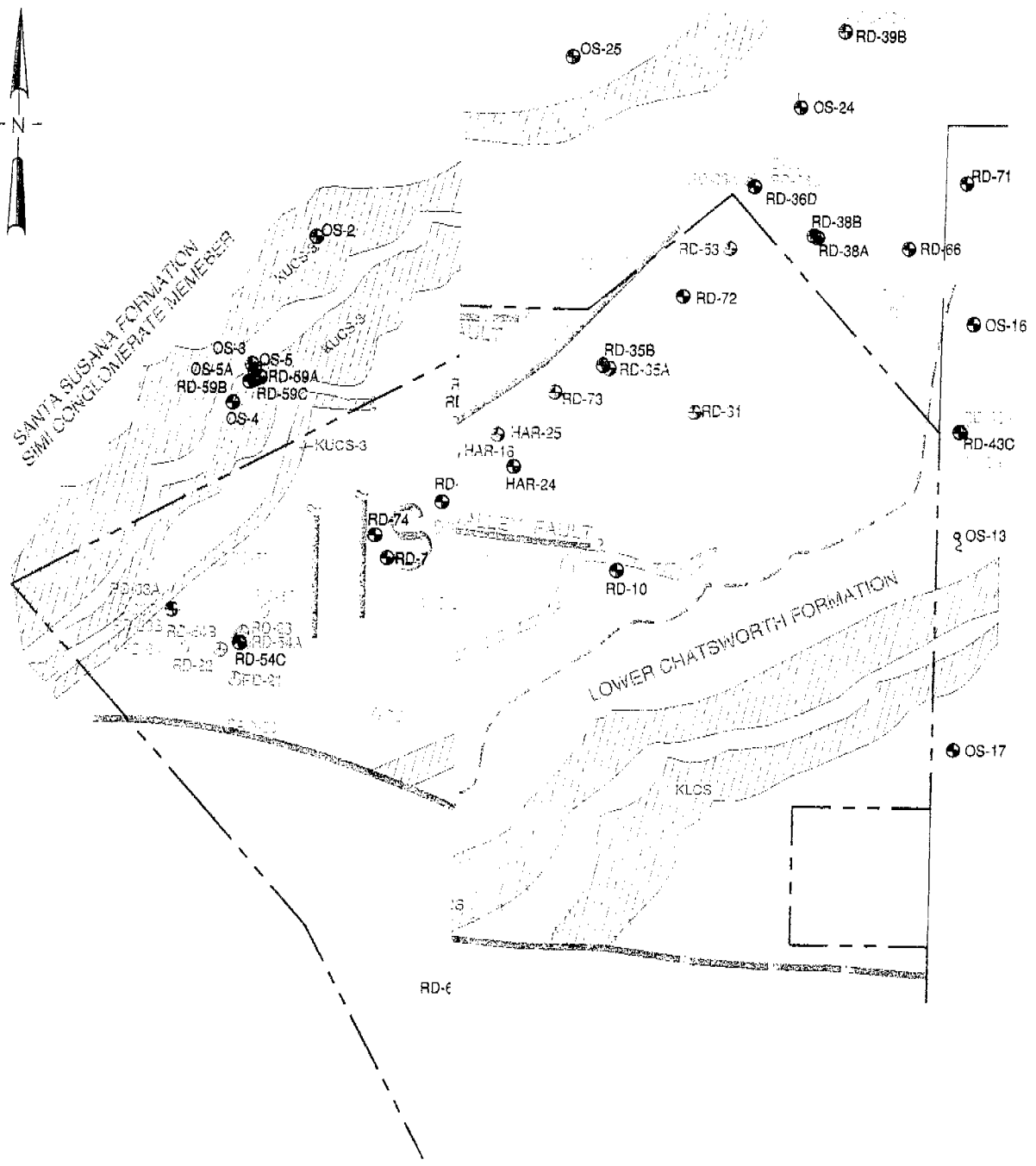
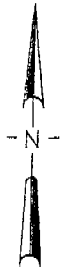
Figure 2.5 Hydraulic Conductivity from Packer Testing.

2.5 Hydraulic Conductivity from Pumping Tests




Pumping tests have been conducted on the majority of the water supply and bedrock monitoring wells at SSFL since the mid-1980s. Single well pumping tests were conducted on most of the wells with a typical duration ranging from one hour to one day. There were 20 tests (out of the approximately 100 single well pumping tests) where a marginal flow rate could not be sustained or the water level decline was very rapid. Water level recovery data is available for these wells, but in many cases it is difficult to analyze because the actual yield of the well could not be determined or the slope of the water level recovery curve is nearly vertical. A value of 1×10^{-6} cm/sec was assumed for these wells, although the actual hydraulic conductivity is probably lower in many cases. The water level recovery plots for these wells are included in Appendix D.

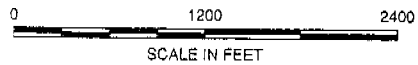
The single well tests were analyzed using the Jacob-Cooper method for drawdown and recovery data and the data are plotted in Appendix D. There are data from about 20 additional wells that were not analyzed for hydraulic conductivity due to a variety of factors. These factors include the obvious influence of nearby streams or other pumping wells, a lack of stabilization in the rate of water level decline during the test, non-uniform responses to pumping, or highly variable pumping rates. In all, data from 57 single well tests were analyzed for hydraulic conductivity. These wells are distributed across the SSFL at the locations shown in Figure 2.6.

Longer duration multi-well pumping tests were conducted at three locations on the site: the RD-73 area in the northeastern portion of the site; at RD-63; and at RD-9. Data from these tests were analyzed using distance drawdown methods and the analyses are plotted in Appendix D. In all, 18 wells were evaluated during the multi-well testing, as shown in Figure 2.6.



LEGEND:

-  SINGLE WELL TEST
-  MULTI-WELL TEST
-  LOW-YIELD - NOT ANALYZED IN SINGLE WELL TEST



SCALE IN FEET



THE BOEING COMPANY
SANTA SUSANA FIELD LABORATORY
SANTA SUSANA, CALIFORNIA

LOCATION OF PUMPING TEST WELLS

SCALE: AS SHOWN

APRIL 2000

86187-014 B09

FIGURE 2.6

2.5.1 Single Well Pumping Tests

Sixty-five single well pumping tests were analyzed to estimate formation hydraulic conductivity and the test data are included in Appendix D. Test Results for the Sandstone 1 wells are summarized in Table 2.2.

Boeing Santa Susana Field Laboratory Hydraulic Conductivities Estimated from Short-Duration, Single Well Pumping Tests Part 1 - Wells Completed in Sandstone 1							
Well	Date of Test	Q (gpm)	Duration (min)	Pump or Recovery	Δs (feet)	Transmissivity T=264*Q/Δs (gpd/ft)	Approximate Hydraulic Conductivity-K (cm/sec)
RD - 1	7/14/1986	25.0	120	P	8.5	776	1.2E-04
RD - 1	7/14/1986	25.0	120	R	10.0	660	1.0E-04
RD - 2	12/3/1985	33.0	135	P	4.0	2178	4.0E-04
RD - 2	12/3/1985	33.0	135	R	5.2	1675	3.1E-04
RD - 5A	3/17/1993	4.8	115	P	3.0	422	2.5E-04
RD - 5A	3/17/1993	4.8	115	R	3.8	333	2.0E-04
RD - 5B	5/19/1993	11.0	300	P	50.0	58	1.1E-05
RD - 5B	5/19/1993	11.0	300	R	72.0	40	7.9E-06
RD - 5C	6/29/1994	25.0	130	P	46.0	143	1.7E-05
RD - 5C	6/29/1994	25.0	130	R	57.5	115	1.3E-05
RD - 31	9/26/1989	24.0	180	P	10.2	621	5.5E-04
RD - 31	9/26/1989	24.0	180	R	10.0	634	5.6E-04
RD - 32	5/5/1994	7.7	160	P	2.5	813	3.2E-04
RD - 32	5/5/1994	7.7	160	R	1.7	1196	4.7E-04
RD - 35	2/5/1993	3.5	240	P	3.4	272	2.6E-04
RD - 35	2/5/1993	3.5	240	R	2.6	355	3.4E-04
RD - 36B	3/18/1994	6.2	180	P	8.5	193	1.9E-04
RD - 36B	3/18/1994	6.2	180	R	4.1	399	4.0E-04
RD - 39	2/25/1994	5.0	165	P	12.4	106	1.4E-04
RD - 39	2/25/1994	5.0	165	R	8.8	150	2.0E-04
RD - 44	3/20/1993	2.8	240	P	7.4	100	8.1E-05
RD - 44	3/20/1993	2.8	240	R	10.5	70	5.7E-05
RD - 47	4/15/1993	2.2	180	P	1.2	484	2.1E-04
RD - 47	4/15/1993	2.2	180	R	1.1	528	2.3E-04
RD - 49A	6/17/1993	2.0	45	P	35.0	15	2.1E-05
RD - 49A	6/17/1993	2.0	45	R	32.0	17	2.2E-05
RD - 49C	8/22/1993	9.5	120	P	1.4	1791	4.5E-04
RD - 52A	2/2/1993	6.2	240	P	8.8	186	2.0E-04
RD - 52C	12/9/1993	7.0	210	P	70.1	26	3.0E-06
RD - 52C	12/9/1993	7.0	210	R	119.4	15	1.8E-06
RD - 55A	4/16/1993	6.8	300	P	4.5	399	1.9E-04
RD - 55A	4/16/1993	6.8	300	R	7.2	249	1.2E-04
RD - 55B	4/23/1993	2.7	100	P	230.0	3	6.8E-07
RD - 55B	4/23/1993	2.7	100	R	75.0	10	2.1E-06
RD - 58B	9/11/1994	7.0	180	P	6.7	276	8.0E-05
RD - 58B	9/11/1994	7.0	180	R	5.9	313	9.0E-05
WS - 4A	4/23/1985	30.0	210	P	30.0	264	6.4E-05
WS - 5	12/4/1985	530.0	80	R	10.5	13326	3.1E-04
WS - 8	8/22/1985	52.5	300	R	70	99	1.9E-05
WS - 9	8/21/1985	49.0	465	R	70.0	185	5.7E-06
WS - 11	8/23/1985	23	515	R	218	27.9	2.0E-06
WS - 13	2/3/1968	294.0	360	P	4.9	15840	9.0E-04
WS - 14	11/15/1985	48.0	450	P	8.0	1584	7.8E-05
Non-Productive Wells: RD-36A, 36C, 40, 41A, 41B, 41C, 42, 55B							<1.0E-6
Geometric Mean*							2.6E-05

*Note: For wells with pumping and recovery data, only recovery data used in geometric mean

Table 2.2 Hydraulic Conductivity Estimates For Sandstone 1 Wells From Single Well Pumping Tests.

The estimated geometric mean of the 35 Sandstone 1 wells tested was 2.6×10^{-5} cm/sec, assuming the hydraulic conductivity of the non-yielding wells was 1×10^{-6} cm/sec. Of the eight wells noted in

There are a limited number of wells installed in the Lower Chatsworth Formation, as shown on Figure 2.2. The results of the single well pumping tests for Lower Chatsworth Formation wells is included in Table 2.4.

Boeing Santa Susana Field Laboratory							
Hydraulic Conductivities Estimated from Short-Duration Pumping Tests							
Part 3: Wells Completed in Lower Chatsworth Formation							
Well	Date of Test	Q (gpm)	Duration (min)	Pump or Recovery	Δs (feet)	Transmissivity $T=264 \cdot Q/\Delta s$ (gpd/ft)	Approximate Hydraulic Conductivity-K (cm/sec)
RD - 43B	11/4/1994	9.3	190	P	1.7	1444	3.5E-04
RD - 43B	11/4/1994	9.3	190	R	1.4	1754	4.3E-04
RD - 46	2/4/1993	2.2	240	R	1.2	484	3.1E-04
RD - 48B	6/17/1993	1.5	115	P	95.0	4	1.6E-06
RD - 48C	5/20/1993	50.0	170	P	4.6	2870	5.0E-04
RD - 48C	5/20/1993	50.0	170	R	5.0	2640	4.6E-04
RD - 62	5/18/1994	6.0	128	P	0.7	2263	2.7E-03
RD - 62	5/18/1994	6.0	128	R	0.7	2263	2.7E-03
Non-Productive Wells: RD-43A, 48A, 61							<1.0E-6
Geometric Mean							2.7E-05
*Note: For wells with pumping and recovery data, only recovery data used in geometric mean							

Table 2.4 Hydraulic Conductivity Estimates For Lower Chatsworth Formation Wells From Single Well Pumping Tests.

The geometric mean estimated for the eight single-well pumping tests conducted in the Lower Chatsworth Formation is 2.7×10^{-5} cm/sec. The three wells in the Lower Chatsworth Formation that did not yield sufficient water to allow testing, RD-43A, 48A and 61, are noted in Table 2.4. RD-61 is located on or immediately adjacent to the Coca Fault.

2.5.2 Multi-Well Pumping Tests

Three multi-well pumping tests were analyzed to estimate hydraulic conductivity and storage coefficient and the results are included in Appendix D. Test results for each of the multi-well tests are summarized below.

The RD-73 pumping test was conducted over a 90-day interval from 27 May to 18 August 1997. The well was pumped at a rate of about 2.7 gpm and water levels were measured in wells RD-73, 31, 35 and 53, and in HAR-1 and WS-14 beginning on 27 May. Water level measurements were also obtained from HAR-16 beginning several weeks after pumping started. A pre-pumping static water level was not available for this well and water level response data was not analyzed. The locations of the pumping and observation wells are shown in Figure 2.7.

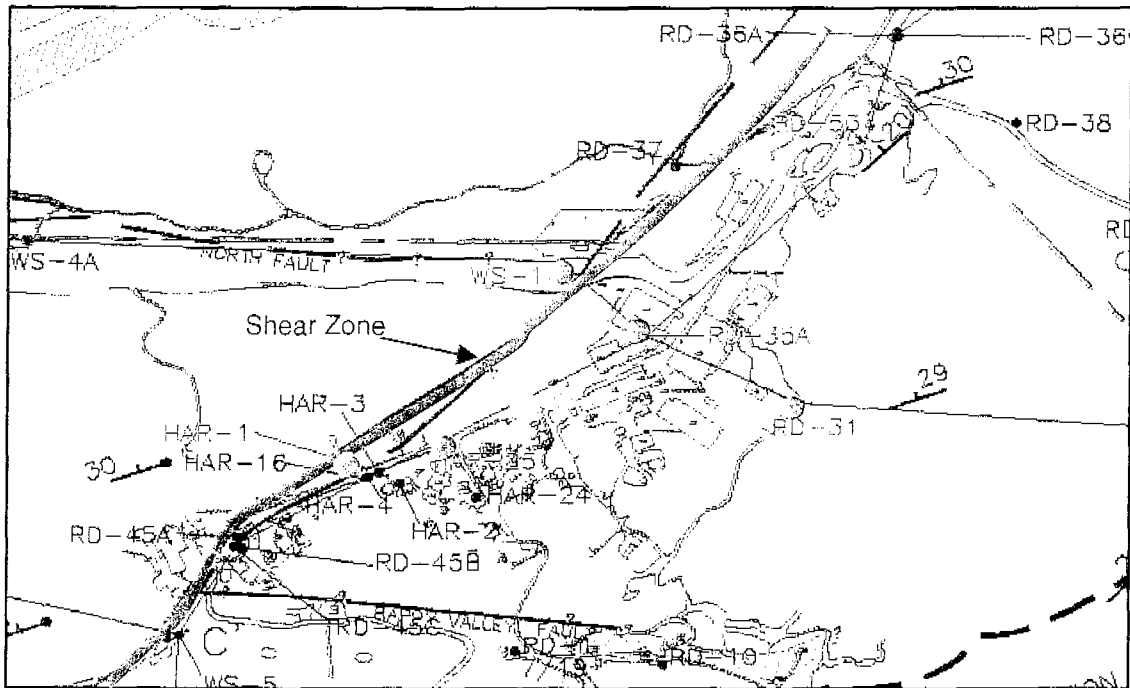


Figure 2.7 Location of RD-73 Pumping Test and Observation Wells

Individual water level response graph for RD-31, 35, 53 and 73 and HAR-1 and 25 are included in Appendix D. The distance-drawdown plot for the test is shown in Figure 2.8.

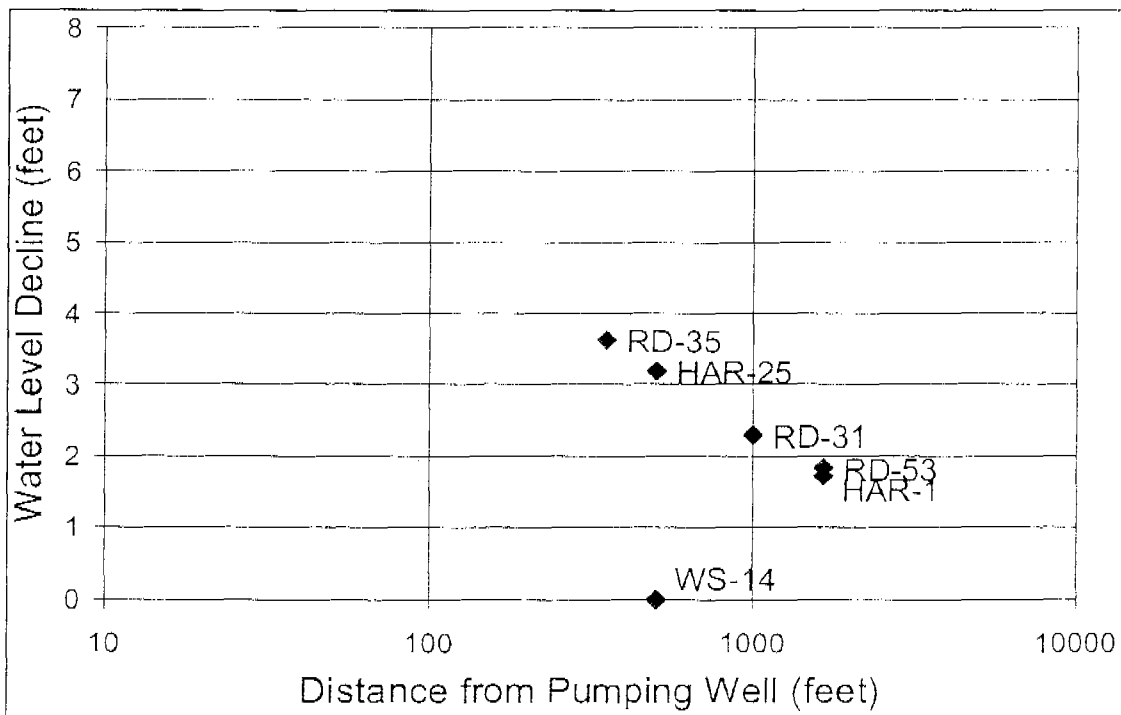


Figure 2.8 Distance-Drawdown Plot For RD-73 Pumping Test.

Water levels in WS-14 did not respond to pumping from RD-73. WS-14 is located on the opposite side of the Shear Zone, as shown in Figure 2.7. The results of the RD-73 pumping test are summarized in Table 2.5.

Well/Analysis	Transmissivity $T=264 \cdot Q/\Delta s$ (gpd/ft)	Approximate Hydraulic Conductivity- K (cm/sec)	Estimated Storage Coefficient
RD- 73	188	7.3E-05	NA
RD- 53	1697	6.6E-04	3.1E-04
RD- 31	123	4.8E-05	1.1E-03
RD- 35	204	7.9E-05	4.2E-03
HAR- 25	137	5.3E-05	2.7E-03
HAR- 1	310	1.2E-04	4.0E-04
Distance-Drawdown	510	2.0E-04	2.7E-04

Table 2.5 RD-73 Pumping Test Results.

The hydraulic conductivities estimated from the RD-73 pumping test are consistent with those measured for Sandstone 1, as shown in Table 2.2. The estimated storage coefficient indicates the bedrock system in the northeast corner of SSFL behaves as confined system even though the bedrock wells are under water table conditions. This apparent confined behavior results from the very low effective porosity of the fracture network that dominates the transmission of the hydraulic stress induced by pumping. The observed drawdown at the end of the testing period is plotted on Figure 2.9.

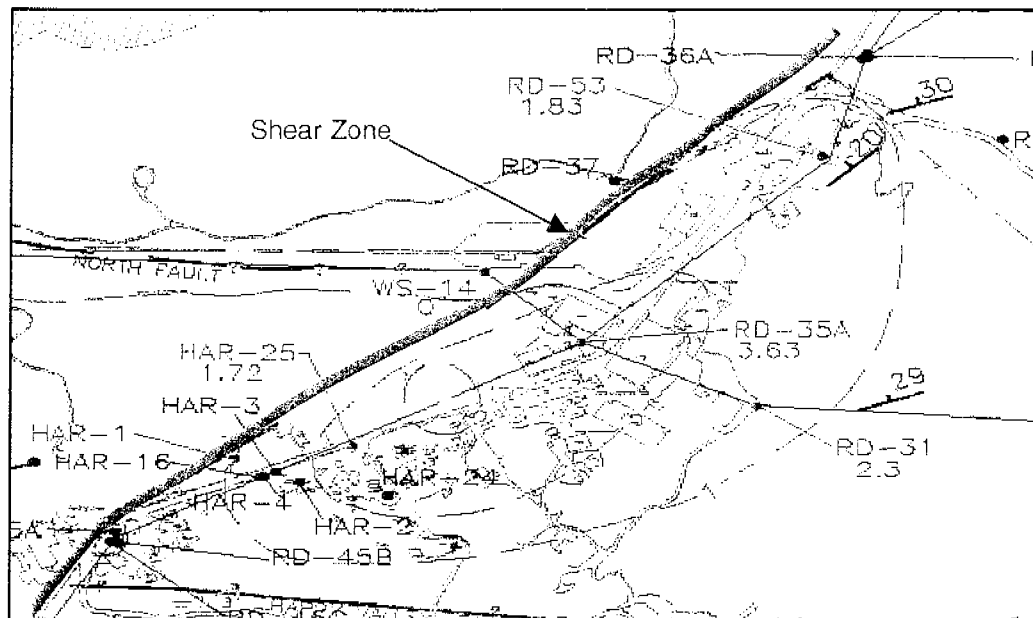


Figure 2.9 Observed Drawdown After 90 Days Of Pumping At RD-73

The drawdown pattern resulting from the 90-day pumping test on RD-73 (Figure 2.9) indicates an apparent elevation in hydraulic conductivity parallel to the strike of the Chatsworth Formation. Drawdown appears to truncate at the shear zone to the west, and at the Happy Valley Fault to the south. The slope of the cone of depression also appears to increase to the southeast opposite the direction of dip of the formation. This suggests the hydraulic conductivity of the Chatsworth Formation is lower parallel to dip, which is consistent with the behavior of most sedimentary rock aquifers.

A 47-day pumping test was conducted on RD-63 from 25 April to 11 June 1996 at a flow rate of 1.7 gpm. Water levels were monitored in wells RD-17, 18, 19, 27, 28, 30, 34A, 34B, 34C, and 63 beginning on 22 April and weekly after the test began on 25 April. A response to pumping was noted in the majority of the wells, as shown in Figure 2.10.

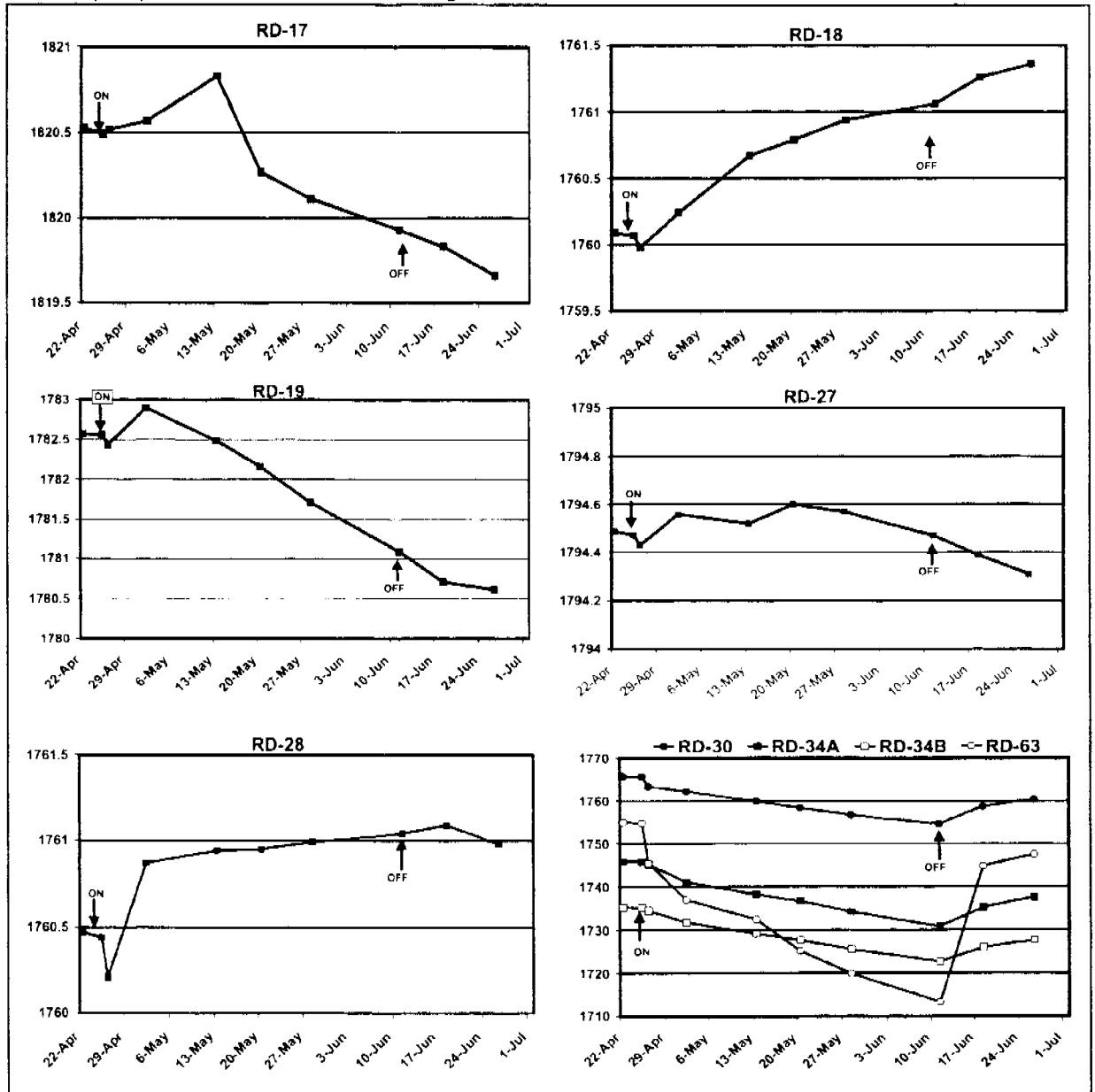


Figure 2.10 Water Level Observations During RD-63 Pumping Test.

Obvious drawdown and recovery was noted in wells RD-30, 34A, 34B and 34C (not plotted) during the test. Normal water level fluctuations appear to have obscured the impact of pumping on the remainder of the wells monitored, but inflections in the trend of the water levels was noted in all the wells at the beginning and end of the test. Accordingly, the water level responses in all of the wells indicate the fracture network in the north-central portion of SSFL is well connected, as exhibited by the spatial distribution of the monitoring wells that responded to pumping from RD-63. It should be noted that other wells in the area may have responded, but water levels were only obtained for those wells indicated. Only those wells that exhibited obvious drawdown throughout the test were evaluated to estimate hydraulic properties and the results are shown in Table 2.6.

Formation	Number of Wells Tested	Geometric Mean K (cm/sec)	Number of Non-Yielding Wells	Range of Storage Coefficient, S
Sandstone 1	41	3.4×10^{-5}	8	0.00027 – 0.0042
Sandstone 2	38	4.2×10^{-6}	9	0.00025 – 0.0053
Lower Chatsworth	8	2.7×10^{-5}	3	NA
All Wells	87	1.3×10^{-5}	20	0.00025 – 0.0053

Table 2.7 Summary of SSFL Pumping Test Results

As is evident in Table 2.7, the hydraulic conductivity of Sandstone 2 is about one order of magnitude less than that of Sandstone 1. There were also more non-producing wells encountered in Sandstone 2. The hydraulic conductivity of the Lower Chatsworth Formation appears to be equivalent to that of Sandstone 1, but the mean was based on data from only eight wells.

The bulk hydraulic conductivity derived from the geometric mean of 101 test results from pumping tests on 87 wells is 1.3×10^{-5} cm/sec, assuming a value of 1×10^{-6} cm/sec for the non producing wells. This value is comparable to the estimated bulk hydraulic conductivities necessary to maintain a high water table elevation on the mountain, as discussed in Section 2.2. The bulk hydraulic conductivity derived in Section 2.2 was 1.25×10^{-5} cm/sec for the dome configuration and 2.5×10^{-5} cm/sec for the ridge, based on a recharge rate of 10 percent. Increasing the recharge rate to 20 percent resulted in bulk hydraulic conductivity estimates of 2.5×10^{-5} cm/sec and 5×10^{-5} cm/sec, respectively.

The bulk hydraulic conductivity measured from the pumping tests assumed a value of hydraulic conductivity for non-producing wells of 1×10^{-6} cm/s. In addition, all of the well installation and packer testing methods employed were targeted to zones of elevated water production, and hence biased to zones of more elevated hydraulic conductivity. Given these factors, the actual bulk hydraulic conductivity of the bedrock at SSFL is less than the measured value based on the 87 tested wells. As a result, the actual rate of annual recharge from infiltration that is required to sustain a groundwater mound on the mountain is probably less than 10 percent of the average annual precipitation.

Within the group of wells for which data was not analyzed due to the questions about data quality identified in Section 2.4, there are three wells (RD-04, RD-6 and WS-12) that exhibited relatively high yields with minimal drawdown. The available drawdown and recovery data for these wells is included in Appendix D. Wells RD-04 and RD-06 were not analyzed because the rate of water level decline had not stabilized by the end of the test. Well WS-12 was not analyzed because only recovery data was available and no significant residual drawdown was evident. If an approximate evaluation of the available data is conducted, the hydraulic conductivity derived is on the order of 10^{-3} cm/sec. Of these wells, RD-04 and WS-12 are screened in Sandstone 1, and RD-06 is screened in the Lower Chatsworth Formation. The inclusion of these values into the data set would not materially alter the geometric mean, particularly in light of the large number of non-yielding, low hydraulic conductivity wells for which data is also not available.

2.5.5 Influence of Open Interval on Hydraulic Conductivity Estimates

The open interval of the bedrock wells at SSFL varies from about 50 to over 600 feet, as noted in Section 1. The wells with the shortest open intervals tend to be the wells exhibiting the highest hydraulic conductivity, as shown in Table 2.8.

Well Group	Open Interval (feet)	Geometric Mean K (cm/sec)
Monitoring Wells	0-50	4.0×10^{-4}
	50-100	1.6×10^{-5}
	100-200	6.7×10^{-6}
	>200	7.1×10^{-6}
Water Supply Wells	580-2100	4.7×10^{-5}

Table 2.8 Hydraulic Conductivity and Open Interval

The apparent relationship between open interval and hydraulic conductivity results in part from the historical method of well installation that targeted water-producing zones for screened interval locations. The "first water" wells were installed in zones where sufficient hydraulic conductivity was encountered to allow discharge of water from the borehole during drilling. The majority of these wells have shorter open intervals. The deeper wells were drilled until water was produced from the borehole at a sufficient rate. If the hydraulic conductivity of the formation was low, a longer open interval was necessary to allow sufficient water production.

2.5.6 Spatial Distribution of Hydraulic Conductivity

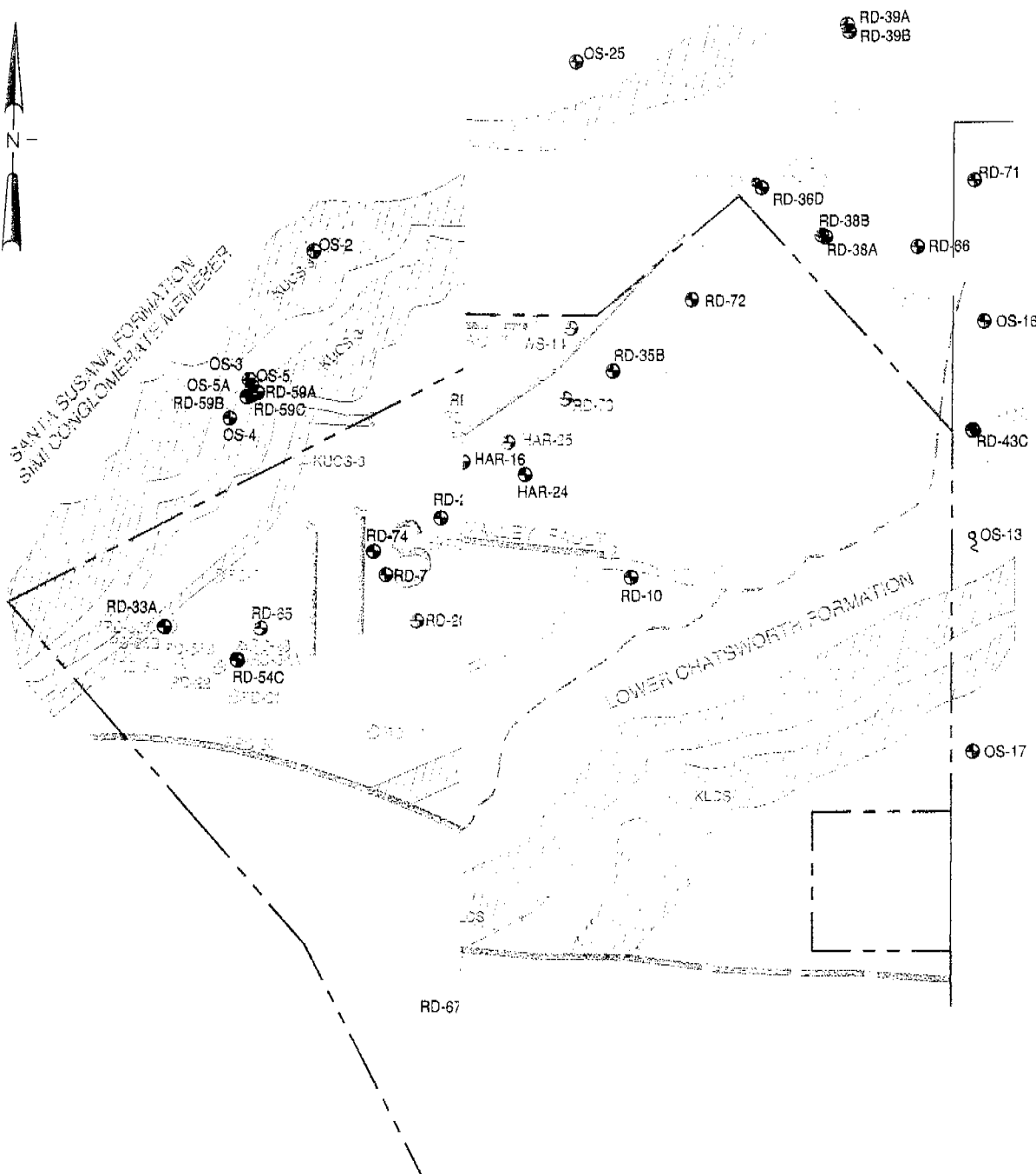
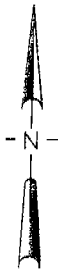
The areal distribution of hydraulic conductivity at SSFL is illustrated on Figure 2.13. The spatial distribution indicates the predominance of low hydraulic conductivity bedrock in Sandstone 2, and the generally moderate hydraulic conductivity of Sandstone 1.

The marginal-yielding wells were located in two primary areas, either along major fault lineaments or in the far-western portion of the site. Wells installed on or immediately adjacent to the Coca Fault (RD-41A, 41B, 41C, 42, and 61) did not yield sufficient water for testing, nor did RD-40 located on or adjacent to the Skyline Fault. RD-21, 22, 23, 33A, 54A and 54B are located within a few hundred feet of each other in an area dominated by low hydraulic conductivity bedrock.

2.5.7 Impacts of Faults and Major Lineaments on Hydraulic Conductivity

Several wells at SSFL have been installed along major lineaments and known fault trends. In the case of the water supply wells, this was often an intentional strategy to improve the likelihood of installing a higher yielding well than would be anticipated in a non-faulted portion of the bedrock. The fact that many of the monitoring wells fall on apparent fault lineaments is probably more a result of the fact the lineaments are often represented on the site by broad topographic lows with easy access.

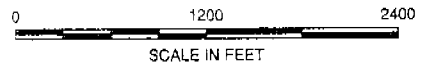
The wells for which hydraulic conductivity data is available or pumping tests attempted that are located on or adjacent to known faults or lineaments in Sandstone 1 are summarized in Table 2.9.



LEGEND:

ESTIMATED HYDRAULIC CONDUCTIVITY

- $\sim 10^{-9}$ cm/sec INSUFFICIENT DATA
- 10^{-3} cm/sec FROM TEST
- 10^{-4} cm/sec
- 10^{-5} cm/sec
- 10^{-6} cm/sec
- 10^{-7} cm/sec
- NON-YIELDING WELL



THE BOEING COMPANY
SANTA SUSANA FIELD LABORATORY
SANTA SUSANA, CALIFORNIA

**HYDRAULIC CONDUCTIVITY
OF SSFL BEDROCK WELLS**

ENGINEERING
ENGINEERING &
ENVIRONMENTAL
SOLUTIONS

SCALE: AS SHOWN

APRIL 2000

86187-014 B06

Well	Location	Estimated Hydraulic Conductivity (cm/sec)
WS-4A	North Fault	6.4×10^{-5}
WS-5	Shear Zone	3.1×10^{-4}
WS-10	Coca Fault	$<1.0 \times 10^{-6}$
WS-13	North Fault	9.0×10^{-4}
WS-14	North Fault	7.8×10^{-5}
RD-5A	Burro Flats Fault	2.0×10^{-4}
RD-5B	Burro Flats Fault	7.9×10^{-6}
RD-5C	Burro Flats Fault	1.3×10^{-5}
RD-40	Skyline Fault	$<1.0 \times 10^{-6}$
RD-41A	Coca Fault	$<1.0 \times 10^{-6}$
RD-41B	Coca Fault	$<1.0 \times 10^{-6}$
RD-41C	Coca Fault	$<1.0 \times 10^{-6}$
RD-42	Coca Fault	$<1.0 \times 10^{-6}$
RD-61	Coca Fault	$<1.0 \times 10^{-6}$
Geometric Mean		1.4×10^{-5}

Table 2.9 Hydraulic Conductivities of Wells on Known Faults or Lineaments in Sandstone 1

The geometric mean hydraulic conductivity for the wells on or near known faults or linear features is 1.4×10^{-5} cm/sec, calculated using a value of 1.0×10^{-6} cm/sec for wells that did not yield sufficient water to allow testing. The geometric mean of wells in Sandstone 1 not installed on or near known faults or linear features is 4.4×10^{-5} cm/sec. The geometric means and the distribution of wells shown on Figure 2.13 indicate wells completed on or in immediate proximity to faults or linear geologic features in Sandstone 1 are more likely to exhibit low hydraulic conductivity than those completed at distance from these features. Accordingly, the major faults at SSFL are not likely to be preferred, through-going groundwater flow pathways.

Water supply wells WS-2, 3, 4, 4A, 12 and 14 are located on the North Fault, along with the RD-52 cluster. Pumping test data are only available and were analyzed for WS-4A, WS-14, RD52A and RD-52C and the hydraulic conductivity ranges between 1.8×10^{-6} cm/sec and 2.0×10^{-4} cm/sec. An accurate estimate of the hydraulic conductivity for WS-12 is not possible based on existing data, as discussed in Section 2.4.3, but it is probably on the order of 10^{-3} cm/sec. Wells WS-2, 3 and 4 were low yielding wells that presumably had low hydraulic conductivity. Based on these data, there is no consistent zone of elevated hydraulic conductivity evident along the North Fault.

WS-10 was installed on the Coca Fault near the intersection of the Skyline Fault. The well was abandoned after completion in 1956 and was noted as being a "dry hole" in a 10 February 1959 Rocketdyne generated table entitled "PFL Water Level Data". When considered together with the other five non-yielding monitoring wells installed along the Coca Fault, as indicated in Table 2.9, the Coca Fault appears to be a low hydraulic conductivity feature.

The occurrence of elevated hydraulic conductivity in individual bedrock wells at SSFL results from the location-specific combination of the matrix hydraulic conductivity, which has been measured to be as high as 10^{-4} cm/sec, and the degree of jointing and fracturing. This local combination of matrix and fracture properties results in the areal distribution of hydraulic conductivity shown on Figure 2.13. As is evident in the figure, wells exhibiting elevated hydraulic conductivity are more likely to be located in areas that are devoid of known faults or linear geologic features.

The absence of through-going high hydraulic conductivity features at SSFL is also supported by the presence of high water table conditions at the site. If a through-going high hydraulic conductivity feature were present at SSFL, the feature would act to drain the mountain.

Well	Approximate Hydraulic Conductivity-K (cm/sec)	Static Water Level Elevation (11/98)
RD - 5A	2.0E-04	1598.79
5B	7.9E-06	1653.18
5C	1.3E-05	1640.11
RD - 33B	1.2E-06	1503.29
33C	5.2E-06	1504.03
RD - 34A	3.3E-05	1718.88
34B	3.1E-06	1713.36
34C	7.7E-06	1756.02
RD - 48B	1.6E-06	1603.49
48C	4.6E-04	1552.40
RD - 49A	2.2E-05	1851.02
49C	4.5E-04	1507.04
RD - 52A	2.0E-04	1628.14
52C	1.8E-06	1486.19
RD - 55A	1.2E-04	1746.56
55B	2.1E-06	1717.91

Table 2.11 Hydraulic Conductivity and Head Data for Cluster Wells

The hydraulic conductivity of individual wells within the well cluster data shown in Table 2.12 varies by up to three orders of magnitude. There are large differences in hydraulic head between some of the intervals within a cluster, but the variation doesn't appear to coincide directly with the observed difference in hydraulic conductivity. The head differences may relate more to the hydraulic conductivities of the bedrock between the open intervals that is not screened by the wells.

Discrete hydraulic conductivity and head data was developed for RD-35B and RD-46B as part of the investigations conducted by the University of Waterloo and Colorado State University, as shown in Figures 2.14 and 2.15, respectively.

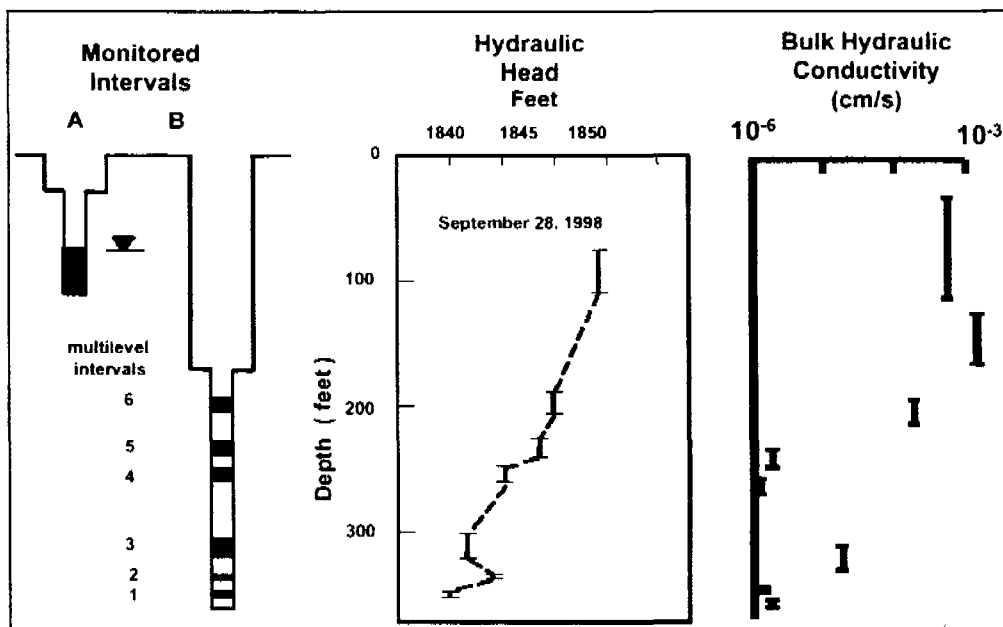


Figure 2.14 Hydraulic Head and Hydraulic Conductivity Distribution in RD-35B

Frequent water level measurements were obtained prior to shutdown, and throughout the sequential restart period. The observed water level recovery and drawdown trends provide inferences about natural hydraulic discontinuities boundaries within the hydrogeologic system at SSFL. The locations of the pumping wells are shown on Figure 2.2. If a monitoring well was in hydraulic communication with one of the pumping wells that was shutdown, the water level would be expected to rise in response to the cessation of pumping. Likewise, the water level in the monitoring well would be expected to fall when pumping resumed. The response of site monitoring wells to the shutdown and restart of pumping is noted on Figure 2.16.

Wells to the north of the Happy Valley Fault/Happy Valley Shale and to the east of the shear zone did not respond to the cessation or restart of pumping. None of the pumping wells are located in the area to the north of the Happy Valley Fault/Happy Valley Shale and to the east of the shear zone.

To the south of the Happy Valley Fault, RD-10 was the only well that appeared to respond to the restart of RD-1, while only RD-44 appeared to respond to the restart of RD-2. Well RD-1 did not respond to the restart of RD-2 or WS-5, and RD-2 did not respond to either RD-1 or WS-5. It is possible that the Happy Valley Shale isolates RD-2 from RD-1.

The only well that apparently responded to the restart of WS-5 was RD-45C, as noted on the hydrographs in Appendix E. The fact that RD-45A and RD-45B did not respond to the restart of WS-5 is likely the result of the screened interval placement of the wells relative to the Happy Valley Shale, as shown in Figure 2.17.

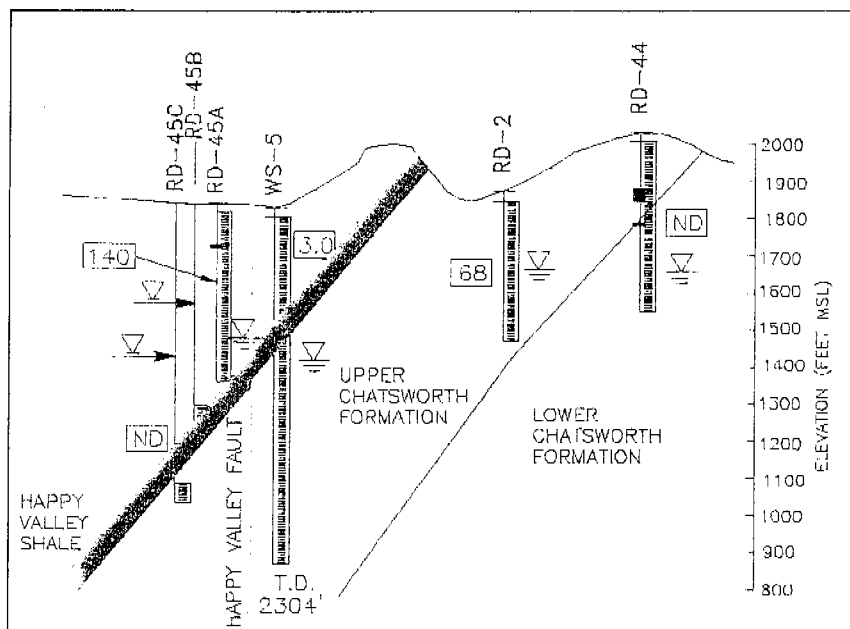
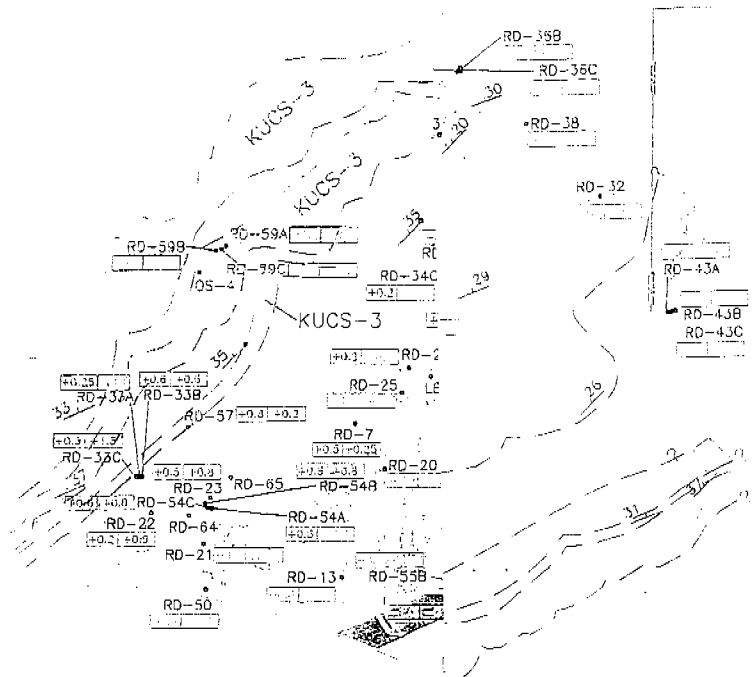
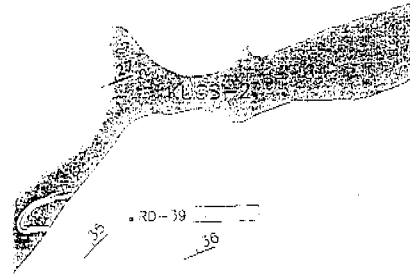
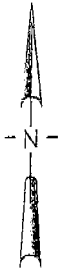


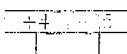
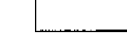

Figure 2.17 Screened Intervals of RD-45 Cluster and WS-5

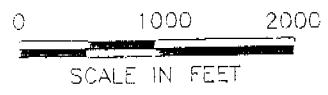
Although RD-45C is screened below the Happy Valley Shale and responded to the restart of WS-5, RD-2, which also installed stratigraphically below the shale, did not. Wells west of the Shear Zone did not appear to respond to the restart of WS-5 either.

The response of wells in the central portion of the site is illustrated in detail in the well hydrographs included in Appendix E. Wells RD-47, RD-45A, RD-45B and RD-4 respond to the shutdown and restart of WS-6 on July 19th. Wells along the North Fault (WS-4A, WS-12 and WS-14) did not appear to respond immediately to the shutdown of WS-5 or WS-6, but water levels in these wells did begin to rise



LEGEND:

-  CHANGE IN WATER LEVEL AT COMMENCEMENT OF PUMPING
-  CHANGE IN WATER LEVEL AT PUMPING WELL SHUTDOWN
-  PUMPING WELL SHUT OFF



THE BOEING COMPANY
SANTA SUSANA FIELD LABORATORY
SANTA SUSANA, CALIFORNIA

**WATER LEVEL RESPONSES
DURING 1993 HYDRAULIC
COMMUNICATION STUDY**

SCALE: AS SHOWN

APRIL 2000

86187-014 B12

five to seven days later. Water level measurements were only obtained for 3 days after the restart of WS-5, and no response was evident in WS-4A, WS-12 and WS-14.

Wells in Sandstone 2 did not respond to the shutdown of pumping wells in Sandstone 1. Wells RD-30 and RD-34B responded to the cessation of pumping at RD-63, consistent with the results of the RD-63 pumping test. WS-SP responded to the shutdown and restart of RD-9, but there was no response in other wells in Sandstone 2.

Wells south of the Coca Fault did not respond to the shutdown of the pumping wells to the north. WS-5A responded to WS-9A, but other nearby wells to the east and west did not. There was no apparent response of any of the wells in the lower Chatsworth Formation south of the Coca fault to the cessation of pumping.

In summary, the following conclusions can be drawn from the hydraulic communication study:

- The hydraulic impact of the cessation and restart of pumping does not appear to have been transmitted across the Shear Zone, the Coca Fault, the Happy Valley Shale/Happy Valley Fault, or Shale 2 which lies stratigraphically between Sandstone 1 and Sandstone 2.
- Wells along major structural features did not show a preferential response to the shutdown and restart of the pumping wells. In fact, the only wells in which a response was obvious were those located at distance from any known structural feature or observed linear feature.
- For wells installed in Sandstone 1 north of the Coca Fault, west of the Shear Zone and east of Shale 2, the impact of the cessation and restart of pumping was evident in monitoring wells located at distances of up to 2,000 feet from the pumping wells.
- The hydraulic effect of the cessation of pumping in Sandstone 2 was only evident a few hundred feet from the pumping wells. The difference in response compared to Sandstone 1 is most likely due to the lower hydraulic conductivity of the formation.

2.8 Observed Water Level Offsets at Major Geologic Features

Significant water level offsets are evident at SSFL coincident with the Shear Zone, Shale 2 and Shale 3. The water level conditions across the shear zone in the northeastern corner of the site are depicted in Figure 2.18.

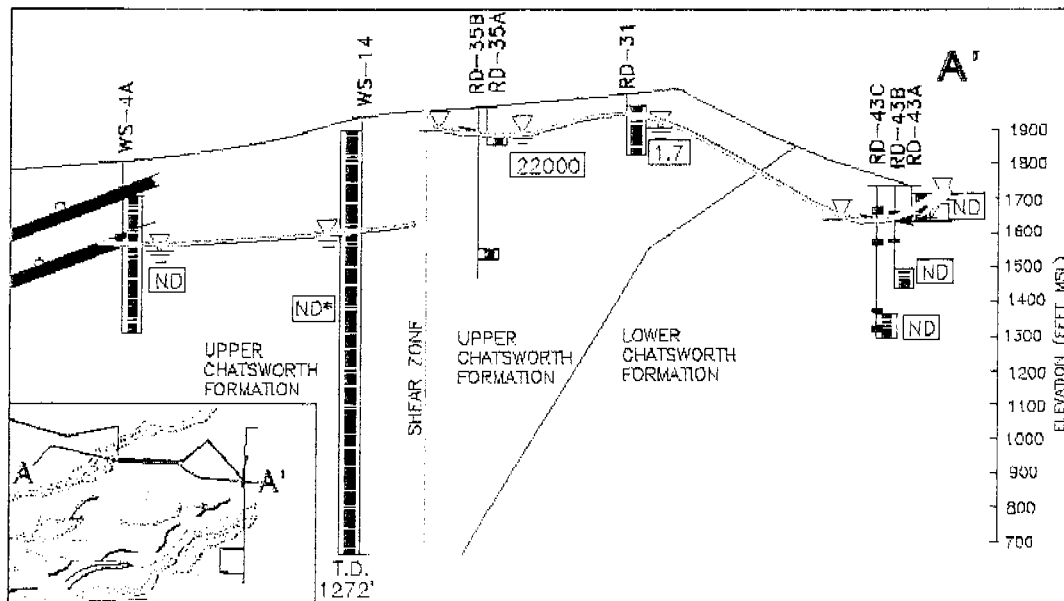


Figure 2.18 Water Level Offset Across Shear Zone

The water level offset across the shear zone creates a substantial groundwater gradient to the west. If groundwater flow occurred from east to west across the Shear Zone, contamination from the RD-35 area would be expected to migrate to the vicinity of WS-14. Contamination has not been detected in WS-14.

In order to maintain the large water level offset across the Shear Zone, there must be a significant reduction in hydraulic conductivity within the Shear Zone. The hydraulic conductivity measured in wells on both sides of the Shear Zone is in the 10^{-4} to 10^{-5} cm/sec range. In order to maintain a water level offset of over 200 feet, the hydraulic conductivity across the shear zone would be on the order of 10^{-7} cm/sec. A hydraulic conductivity in this range is consistent with the lack of transmission of the impact of the cessation and restart of pumping across the shear zone during the hydraulic communication study.

The observed water level offset across Shale 2 is evident in Figure 2.19.

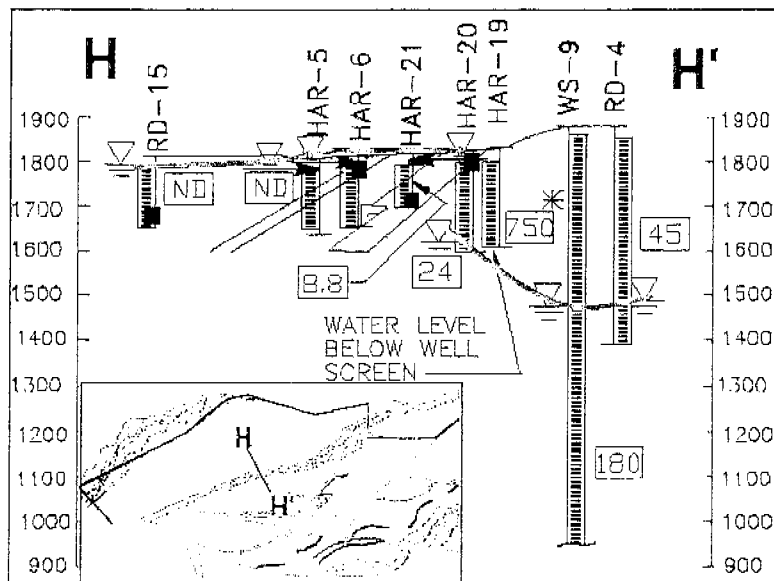


Figure 2.19 Water Level Offset Across Shale 2

The water level offset across Shale 2 is evident along the outcrop area of Shale 2 in the central portion of SSFL. The water level offset most likely results from the low hydraulic conductivity of the shale units.

Matrix hydraulic conductivity values for shale samples obtained from RD-55 were in the 10^{-9} to 10^{-10} cm/sec range, as shown in Table 2.1. The low hydraulic conductivity of Shale 2 is consistent with the lack of transmission of the pumping impacts during the hydraulic communication study.

The water level offset across shale 3 is evident in Figure 2.20. In this case, the hydraulic gradient is

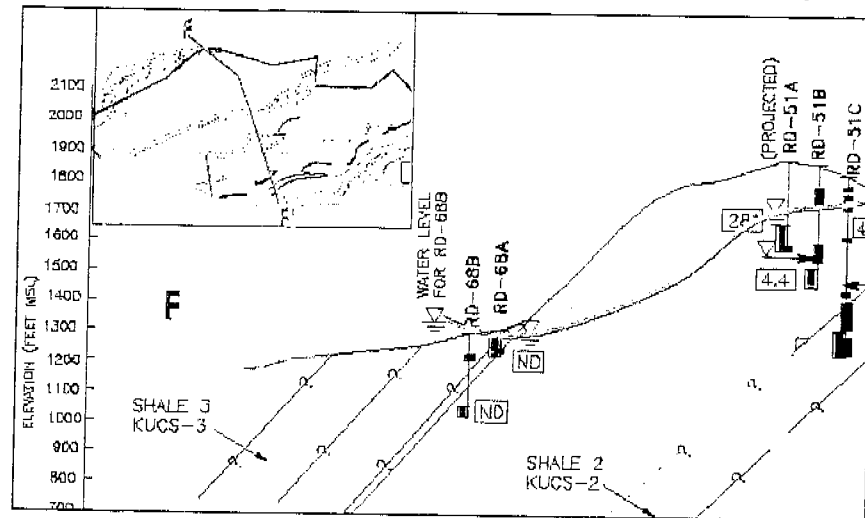


Figure 2.20 Water Level Offset Across Shale 3

upward across Shale 3 because Sandstone 2 is under confined conditions as it dips beneath Shale 3 to the north and west of SSFL.

Water level data is limited along the north side of the Coca Fault, so that direct evidence of significant water level offset across the Coca Fault is not available. Indirect evidence in the form of a long-term water level response to pumping is included as Figure 1.10. Drawdown resulting from pumping in the central portion of SSFL appears to terminate at the Coca Fault, Shale 2, and the Shear zone. There is some amount of water level decline shown west of Shale 2 in Figure 1.10, but that results from the fact that WS-13 is located to the west of the Shale 2 contact but is actually screened into Sandstone 1. There is also water level decline noted to the west of the Shear Zone near WS-5, but that may result from the long term pumping of RD-1 and RD-2.

Due to their low hydraulic conductivity, the Shear Zone, Shale 2, Shale 3 and the Coca Fault appear to act as aquitards that restrict groundwater flow at SSFL.

2.9 Correlations in Water Levels Between Wells

The elevation of the water table at a site is a function of many factors including the formation hydraulic conductivity and storage coefficient, infiltration from precipitation, the influence of pumping wells or nearby streams, and geologic discontinuities in a groundwater system. Wells at a given site are expected to respond in a similar manner to similar hydrologic stimuli. Notable variations in the fluctuations of the water table may result from local differences in recharge, pumping, and the presence of hydrogeologic discontinuities within a groundwater system. Water level hydrographs for several wells at SSFL are potted in Figure 2.21.

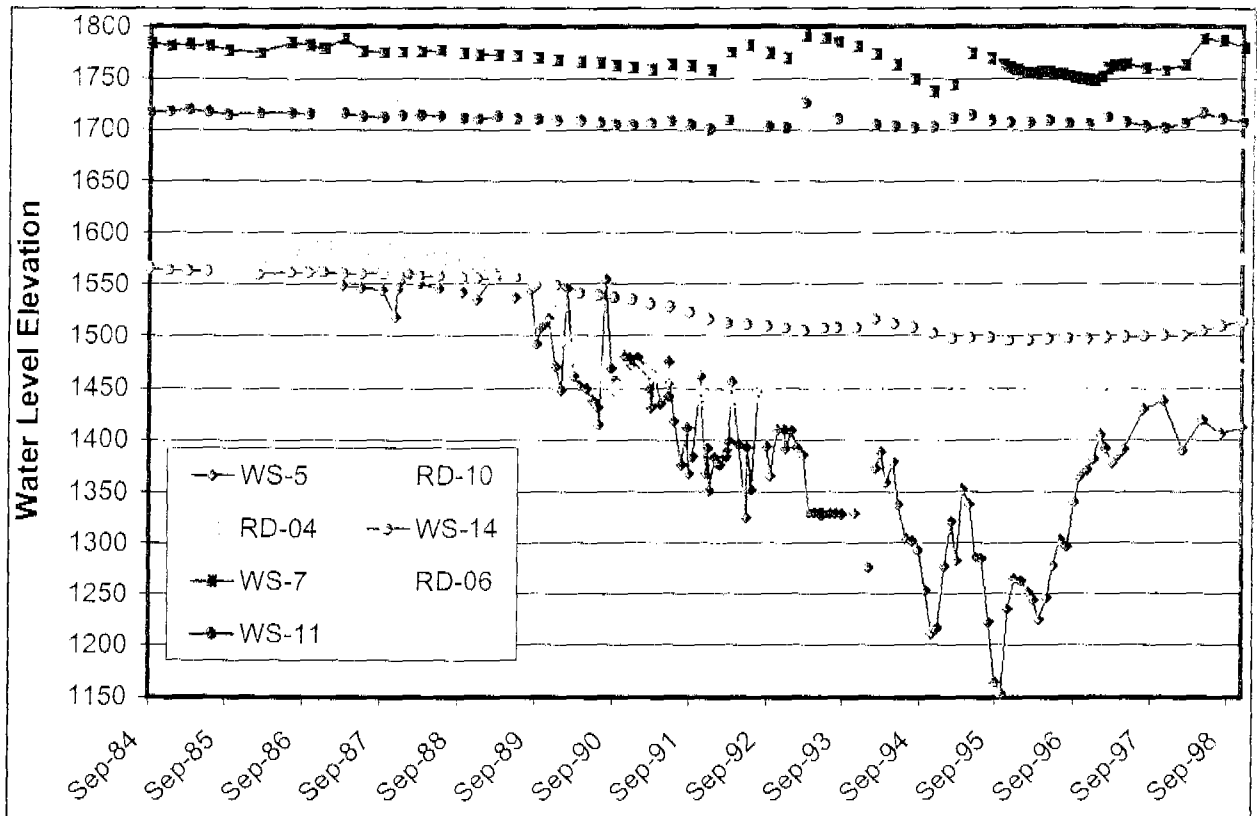


Figure 2.21 Water Level Fluctuations in Selected SSFL Wells

Some of the wells represented by the selected water level hydrographs shown in Figure 2.21 appear to show similar water level trends, while others appear quite distinct. In order to evaluate the similarities and differences in water level trends between wells on site, a water level correlation analysis was performed using neighboring well pairs. Correlograms were prepared for about 120 neighboring well pairs, and the correlation coefficient and variance explained (" R^2 ") were calculated. The value of R^2 was adjusted for sample size. Example correlograms are shown in Figure 2.22.

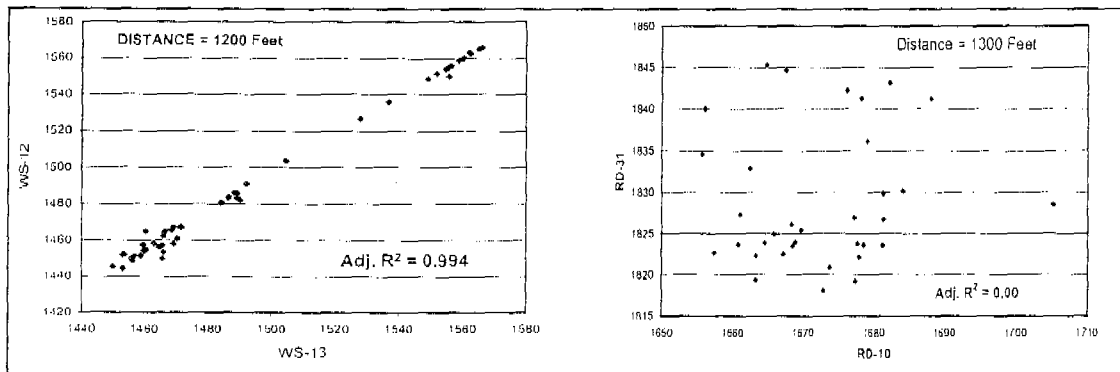


Figure 2.22 Water Level Correlograms of WS-12 vs WS-13 and RD-10 vs RD-31

The calculated R^2 values for each of the well pairs analyzed is included in Appendix F. The relative degree of correlation in water levels between analyzed well pairs is illustrated on Figure 2.23.

The water levels in the central portion of SSFL appear to be well correlated, but there is no apparent correlation across the Shear Zone or the Coca Fault. There appears to be some degree of correlation in water levels across Shale 2 in the northern portion of the site, but this is a result of the correlation in water

levels between WS-13 and water levels in wells completed in Sandstone 1. WS-13 is installed to the west of the Shale 2 outcrop area, but is screened in Sandstone 1, as illustrated in Figure 2.24

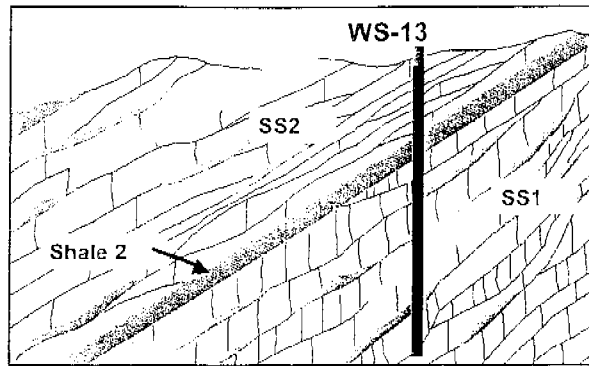


Figure 2.24 Screened Interval of WS-13

Water levels in the northeastern portion of the site appear well correlated, but there is no apparent correlation in water levels across the Happy Valley Shale/Happy Valley Fault to the south. The degree of correlation appears greatest along a trend parallel to strike, consistent with the results of the RD-73 pumping test described in Section 2.5.

Water levels in wells installed in Sandstone 2 do not appear to correlate over large distances, probably reflecting the low hydraulic conductivity of the unit.

2.10 Summary of SSFL Chatsworth Formation Hydrogeology

The hydrogeology of the Chatsworth Formation can be summarized as follows:

2.10.1 Stratigraphic Considerations

- The Chatsworth Formation beneath SSFL is composed of interbedded sandstone and mudstone (shale) units with distinct hydrogeologic properties.
- The matrix hydraulic conductivity of 18 sandstone samples ranged between 10^{-6} cm/sec and 10^{-4} cm/sec, while the matrix hydraulic conductivity of three mudstone samples was measured between 10^{-11} cm/sec and 10^{-9} cm/sec.
- The Upper Chatsworth Formation underlying is composed of two primary sandstone units, Sandstone 1 and Sandstone 2 that are hydrogeologically distinct.
- Sandstone 1 exhibits a geometric mean hydraulic conductivity of about 3.4×10^{-5} cm/sec, with values measured in wells ranging from 10^{-6} cm/sec to 10^{-4} cm/sec. There were 8 wells in Sandstone 1 that did not yield sufficient water to allow testing, and these wells are constructed in bedrock with a hydraulic conductivity that is probably less than 1×10^{-6} cm/sec. There were also two wells in Sandstone 1 that had relatively high water yields but with minimal drawdown during testing, such that the data could not be readily analyzed. The hydraulic conductivity of the bedrock screened by these wells is likely on the order of 10^{-3} cm/sec.
- Sandstone 2 is stratigraphically above Sandstone 1 and exhibits a geometric mean hydraulic conductivity of about 4.2×10^{-6} cm/sec. Measured values of hydraulic conductivity from pumping tests ranged between 10^{-7} cm/sec and 10^{-5} cm/sec. There were 9 wells in Sandstone 2 that did not yield sufficient water to allow testing, with a probable hydraulic conductivity of less than 1×10^{-6} cm/sec.

- Sandstone 1 and Sandstone 2 are separated by a continuous, through-going shale identified as Shale 2. Sandstone 2 is abounded above by Shale 3.
- Shale 2 and Shale 3 have very low hydraulic conductivities, as evidenced by significant water level differences across the units. They act as site-wide aquitards to groundwater flow.
- There are several smaller, discontinuous shale beds within Sandstone 1 that probably exert a localized influence on groundwater flow. The most notable of these units are Shale 1 that extends to the northeast from the Coca Fault to the vicinity of RD-47; the Happy Valley Shale that extends to the northeast from the Shear Zone to the vicinity of RD-10; and a unit that extends to the northeast from the Burro Flats Fault and truncates at the Skyline Fault in the vicinity of RD-40.
- The storage coefficient derived from multi-well pumping tests on Sandstone 1 and Sandstone 2 ranged between 0.00025 and 0.0053. This low coefficient of storage is consistent with large observed water level fluctuations observed in bedrock wells and the low rate of groundwater recharge.
- The Lower Chatsworth Formation lies stratigraphically beneath Sandstone 1 and outcrops in the eastern portion of the SSFL. Hydraulic conductivity data are available for 5 wells and ranged between 10^{-6} cm/sec and 10^{-3} cm/sec, with a geometric mean of 2.7×10^{-5} cm/sec. There were three wells in the Lower Chatsworth Formation that did not yield sufficient water to allow testing, with a probable hydraulic conductivity of less than 1×10^{-6} cm/sec.

2.10.2 Structural Considerations

- The Shear Zone that trends from southwest to northeast in the eastern portion of the site acts as an aquitard that limits the lateral migration of groundwater across the structure. The low hydraulic conductivity of the feature is demonstrated by the more than 200 feet of water level offset that has been induced across it, and by the lack of response to pumping across the structure.
- The Coca Fault that trends from east to west across the southern portion of the site also acts as an aquitard. Five wells installed on or immediately adjacent to the structure did not yield sufficient water to facilitate hydraulic conductivity testing, and the impacts of pumping do not appear to be transmitted across the fault.
- The available site data do not support the existence of through-going structural features that could act as preferred groundwater flow pathways. The areal distribution of hydraulic conductivity at SSFL indicates that the major structural features are more likely to be zones of lower hydraulic conductivity. The hydraulic conductivity observed at each location is a combination of the matrix hydraulic conductivity (which has been measured at up to 10^{-4} cm/sec) and the local degree of fracturing. Although elevated hydraulic conductivity has been observed at some locations, it does not appear to occur in laterally continuous zones.

2.10.3 Inter-connection of the Fracture Network

- Multi-well pumping tests conducted at SSFL indicate the fracture network between the identified aquitards (Shear Zone, Coca Fault, Shale 2 and Shale 3) is well connected. Responses to pumping from wells in Sandstone 1 have been observed at distances of over 2,000 feet, while the areal response to pumping in Sandstone 2 has been somewhat less. The difference in response probably reflects the lower hydraulic conductivity of Sandstone 2.

3.0 DELINATION OF GROUNDWATER UNITS AT SSFL

Several stratigraphic and structural geologic features at SSFL behave as aquitards, namely Shale 2, Shale 3, the Shear Zone, and the Coca Fault, as discussed in Section 2. The Happy Valley Fault and the Happy Valley Shale may act together to isolate the areas to the north and south. When taken together, these features act to compartmentalize groundwater flow at SSFL and are depicted on Figure 3.1. Pumping tests and the long-term water level response to groundwater withdrawal indicate the fracture network between these major features is inter-connected. Accordingly, the groundwater system in the Chatsworth Formation beneath SSFL can be divided into discrete units bounded by the stratigraphic and structural geologic features depicted on Figure 3.1.

3.1 Groundwater Unit 1A

Groundwater Unit 1A comprises the northeastern portion of SSFL as shown on Figure 3.1. The unit is bounded by Shear Zone on west, the Happy Valley Fault/Happy Valley Shale on the south, and may be bounded at depth and on the east by the northeastward extension of the Happy Valley Shale. The elevation of the water level measured in monitoring wells in Unit 1A is depicted on Figure 3.2.

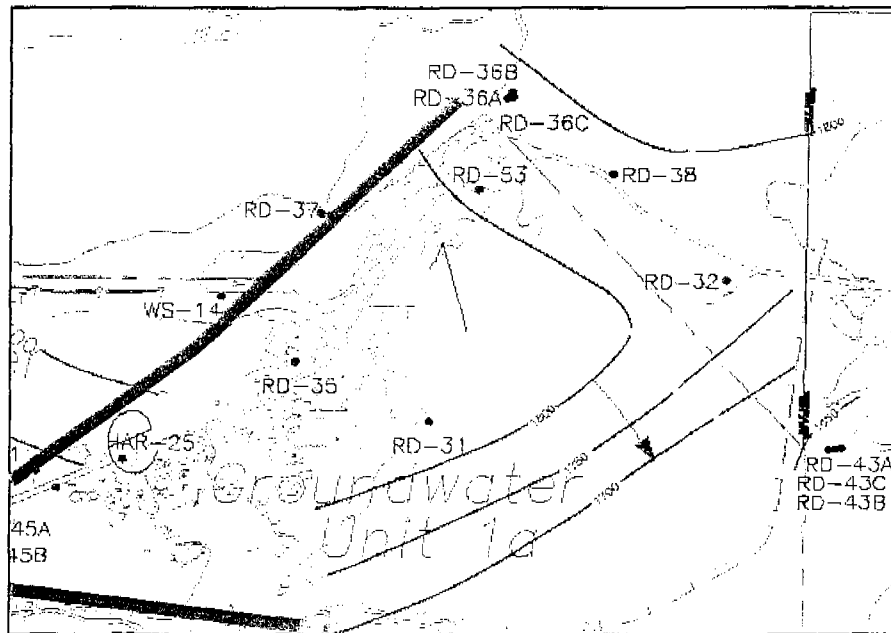


Figure 3.2 Water Level Elevations in Wells in Groundwater Unit 1A

The fracture network within Groundwater Unit 1A is inter-connected, based on the response to pumping shown in Figure 2.9 and the water level correlation shown in Figure 2.21. The response to pumping from RD-73 indicated an increase in hydraulic conductivity parallel to the strike of the Chatsworth Formation and the Shear Zone, with lower hydraulic conductivity perpendicular to strike.

The cone of depression illustrated in Figure 2.21 was generated by pumping less than three gpm over a 90-day interval. The extensive areal extent of the cone of depression results from the very low storage coefficient of the bedrock, which is on the order of 0.0001.

3.2 Groundwater Unit 1B

Groundwater Unit 1B lies to the south of Unit 1A as shown on Figure 3.1. The unit is bounded by Shear Zone on west, the Happy Valley Fault on the north, and may be bounded at depth and on the east by the major shales of the Lower Chatsworth Formation. The hydrogeologic significance of the Happy Valley Shale that trends through Unit 1B is not known, and well responses during the hydraulic communication study in 1996 were not conclusive. The locations of wells in Unit 1B are shown with the observed water levels in the wells on Figure 3.3.

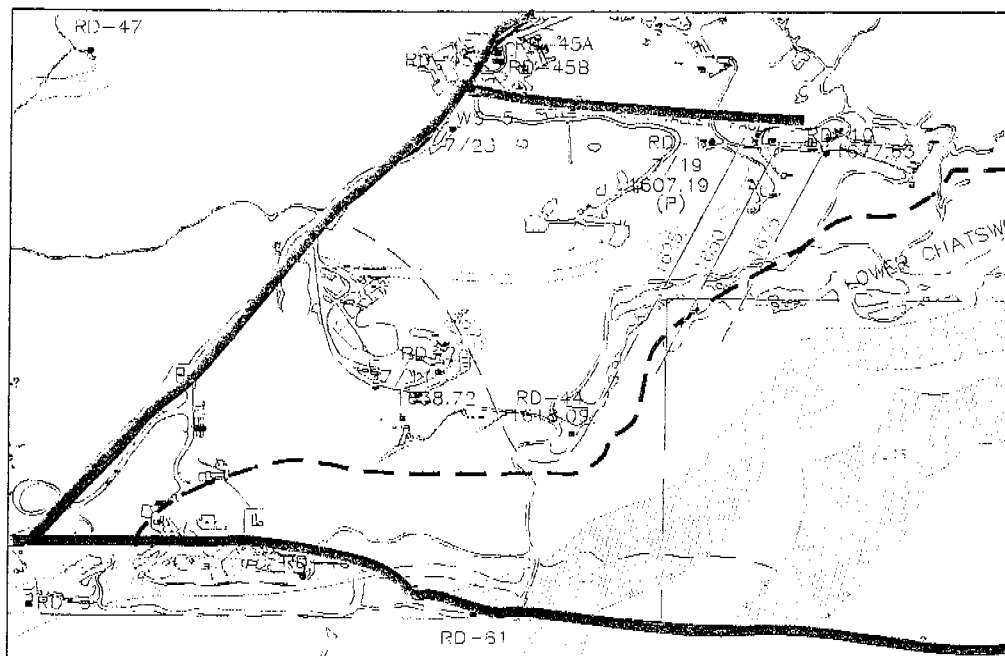


Figure 3.3 Water Levels in Wells in Groundwater Unit 1B

During the hydraulic communication study described in Section 2. Well RD-10 was the only well that appeared to respond to the restart of RD-1. Well RD-1 did not respond to the restart of RD-2 or WS-5, and RD-2 did not respond to either RD-1 or WS-5. It is possible that the Happy Valley Shale isolates RD-2 from RD-1.

3.3 Groundwater Unit 2

Groundwater Unit 2 comprises the area bounded by the Shear Zone on the east, Shale 2 on the west, and the Coca Fault on the south, as shown on Figure 3.1. Unit 2 is also likely bounded at depth by shales of Lower Chatsworth Formation. Sandstone 1 dips to the northwest beneath Shale 2, and Unit 2 has lateral continuity in that direction, as indicated by the response in water levels in WS-13 to pumping in Sandstone 1.

There are no wells installed south of the Shale 1 contact in the central portion of Unit 2, and the degree of hydraulic continuity in Unit 2 below Shale 1 is not known. The measured water levels in Unit 2 wells are shown in Figure 3.4. The lowest water levels are observed in the central portion of Unit 2 due to groundwater pumping.

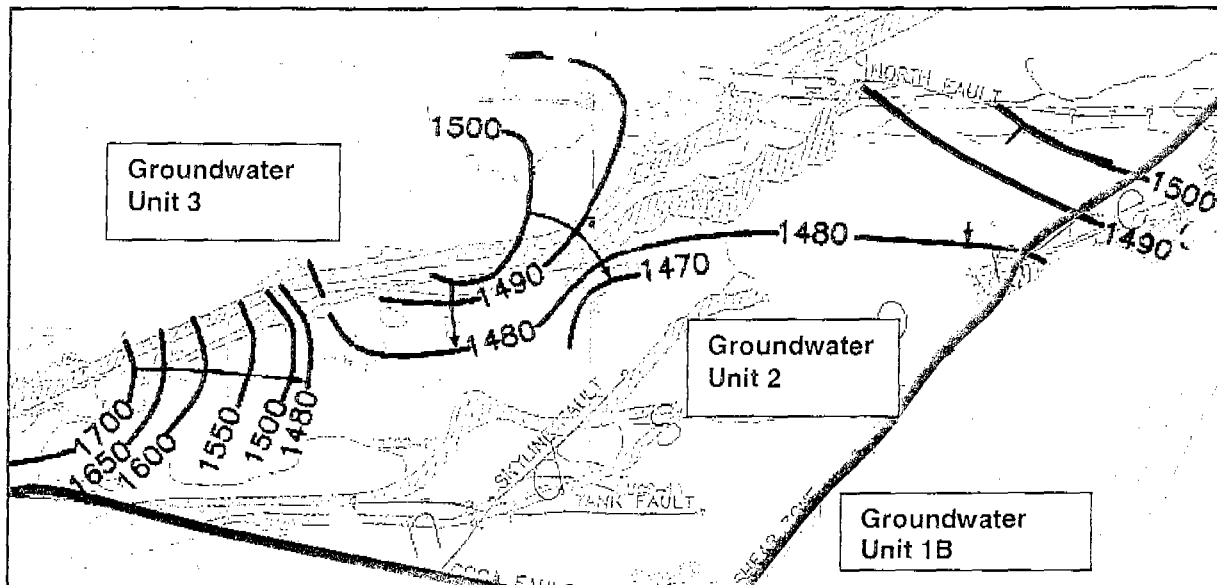


Figure 3.4 Water Level Elevations in Wells in Groundwater Unit 2

The degree of inter-connection of the fracture network in Unit 2 is illustrated by the degree of water level correlation within the Unit as shown in Figure 2.22. The degree of inter-connection in Unit 2 is also illustrated by the water level response to long-term pumping that is shown in Figure 3.5.

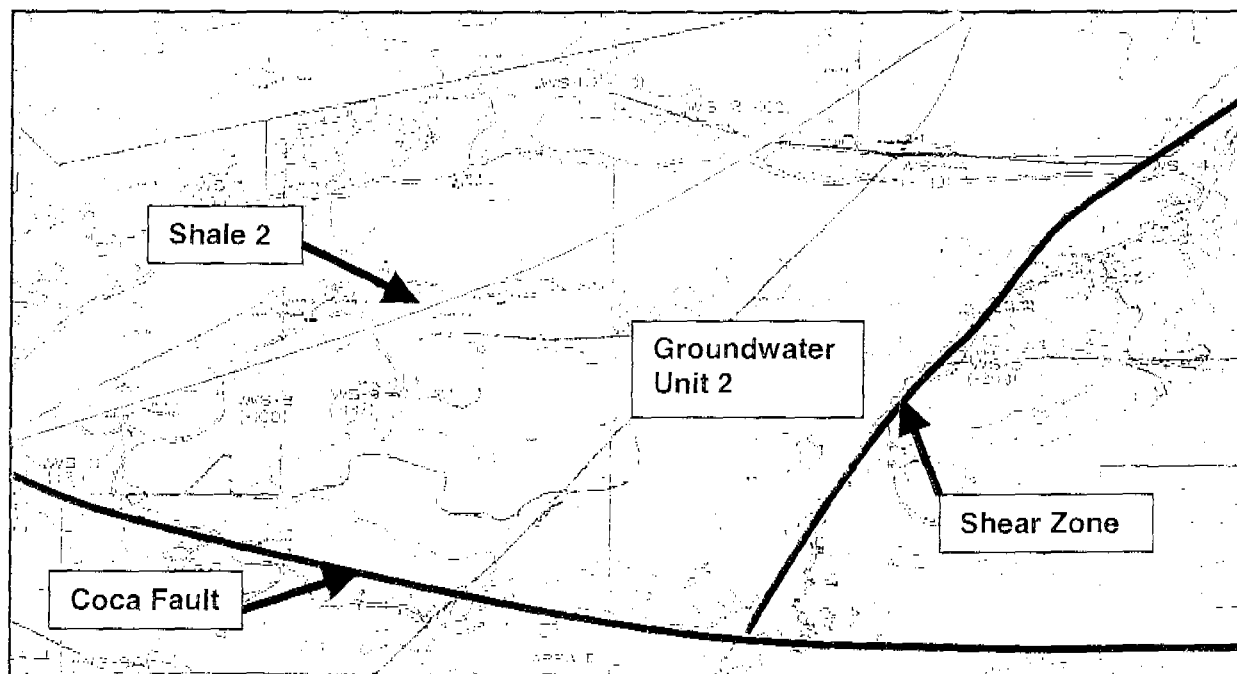


Figure 3.5 Water Level Decline at SSFL From 1954-1997 (After GWRC, 1998)

The apparent water level decline that extends to the north of the Shale 2 contact reflects the water levels measured in WS-12 and WS-13 that are screened through Sandstone 2 into Sandstone 1. The water level decline observed to the east of the Shear Zone results from the operation of RD-1 and RD-2 as pumping wells since the late 1980s. The boundary conditions at the Contact with Shale 2 are illustrated in Figure 3.6.

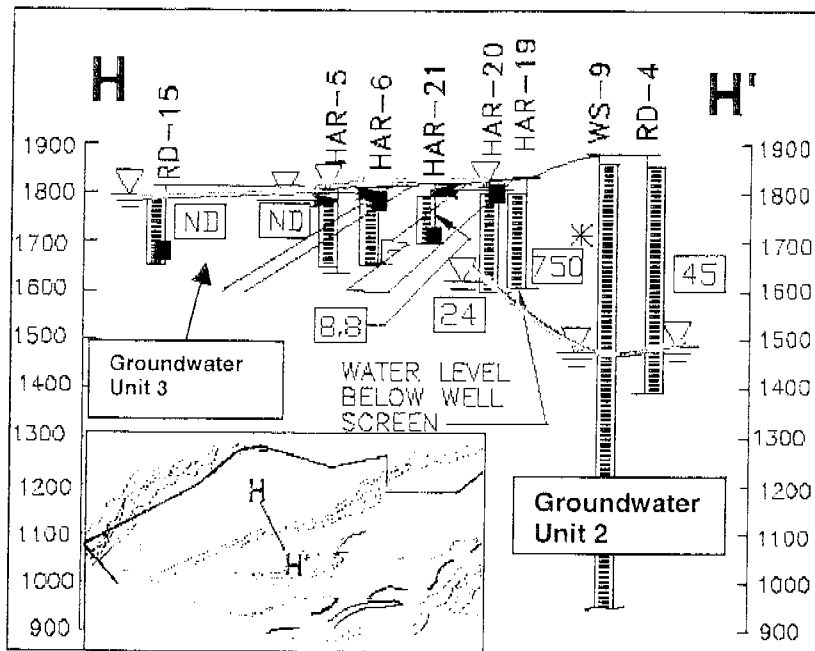


Figure 3.6 Water Level Conditions at Groundwater Unit 2 Contact with Shale 2.

The boundary conditions at the contact with the Shear Zone in the northeastern portion of Unit 2 are shown in Figure 3.7.

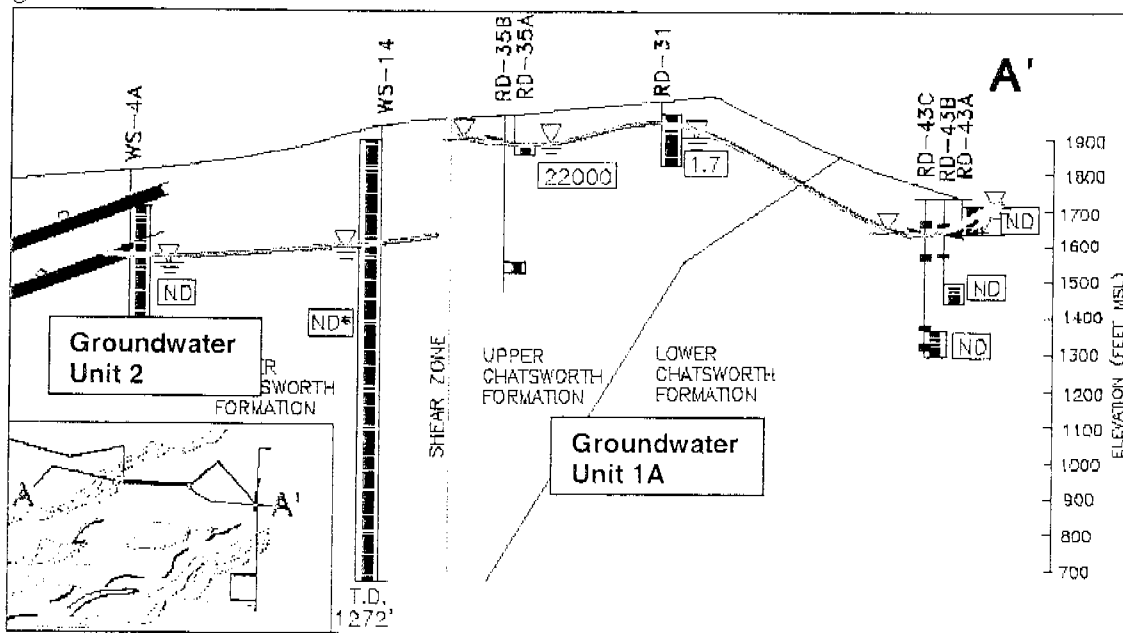


Figure 3.7 Water Level Conditions at Groundwater Unit 2 Contact with the Shear Zone

3.4 Groundwater Unit 3

Groundwater Unit 3 consists of Sandstone 2 and is bounded by Shale 2 on the east and Shale 3 on the west. Sandstone 2 dips to the northwest beneath Shale 3, and Unit 3 has lateral continuity in that direction, as indicated by the artesian water levels observed in the RD-59 well cluster. The water levels observed in Groundwater Unit 3 are shown in Figure 3.8.

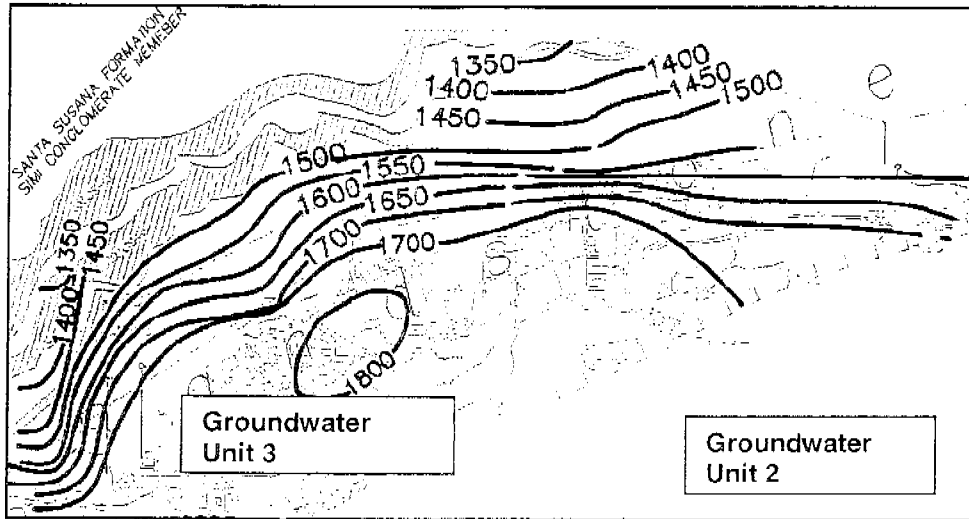


Figure 3.8 Water Levels Measured in Wells in Groundwater Unit 3.

The gradient of the water level elevation surface steepens to the northwest. This likely results from the drop-off in surface topography and a reduction in hydraulic conductivity perpendicular to the strike of the Chatsworth Formation. The water level elevation contours are more closely spaced in Groundwater Unit 3 as a result of the order of magnitude lower hydraulic conductivity of Sandstone 2 compared to Sandstone 1. The boundary conditions created by the Shales 2 and 3 contacts are shown in Figure 3.9.

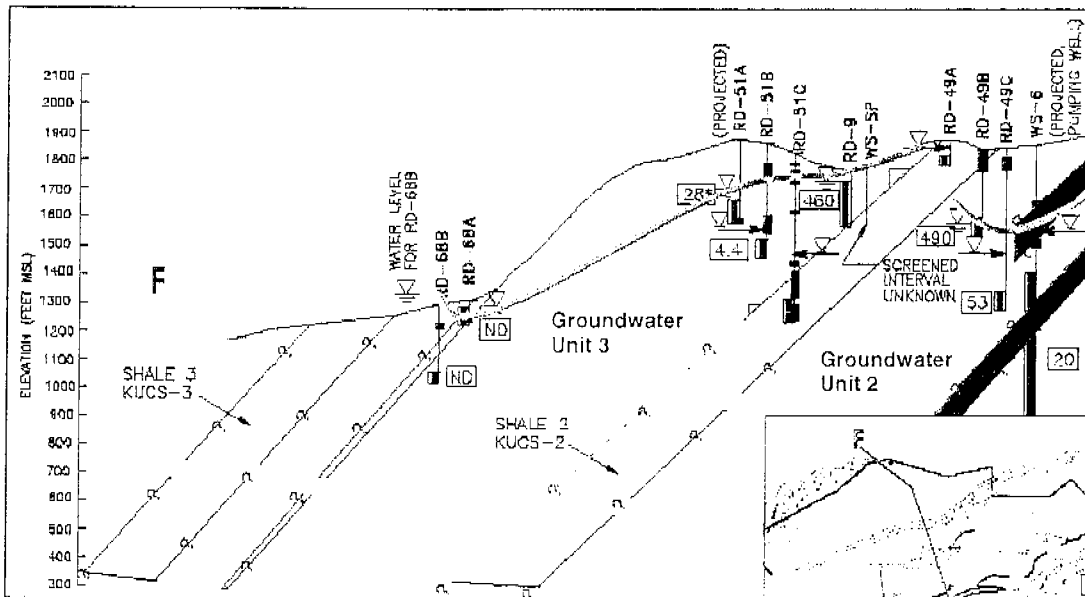


Figure 3.9 Water Level Conditions at Shale 2 and Shale 3 Boundaries of Groundwater Unit 3

3.5 Groundwater Unit 4

Groundwater Unit 4 is bounded by the Coca Fault on the north, and by the Burro Flats Fault on the south. Minimal well data is available south of the Burro Flats Fault, and the actual hydraulic character of the fault is not known. The Burro Flats Fault was selected as the southern boundary of Unit based on the observed hydraulic impact of the other major faults at SSFL. A map showing water levels measured in wells completed in Groundwater Unit 4 are shown in Figure 3.10.

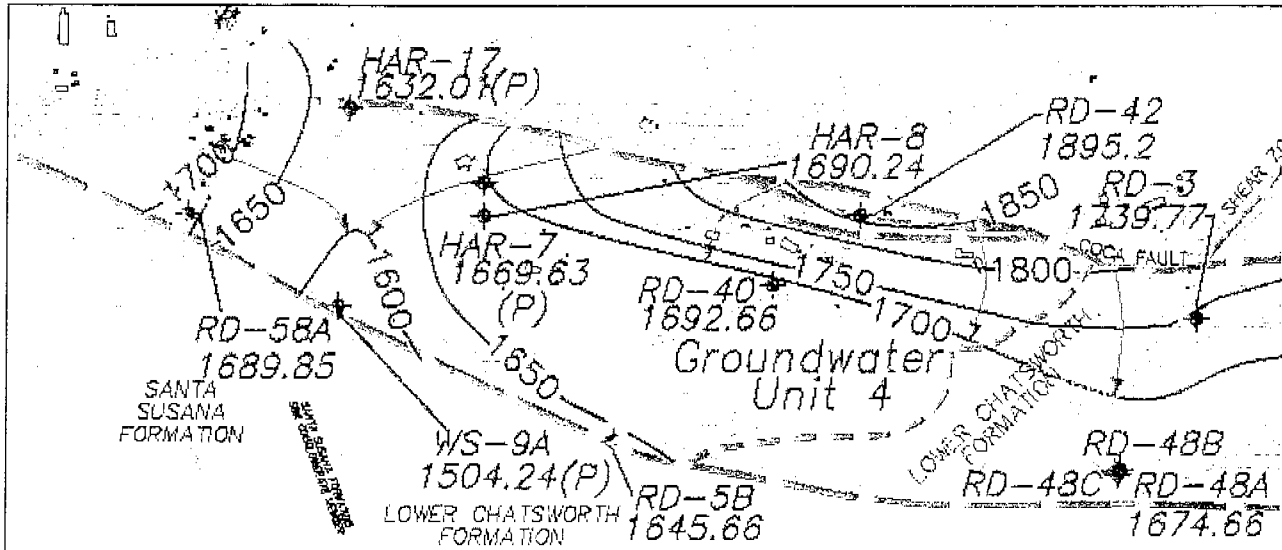


Figure 3.10 Water Levels Measured in Wells in Groundwater Unit 4.

Five monitoring wells were installed on or immediately adjacent to the Coca Fault and did not yield sufficient water to allow a pumping test to be conducted. In addition, WS-10 was drilled on the Fault and was considered a "dry hole" and was never tested. Water table conditions along the Coca Fault are depicted in Figure 3.11.

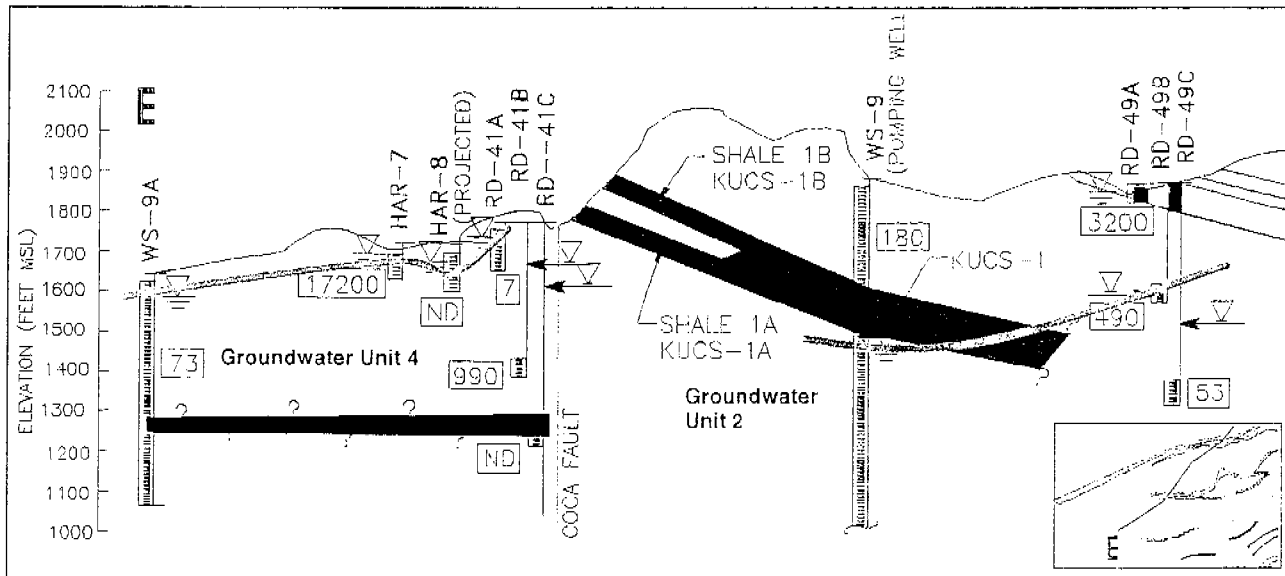


Figure 3.11 Water Level Conditions Along the Coca Fault

The wells in Unit 4 east of the Skyline Fault are all installed in or stratigraphically below the shales of the Lower Chatsworth Formation, as shown on Figure 3.1. It is possible that groundwater flow within Unit 4 is further segmented by a combination of these shales, the Skyline fault, and the shale that runs northeasterly from the Burro Flats fault to the vicinity of RD-40 and the Skyline Fault.

3.6 SSFL Site Water Levels

An integrated map showing water level elevations in wells on the SSFL was prepared based on the groundwater unit boundaries described above and is included as Figure 3.12. The discontinuities in water level elevation contours reflect the presence of aquitards within the groundwater system at SSFL.

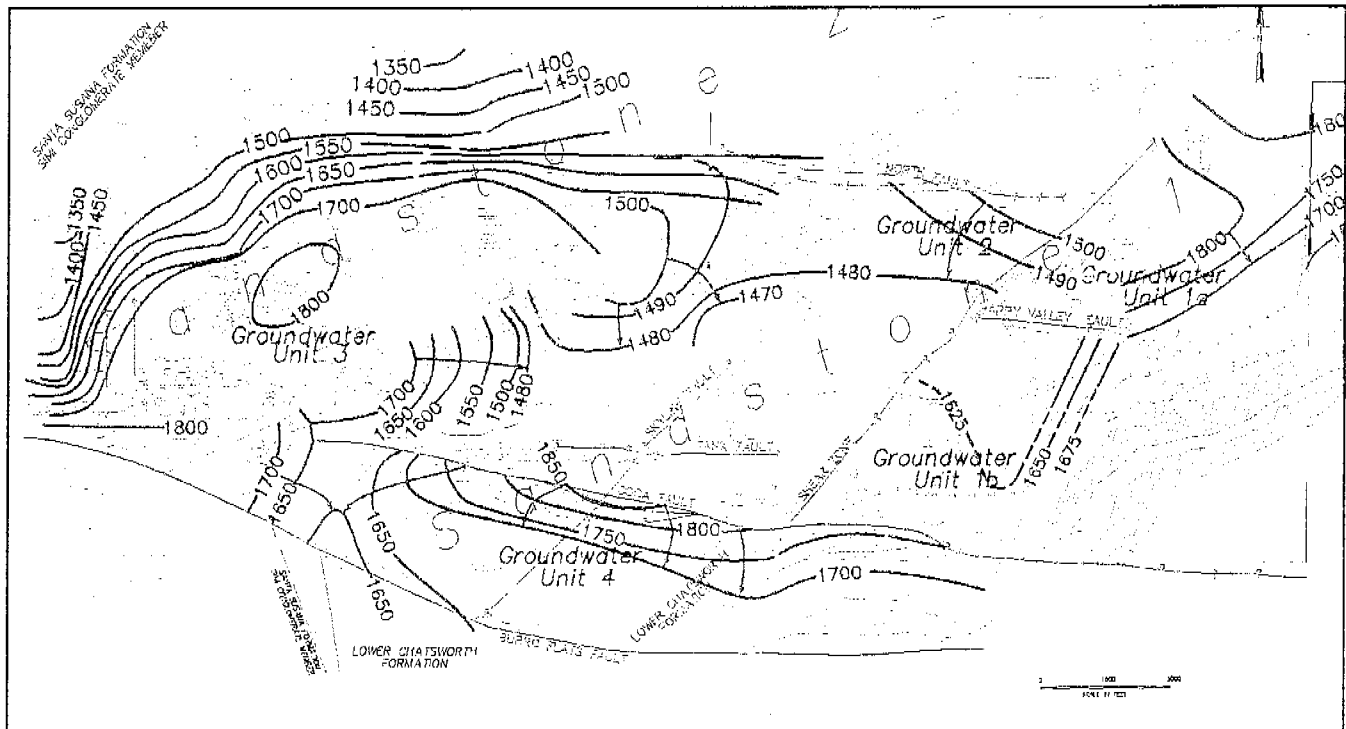


Figure 3.12 Water Levels Measured in SSFL Wells

4.0 GROUNDWATER FLOW CONDITIONS AT SSFL

Groundwater flow in the Chatsworth Formation at SSFL occurs within a fractured bedrock system that exhibits that contains a high degree of variability. Matrix hydraulic conductivity was measured in 21 samples of rock core and ranged between 10^{11} cm/sec and 10^{-4} cm/sec. The hydraulic conductivity measured from pumping tests on monitoring and water supply wells in the Chatsworth Formation ranged between 10^{-7} cm/sec and 10^{-3} cm/sec. Fracture spacing also varies across the site, within individual beds, and between Sandstone 1 and Sandstone 2. Superimposed on this variable groundwater system is a combination of stratigraphic and structural features that act as aquitards to disrupt groundwater flow. The presence of these aquitards was the basis for dividing SSFL into five discrete groundwater units, as discussed in Section 3.

4.1 Conceptual Simulation of Groundwater Flow at SSFL

The lateral and vertical variation in hydraulic conductivity of several orders of magnitude results in a complex flow system. To illustrate this concept, the University of Waterloo conducted a two-dimensional numerical simulation of groundwater flow paths. The a simple conceptual model of the SSFL site without considering the presence of fractured rock or aquitards is shown in Figure 4.1, and a model that includes these features in includes as Figure 4.2.

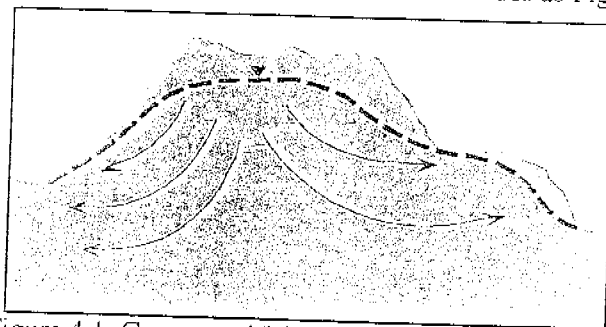


Figure 4.1 Conceptual View of SSFL Groundwater Flow without Fractures or Aquitards

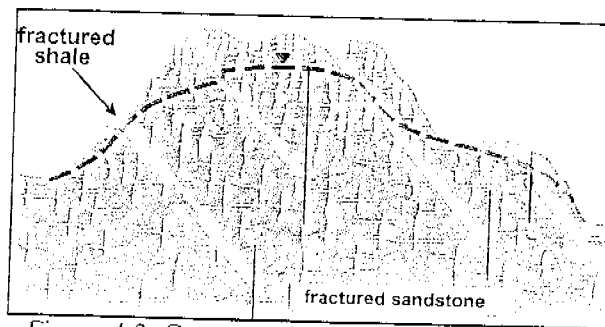


Figure 4.2 Conceptual View of SSFL with Fractures and Aquitards

To simulate groundwater flow conditions at SSFL, a model domain was selected to represent the groundwater mound depicted in Figures 4.1 and 4.2, and the domain is illustrated in Figure 4.3.

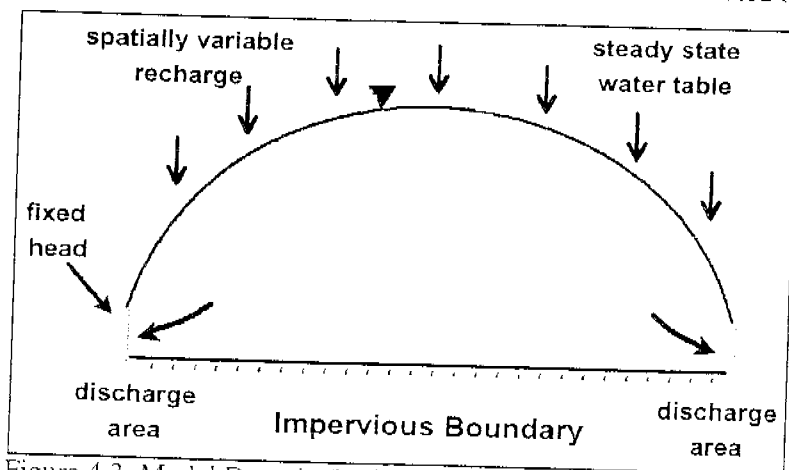


Figure 4.3 Model Domain for Simulation of Groundwater Flow

Model runs were conducted to simulate a homogeneous groundwater system similar to that depicted in Figure 4.1 and the results are shown in Figure 4.4.

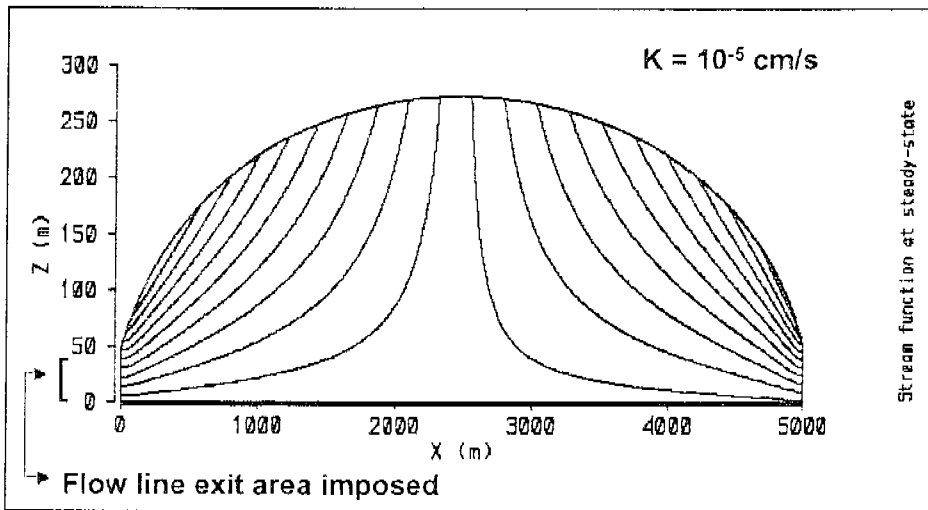


Figure 4.4 Simulated Flow Lines in a Homogeneous Groundwater System

For the homogeneous case, the groundwater flow lines follow a uniform pathway, and the elevation of the hydraulic head at any location is easily estimated. The high degree of lateral and vertical variability in hydraulic conductivity at SSFL, coupled with the presence of significant aquitards, make the estimation of groundwater flow lines far more complicated. To illustrate this point, a simulation was conducted that included the presence of some sloping, lower and higher hydraulic conductivity beds in the model domain, as depicted in Figure 4.5.

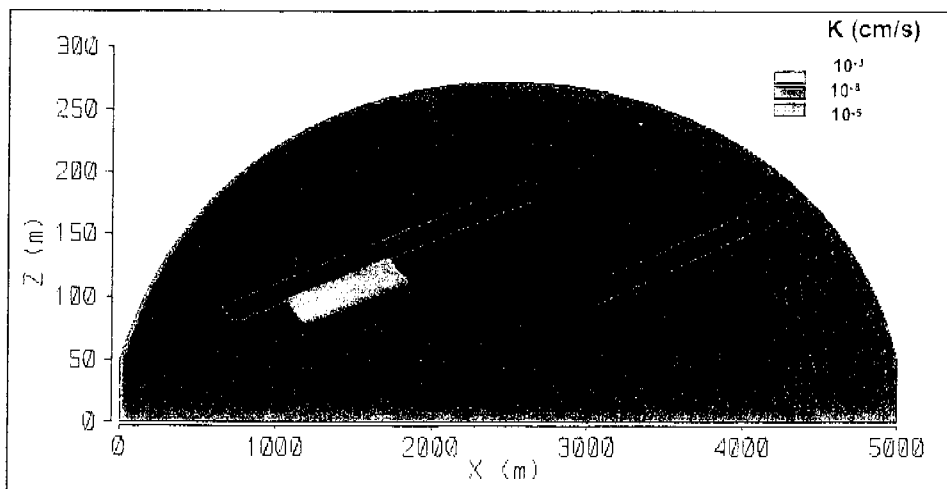


Figure 4.5 Placement of Lower and Higher Hydraulic Conductivity Beds in the Model Domain

The low hydraulic conductivity beds at SSFL consist of massive through-going shales as discussed in Section 2. The beds depicted in Figure 4.5 are discontinuous, and are surrounded by higher hydraulic conductivity rock in order to make the simulation simpler to execute. The simulation also did not include any through-going vertical aquitards, for the same reason. The groundwater flow lines resulting from the conceptual model domain depicted in Figure 4.5 are shown on Figure 4.6.

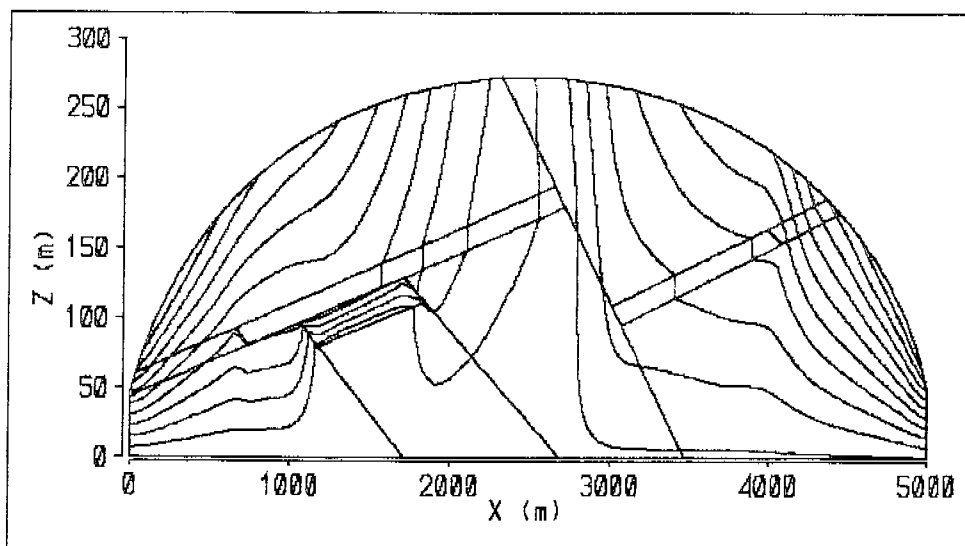


Figure 4.6 Groundwater Flow Lines in Model Domain with Sloping Beds of Lower and Higher Hydraulic Conductivity

In contrast with the simplistic, homogeneous model of groundwater flow, the simulation that includes variable hydraulic conductivity beds is more complex. The distribution of hydraulic head and the groundwater flow lines that result from the presence of variable hydraulic conductivity strata is illustrated in Figure 4.7 and is an enlarged view of a portion of the model simulation.

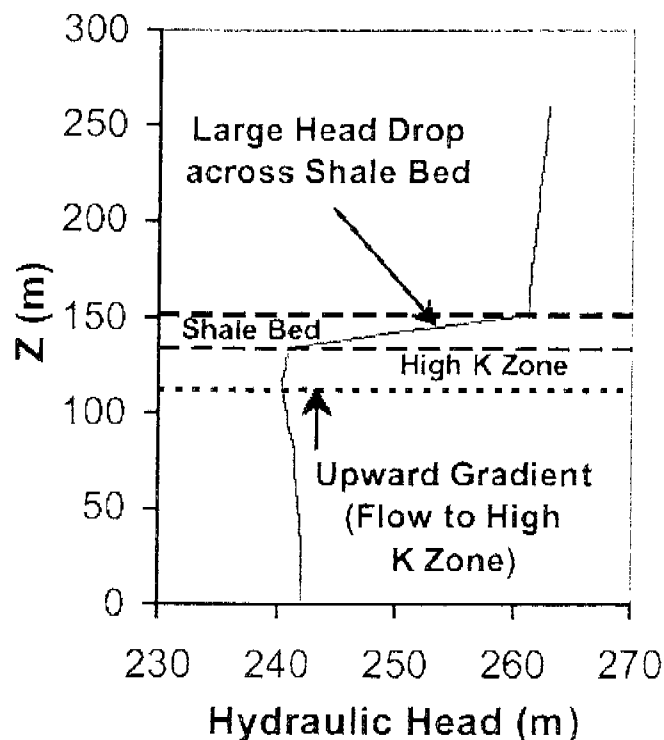


Figure 4.7 Hydraulic Head Profile at X = 1,800 Meters

The model simulation indicates that large variations in hydraulic head can result from the stratigraphic variation in hydraulic conductivity observed at SSFL. This is important when considering the hydraulic head data available for the monitoring wells at SSFL, the majority of which have long open intervals that cross numerous strata.

The actual stratigraphy at SSFL contains inter-layered and discontinuous beds that range in hydraulic conductivity over five or six orders of magnitude. Superimposed on this stratigraphic variability in hydraulic conductivity is a variably spaced fracture network and a system of aquitards comprised of massive, through-going shales and low hydraulic conductivity structural features. Accordingly, the groundwater flow system that result from the site-specific combination of these factors is far more complex than depicted in Figures 4.6 and 4.7.

4.2 Factors Influencing the Understanding of Groundwater Flow at SSFL

The ability to adequately describe the groundwater flow system at SSFL requires an understanding of the variability of site hydraulic conductivity, sufficient monitoring well coverage and hydraulic head resolution. The hydraulic conductivity of the Chatsworth Formation at SSFL has been defined by more than 100 pumping tests, 21 analyses of rock core and 11 packer tests. As a result, the overall variability in hydraulic conductivity at SSFL has been well defined, as shown in Table 4.1.

Sample Group	Number of Tests	Range of K (cm/sec)	Geometric Mean K (cm/sec)
Matrix – Sandstone	18	10^{-6} to 10^{-4}	7.4×10^{-6}
Matrix – Shale	3	10^{-11} to 10^{-9}	5.1×10^{-10}
Sandstone 1 Wells	41	10^{-6} to 10^{-4}	3.9×10^{-5}
Sandstone 2 Wells	38	10^{-7} to 10^{-5}	5.1×10^{-6}
Lower Chatsworth Wells	8	10^{-6} to 10^{-3}	6.7×10^{-5}
Wells on Faults – SS1	14	10^{-7} to 10^{-4}	1.4×10^{-5}
Wells off Faults – SS1	22	10^{-6} to 10^{-4}	4.4×10^{-5}
All Wells	101	10^{-7} to 10^{-3}	1.3×10^{-5}
Packer Tests	11	10^{-7} to 10^{-4}	4.5×10^{-5}

Table 4.1 Summary of SSFL Hydraulic Conductivity Data

More than 100 monitoring wells have been installed in the Chatsworth Formation at SSFL in an effort to delineate contaminant concentrations and general groundwater conditions. The majority of these wells are single well completions with large open intervals that provide a reliable estimate of vertically averaged hydraulic conductivity. As a result, a reasonable estimate of the rate of groundwater discharge through the upper portion of the Chatsworth Formation can be developed from the hydraulic conductivity data derived from the pumping tests on the SSFL monitoring well network.

Depth-specific hydraulic head data and information regarding the vertical variability of hydraulic conductivity at SSFL is available only at well cluster locations. An illustration of the cluster well coverage at SSFL is shown in Figure 4.8. Actual well locations are shown on Figure 1.1.

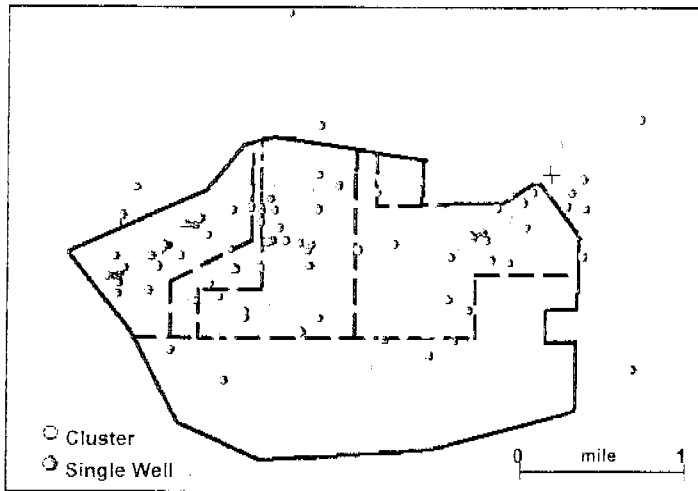


Figure 4.8 Cluster Well Coverage at SSFL

The distribution of monitoring well clusters at SSFL is not currently adequate to define groundwater flow lines in each of the groundwater units identified at SSFL, particularly when the complexity of groundwater flow pathways illustrated by the simulation depicted in Figure 4.6 is considered. There is a relatively large number of cluster wells in Groundwater Unit 1A, and together with the depth-specific hydraulic head data developed during multi-level testing at RD-35B, provides a reasonable understanding of groundwater flow conditions.

4.3 Groundwater Flow within Groundwater Units at SSFL

4.3.1 Groundwater Flow in Groundwater Unit 1 A

Groundwater elevations in Unit 1A are depicted in Figure 4.9. While the groundwater elevation

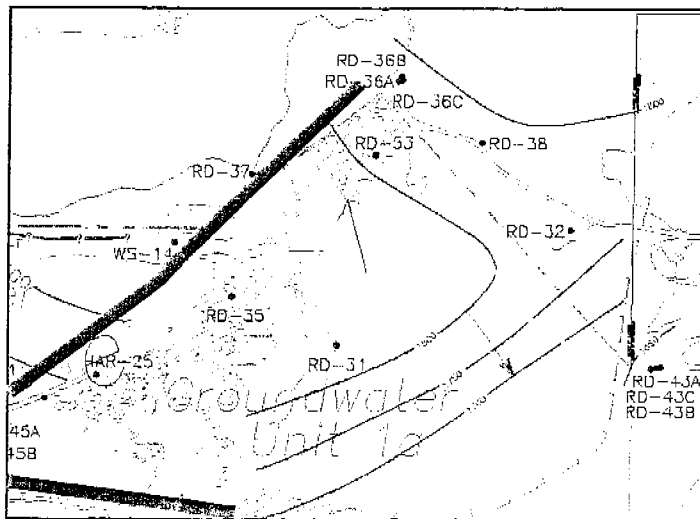


Figure 4.9 Groundwater Elevations in Groundwater Unit 1A

data from wells suggest groundwater flow to the northeast and southeast, the distribution of drawdown observed during the RD-73 pumping test indicates the primary direction of groundwater flow is to the northeast. This direction of flow is supported by the distribution of TCE in Chatsworth Formation groundwater, which also trends to the northeast.

The geometric mean hydraulic conductivity in from the 90-day pumping test on RD-73 was 6.7×10^{-5} cm/sec, consistent with the values derived from the single well pumping tests conducted in the unit. The estimated coefficient of storage from RD-73 pumping test was on the order of 0.0001.

The rate of groundwater discharge to the northeast in Groundwater Unit 1A can be estimated from Darcy's law:

$$Q = KIA$$

where Q is the rate of groundwater discharge, K is the hydraulic conductivity, I is the groundwater gradient and A is the cross sectional area through which flow is occurring. From the RD-73 pumping test, the geometric mean hydraulic conductivity was 6.7×10^{-5} cm/sec, and 3×10^{-4} cm/sec was the maximum observed value. The groundwater gradient is about 0.001 from RD-53 to RD-38A, and about 0.0018 from HAR-25 to RD-35A. The cross sectional area is estimated at about 1,000 ft wide by 300 ft deep based on TCE distribution in groundwater. Using these values, the estimated rate of groundwater discharge to the northeast ranges from about 0.3 gpm to about 2.2 gpm. This rate of discharge is consistent with the groundwater yield of 2.7 gpm derived from RD-73 during the 90-day pumping test. The drawdown resulting from that test is shown in Figure 4.10.

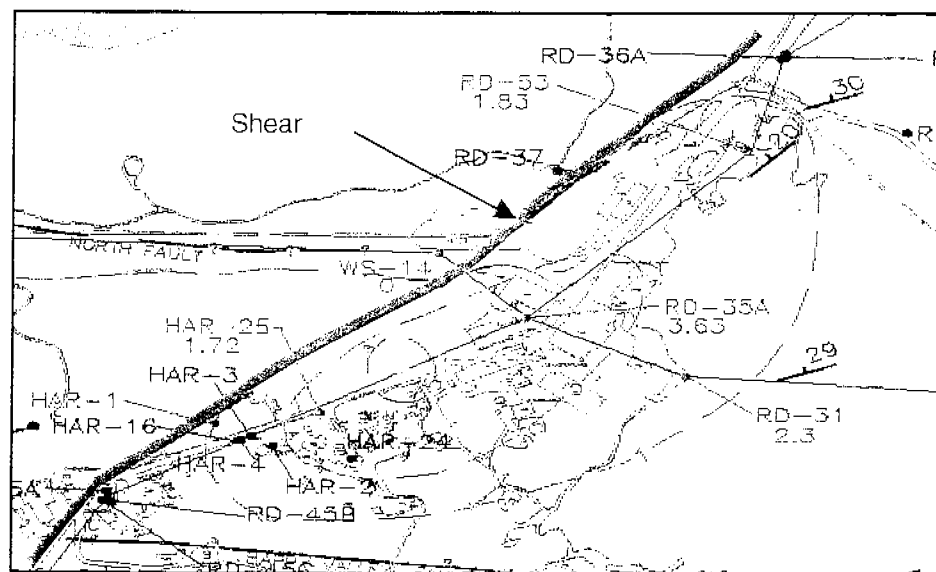


Figure 4.10 Drawdown Resulting from RD-73 Pumping Test at 2.7 GPM

The vertical distribution of hydraulic head and hydraulic conductivity in Unit 1A has been investigated by the installation of five well clusters (RD-35A and B, RD-36A, B, C and D, RD-38A and B, RD-39A and B, and RD-43A, B and C) and a multi-port sampling system in the RD-35B well bore prior to the construction of the current well. The hydraulic head distribution in RD-35B is included on Figure 2.14.

4.3.2 Groundwater Flow in Groundwater Unit 1B

Groundwater elevations in Unit 1B are shown on Figure 4.11. There are a limited number of wells in Unit 1B, and the degree of interconnection between all the wells in the unit has not been established, as discussed in Section 2.

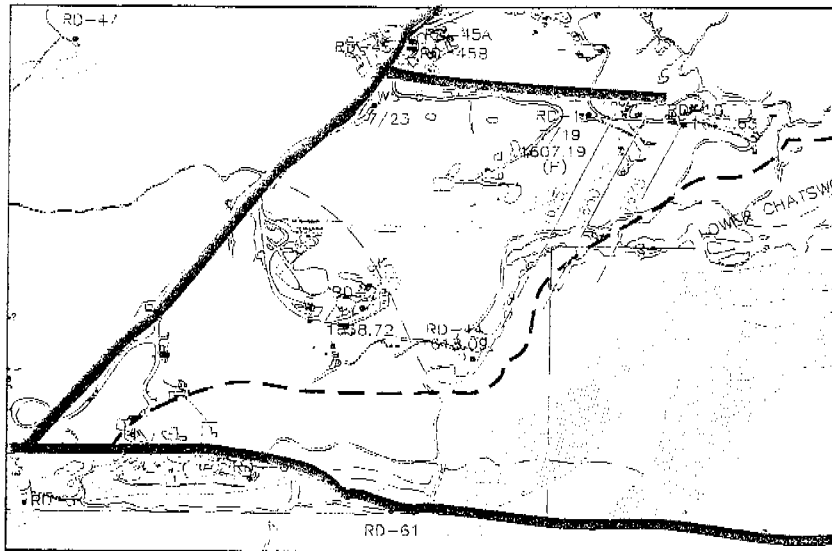


Figure 4.11 Groundwater Elevations in Groundwater Unit 1B

Groundwater flow in Unit 1B appears to be captured by pumping wells RD-1 and RD-2, with likely influence from WS-5, although no obvious connection between WS-5 and the other wells in Unit 1B is evident in available data. An estimate of groundwater discharge was not calculated for Unit 1B because of the limited data set.

4.3.3 Groundwater Flow in Groundwater Unit 2

Groundwater elevations in Unit 2 are shown on Figure 4.12.

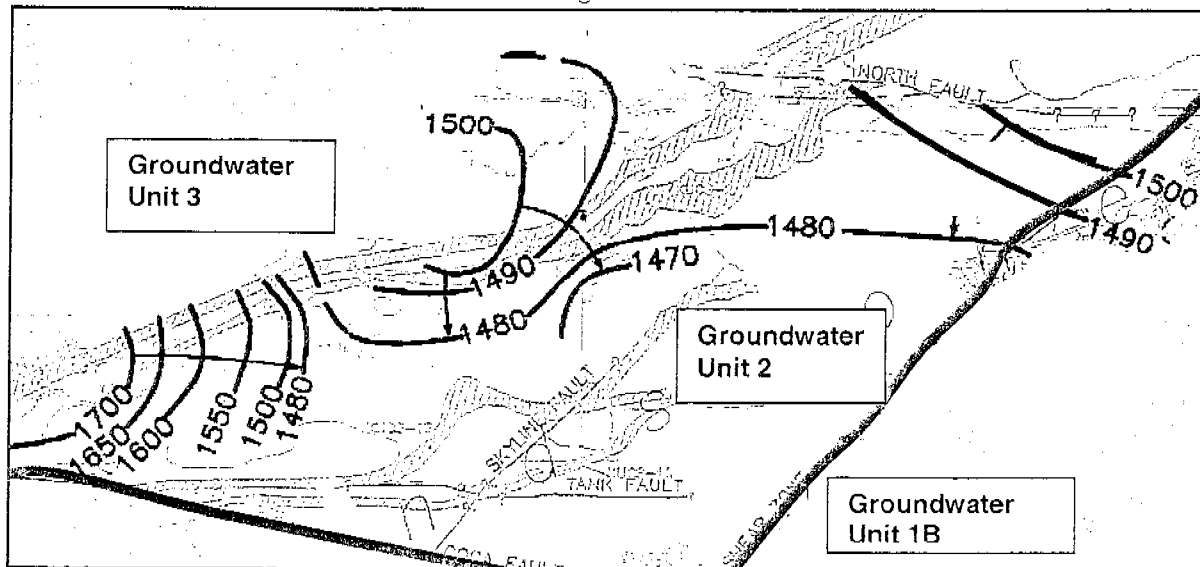


Figure 4.12 Water Level Elevations in Groundwater Unit 2

Water level data for Groundwater Unit 2 are limited to wells with long open intervals concentrated in the northern half of the unit. As a result, estimates of groundwater were not attempted for Unit 2. Groundwater flow is primarily to the center of the unit coincident with the location of the major pumping wells.

4.3.4 Groundwater Flow in Groundwater Unit 3

Groundwater elevations in Unit 2 are shown on Figure 4.13.

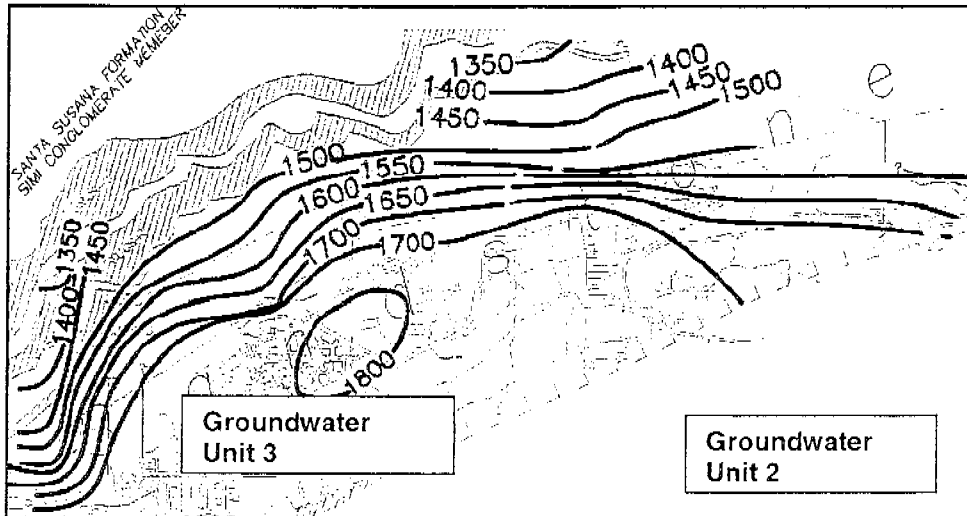


Figure 4.13 Water Level Elevations in Groundwater Unit 3

Hydraulic head data for Unit 3 is limited primarily to data from single well completions. As such, it is not possible to estimate groundwater flow conditions. There is sufficient data with which to estimate groundwater discharge from the unit to the north and west. The rate of groundwater discharge to the north and west along the approximate 5,000 ft perimeter is estimated at about 12 gpm based on a geometric mean hydraulic conductivity of 6.8×10^{-6} cm/sec, a groundwater gradient of about 0.15, and a cross sectional area of 5,000 ft wide by 200 ft deep.

4.3.5 Groundwater Flow in Groundwater Unit 4

Groundwater elevations in Unit 4 are shown on Figure 4.14.

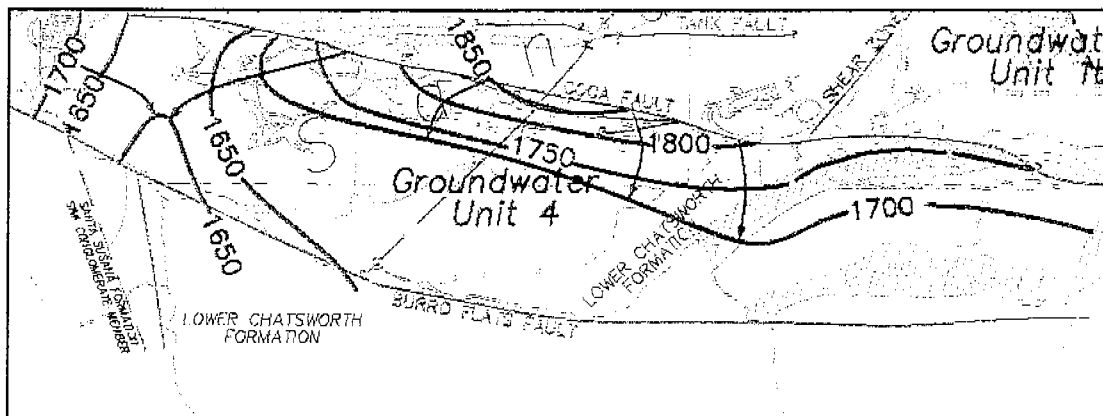


Figure 4.14 Water Level Elevations Measured in Groundwater Unit 4

Sufficient depth discrete head data does not exist in Unit 4 to allow estimation of groundwater flow directions. Groundwater in the western portion of the unit appears to be captured by WS-9A and HAR-7. Groundwater in the eastern half of the unit appears to migrate to the south, but the rate of discharge was not estimated.



MONTGOMERY WATSON

APPENDIX A
HISTORICAL BEDROCK GROUNDWATER PUMPING

APPENDIX A
CHATSWORTH FORMATION GROUNDWATER PRODUCTION

Santa Susana Field Laboratory

MONTH/YEAR	WELL PRODUCTION (gallons x 1,000)										
	RD-1	RD-2	RD-4	RD-9	RD-63	WS-5	WS-6	WS-9	WS-9A	WS-12	WS-13
1961						20,649.0	28,281.0		1,238.0	43,208.0	26,929.0
1962						37,558.0	35,892.0	24.0		56,762.0	21,710.0
1963						47,863.0	25,639.0			48,168.0	4,581.0
1964											
1967						5,424.0				3,870.0	5,654.0
1968						497.0				28.0	30.0
1969						564.0				0.0	0.0
1984						32,353.0					14,124.0
1985						5,742.0					25,198.0
1986						35,631.0					6,168.0
1987	1,963.0	0.0	1.0	615.0	0.0	38,105.0	1,326.0	1,318.0	8,466.0		
1988	5,955.0	0.0	30.9	0.0	0.0	38,811.9	11,183.0	33.0	9,363.0	0.0	0.0
1989	9,452.0	1,361.0	3,406.8	0.0	0.0	39,206.0	102,406.0	8,674.8	50,729.0	0.0	0.0
1990	10,224.0	8,279.0	16,424.0	0.0	0.0	34,733.0	60,760.0	6,641.0	21,847.0	0.0	0.0
1991	4,697.0	8,179.0	3,264.0	61.8	0.0	48,852.0	62,110.0	6,891.0	13,170.0	0.0	0.0
1992	5,932.0	8,687.0	611.0	78.6	0.0	57,943.0	55,687.0	4,742.0	7,846.0	0.0	0.0
1993	5,540.0	5,542.0	0.0	665.7	0.0	54,447.0	44,322.0	4,450.0	21,851.0	0.0	0.0
1994	7,837.0	4,537.0	606.0	986.5	0.0	70,047.0	38,529.0	5,483.0	10,199.0	0.0	0.0
1995	3,642.0	6,665.0	31.0	834.6	0.0	50,266.0	49,653.0	4,825.0	11,046.0	0.0	0.0
1996	6,465.0	4,203.0	906.0	953.0	484.0	27,567.0	19,029.0	4,240.0	12,529.0	0.0	0.0
1997	6,751.1	7,006.4	4,691.2	517.2	0.0	21,148.4	33,660.9	6,930.3	25,152.7	0.0	0.0
1998	5,139.2	4,847.7	5,847.1	115.2	0.0	26,028.7	27,740.4	3,845.0	58,356.4	0.0	0.0
TOTAL	73,597.3	59,307.1	35,819.0	4,827.6	484.0	693,436.0	596,218.3	58,097.1	251,793.1	152,036.0	104,394.0

Appendix B



MONTGOMERY WATSON

APPENDIX B
WELL CONSTRUCTION DETAILS

TABLE B-1
CHATSWORTH FORMATION WELL COMPLETION INFORMATION AND DESIGNATION OF
HYDROSTRATIGRAPHIC UNIT AND SUB-BASIN
 Santa Susana Field Laboratory

AREA	HYDRO-STRATIGRAPHIC UNIT/SUB-BASIN	WELL IDENTIFIER	MEASURING POINT (feet MSL)	TOP OF PERFORATIONS (ft above MSL)	BOTTOM OF WELL (ft above MSL)	DEPTH OF WELL (feet)	PERFORATED INTERVAL (feet)
Area I	Sub-Basin 2 - SS1	HAR-01	1874.13	1844.13	1764.13	110	OPEN HOLE
Area II	Sub-Basin 3 - SS2	HAR-05	1812.65	1782.65	1632.65	180	OPEN HOLE
Area II	Sub-Basin 3 - SS2	HAR-06	1815.03	1785.03	1655.03	160	OPEN HOLE
Area II	Sub-Basin 4 - SS1	HAR-07	1728.38	1698.38	1628.38	100	OPEN HOLE
Area II	Sub-Basin 4 - SS1	HAR-08	1730.75	1700.75	1600.75	130	OPEN HOLE
Area I	Sub-Basin 1A - SS1	HAR-16	1872.31	1842.31	1752.31	120	OPEN HOLE
Area II	Sub-Basin 4 - SS1	HAR-17	1711.59	1681.59	1611.59	100	OPEN HOLE
Area III	Sub-Basin 4 - SS1	HAR-18	1749.41	1719.41	1669.41	80	OPEN HOLE
Area II	Sub-Basin 2 - SS1	HAR-19	1833.46	1803.46	1613.46	220	OPEN HOLE
Area II	Sub-Basin 2 - SS1	HAR-20	1830.6	1800.6	1600.6	230	OPEN HOLE
Area II	Sub-Basin 2 - SS1	HAR-21	1821.3	1791.3	1691.3	130	OPEN HOLE
Area II	Sub-Basin 3 - SS2	HAR-22	1816.41	1786.41	1726.41	90	OPEN HOLE
Area II	Sub-Basin 3 - SS2	HAR-23	1805.87	1775.87	1715.87	90	OPEN HOLE
Area I	Sub-Basin 1A - SS1	HAR-24	1906.89	1876.89	1796.89	110	OPEN HOLE
Area I	Sub-Basin 1A - SS1	HAR-25	1889.75	1859.75	1799.75	90	OPEN HOLE
Area III	Sub-Basin 2 - SS1	HAR-26	1763.17	1733.17	1673.17	90	OPEN HOLE
Area I	Sub-Basin 1B - SS1	RD-01	1935.89	1909.89	1429.89	506	OPEN HOLE
Area I	Sub-Basin 1B - SS1	RD-02	1873.92	1847.92	1473.92	400	OPEN HOLE
Area I	Sub-Basin 4 - SS1	RD-03	1743.5	1716.5	1443.5	300	OPEN HOLE
Area II	Sub-Basin 2 - SS1	RD-04	1883.85	1856.85	1387.85	496	OPEN HOLE
Undeveloped Land	Sub-Basin 4 - SS1	RD-05A	1704.66	1675.16	1546.66	158	OPEN HOLE
Undeveloped Land	Sub-Basin 4 - SS1	RD-05B	1705.89	1678.89	1395.89	310	257.6 - 310.0
Undeveloped Land	Sub-Basin 4 - SS1	RD-05C	1705.25	1284.25	1225.25	480	OPEN HOLE
Undeveloped Land	Out-Side of Sub-basins	RD-06	1617.21	1481.21	1357.21	260	OPEN HOLE
Undeveloped Land	Out-Side of Sub-basins	RD-06	1617.21	1590.21	1357.21	260	70.0 - 140.0

TABLE B-1
CHATSWORTH FORMATION WELL COMPLETION INFORMATION AND DESIGNATION OF
HYDROSTRATIGRAPHIC UNIT AND SUB-BASIN

Santa Susana Field Laboratory

AREA	HYDRO-STRATIGRAPHIC UNIT/SUB-BASIN	WELL IDENTIFIER	MEASURING POINT (feet MSL)	TOP OF PERFORATIONS (ft above MSL)	BOTTOM OF WELL (ft above MSL)	DEPTH OF WELL (feet)	PERFORATED INTERVAL (feet)
Sage Ranch Park	Sub-Basin 1A - SS1	RD-32	1808.47	1709.47	1658.47	150	OPEN HOLE
Undeveloped Land	Sub-Basin 3 - SS2	RD-33A	1792.97	1692.97	1472.97	320	OPEN HOLE
Undeveloped Land	Sub-Basin 3 - SS2	RD-33B	1793.21	1433.21	1378.21	415	OPEN HOLE
Undeveloped Land	Sub-Basin 3 - SS2	RD-33C	1793.54	1313.54	1273.54	520	OPEN HOLE
Undeveloped Land	Sub-Basin 3 - SS2	RD-34A	1761.83	1745.83	1701.83	60	OPEN HOLE
Undeveloped Land	Sub-Basin 3 - SS2	RD-34B	1762.51	1582.51	1522.51	240	OPEN HOLE
Undeveloped Land	Sub-Basin 3 - SS2	RD-34C	1762.6	1382.6	1312.6	450	OPEN HOLE
Area I	Sub-Basin 1A - SS1	RD-35A	1906.68	1887.18	1796.68	110	65.0 - 105.5
Area I	Sub-Basin 1A - SS1	RD-35B	1906 est.	1744 est.	1547 est.	359	162-359
Sage Ranch Park	Sub-Basin 1A - SS1	RD-36A	1913.09	1893.09	1815.78	97.31	OPEN HOLE
Sage Ranch Park	Sub-Basin 1A - SS1	RD-36B	1915.26	1795.26	1744.58	170.68	OPEN HOLE
Sage Ranch Park	Sub-Basin 1A - SS1	RD-36C	1913.82	1715.82	1447.9	465.92	405.0 - 455.5
Sage Ranch Park	Sub-Basin 1A - SS1	RD-36D	1920.08	1366.08	1316.2	603.88	575 - 605
Sage Ranch Park	Sub-Basin 2 - SS1	RD-37	1870.01	1610.01	1470.01	400	272.0 - 377.0
Sage Ranch Park	Sub-Basin 1A - SS1	RD-38A	1878.92	1858.92	1758.92	120	OPEN HOLE
Sage Ranch Park	Sub-Basin 1A - SS1	RD-38B	1881.45	1602.45	1511.45	370	OPEN HOLE
Sage Ranch Park	Sub-Basin 1A - SS1	RD-39A	1960.23	1940.23	1801.23	159	OPEN HOLE
Sage Ranch Park	Sub-Basin 1A - SS1	RD-39B	1959.48	1746.48	1482.53	476.95	440 - 470
Area II	Sub-Basin 4 - SS1	RD-40	1972.02	1952.52	1672.02	300	OPEN HOLE
Area II	Sub-Basin 4 - SS1	RD-41A	1773.09	1753.59	1653.09	120	OPEN HOLE
Area II	Sub-Basin 4 - SS1	RD-41B	1774.32	1434.32	1384.32	390	OPEN HOLE
Area II	Sub-Basin 4 - SS1	RD-41C	1773.33	1281.33	1215.33	558	OPEN HOLE
Area II	Sub-Basin 4 - SS1	RD-42	1945.46	1925.96	1825.46	120	OPEN HOLE

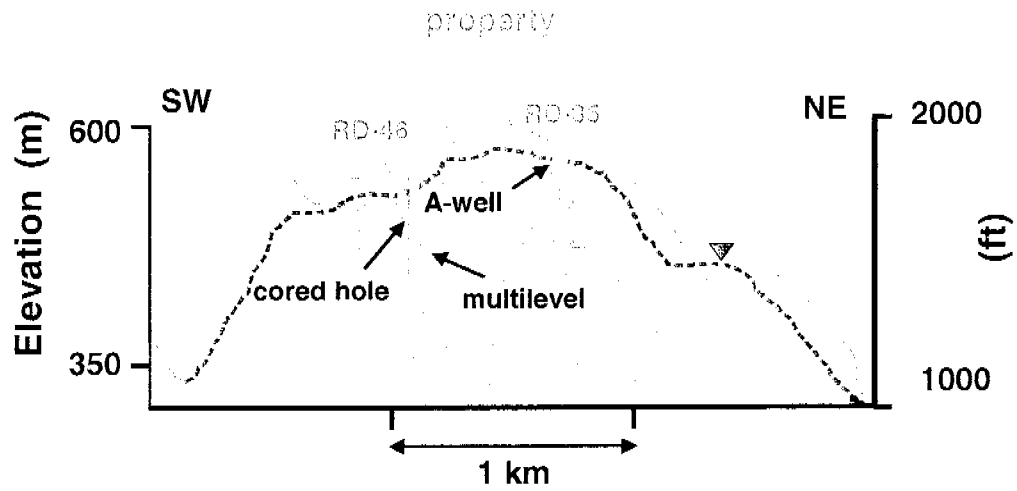


Figure 5-3: East-west section through study area

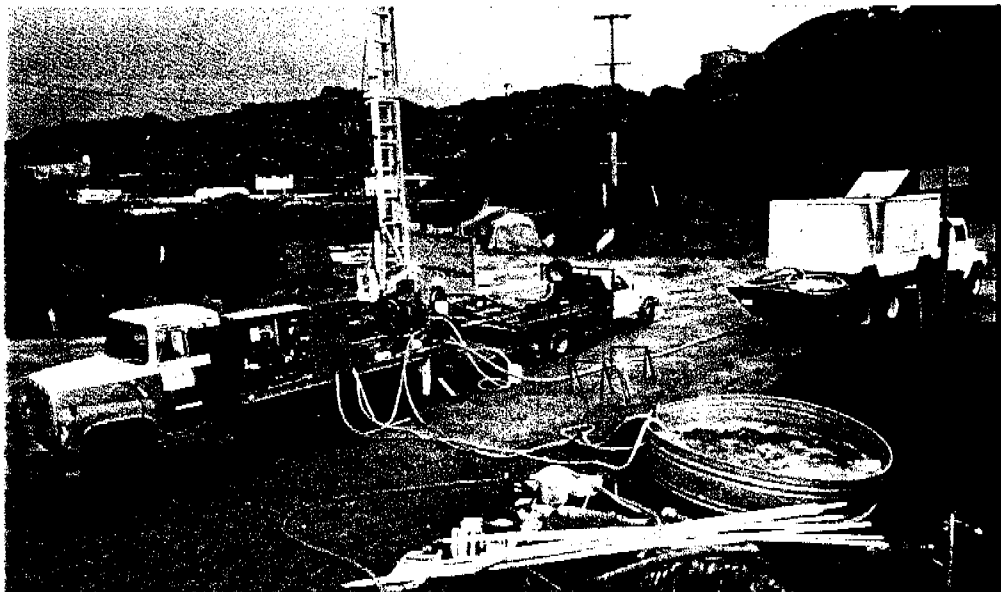


Figure 5-4: Drilling of RD-46B

Figure 5-5: Diamond bit on core barrel used for continuous coring

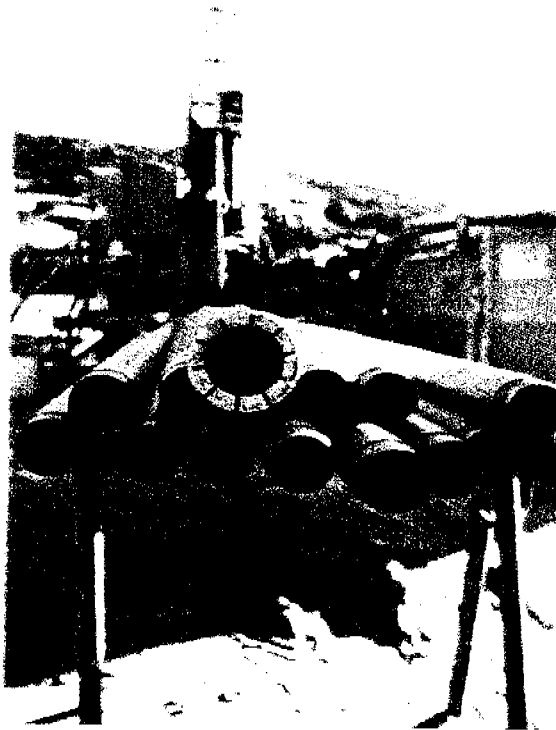


Figure 5-6: Field examination of typical core segment 5-foot long



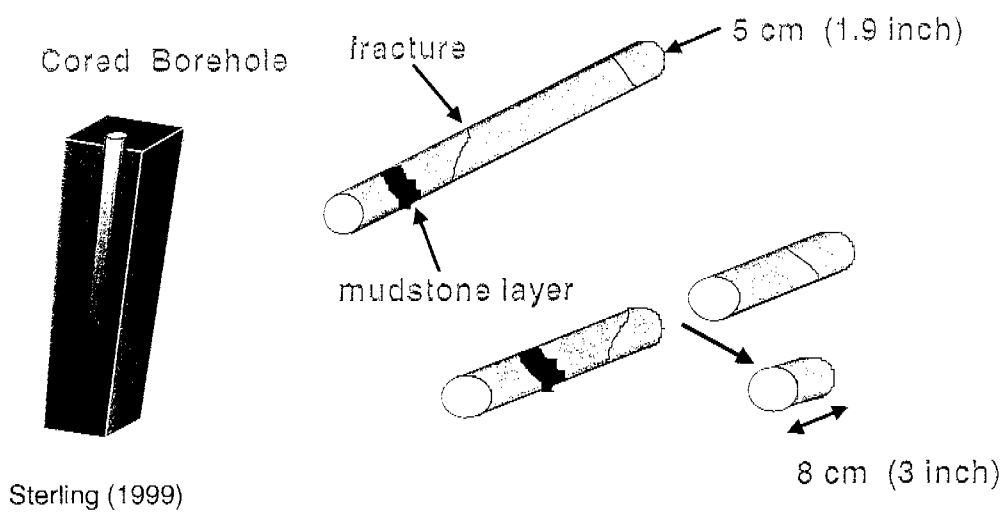
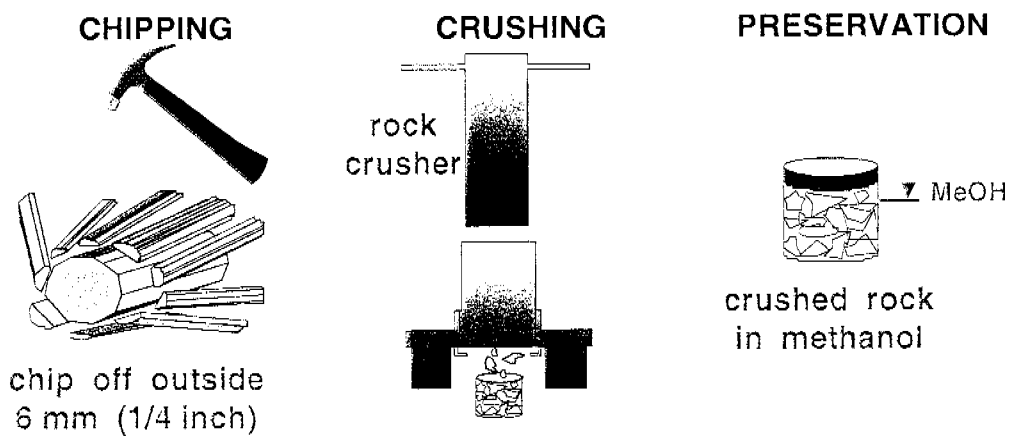


Figure 5-7: Stage 1. Coring and removal of a small core segment for processing



Sterling (1999)

Figure 5-8: Stage 2. Rock crushing and preservation



Figure 5-9: Chipping away outer core segments

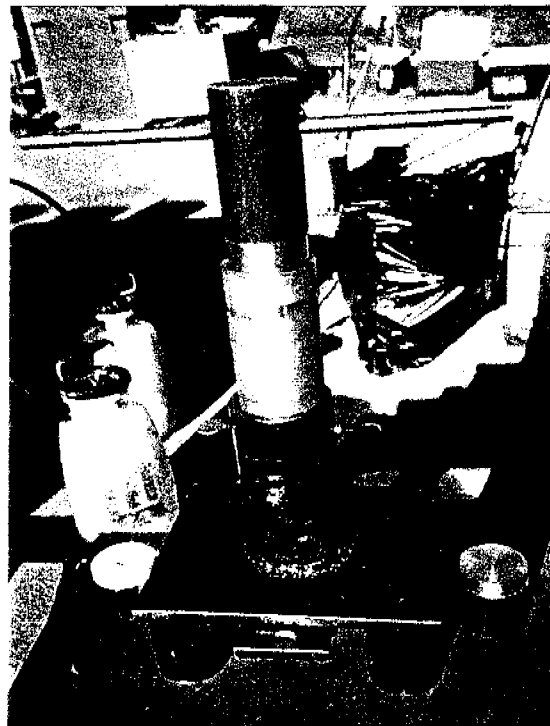


Figure 5-10: Sterling Rock Crusher



Figure 5-11: Broken up rock core preserved in methanol

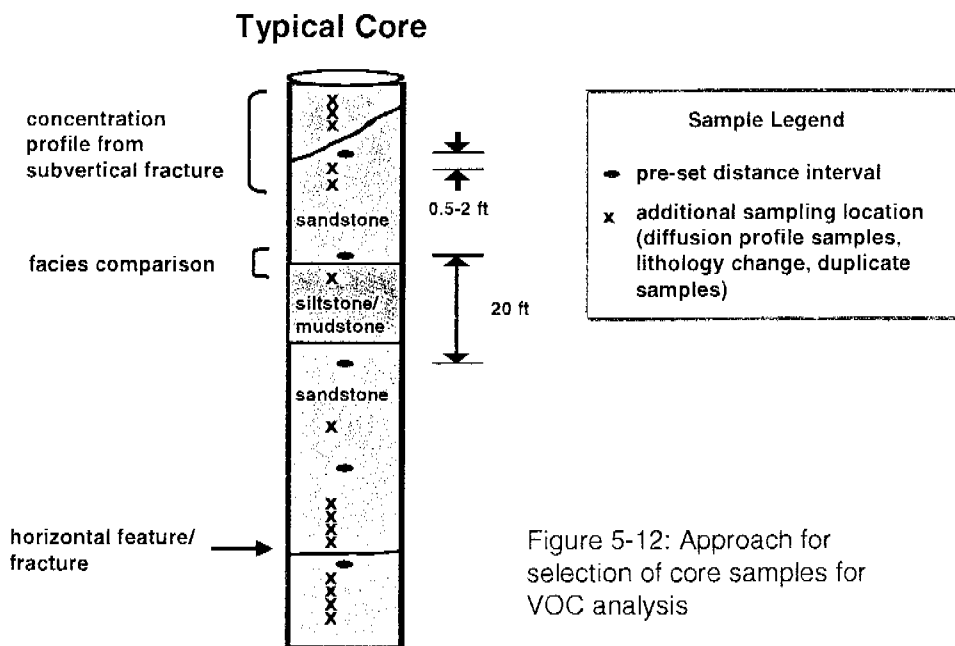
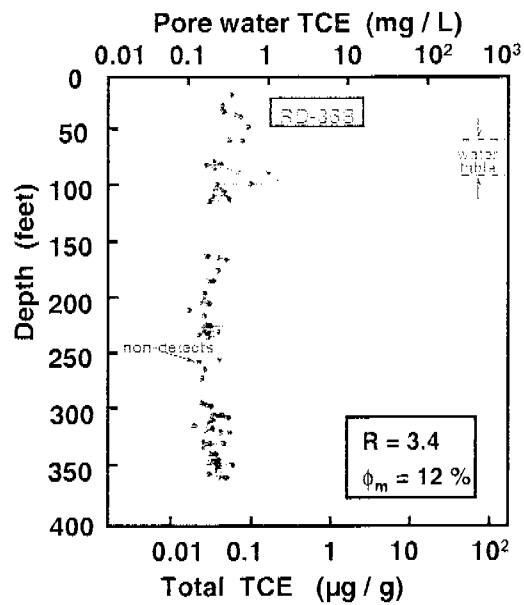


Figure 5-12: Approach for selection of core samples for VOC analysis



Sterling (1999)

Figure 5-13: RD-35B Rock sample results expressed as TCE in pore water

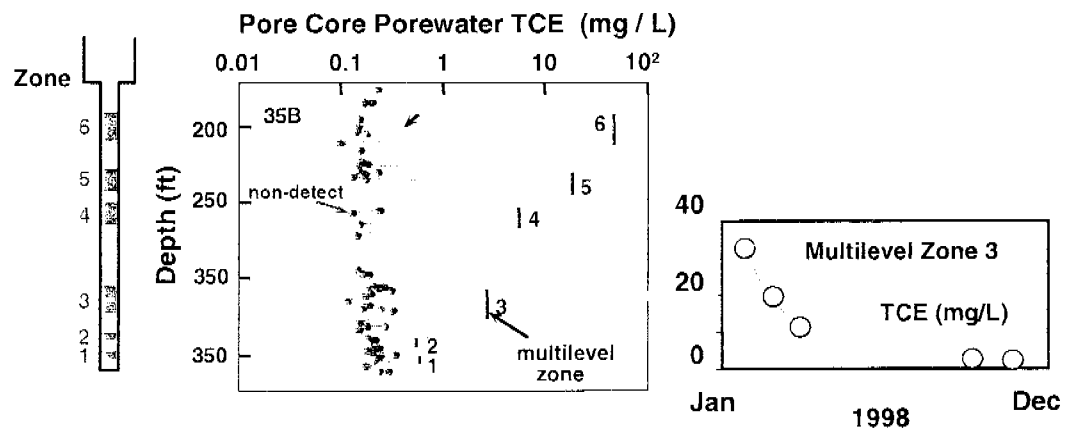
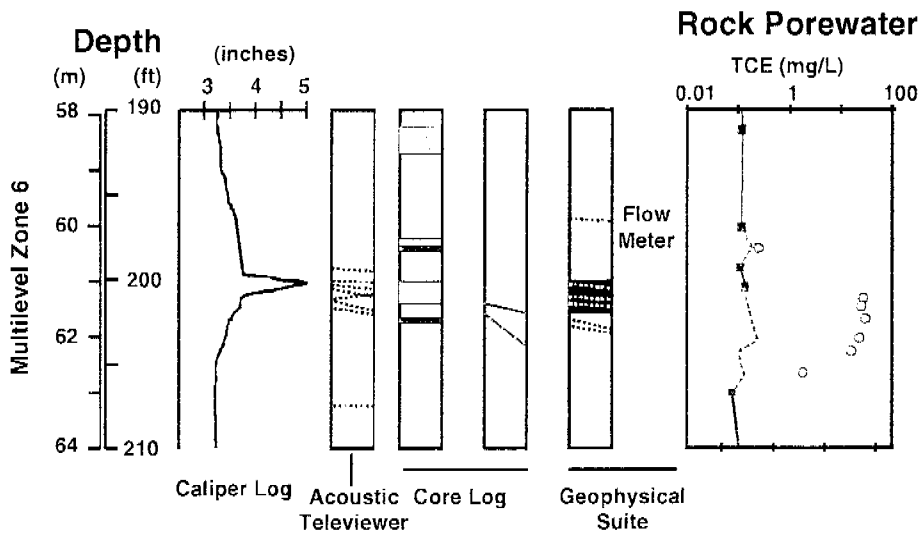


Figure 5-14: Comparison of RD-35B rock core TCE results with TCE in water samples from the removable multilevel system



December 04, 1998

Figure 5-15 : RD-35B (Zone 6) showing borehole geophysics and rock core TCE bulge

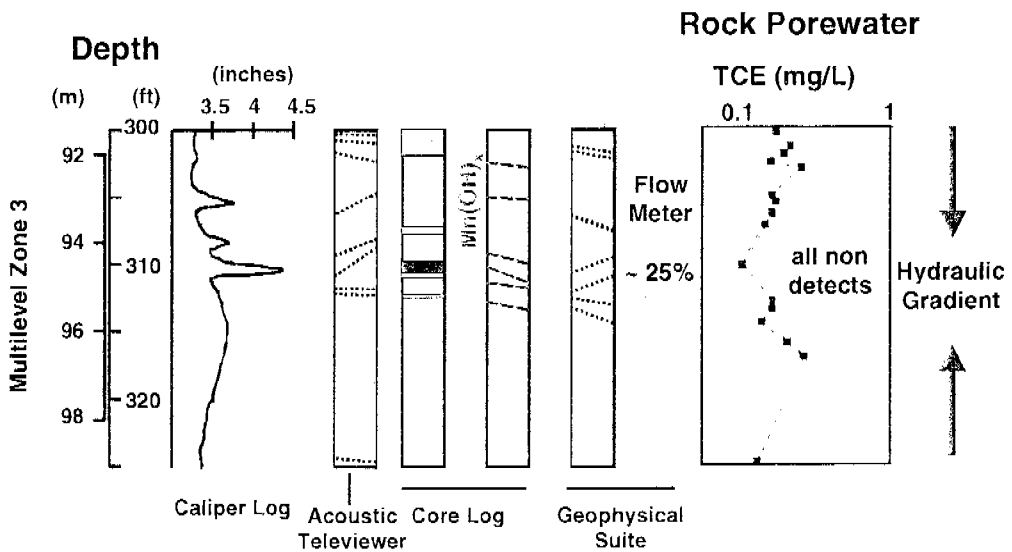


Figure 5-16: RD-35B (Zone 3) showing borehole geophysics, fractures and no TCE occurrence

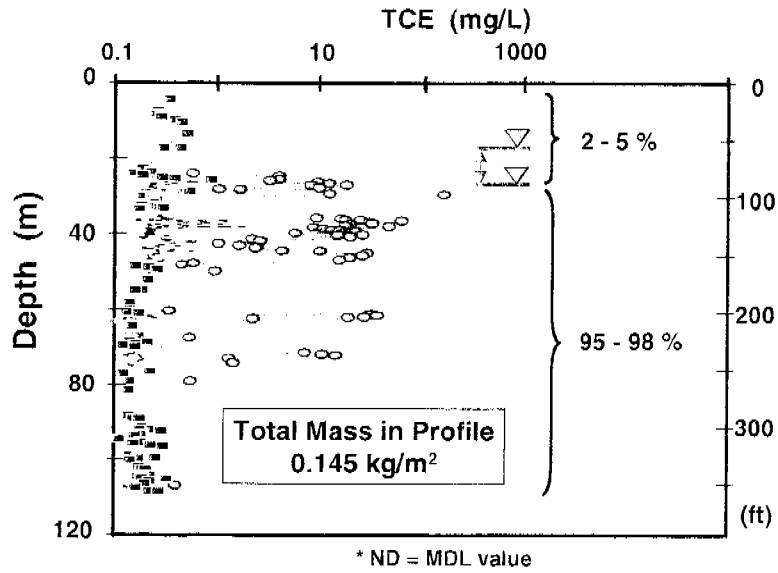


Figure 5-17 : TCE mass distribution: RD-35B

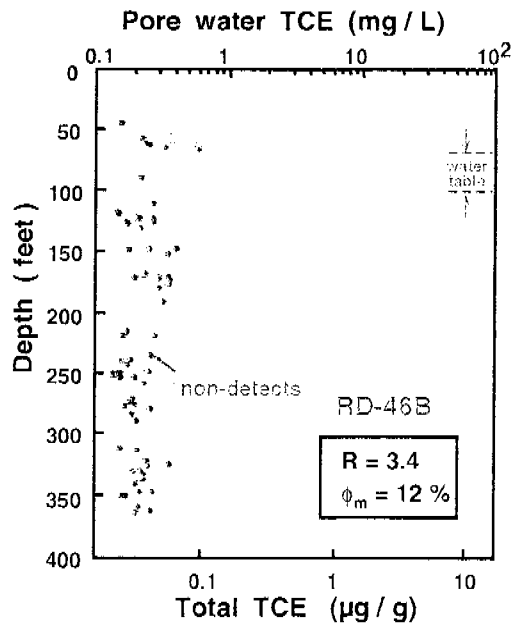
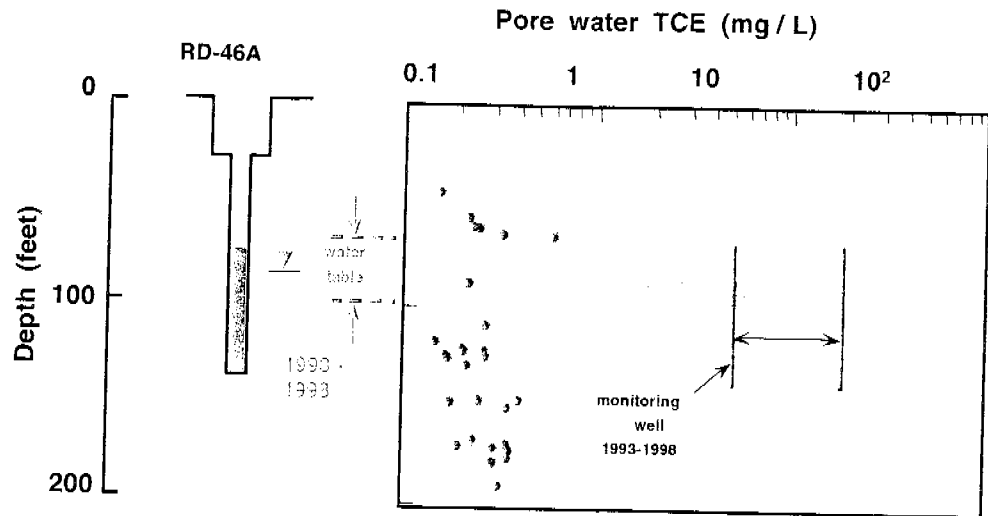


Figure 5-18 : RD-46B rock core sample results expressed as TCE in pore water

Sterling (1999)



Sterling (1999)

Figure 5-19 : Comparison of TCE in RD-46 rock core and A-Well

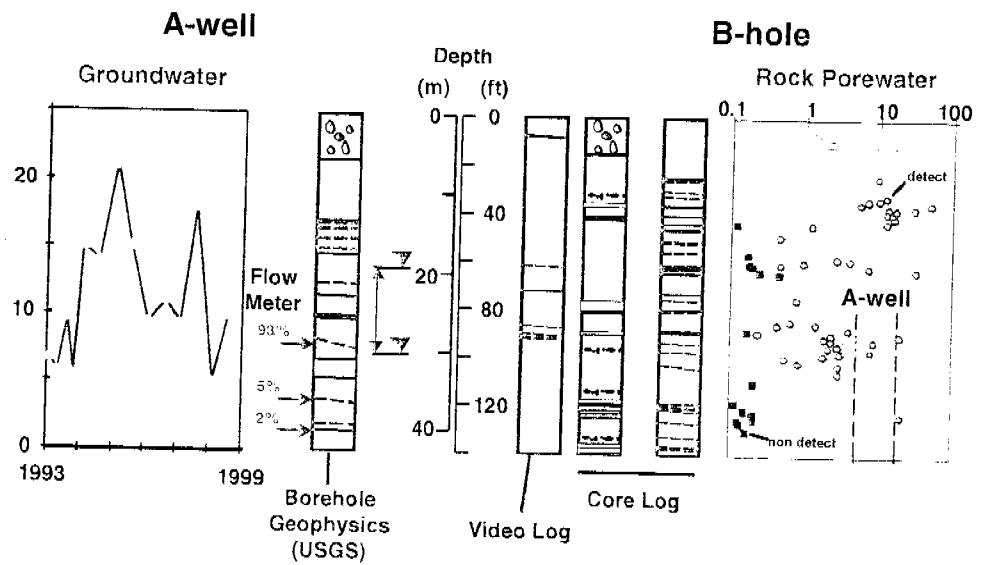
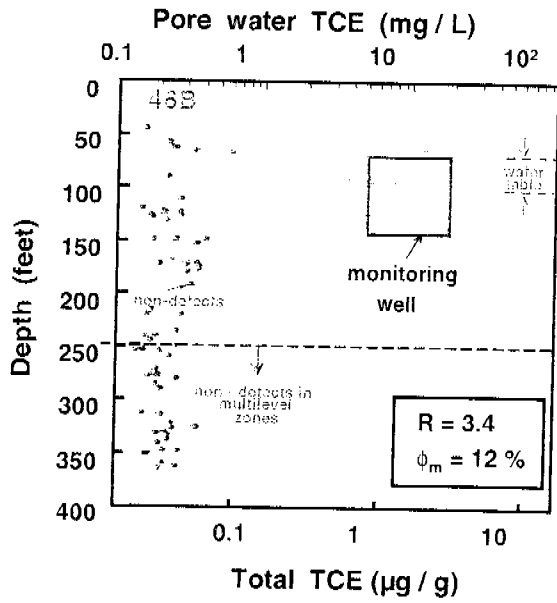


Figure 5-20: Comparison of TCE in A-Well and rock core at RD-46



Sterling (1999)

Figure 5-21 : Comparison of TCE in RD46B rock core and A-well

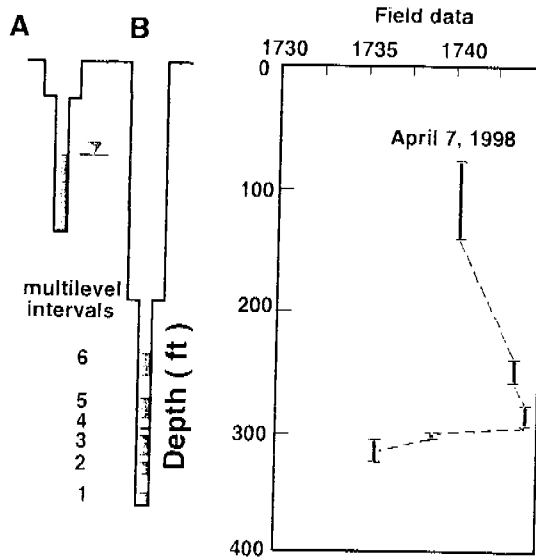


Figure 5-22 : Head at RD-46 measured in A-Well and removable multilevel system

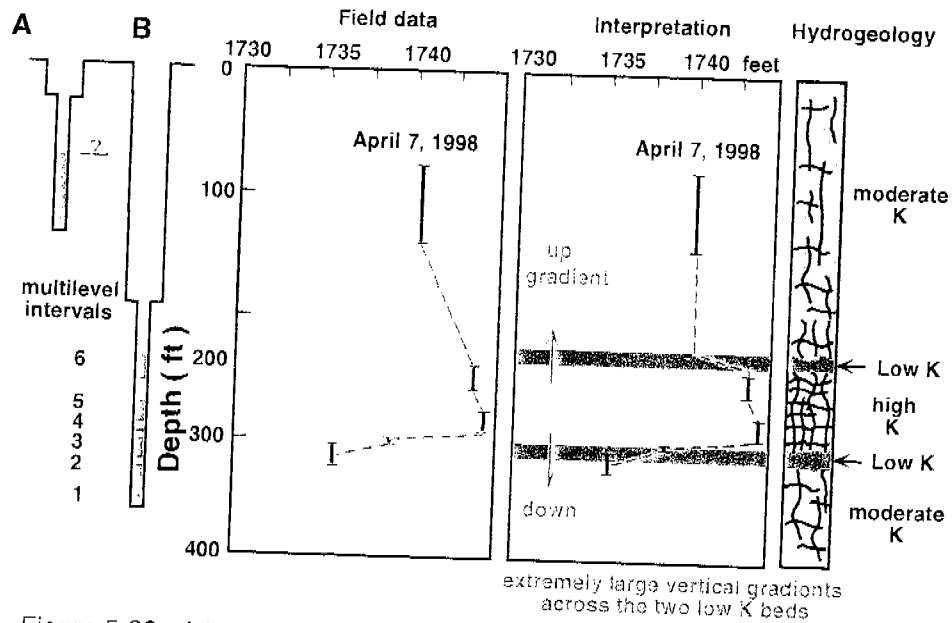


Figure 5-23 : A hypothetical interpretation of head profile at RD-46 in which the large head differentials cause large gradients across thin shale beds

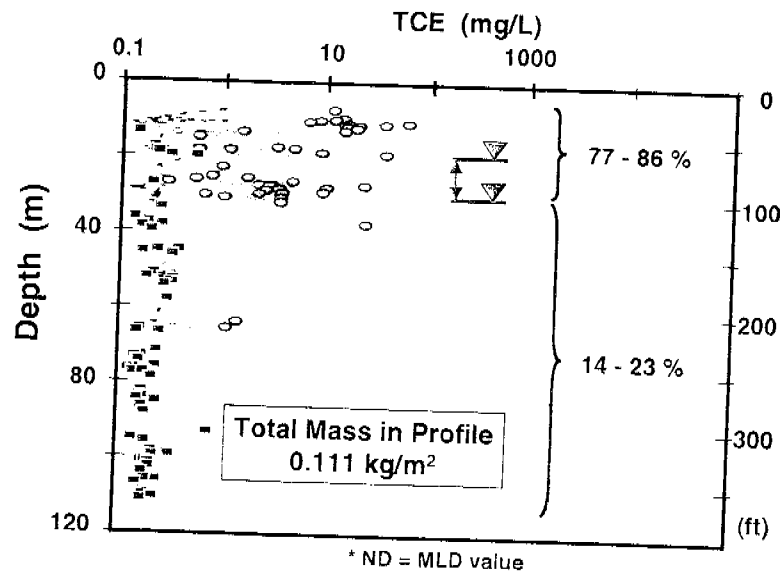


Figure 5-24 : TCE Mass Distributions: RD-46B

Sample	Depth (ft)	Lithology ¹	Dry Density ² (g/cm ³)	Porosity ³ (%)	Total ⁴ Organic Carbon (%)	Cl Matrix ⁵ Diff, D (cm ² /s)	Matrix Tortuosity ⁶ Factor, τ	Intrinsic Permeability (m ²)	Estimated R (TCE)	K (cm/s)
CH1	114-115	sandstone, lt brown, v. fine to fine grained	2.370	11.9	0.14	1.6E-6	0.10	1.60E-15	3.6	1.6E-06
CH1	209-210	sandstone, lt grey, fine to coarse grained	2.336	12.5	0.10	0.9E-6	0.06	1.13 E-14	2.7	1.1E-05
CH1	272.5-274	sandstone, coarse grained, lt grey	2.328	13.1	0.05	1.1E-6	0.07	1.57E-14	1.8	1.5E-05
CH2	40.25-41	siltstone, grey, massive	2.540	6.6	0.39	0.7E-6 - 0.8E-6	0.05	8.70E-20	14.8	8.5E-11
CH2	62.8-64	sandstone, lt brown, fine to coarse grained	2.313	13.4	0.02	1.4E-6	0.09	2.00E-15	1.3	2.0E-06
CH2	68.5-70	sandstone, grey, coarse grained	2.409	10.8	0.15	1.4E-6	0.09	1.54E-15	4.1	1.5E06
CH3	26.5-28	claystone/siltstone, dk grey	2.333	10.6	1.22	claystone sample fractured during saturation		6.50E-18	25.7	6.4E-09
CH3	46-47	siltstone, grey	2.392	11.4	0.70	1.5E-6 - 1.8E-6	0.10 - 0.12	2.60E-19	14.5	2.5E-10
CH3	76.4-78	sandstone, lt brown, fine to coarse grained	2.220	15.9	0.07	2.1E-6 - 2.3E-6	0.14 - 0.15	6.90E-15	1.9	6.8E-06
CH3	90-91	sandstone, lt grey, fine to coarse grained with some gravel	2.341	13.3	0.15	2.0E-6 - 2.3E-6	0.13 - 0.15	1.13E-14	3.4	1.1E-05
RD54-C	28-29.1	sandstone, lt grey, fine to coarse grained	2.328	13.4	0.13	1.3E-6 - 1.7E-6	0.08 - 0.11	1.60E-15	3.1	1.6E.06

¹ Lithology provided by Groundwater Resources Consultants, Inc.

² ASTM Method D4531-86 (1992)

³ Total porosity (n) of rock matrix calculated using the equation: $n = 1 - \rho_d / G_s \rho_{water}$

where ρ_d = dry density [Mg/m³]
 G_s = specific gravity of the rock matrix
 ρ_{water} = density of water and 23°C = 0.998 Mg/m³

⁴ Walkley and Black Wet Oxidation Method (Walkley, 1947)

⁵ Chloride matrix diffusion coefficient) obtained at 23°C using the test method described in this report

⁶ Matrix tortuosity factor (τ) calculated as D_{Cl} / D_{0Cl} where D_{0Cl} is the aqueous diffusion coefficient for chloride when diffusing together with sodium from a source solution containing 0.03 Molar NaCl at 23°C. The value used for D_{0Cl} is 15.5×10^{-6} cm²/s (American Institute of Physics Handbook, 1972)

Figure 5-25: Chatsworth Formation rock matrix property measurements (Golder Associates, 1997).

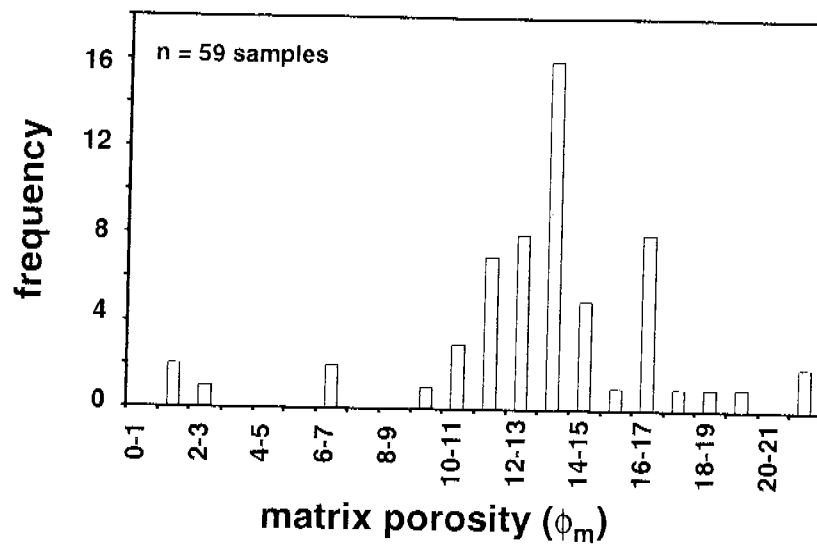


Figure 5-26: Distribution of Matrix Porosity Values: Chatsworth Formation

	Minimum	Maximum	Sandstone Average	
ϕ_m (%)	1.0	21.6	12.9	(n=58)
$D_e^{Cl^-}$ (cm ² /s)	7.5×10^{-7}	2.2×10^{-6}	1.5×10^{-6}	(n = 10)
f_{oc} (%)	0.02	1.22	0.10	(n = 8)
R	1.5	28.7	3.3	($f_{oc} = 0.1\%$)

Figure 5-27: Matrix Parameters for Chatsworth Formation

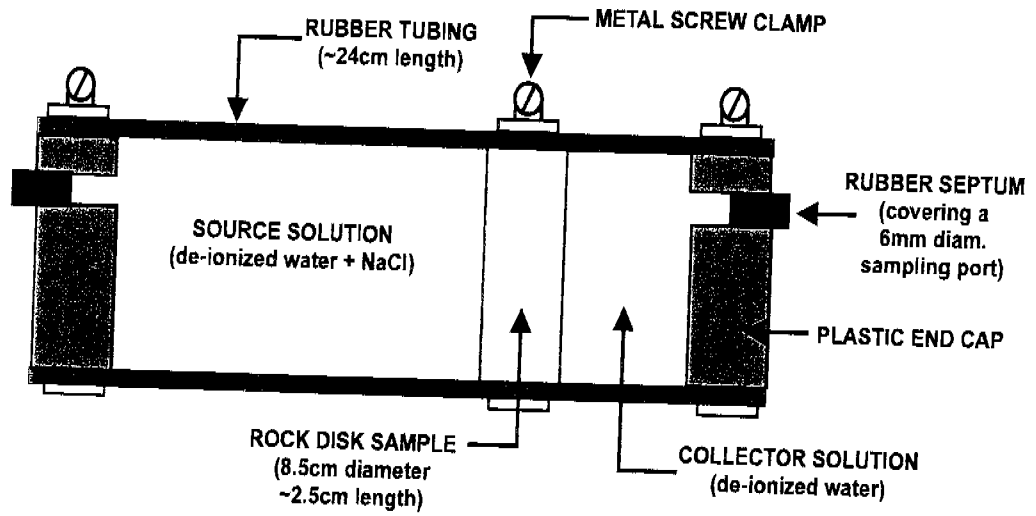


Figure 5-28: Schematic Drawing of the Chloride Diffusion Cell

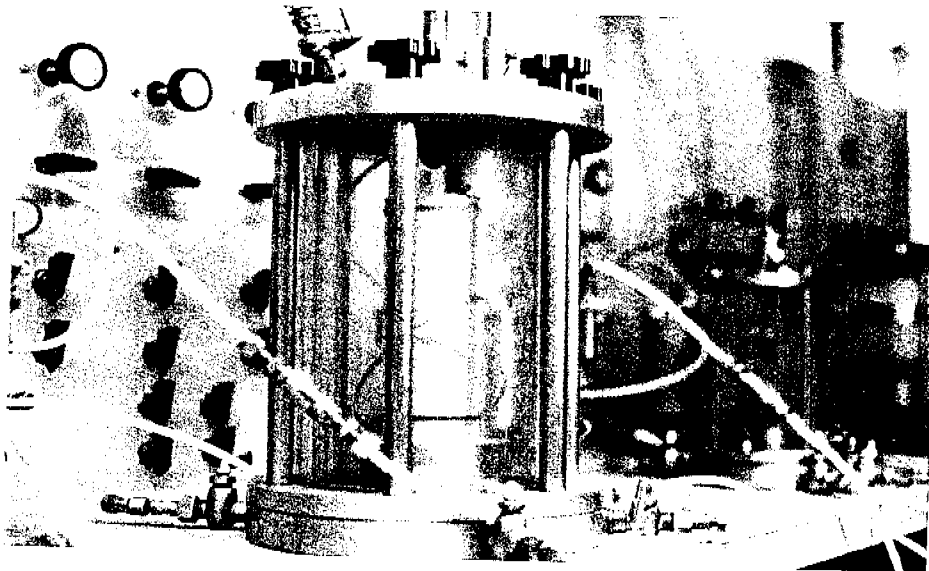


Figure 5-29: Triaxial cell for saturation of core samples and hydraulic conductivity measurements (Golder Associates, 1997)

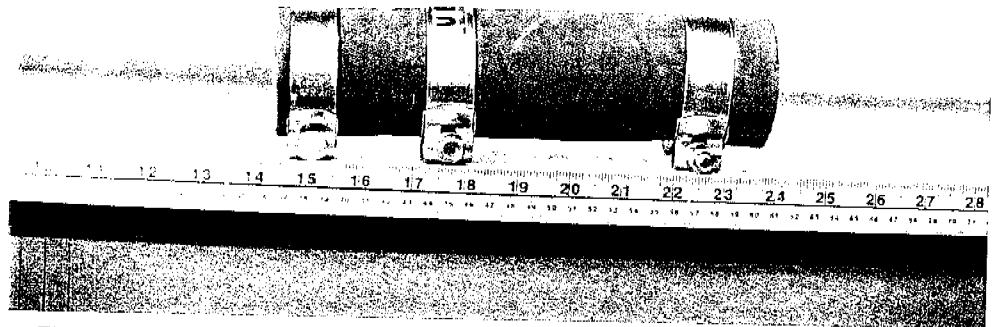
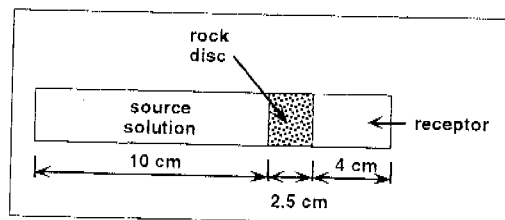


Figure 5-30: Dual reservoir diffusion test apparatus for chloride and porous rock (Golder Associates, 1997)



Sandstone : light grey,
fine to coarse grained

Depth : 209 - 210 ft

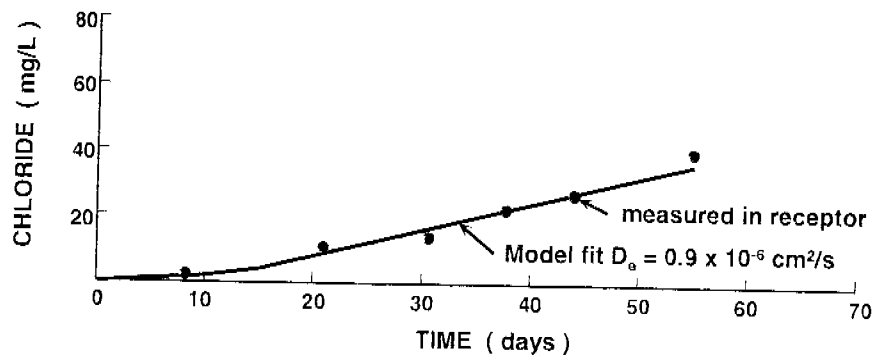


Figure 5-31: Chloride diffusion test results for a fine to coarse grained sandstone sample from the Chatsworth Formation (Golder Associates, 1997)

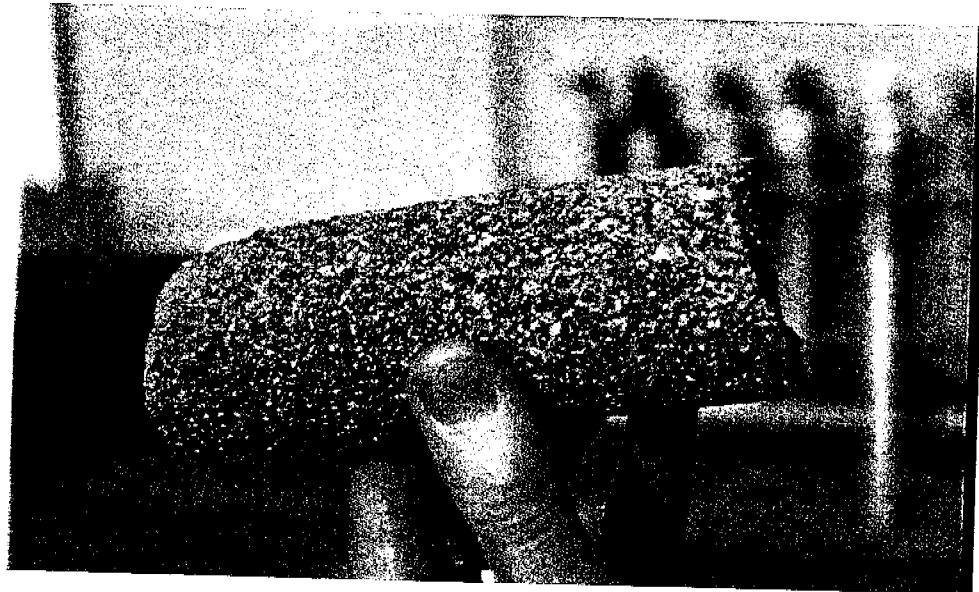
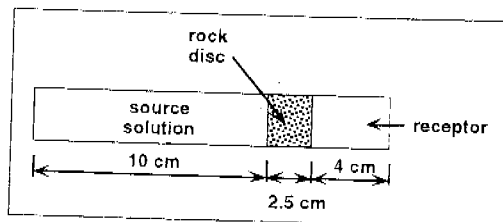


Figure 5-32: Course sandstone sample from SSFL Chatsworth Formation



Sandstone : light brown,
very fine grained
Depth : 114 - 115 ft

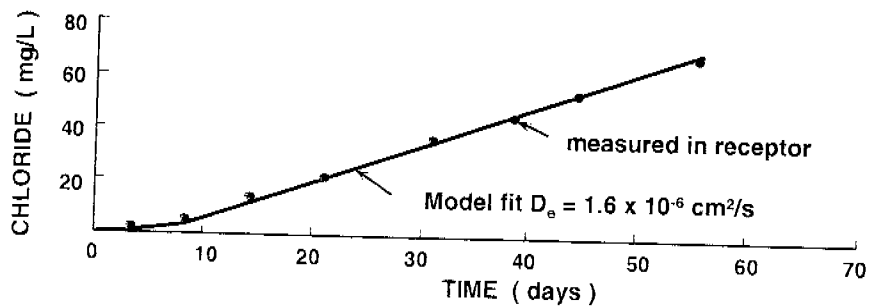


Figure 5-33: Chloride diffusion test results for a very fine grained sandstone-siltstone sample from the Chatsworth Formation (Golder Associates, 1997)

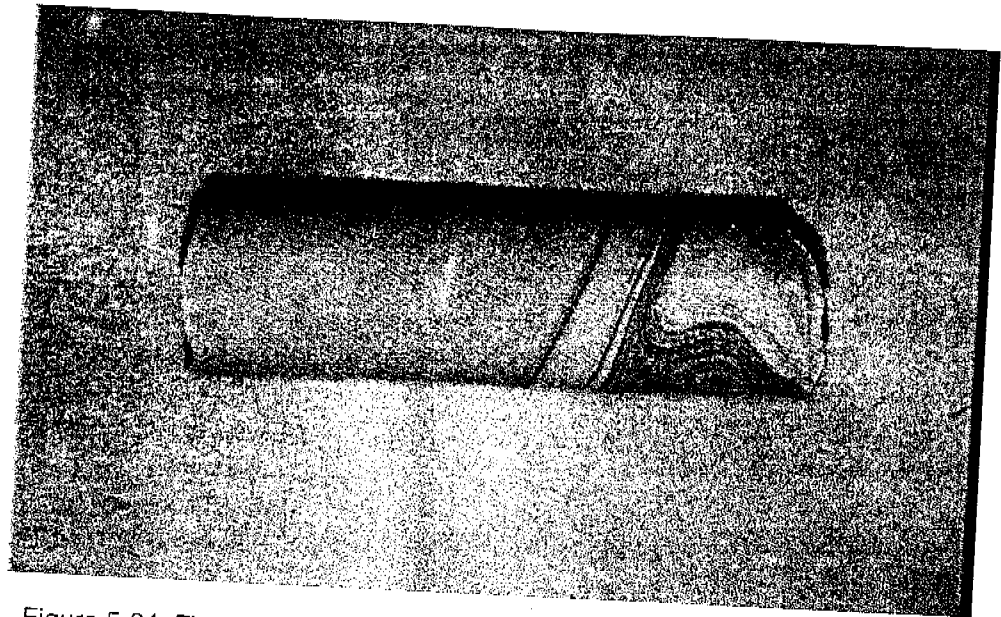


Figure 5-34: Fine sandstone – siltstone sample from SSFL Chatsworth Formation

1. Measure Cl^- diffusion coefficient ($D_e^{\text{Cl}^-}$)
2. Calculate Cl^- tortuosity factor ($\tau = D_e / D_o$)
3. Calculate TCE free solution diffusion coefficient (D_o^{TCE}) from correlation equation
4. Calculate TCE porous medium diffusion coefficient ($D_e^{\text{TCE}} = \tau^{\text{Cl}^-} D_o^{\text{TCE}}$)

Figure 5-35: Steps for estimating TCE - sandstone diffusion coefficient based on chloride diffusion test results

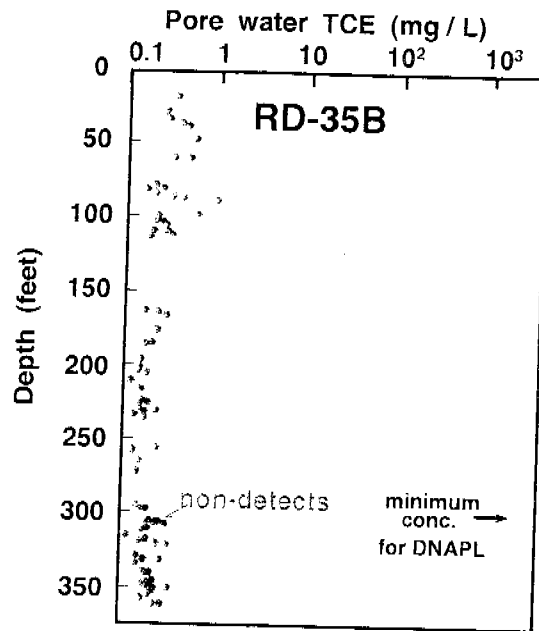


Figure 5-36: Results of core analyses for RD-35B compared to TCE solubility

Sterling (1999)

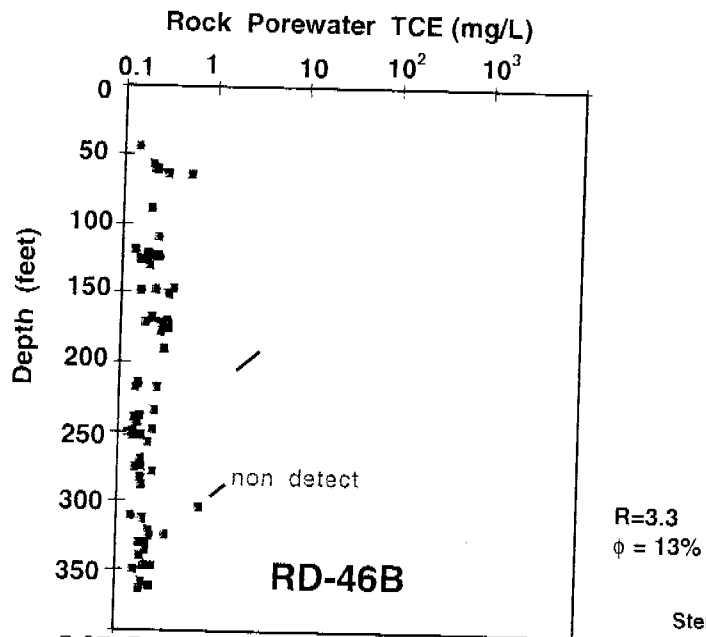


Figure 5-37: Results of core analyses for RD-46B compared to TCE solubility

Sterling (1999)

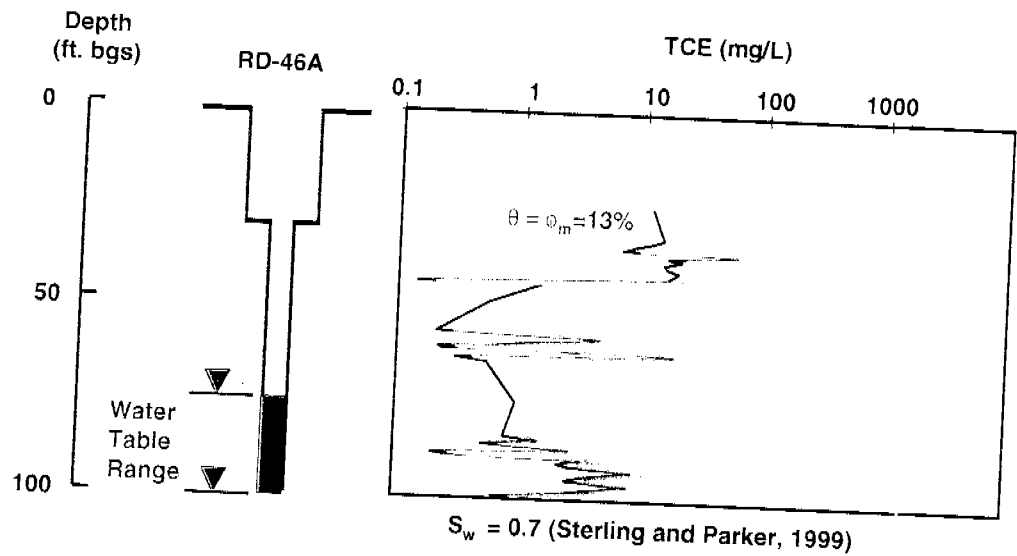


Figure 5-38: RD-46B vadose zone rock pore water concentrations compared to TCE solubility

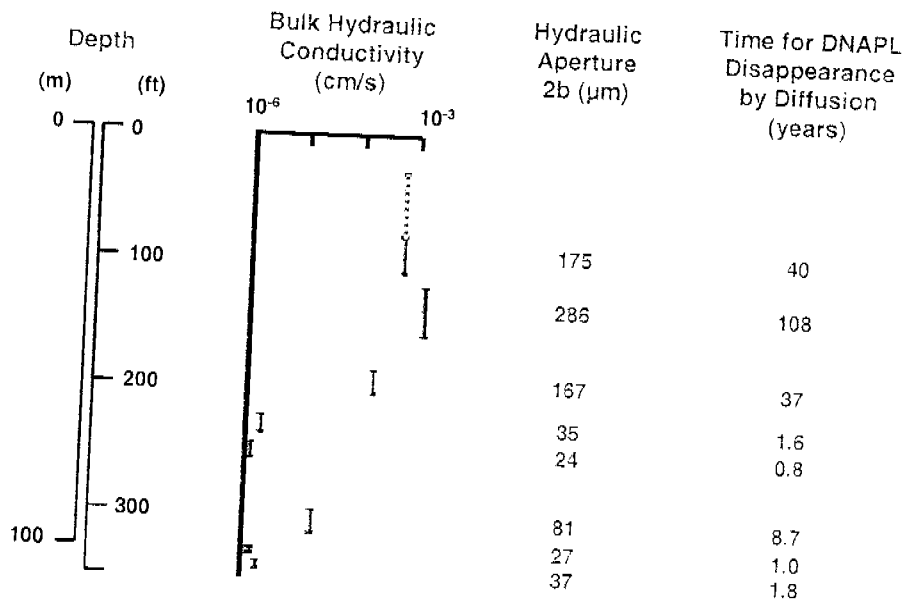


Figure 5-39: Calculated TCE disappearance times for DNAPL film thicknesses equal to hydraulic apertures for RD-35B

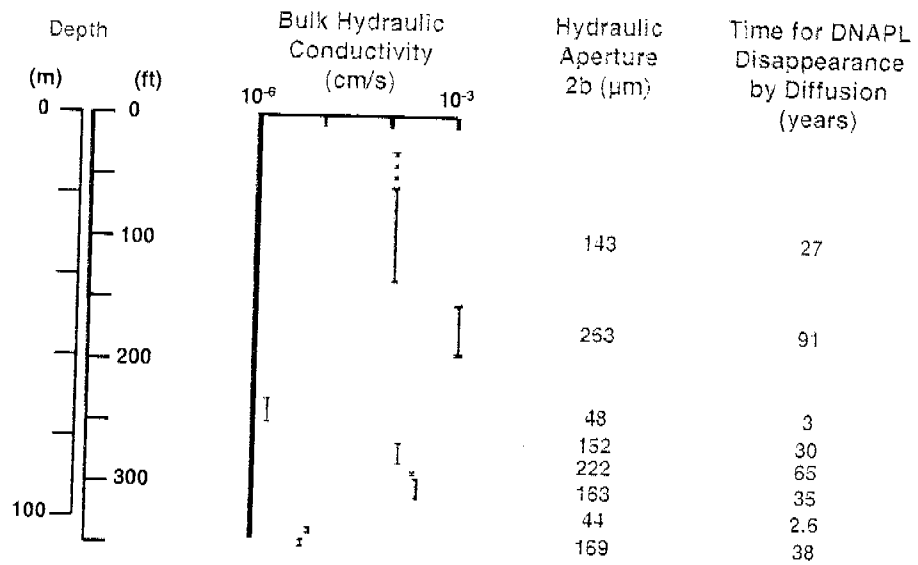
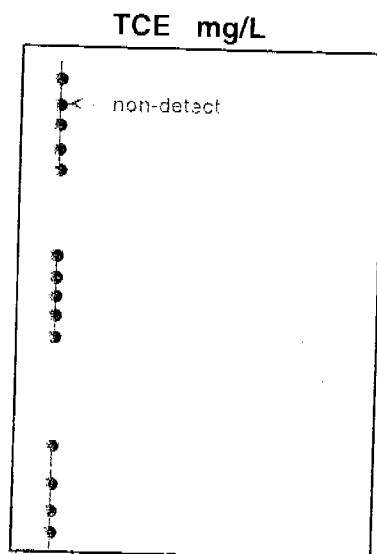


Figure 5-40: Calculated TCE disappearance times for DNAPL film thicknesses equal to hydraulic apertures in RD-46

ROCK CORE RESULTS



CONCEPTUAL MODEL

Rock core TCE identifies fractures where DNAPL or contaminated groundwater flowed

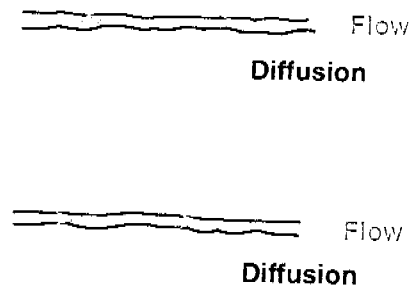


Figure 5-41: Illustration of the rock core TCE peaks expected at fractures in which TCE migration occurs.

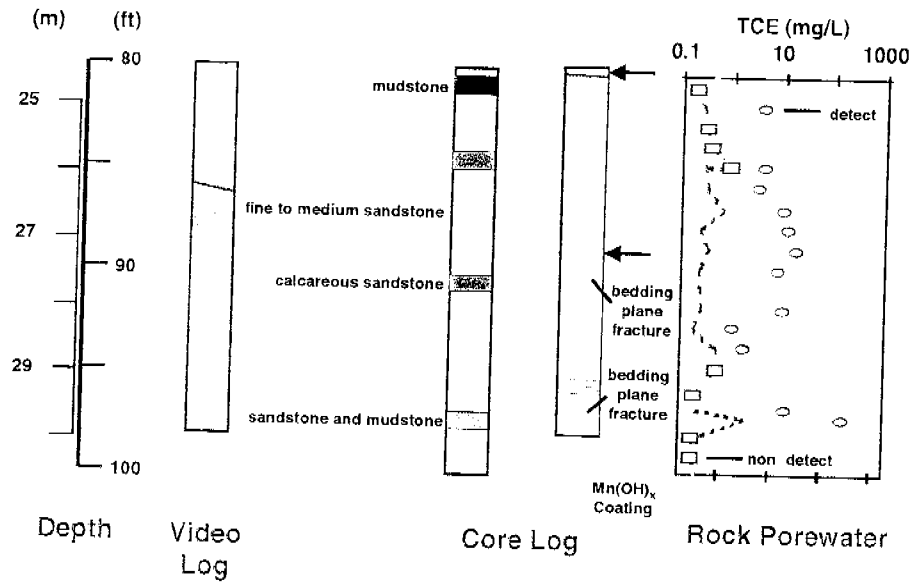


Figure 5-42: Examples of rock core halos at three fracture zones in RD-35B: Two peaks and one bulge.

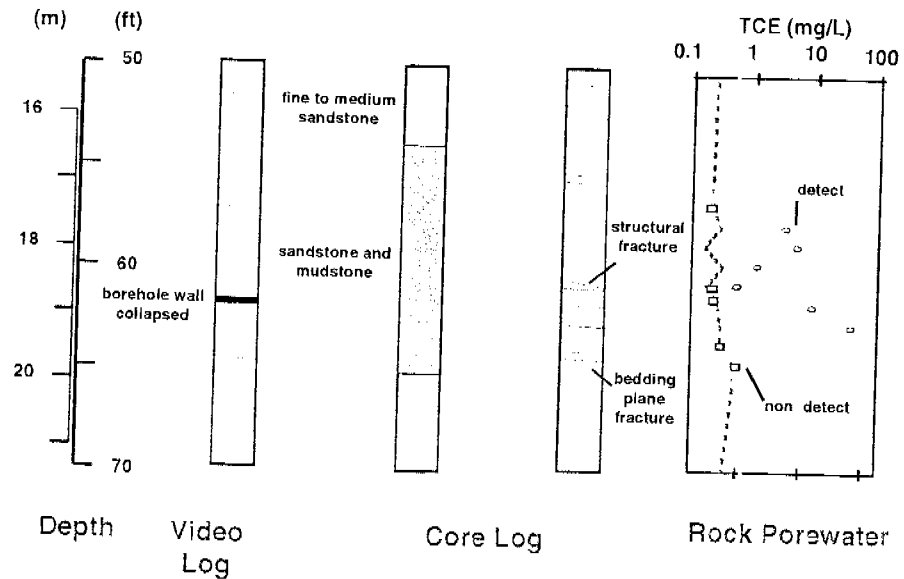
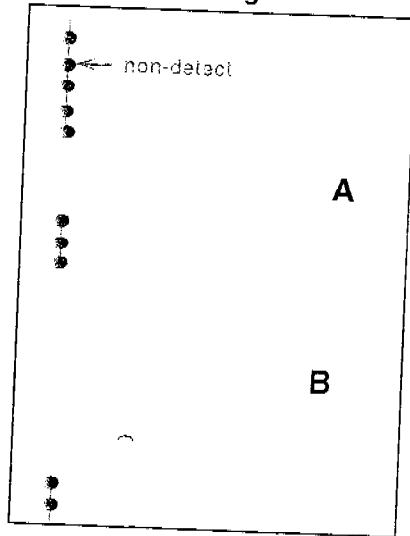


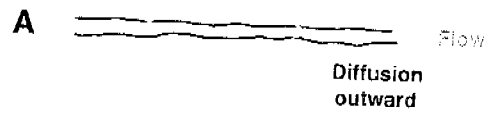
Figure 5-43: Example of rock core TCE results showing features indicative of reverse diffusion.

HYPOTHETICAL ROCK CORE RESULTS
TCE mg/L



CONCEPTUAL MODEL

Inward Diffusion



Reverse Diffusion

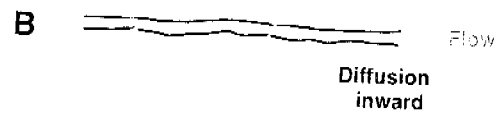
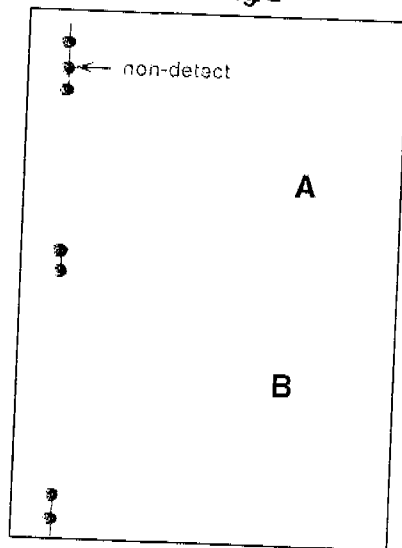


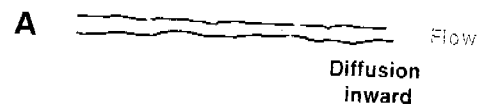
Figure 5-44: Conceptualization of a double peak caused by reverse diffusion from a single fracture.

HYPOTHETICAL ROCK CORE RESULTS
TCE mg/L



CONCEPTUAL MODEL

Reverse Diffusion



Reverse Diffusion

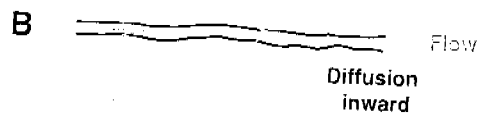


Figure 5-45: Conceptualization of reverse diffusion from two fractures causing four peaks.

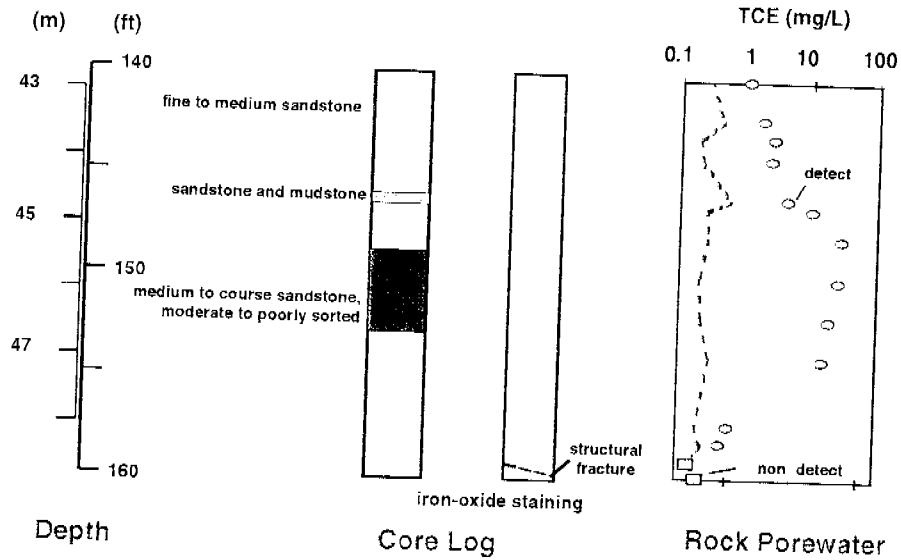


Figure 5-46: Example of a TCE bulge in rock core profile associated with a coarse grained sandstone bed; this bed is likely a TCE migration pathway.

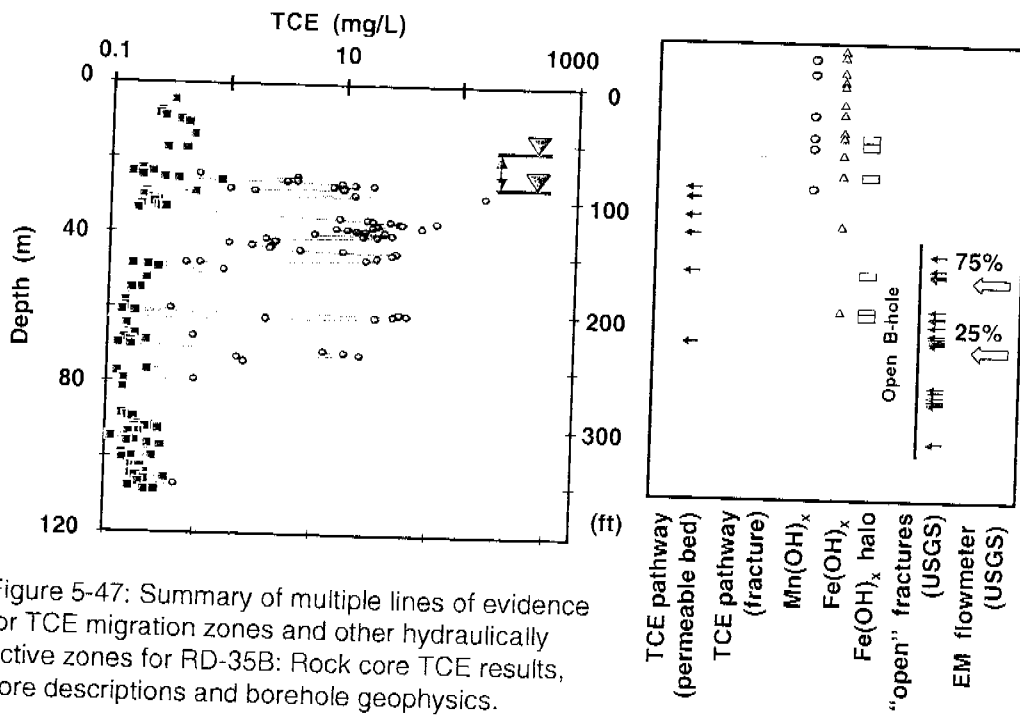


Figure 5-47: Summary of multiple lines of evidence for TCE migration zones and other hydraulically active zones for RD-35B: Rock core TCE results, core descriptions and borehole geophysics.

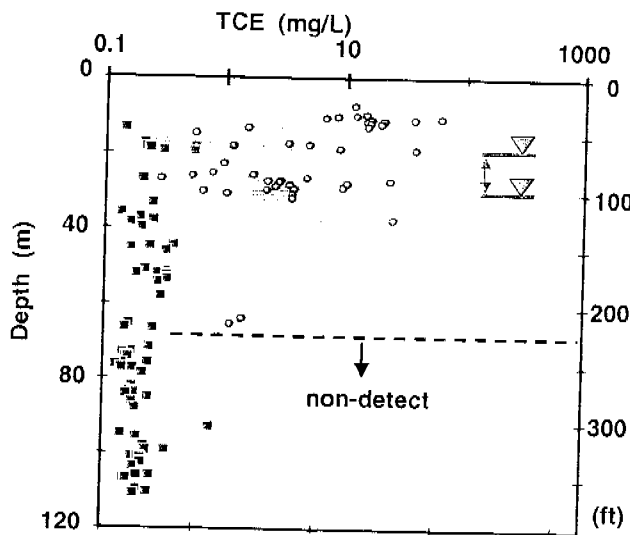
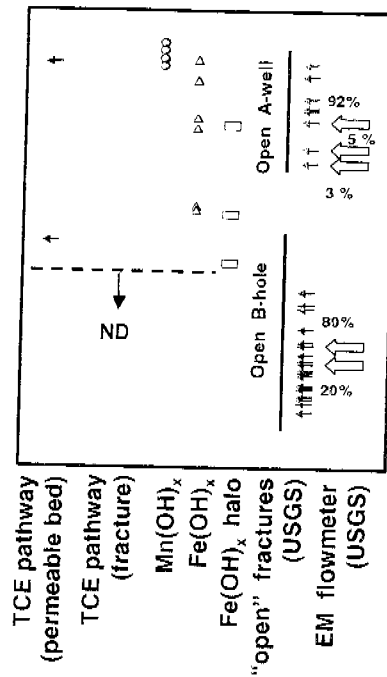
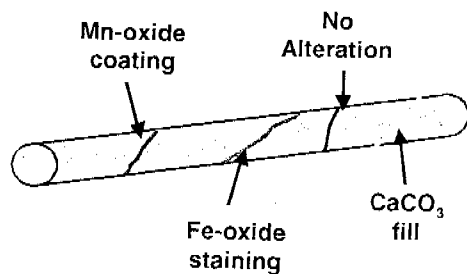


Figure 5-48: Summary of multiple lines of evidence for TCE migration zones and other hydraulically active zones for RD-46A & 46B: Rock core TCE results, core descriptions and borehole geophysics.



Geochemical Alteration of Fractures



Fracture Types

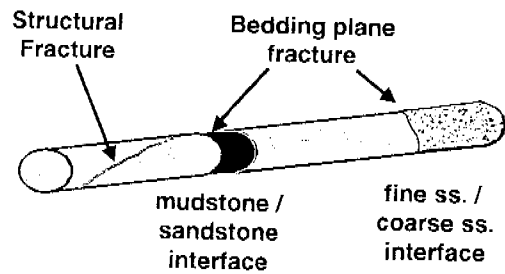


Figure 5-49: Fracture types and characteristics

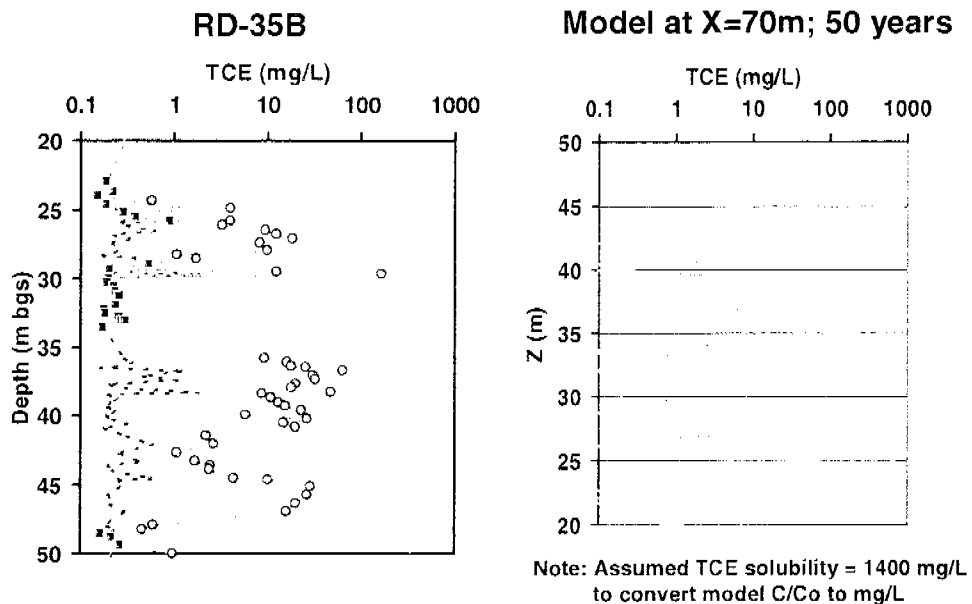


Figure 5-50: Comparison of a simulated field TCE profile for a location 70 m from source after 50 years with the measured profile at RD-35B.

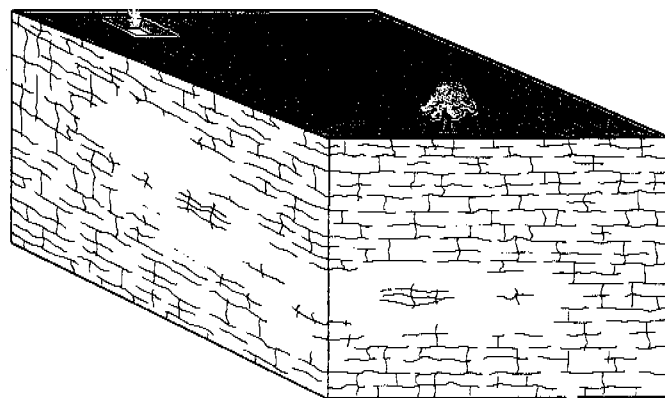


Figure 5-51: Schematic of plume in fractured sandstone

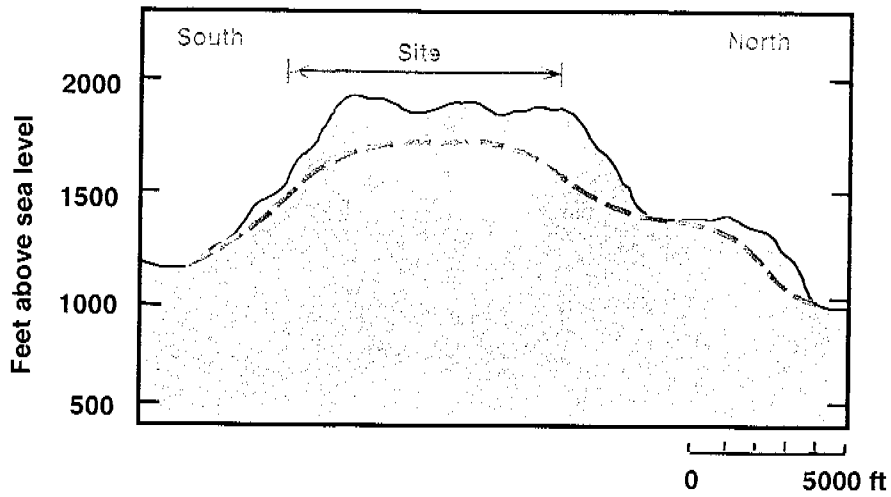


Figure 5-52: Conceptual diagram for SSFL showing small plume expansion due to strong retardation caused by matrix diffusion.

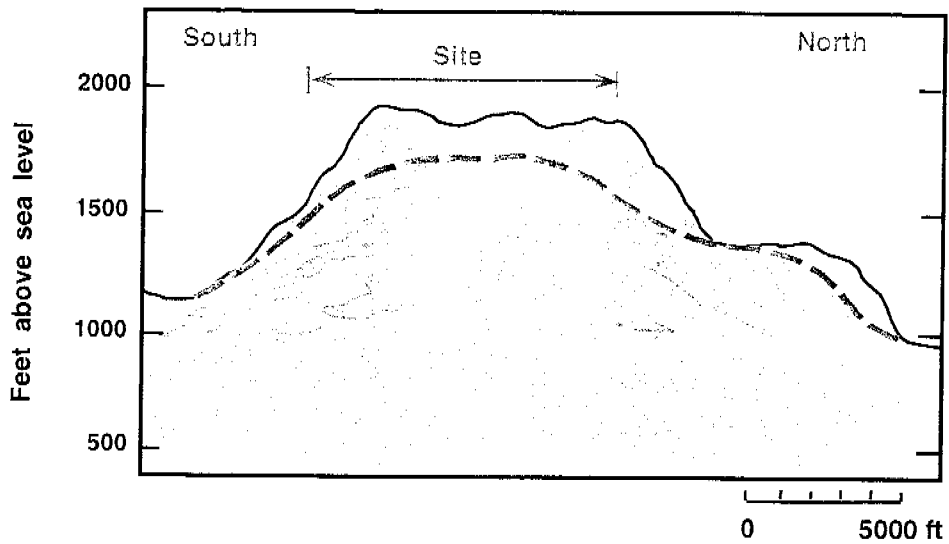


Figure 5-53: Conceptual diagram for SSFL showing extensive plume caused by large groundwater velocity with weak retardation.

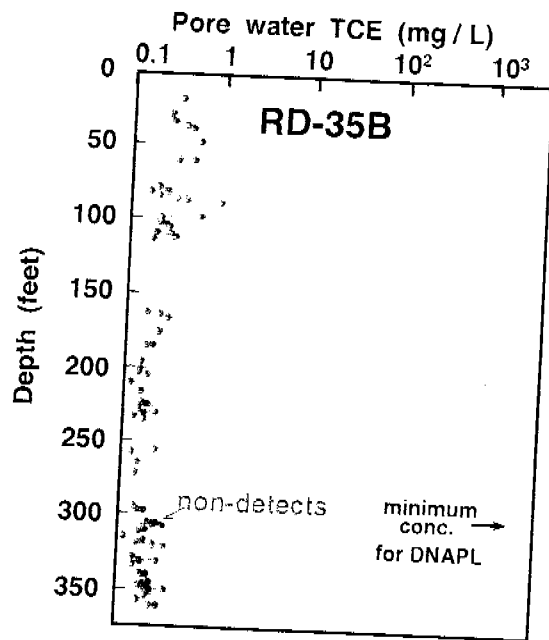


Figure 5-36: Results of core analyses for RD-35B compared to TCE solubility Sterling (1999)

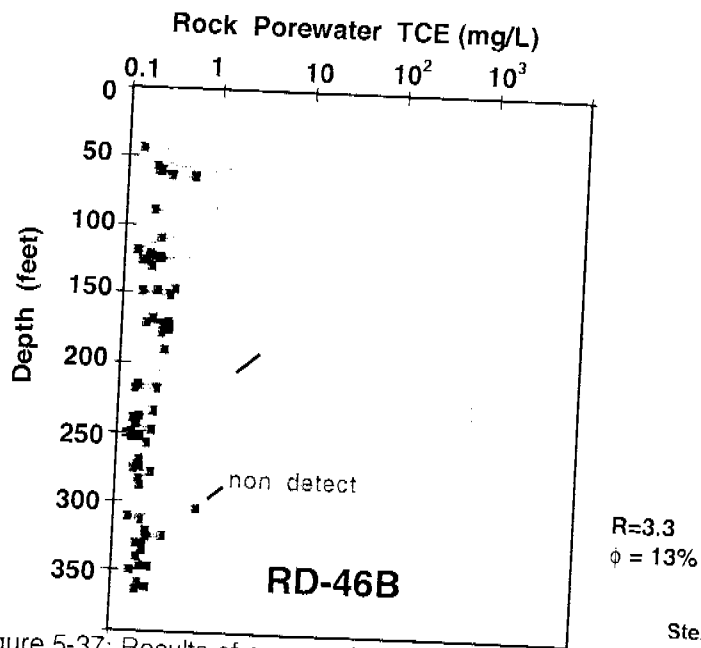


Figure 5-37: Results of core analyses for RD-46B compared to TCE solubility Sterling (1999)

Appendix F

Modeling Simulations of TCE Solute Transport and Fate in the Chatsworth Formation Groundwater

Santa Susana Field Laboratory
Ventura County, CA

April 2000

Prepared by:

Steven W. Chapman, Beth L. Parker and John A. Cherry

Department of Earth Sciences
University of Waterloo
Waterloo, ON Canada N2L 3G1
Tel: (519) 888-4516
Fax: (519) 883-0220

Prepared for:

Boeing North America, Inc.
Rocketdyne Propulsion and Power Division
6633 Canoga Avenue
Canoga Park, CA 91309-7922

TABLE OF CONTENTS

<u>TABLE OF CONTENTS</u>	ii
<u>LIST OF FIGURES</u>	iii
<u>LIST OF TABLES</u>	vii
<u>1.0 INTRODUCTION</u>	1
<u>2.0 NUMERICAL MODELS</u>	2
<u>3.0 MODEL DOMAINS AND PARAMETERS</u>	4
<u>4.0 SINGLE FRACTURE SIMULATIONS</u>	5
<u>5.0 VERTICAL CROSS-SECTION SIMULATIONS</u>	8
5.1 Small Model Domain Simulations.....	8
5.2 Large Model Domain Simulations.....	15
5.3 Comparison of Model Results with Field Data.....	23
<u>6.0 MAJOR OBSERVATIONS AND CONCLUSIONS</u>	25
<u>REFERENCES</u>	27

LIST OF FIGURES

Figure 1. Model domain for the single fracture simulations.

Figure 2. Breakthrough curves at $x=10$ m in the fracture for cases with a constant source and a finite life source of 10 years. Concentrations are plotted using (a) a linear scale, and (b) a log scale to illustrate the tailing effect for the finite source case.

Figure 3. Concentration profiles at $x=10$ m for (a) the base case with no vertical gradient and no matrix sorption, (b) a case with a downward gradient, (c) a case with a downward gradient and matrix sorption included, (d) a case with a finite life source, and (e) a case with a finite life source and a downward gradient.

Figure 4. Comparison of breakthrough curves at $x=10$ m in the fracture for cases with and without vertical flow in the matrix, and a finite life source.

Figure 5. Model domain and fracture network for the smaller vertical cross-section simulations.

Figure 6. Steady state hydraulic head contours for the “base case” smaller vertical cross-section simulation.

Figure 7. Concentration contours for the “base case” smaller vertical cross-section simulation at (a) 5 years, (b) 10 years, (c) 20 years, and (d) 50 years.

Figure 8. Concentration profiles at $x=10$ m, 50 m and 100 m for the “base case” smaller vertical cross-section simulation at 5, 10, 20 and 50 years. The profiles are plotted to a linear concentration scale over a C/C_0 range of 0 to 1 for comparison, and then with a linear scale modified for the range of concentrations observed.

Figure 9. Concentration profiles at $x=10$ m, 50 m and 100 m for the case with matrix sorption included ($R_m=3.0$) at 5, 10, 20 and 50 years.

Figure 10. Concentration profiles at $x=10$ m, 50 m and 100 m for the case with a “stepped” declining source and no matrix sorption at 5, 10, 20 and 50 years.

Figure 11. Concentration profiles at $x=10$ m, 50 m and 100 m for the case with a “stepped” declining source and matrix sorption included ($R_m=3.0$) at 5, 10, 20 and 50 years.

Figure 12. Concentration profiles at $x=10$ m, 50 m and 100 m for the case with a 5 year finite life source and matrix sorption included ($R_m=3.0$) at 5, 10, 20 and 50 years.

Figure 13. Concentration profiles at $x=10$ m, 50 m and 100 m for the case with a residual NAPL source ($S_{nw}=20\%$) and matrix sorption included ($R_m=3.0$) at 5, 10, 20 and 50 years.

Figure 27. Concentration contours ($\log C/C_0$ scale) at (a) 20 years and (b) 50 years for a variable aperture case with a 10 year source life.

Figure 28. Concentration contours ($\log C/C_0$ scale) at (a) 20 years and (b) 50 years for a case with a different realization of variable apertures and a 10 year source life. This simulation is taken as the large model domain "base case".

Figure 29. Concentration contours ($\log C/C_0$ scale) at (a) 20 years and (b) 50 years for a case with a different realization of variable apertures and a 10 year source life.

Figure 30. Breakthrough curves (linear and log concentration scales) for the arrival of the plume front at the model boundary (at $x=200$ m) for the "base case" large vertical cross-section simulation with a 10 year source life.

Figure 31. Concentration profiles at $x=50$ m for the "base case" simulation with variable apertures and a 10 year source at 20 and 50 years, with (a) a linear concentration scale and (b) a log concentration scale.

Figure 32. Concentration profiles at $x=102$ m for the "base case" simulation with variable apertures and a 10 year source at 20 and 50 years, with (a) a linear concentration scale and (b) a log concentration scale.

Figure 33. Concentration profiles at $x=200$ m for the "base case" simulation with variable apertures and a 10 year source at 50 years with (a) a linear concentration scale and (b) a log concentration scale.

Figure 34. Concentration profiles at $x=50$ m for the "base case" simulation with variable apertures and a 10 year source at (a) 20 years and (b) 50 years. Average concentrations, estimated by spatial averaging over the entire profile and over a zone between $z=25$ and 40 m, are also plotted.

Figure 35. Concentration profiles at $x=102$ m for the "base case" simulation with variable apertures and a 10 year source at (a) 20 years and (b) 50 years. Average concentrations, estimated by spatial averaging over the entire profile and over a zone between $z=25$ and 40 m, are also plotted.

Figure 36. Concentration contours ($\log C/C_0$ scale) at (a) 20 years and (b) 50 years for the simulation with variable apertures and a constant source.

Figure 37. Concentration profiles at $x=200$ m for the simulation with variable apertures and a constant source, at 50 years with (a) a linear concentration scale and (b) a log concentration scale.

Figure 38. Concentration contours ($\log C/C_0$ scale) at (a) 20 years, and (b) 50 years for the simulation with variable apertures with a mean of 100 μm , and a 10 year source.

LIST OF TABLES

Table 1. Summary of matrix and fracture properties for the single fracture simulations.

Table 2. Summary of matrix and fracture properties for the “base case” small vertical cross-section model domain simulation.

Table 3. Summary of matrix and fracture properties for the “base case” large vertical cross-section model domain simulation.

Table 4. Bulk hydraulic conductivity for a uniform aperture case (70 microns) and three realizations with random aperture fractures (mean = 70 microns).

1.0 INTRODUCTION

Numerical modeling studies of groundwater flow and solute transport in fractured sandstone systems are ongoing as part of the University of Waterloo research efforts at the SSFL Site. These simulations have been designed to improve our understanding of the influence of various parameters on the mobility of dissolved TCE in fractured sandstone. Phase I of this modeling (Chapman and Parker, 1998) involved sensitivity analyses of various parameters on solute transport in generic fractured sandstone. Many of these simulations were conducted on plan view model domains, although a few vertical cross-section simulations were also performed. Cases with uniform fracture apertures and cases where apertures were varied either on a fracture-by-fracture basis or along individual fractures were investigated. Sandstone matrix properties were assigned that were considered reasonable in the context of what was known about the sandstone at the Santa Susana Field Laboratory (SSFL), and were within the range typically expected for similar sandstones. This conceptual modeling effort was conducted concurrently with two other University of Waterloo projects pertaining to the SSFL site, which involved monitoring with removable multilevel systems and rock core subsampling and analysis for volatile organic concentrations. Results from these projects are described by Cherry et al. (1998) and Sterling and Parker (1999). Cherry et al. (1999) provide an integrated interpretation of the data from the field studies and numerical modeling.

Results from the Phase I numerical modeling exercise showed, in a generic manner, the significance of matrix diffusion in slowing down the transport of dissolved TCE in fractured sandstone systems. Thus the results indicated that the *TCE attenuation conceptual model* is a plausible explanation for the limited extent of plumes observed at the SSFL Site. In this conceptual model, the combined affect of matrix diffusion and sorption within the matrix acts to transfer contaminant mass from the fractures to the porous matrix where the TCE movement is slowed considerably relative to movement in fractures. This diffusive mass transfer causes the maximum TCE concentrations to decline slowly over time and acts to slow the rate of advance of plume fronts relative to the average groundwater velocity in the fracture network. The model also explains the persistence of high TCE concentrations or "hot spots" in source zones that at one time contained DNAPL. In these zones, after the DNAPL has disappeared from the fractures

model can be found in Sudicky and McLaren (1992), and Sudicky and McLaren (1997). For the FRACDNT model, additional information can be found in VanderKwaak and Sudicky (1996). Simulations for Phase II were conducted either on a Pentium II-300MHz PC with 512 MB of RAM, or a Windows NT Workstation with dual Pentium III-500 MHz processors and 1 GB of RAM.

FRACTRAN is a two-dimensional numerical model for the simulation of groundwater flow and contaminant transport in a discretely fractured porous medium. In the model, fractures are represented by line elements, which are superimposed on a rectangular element mesh representing the porous matrix. The program computes both the steady-state groundwater flow solution and the transient evolution of a contaminant plume. Groundwater flow and advective contaminant transport within the porous matrix is rigorously accommodated, which can be important for moderately permeable geologic materials including sandstones. First-order decay of the contaminant and sorption both within the matrix and on fracture walls can also be included. The model utilizes the Laplace Transform Galerkin (LTG) method for solution of the transient solute transport equations. This method allows coarser grid discretization than conventional finite-element methods, without loss of accuracy in capturing the effects of matrix diffusion. The method also provides a solution that is continuous in time, which avoids time stepping when evaluating the transport solution at any future time. With this method large-scale, long-term problems of solute transport in discretely fractured porous media can be handled.

FRACDNT is a two-dimensional groundwater flow and contaminant transport model developed to study dissolution of immobile DNAPL in discrete fracture networks. Concepts for the diffusive disappearance of stationary non-aqueous phase liquids in single fracture and idealized fracture networks are provided in Parker et al. (1994) and Parker et al. (1997). The FRACDNT model allows more complex cases to be investigated with random fracture networks and groundwater flow both within the matrix and along fractures. The model differs from FRACTRAN in that it uses a standard finite element solution with an adaptive time-stepping algorithm, which allows more efficient solution of transient solute transport. FRACDNT permits the simulation of DNAPL dissolution in fractures within a defined "source" zone, and allows the incorporation of

the source is shut off, reverse diffusion continues to slowly release dissolved mass back into the plume from the matrix blocks.

A second series of fracture network simulations were conducted using a larger model domain (50 m x 200 m) to investigate longer-term plume behaviour. Simulation times up to 50 years were used in the simulations presented in this report. For the next phase of modelling (Phase IV), time periods up to 500 years will be considered. Parameters were modified to be more consistent with conditions at the SSFL Site. In particular, matrix porosity was increased from 10 to 13%, and mean apertures were decreased from 100 μm to 70 μm , to provide bulk hydraulic conductivities within the range expected at the SSFL Site for large flow domains. Most of the simulations also used cases where fracture apertures were variable, also to be more consistent with conditions expected in the field.

4.0 SINGLE FRACTURE SIMULATIONS

Single fracture simulations were conducted, using FRACTRAN, to illustrate the nature of TCE profiles close to a source zone for a relatively simple case. Later on, more complex cases involving fracture networks are considered. Comparisons are made between cases with no vertical gradients and cases where vertical gradients exist, as well as cases where the source is constant versus a source with a finite life.

The model domain (Figure 1) is 100 m in the x-direction and 10 m in the z-direction. A single 100 μm fracture is located in the middle of the model domain at $z = 5.0$ m. For the "base case" simulation, constant head boundaries were set at the left and right sides of the domain to provide an average horizontal gradient across the domain of 0.02, with no vertical flow gradient. Table 1 is a summary of the relevant flow and transport parameters used in these simulations. Sorption within the sandstone matrix is not included in the base case simulation ($R_m=1.0$). A constant source with a specified concentration of $C_0=1.0$ is located in the fracture at the left side of the domain. With the 100 μm fracture aperture, and horizontal hydraulic gradient along the fracture of 0.02, the groundwater velocity in the fracture is estimated to be about 5200 m/year (over 3 miles per year).

Therefore flow in the matrix has significantly enhanced mass transfer into the matrix below the fracture, compared to the base case with no vertical flow in the matrix.

For the second variation, sorption in the matrix is included ($R_m=3$) in addition to downward flow in the matrix. With the inclusion of sorption, the rate of solute mass transfer to the matrix is increased, but solute transport within the matrix below the fracture is slowed, so the extent of solute invasion into the matrix is less than the case with no sorption. Figure 3(c) shows concentration profiles at $x = 10$ m. In this case, the solute front below the fracture has migrated about 1.9 m into the matrix after 50 years, significantly lower than the case with no sorption. However, the total mass stored in the matrix is probably greater, due to an increase in the storage capacity of the matrix.

The third variation is similar to the base case, except the source is assumed to have a finite life of 10 years. Plots of solute concentration in the fracture at $x=10$ m are plotted in Figure 2, for comparison to the base case with an infinite source. For this case where the source is shut off after 10 years, concentrations in the fracture decline rapidly as clean water is allowed to enter the fracture at the left boundary after the source is shut off. However, significant tailing is evident due to slow reverse diffusion back out of the matrix blocks. Profiles for this case are plotted in Figure 3(d). Even 40 years after the source is shut off, significant mass remains in the matrix that is being slowly released back into the fracture. Over time, the peak concentration in the matrix decreases as the solute continues to diffuse back towards the fracture, as well as further into the matrix. The slow process of reverse diffusion causes mass to persist in zones where DNAPL once existed for long periods of time. However concentrations in the matrix also decrease over time, along with rates of release of mass back into the fracture.

For the final variation, the source life is 10 years, and a downward gradient of 0.01 is also applied. Figure 3(e) shows profiles for this case. Peak concentrations in the matrix also decrease over time after the source is shut off, similar to the previous case. However with downward flow also occurring, the solute peak also migrates vertically downward further into the matrix. Figure 4 shows a comparison of concentrations over time in the fracture at $x=10$ m for both cases with a 10 year source life, to illustrate the difference in rates of reverse diffusion for cases with and without vertical flow in the matrix. With downward flow in the matrix included, release of solute mass back to the

Parameter	Value
Matrix Hydraulic Conductivity, K_m	10^{-6} cm/sec
Matrix Porosity ϕ_m	10%
Matrix Longitudinal Dispersivity, α_L	0.01 m
Matrix Transverse Dispersivity, α_t	0.01 m
Effective Diffusion Coefficient, D_e	10^{-6} cm ² /sec
Matrix Retardation Factor, R_m	1.0
Fracture Aperture, $2b$	100 μ m
Fracture Dispersivity, α_f	0.2 m
Fracture Retardation Factor, R_f	1.0
Minimum Horizontal Fracture Length	10 m
Maximum Horizontal Fracture Length	20 m
Density of Horizontal Fractures	0.05 fractures/m ²
Minimum Vertical Fracture Length	2 m
Maximum Vertical Fracture Length	5 m
Density of Vertical Fractures	0.075 fractures/m ²

Table 2. Summary of matrix and fracture properties for the “base case” small vertical cross-section model domain simulation.

Constant head boundaries were assigned on all four sides of the model domain, to establish an average horizontal gradient of 2% and average downward vertical gradient of 1%. Horizontal fractures range in length from 10 to 20 m, with an average vertical spacing of about 1.8 m, and a minimum spacing between horizontal fractures of 0.5 m. Vertical fractures range in length from 2 to 5 m, with an average horizontal spacing of about 5.0 m and a minimum spacing of 1.5 m. The bulk hydraulic conductivity of this fracture network was estimated, in both the horizontal and vertical directions, using Darcy’s Law:

$$K_{bx} = \frac{Q_x}{i_x A_x} \qquad K_{bz} = \frac{Q_z}{i_z A_z}$$

In these equations, Q_x and Q_z are the average horizontal and vertical flow through the model domain in the horizontal and vertical directions, respectively. These are estimated by averaging the inflow and outflow at the top and bottom of the model domain for Q_z ,

only about 13 days. With a constant source and no sorption in the matrix, this “base case” is expected to represent an unrealistic case with very rapid advance of the plume front. This will be compared later to cases where matrix sorption is included, and the source is not constant.

Figure 8 shows plots of profiles at $x=10$ m (close to the source), $x=50$ m (midway across the model domain), and $x=100$ m (end of the model domain) at time periods of 5, 10, 20, and 50 years. The profiles are plotted on a linear concentration scale with a C/C_0 range of 0 to 1, which allows easier comparison of concentrations. Below each of these plots, the concentration scale is modified for each location, to better show the nature of the profiles. Even with no sorption in the matrix and a constant source, it is evident that plume attenuation is occurring with distance from the source due to the decline in concentration with distance from the source. The maximum relative concentration at 50 years, at the end of the model domain, is nearly $C/C_0=0.30$. With a constant source, concentrations downgradient will continue to increase over time. The profiles also indicate that significant transfer of mass is occurring from fractures into the matrix blocks.

Several variations of the “base case” scenario were simulated. These simulations are briefly summarized below:

- (a) Sorption in the matrix included ($R_m=3.0$).
- (b) Declining source with an assumed “stepped” function; no matrix sorption.
- (c) Declining source with an assumed “stepped” function; sorption included ($R_m=3.0$).
- (d) Source that is constant for 5 years and then shut off; sorption included ($R_m=3.0$).
- (e) Stationary residual DNAPL source (20% initial saturation in fractures).
- (f) Variable aperture case; no matrix sorption
- (g) Matrix hydraulic conductivity decreased by 1 O.M.; no matrix sorption

Figures 9 through 13 show profiles at $x=10$ m, 50 m, and 100 m at time periods of 5, 10, 20, and 50 years for cases (a) through (e), respectively. In each of these figures, the profiles are plotted on a linear concentration scale with a C/C_0 range of 0 to 1, which allows easier comparison of profiles between each case, and with the concentration scale

$x=100$ m at 50 years is only about 0.01, and concentrations at this location are declining, with the highest concentration of about 0.015 occurring at around 10 years. However, even with the source shut off after 5 years, high concentrations persist near the former source area, due to slow reverse diffusion from the matrix blocks. At 50 years, peak concentrations 10 m downgradient of the source are still almost 10% of the initial source concentration.

For case (e), with a residual DNAPL source located within several fractures near the upgradient boundary, the plume is even more attenuated compared to case (d) where the source was constant for 5 years. The maximum relative concentration at the exit boundary at $x=100$ m was less than 0.004, occurring at around 10 years. In this case, complete DNAPL disappearance occurred in about 1.5 years, with 90% of the DNAPL depleted in about 0.8 years. Rapid DNAPL disappearance occurs in this case due to both dissolution of the DNAPL in groundwater flowing in the fractures and matrix diffusion.

Estimates of the time for complete DNAPL disappearance from a 100 μm fracture were performed using methods described in Parker et al. (1994). A plot of fracture aperture versus time for complete TCE DNAPL disappearance is presented in Figure 15. These estimates indicate that complete disappearance from a 100 μm fracture will occur in about 20 years, assuming a matrix retardation factor of 3.0. In fracture networks with groundwater flow included, DNAPL disappearance is expected to occur even more rapidly. The above estimate is based on diffusion only, and therefore neglects DNAPL dissolution in groundwater flowing through the fractures, which is expected to significantly decrease times for DNAPL disappearance. Estimates also assume the fracture is initially fully saturated with DNAPL, although in field cases DNAPL saturation in a fracture is probably much lower.

Based on estimates of times for DNAPL disappearance based on diffusion only, and results from the simulation with an initial NAPL source, a source with a finite life in the range of 5 to 10 years may be a reasonable source condition for a single DNAPL release. However, if intermittent releases occurred over a longer time period, the use of a "stepped" source condition may be more appropriate. Such a source condition was not investigated in these larger scale simulations, but may be considered in future

so significant solute transport does not occur along this pathway. This also influences flow to the middle fracture, where the gradient above this fracture is now towards the fracture so upwards diffusion from this fracture is opposed by groundwater flow. This illustrates the variability in local flow conditions, as a result of variability in fracture apertures. For case (g), where the matrix hydraulic conductivity is one order of magnitude lower than the base case, flow velocities in the matrix are low compared to rates of diffusion, so the profiles appear to be mainly diffusion controlled. Finally, for case (h), with a finite source life of 10 years, reverse diffusion is evident at 20 and 50 years, with declining peak concentrations in the matrix at these time periods.

A major assumption inherent in all of these model simulations is that of a steady state flow system. Temporal variations in the flow field at real sites, due to seasonal and annual variations in groundwater recharge, would further influence the style of head and concentration profiles.

5.2 Large Model Domain Simulations

Simulations with a larger model domain (50 m by 200 m) were conducted. These simulations were conducted using a Windows NT workstation with dual PIII-500 MHz Processors and 1GB of RAM. This system allows the simulations to be conducted efficiently with adequate grid discretization, given the larger model domain used.

Parameters were modified for these simulations to be more consistent with those expected at the SSFL Site. These parameters include the matrix porosity, average fracture apertures, and the use of a finite-life source condition. The matrix porosity is now assumed to be 13%, instead of 10% typically assumed for simulations performed in the Phase I modeling study and the earlier Phase II simulations. This value for matrix porosity is consistent with the average sandstone value based on measurements on core samples taken from the SSFL Site (Sterling, 1999). The higher porosity acts to increase plume attenuation by enhancing the rate of diffusive flux into the matrix (according to Fick's First Law, diffusive flux is proportional to matrix porosity) and increasing the matrix storage capacity.

Fracture apertures are now assumed to have a mean aperture of 70 μm , instead of the previous assumption of 100 μm . With this new aperture size and fracture spacing

Figure 17 shows the model domain and fracture network for the “base case” simulation. As described later, the base case simulation was selected from three simulations performed with different realizations of random fracture apertures. The model domain is 200 m in the x-direction (horizontal) and 50 m in the z-direction (vertical). Constant head boundaries are set along all four sides of the domain, to establish an average horizontal gradient of 2% and an average downward vertical gradient of 1%. The source is located along the upgradient boundary at $x=0$ m, between $z=35$ and 45 m. The source is assumed to be constant at $C_0=1.0$ for 10 years, at which point the source is shut off and clean water is allowed to enter the fractures along the former source boundary. Conceptually, this is equivalent to having DNAPL in these fractures for a period of 10 years, with solubility levels of TCE occurring in groundwater leaving the source during this time period. After 10 years, the source is shut off, which is equivalent to assuming that the DNAPL has completely disappeared, thus allowing reverse diffusion to occur back out of the matrix blocks. Therefore, mass stored in the matrix near the source is then slowly released to the groundwater by this reverse diffusion process. Once the source is shut off, the concentrations in the fractures in the source area gradually decline even though reverse diffusion occurs. Table 3 is a summary of the relevant flow and transport parameters used for the “base case” simulation.

of about 1.7 m. Histograms of fracture lengths (vertical and horizontal fractures separately) are plotted in Figure 19. In the FRACTRAN model, fracture lengths are generated randomly between specified upper and lower limits, according to a uniform probability density function. The fracture network used for these simulations is the same except for the variation in fracture apertures. Using Darcy's Law, as described previously, bulk hydraulic conductivities were estimated for each of these generated fracture networks. The bulk hydraulic conductivity was also estimated for the uniform aperture case for comparison. These estimates are summarized in Table 4.

Apertures	K_{bx} (cm/sec)	K_{bz} (cm/sec)	Anisotropy Ratio (K_{bx}/K_{bz})
Uniform	1.3×10^{-5}	3.5×10^{-6}	3.7
Variable	1.6×10^{-5}	4.2×10^{-6}	3.8
Variable	1.5×10^{-5}	3.0×10^{-6}	5.0
Variable	1.8×10^{-5}	4.5×10^{-6}	4.0

Table 4. Bulk hydraulic conductivity for a uniform aperture case (70 microns) and three realizations with random aperture fractures (mean = 70 microns).

Contour plots showing hydraulic heads for the uniform aperture case, and the three variable aperture cases, are shown in Figures 20 through 23, respectively. Hydraulic head profiles at two distances from the source ($x=90m$ and $x=102m$) are shown for the base case in Figure 24. These plots illustrate the variable nature of head profiles, even over the relatively short distance between the profile locations. As indicated in the profiles, both upward and downward flow is occurring in different zones, even though the average gradient is downward. Locally within the model domain, hydraulic gradients can be much larger than the average gradients of 2% horizontal and 1% vertical. At some locations near where fractures "dead end", localized gradients can exceed 20%. Such large gradients may have an influence on DNAPL flow in the source zone early on, when the DNAPL is in the flow stage. Figure 25 is a comparison of head profiles at $x=102m$ for the uniform aperture case and the variable aperture base case. The difference in these plots, with the same fracture locations, illustrates that the aperture distribution also influences the hydraulic head distribution.

boundary. Such estimates will be conducted in the Phase IV modeling effort, where simulations are conducted to time periods of 500 years. Average concentrations were calculated for the entire 50 m vertical interval, and then for a 15 m interval (between $z=25$ and 40 m) near the core of the plume where concentrations are relatively high. Figure 34 shows the concentration profiles at $x=50$ m at 20 years and 50 years, along with the estimated average concentrations. Similarly, profiles at $x=102$ m are plotted in Figure 35. Estimated average concentrations for profiles at $x=200$ m at 50 years are not plotted, as the average concentrations are lower than the range of concentrations shown in Figure 33. As shown in the plots, average concentrations are typically several times lower than peak concentrations, particularly when the concentrations are averaged over a greater depth interval. This is important when trying to relate model results to data collected in the field, particularly concentration data collected using standard monitoring wells, where long screened intervals are common (typically >50 ft at the SSFL Site). The model provides "exact" concentrations at individual nodes in the domain, whereas averaged concentrations may be significantly lower than the peak concentrations.

Several variations of the "base case" simulation were performed. These include a simulation with a constant source and simulations with a greater mean aperture of 100 μm and 200 μm . Also performed were a simulation with greater aperture variability and a final simulation where horizontal and vertical gradients were reduced by a factor of 2.

Plots of solute concentration at 20 and 50 years for the case with a constant source are shown in Figure 36. Concentration profiles at the boundary at $x=200$ m at 50 years are plotted in Figure 37 (linear and log concentration scales). These can be compared to the base case concentration profiles in Figure 33, where the source life was 10 years. At 50 years, the maximum relative concentration along this boundary is 6.1×10^{-5} , compared to 3.7×10^{-5} for the base case with a 10 year source. When the source is constant, concentrations at the downgradient boundary are expected to continue to increase over time, while for cases when the source has a finite life, concentrations are expected to reach a plateau and then gradually decline over time. This will be explored in more detail in the Phase IV modeling study on long-term plume attenuation, where these simulations will be conducted to a time period of 500 years.

due to higher velocity pathways along larger aperture fractures. However the plumes are similar to the base case. At 50 years, the maximum concentration at $x=200$ m is about 1.2×10^{-4} , about a factor of 3 higher than the base case.

For a final case, horizontal and vertical hydraulic gradients were reduced by a factor of 2 compared to the base case, so the average horizontal gradient is 1% and the average downward vertical gradient is 0.5%. Figure 42 is a plot of solute concentrations at 20 and 50 years. Under these lower gradient conditions, plume transport is slowed significantly compared to the base case. The relative importance of matrix diffusion is increased relative to advection in the fractures. By 50 years the plume front has only migrated to about 135 m from the source. Lower average gradients in this range may be more representative of conditions at the SSFL Site. Long-term plume behavior for this case will also be investigate in the Phase IV modeling study.

5.3 Comparison of Model Results with Field Data

Detailed data on the TCE concentration distribution in the fractured rock matrix at the SSFL Site were obtained by the University of Waterloo at RD-35B and RD-46B (Sterling and Parker, 1999). The style of the concentration distribution at these locations is consistent with the style of model generated concentration distributions. As an example, a plot of rock porewater TCE concentration at RD-35B is shown in Figure 43. The profile covers a total depth interval of 120 m. Figure 44 shows a blowup of the profile from 20 to 50 m bgs. For comparison to the data at this location, a profile of model concentrations from the "base case" large vertical cross-section simulation at $x = 70$ m, at a time period of 50 years, is plotted next to the field profile. The model simulation had an assumed source life of 10 years. Model concentrations were converted from relative values (assumed $C_0=1.0$) to TCE concentrations, assuming the source concentration was at TCE solubility (~ 1400 mg/L). No effort was made in the design of the model simulations to try and match the field data. However, the field and model profiles have similar shapes and peak concentrations. Both profiles show zones where significant mass occurs in the sandstone matrix, and gaps in the matrix where TCE concentrations are below detection limits. Such comparisons provide more confidence in

6.0 MAJOR OBSERVATIONS AND CONCLUSIONS

Numerical modeling studies have been conducted as part of the UW research efforts at the SSFL Site. Phase I of this work (Chapman et al., 1998) focused on investigating the influence of matrix diffusion on the mobility of dissolved TCE in fractured sandstone, and parameter sensitivity analyses. This first phase showed the strong influence of matrix diffusion on slowing down the transport of dissolved TCE, and therefore indicated that the *TCE Attenuation Conceptual Model*, is a plausible explanation for the limited extent of plumes observed at the SSFL Site.

In the second and third phases of modeling, simulations were tailored more closely to SSFL conditions to provide more insight into the processes controlling the nature or style of TCE profiles in the rock matrix. These included the influence of hydraulic head patterns and flow in the matrix, along with source conditions. Results of the simulations showed that in sandstone with relatively low matrix permeability, flow velocities in the matrix may be appreciable compared to rates of diffusion, and therefore influence the style of concentration profiles. The concentration history in the fracture, dependent on factors such as distance from the source, hydraulic head distribution, fracture connectivity and aperture distribution and source history, also influences the nature of matrix profiles.

Results from these simulations also show the strong influence of source conditions on the attenuation of plumes. When sources are not continuous but have a finite life, plumes are more attenuated downgradient. Finite life sources are consistent with expectations of DNAPL disappearance due to the combined effects of matrix diffusion and dissolution in groundwater flowing in fractures. However, long-term release of dissolved TCE from such sources is expected, and observed in the modeling simulations, due to slow reverse diffusion. At the SSFL site, the former source areas are observed to persist as "hotspots", consistent with DNAPL disappearance and slow reverse diffusion.

Comparison between the nature of the profiles collected at the SSFL Site at RD-35B and RD-46B, with profiles from model simulations, indicated the similar nature of field and model profiles. Such comparisons provide more confidence in the applicability

REFERENCES

Chapman, S.W. and B.L. Parker. Sensitivity analysis of solute transport in fractured sandstone using discrete fracture mathematical models. Unpublished Report, September 25, 1998, Department of Earth Sciences, University of Waterloo, Waterloo, ON.

Cherry, J.A., B.L. Parker and S.N. Sterling. Design and use of removeable multilevel devices in boreholes RD-35B and RD-46B at the Santa Susana Field Laboratory, Ventura County, California. Unpublished Report, September 18, 1998, Department of Earth Sciences, University of Waterloo, Waterloo, ON.

Parker, B.L., R.W. Gillham and J.A. Cherry. 1994. Diffusive disappearance of immiscible phase organic liquids in fractured porous geologic media. *Groundwater*, 32(5): 805-820.

Parker, B.L., D.B. McWhorter and J.A. Cherry. 1997. Diffusive loss of non-aqueous phase organic solvents from idealized fracture networks in geologic media. *Groundwater*, 35(6): 1077-1088.

Sterling, S.N. 1999. Comparison of discrete depth sampling using rock core and multilevel wells in a TCE contaminated fractured sandstone. M.Sc. Thesis, Department of Earth Sciences, University of Waterloo, Waterloo, Ontario, Canada.

Sterling, S.N. and B.L. Parker. Rock core sampling and analysis for volatile organic concentrations and hydraulic parameters in boreholes RD-35B and RD-46B at the Santa Susana Field Laboratory, Ventura County, California. Unpublished Report, February 2, 1999, Department of Earth Sciences, University of Waterloo, Waterloo, ON.

Sudicky, E.A. and R.G. McLaren, 1992. The Laplace Transform Galerkin Technique for large-scale simulation of mass transport in discretely fractured porous formations. *Water Resources Research*, 28(2): 499-514.

Sudicky, E.A. and R.G. McLaren. 1997. FRACTRAN 5.01: User's Guide. An efficient simulator for two-dimensional, saturated groundwater flow and solute transport in porous or discretely-fractured porous formations. Groundwater Simulations Group, University of Waterloo, Waterloo, ON.

Therrien, R., and E.A. Sudicky. 1996. Three-dimensional analysis of variably saturated flow and solute transport in discretely-fractured porous media. *Journal of Contaminant Hydrology* 23: 1-44.

VanderKwaak, J.E. and E.A. Sudicky, 1996. Dissolution of non-aqueous phase liquids and aqueous-phase contaminant transport in discretely-fractured porous media. *Journal of Contaminant Hydrogeology*, 23: 45-68.

FIGURES

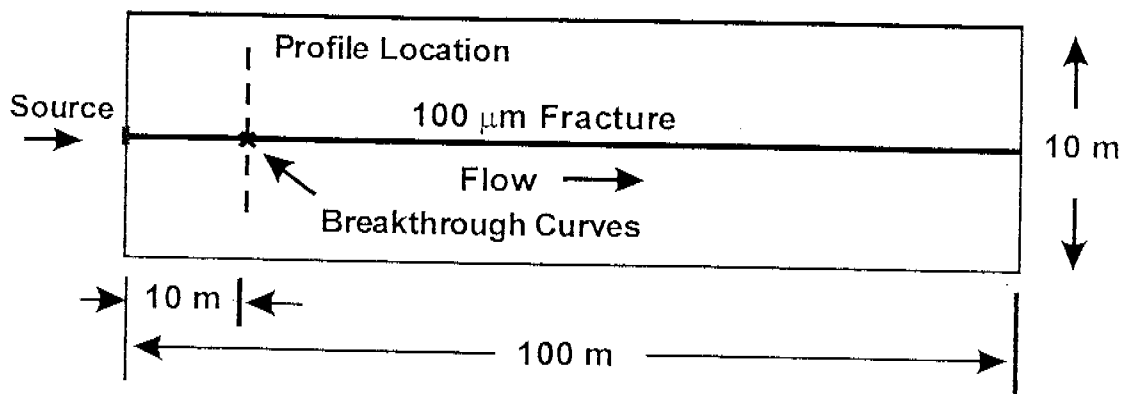
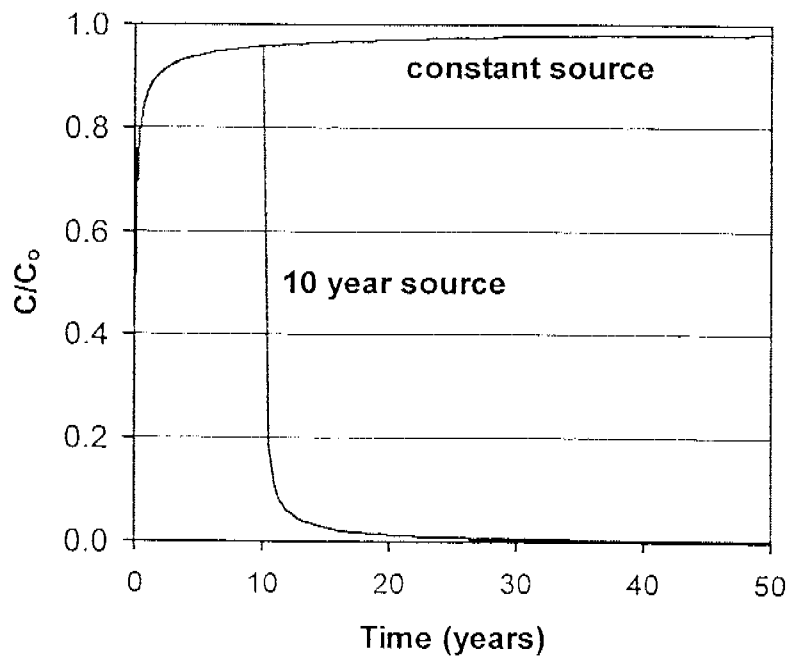


Figure 1

(a)



(b)

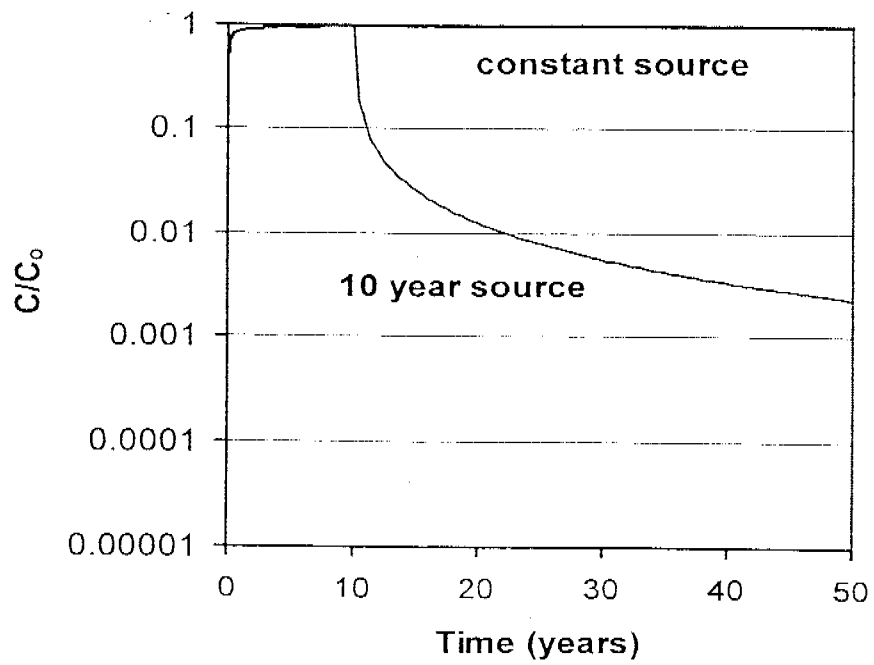


Figure 2

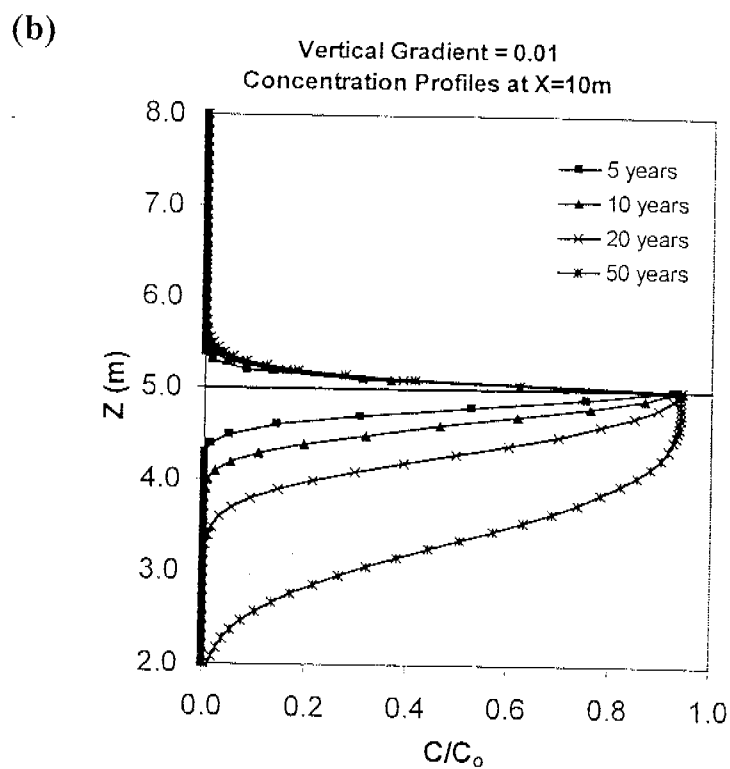
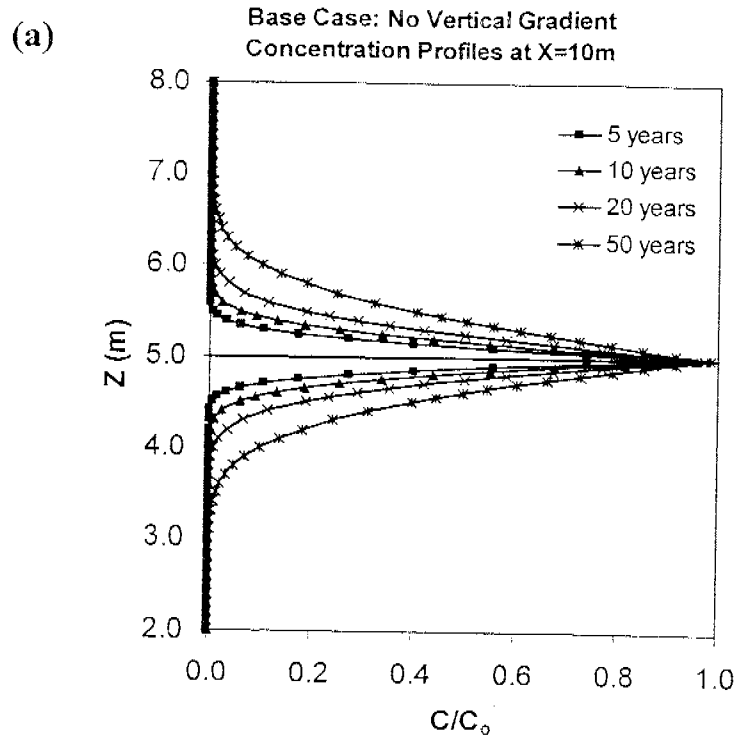


Figure 3

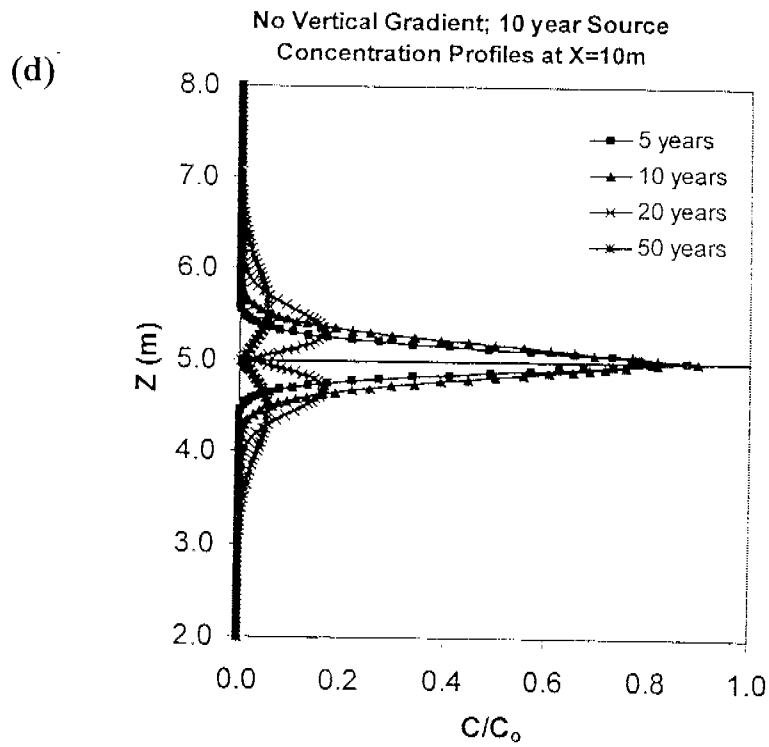
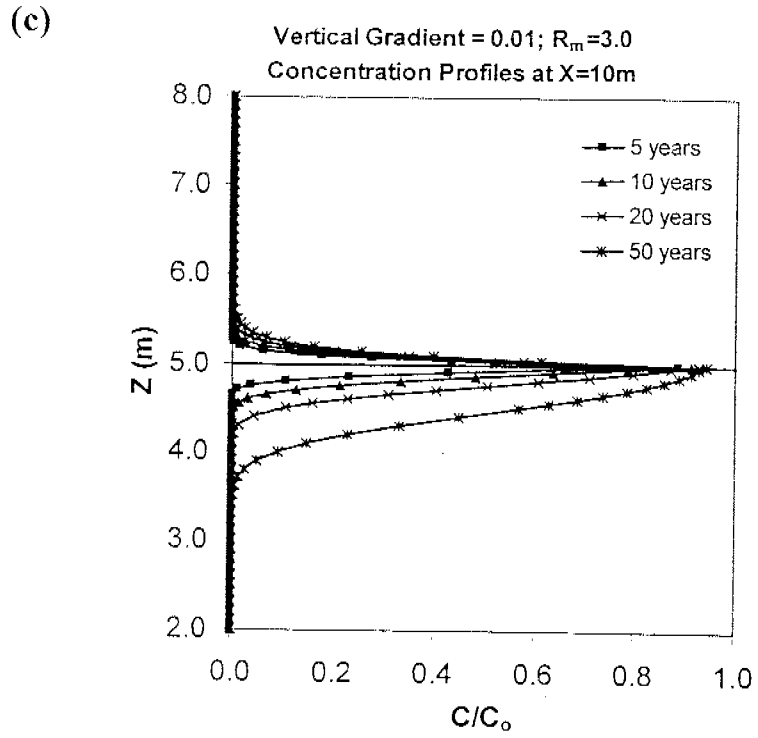


Figure 3 (cont'd)

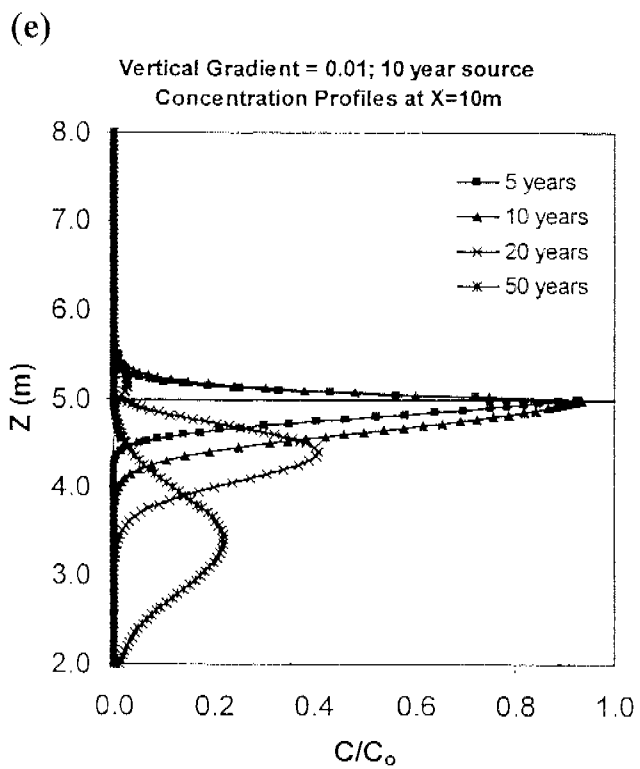


Figure 3 (cont'd)

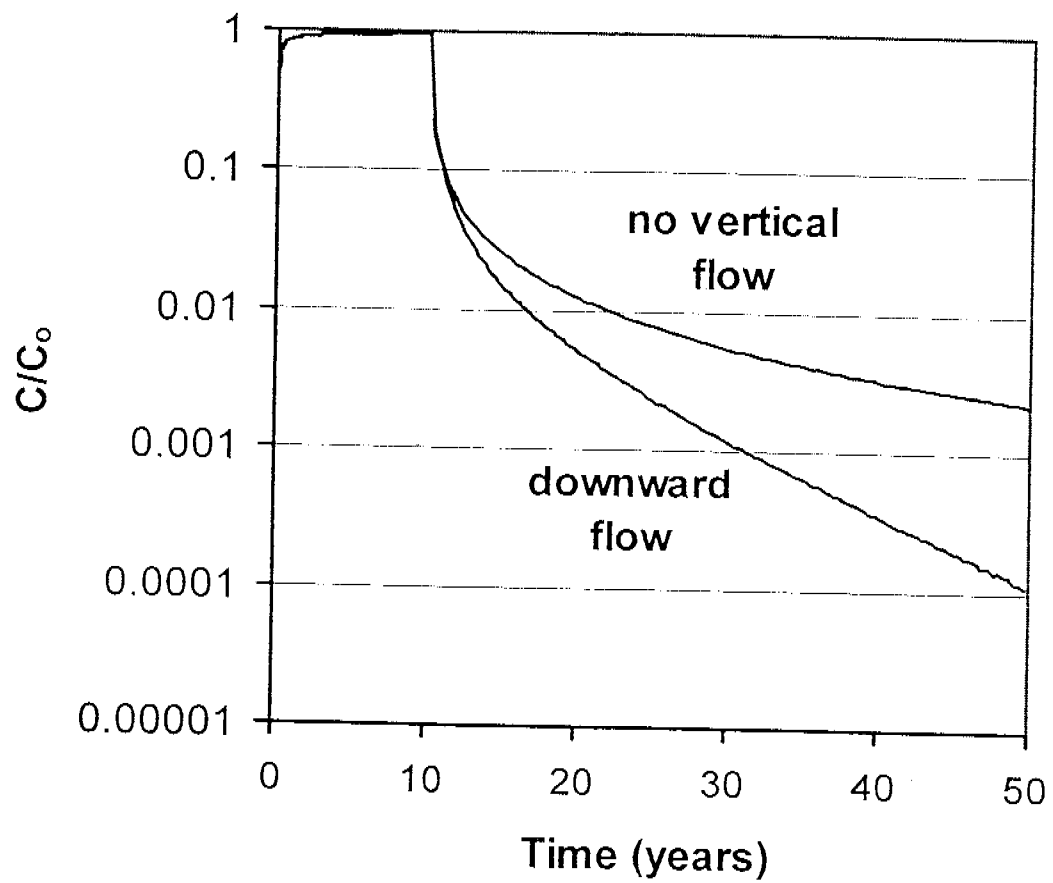


Figure 4

Vertical Cross-Section Model Domain

DNAPL Source Zone
(FRACDNT Simulation)

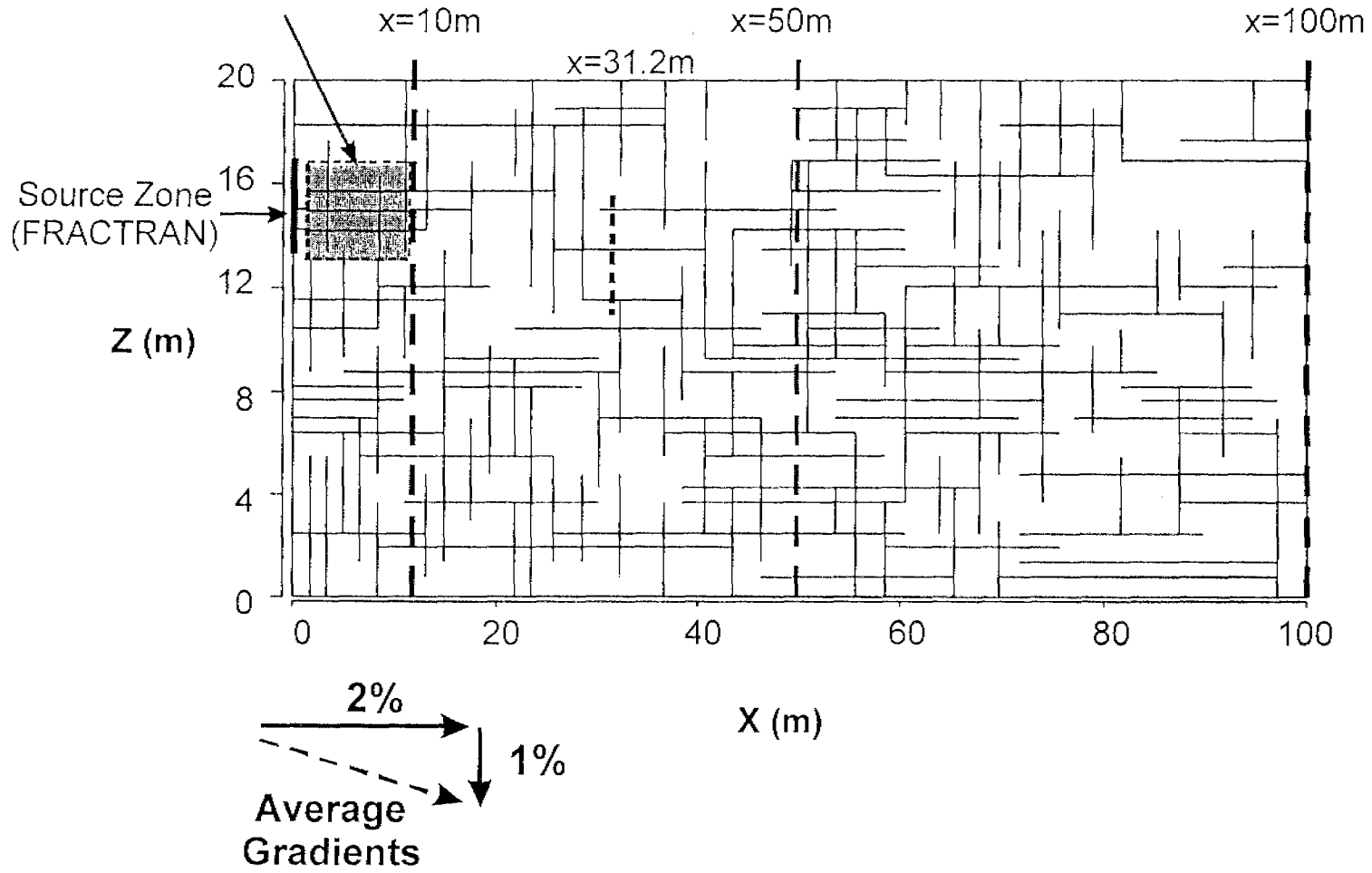


Figure 5

Function: Hydraulic Head
Set : Heads at steady-state
Data set: vert10

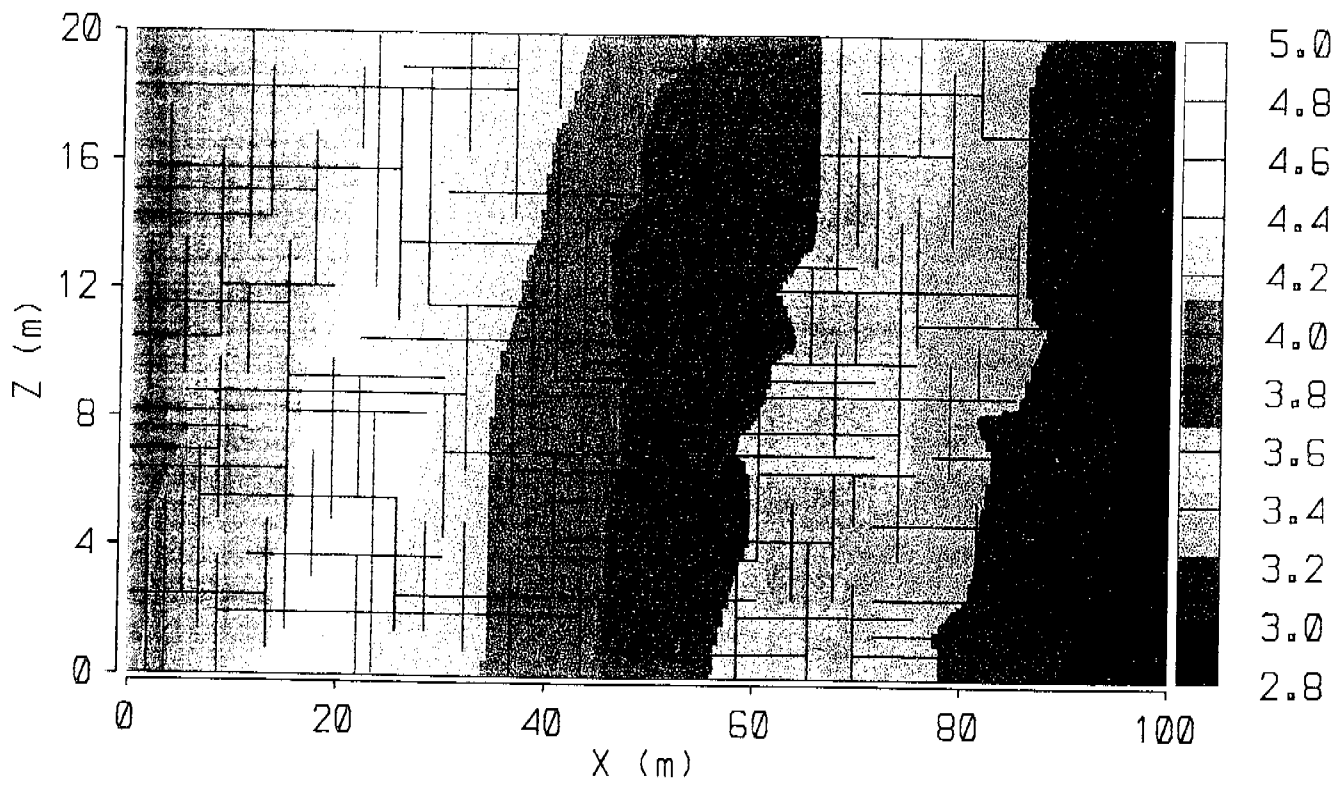
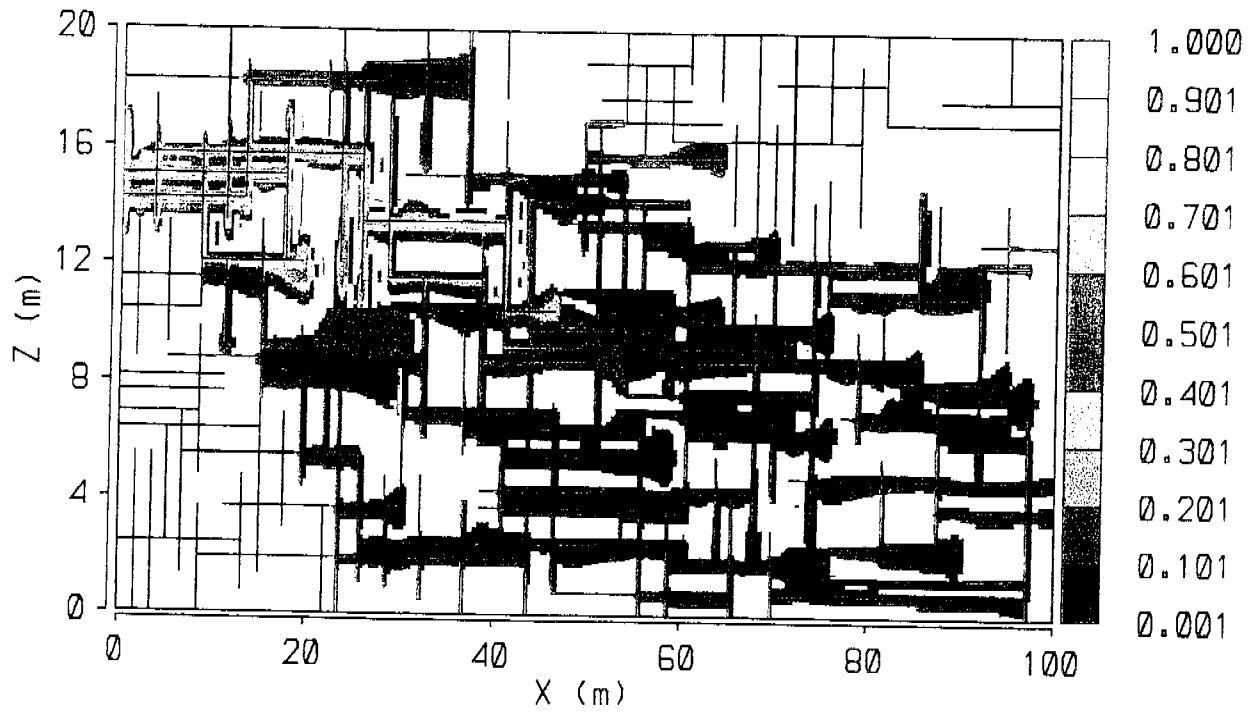


Figure 6

(a)

Function: Concentration
Set : Concentration at 5.0
Data set: vert10



(b)

Function: Concentration
Set : Concentration at 10.0
Data set: vert10

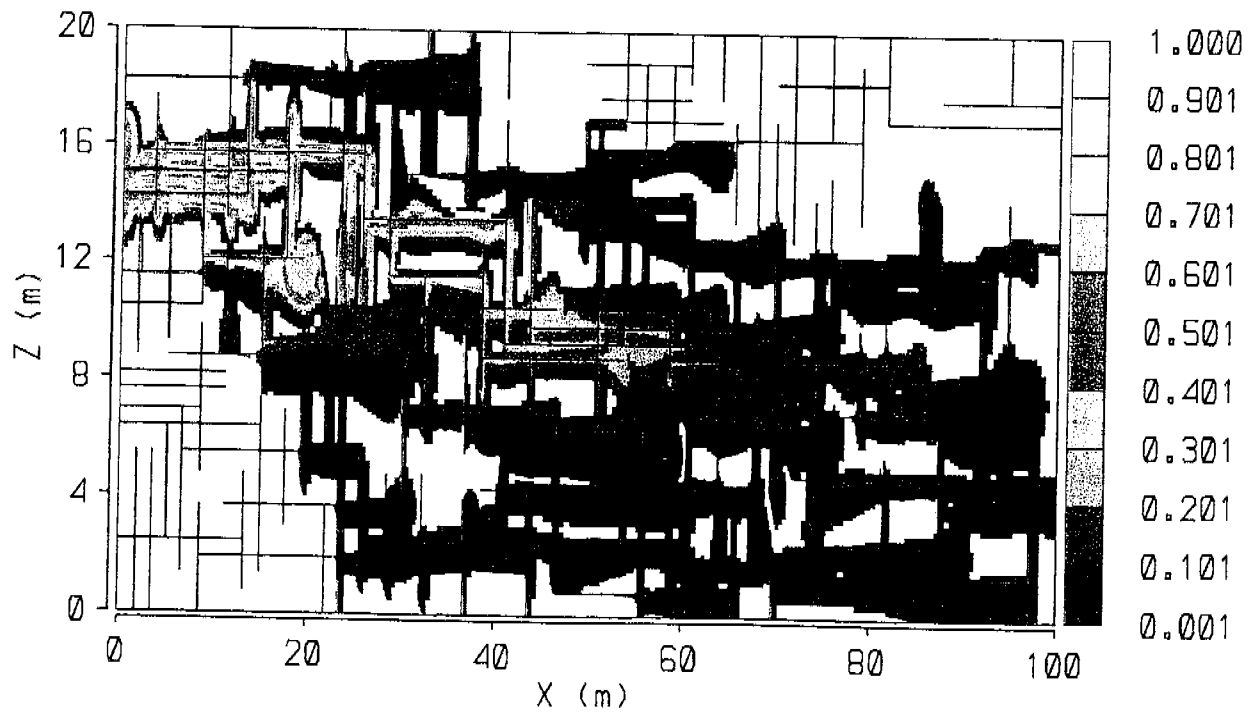
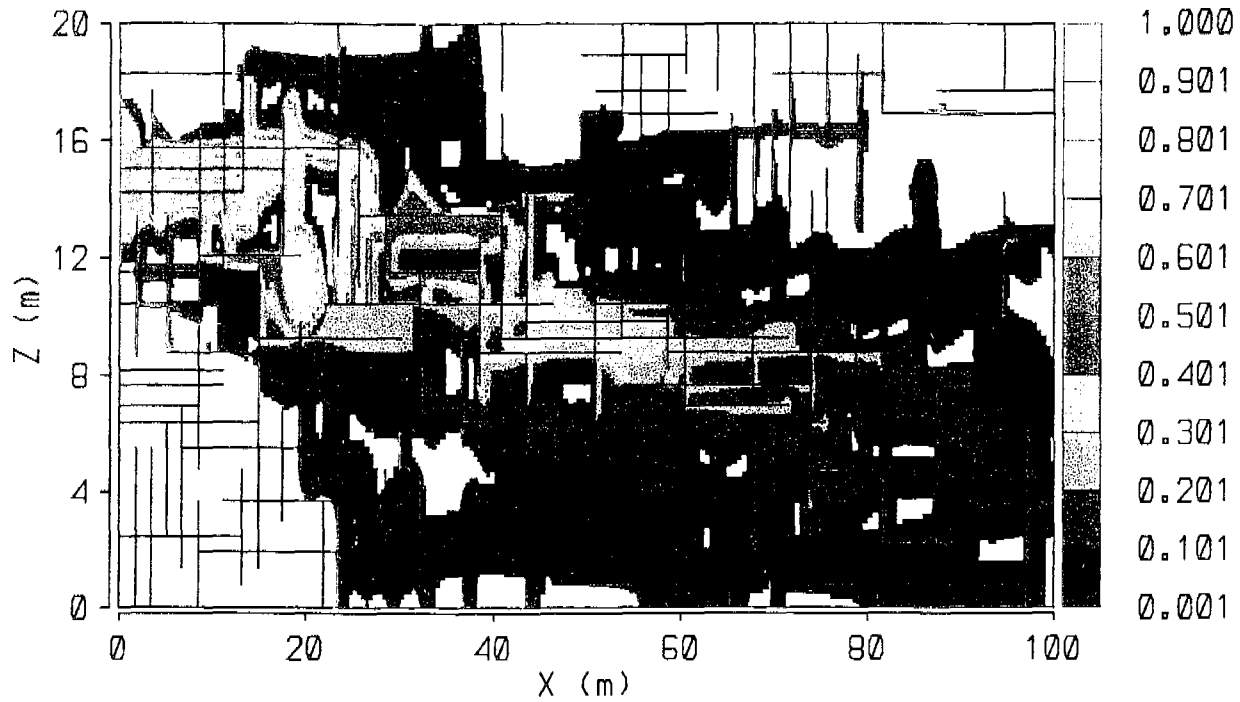


Figure 7

(c)

Function: Concentration
Set : Concentration at 20.0
Data set: vert10



(d)

Function: Concentration
Set : Concentration at 50.0
Data set: vert10

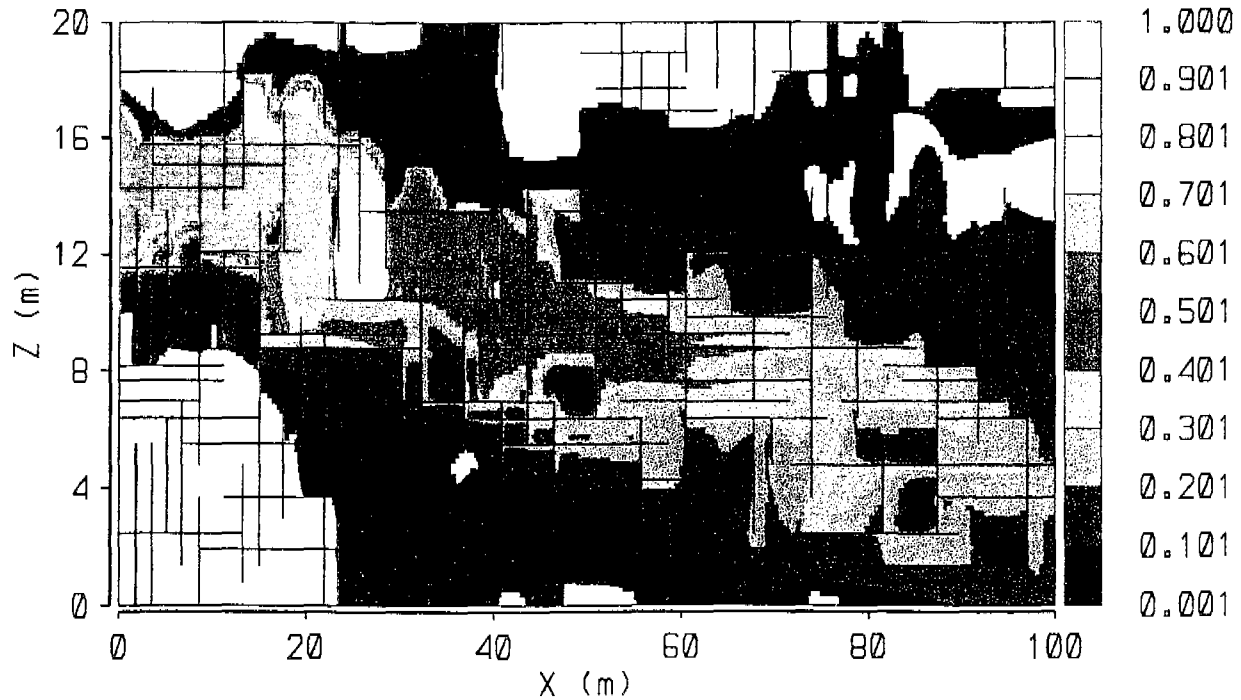


Figure 7 (cont'd)

“Base Case”: Constant Source, No Matrix Sorption

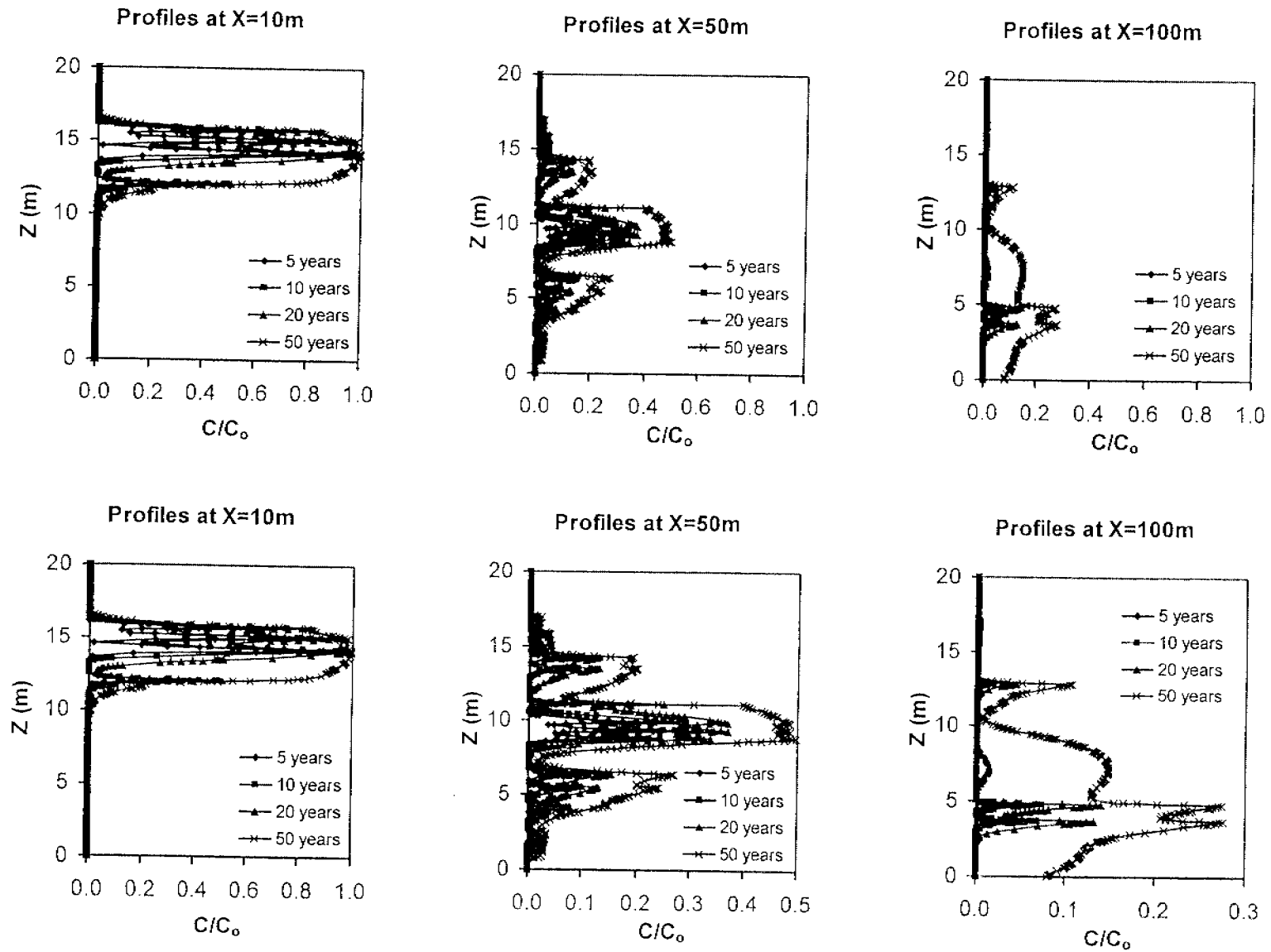


Figure 8

Case (a): Matrix Sorption Included

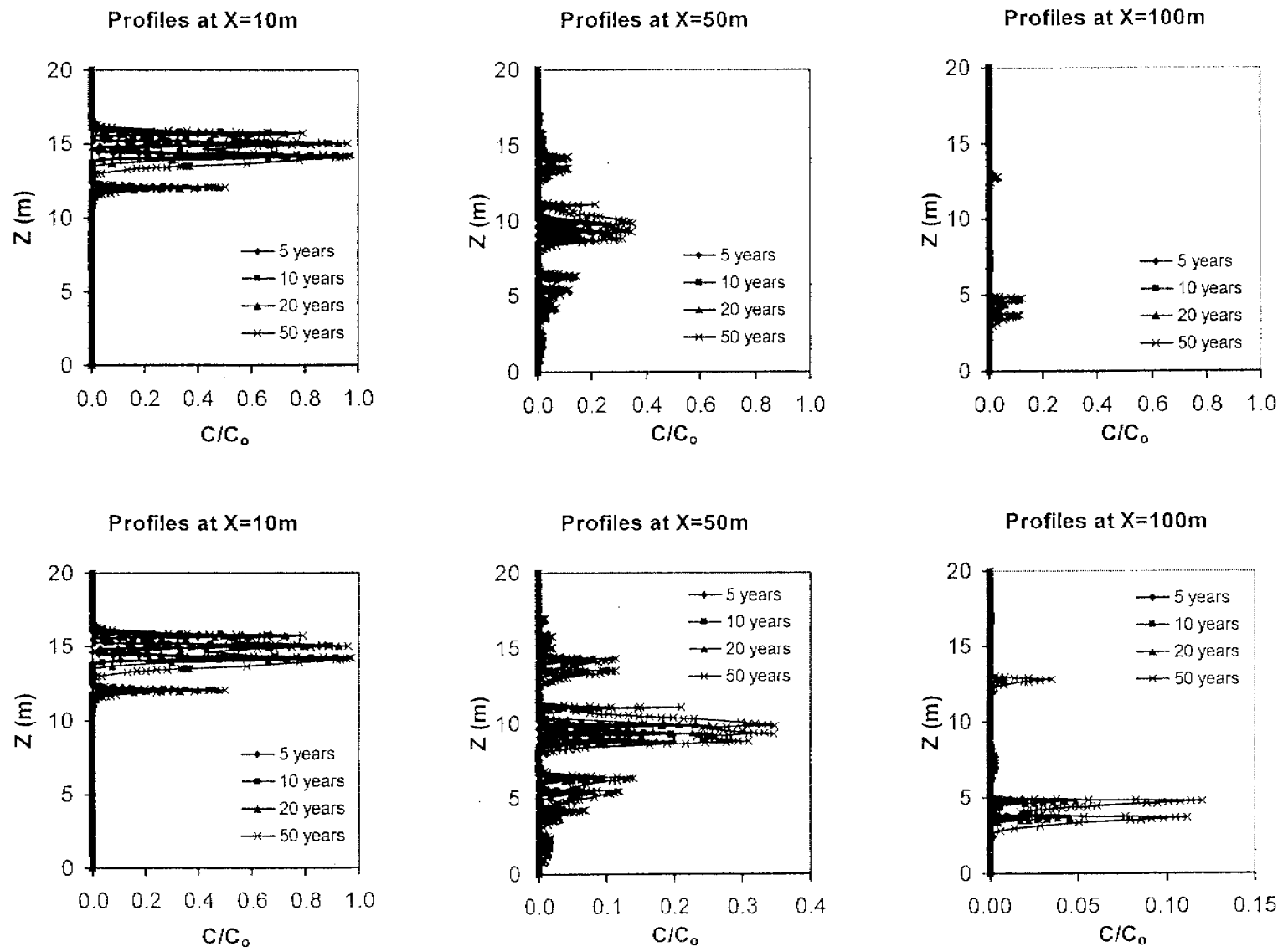
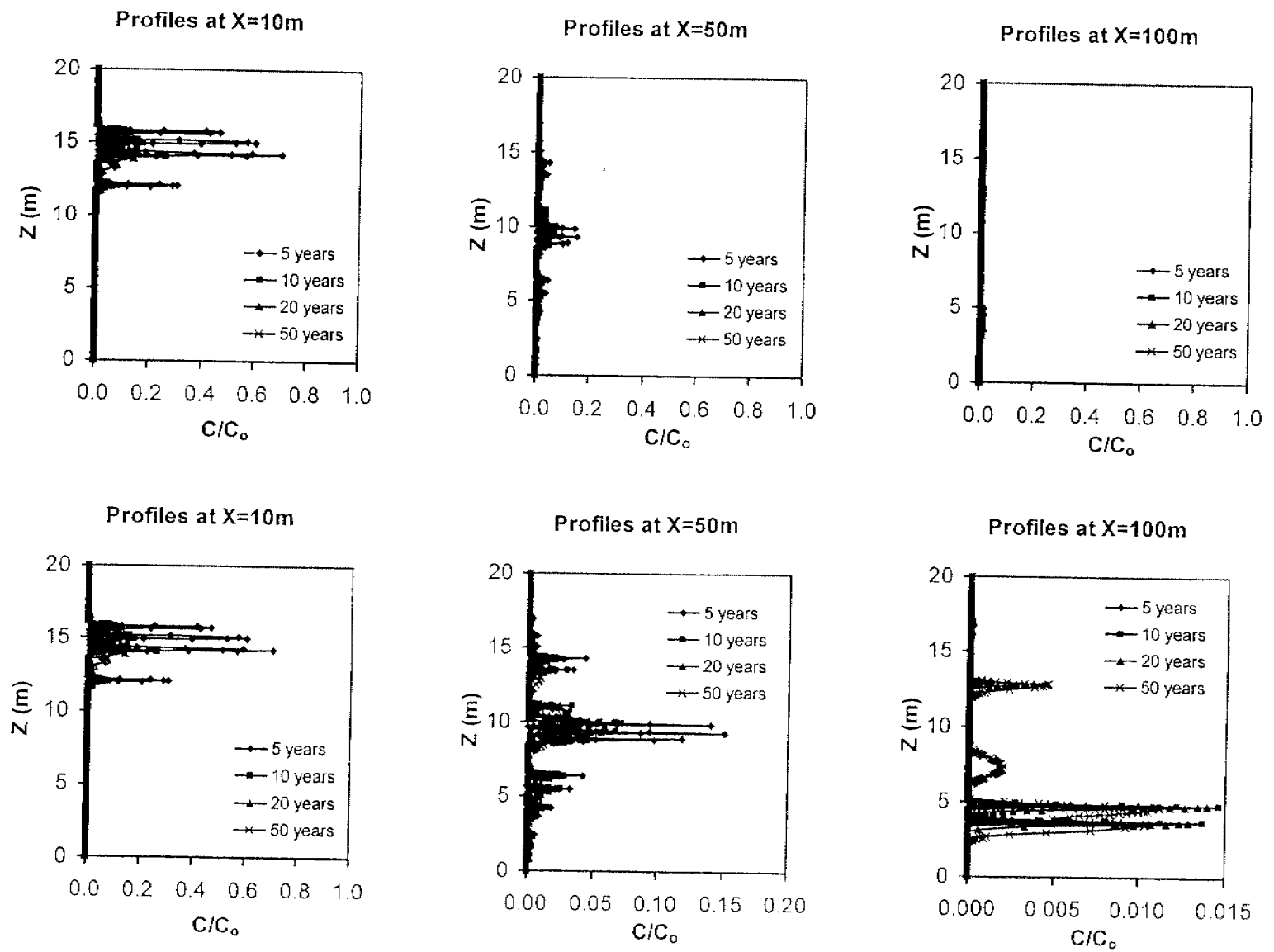


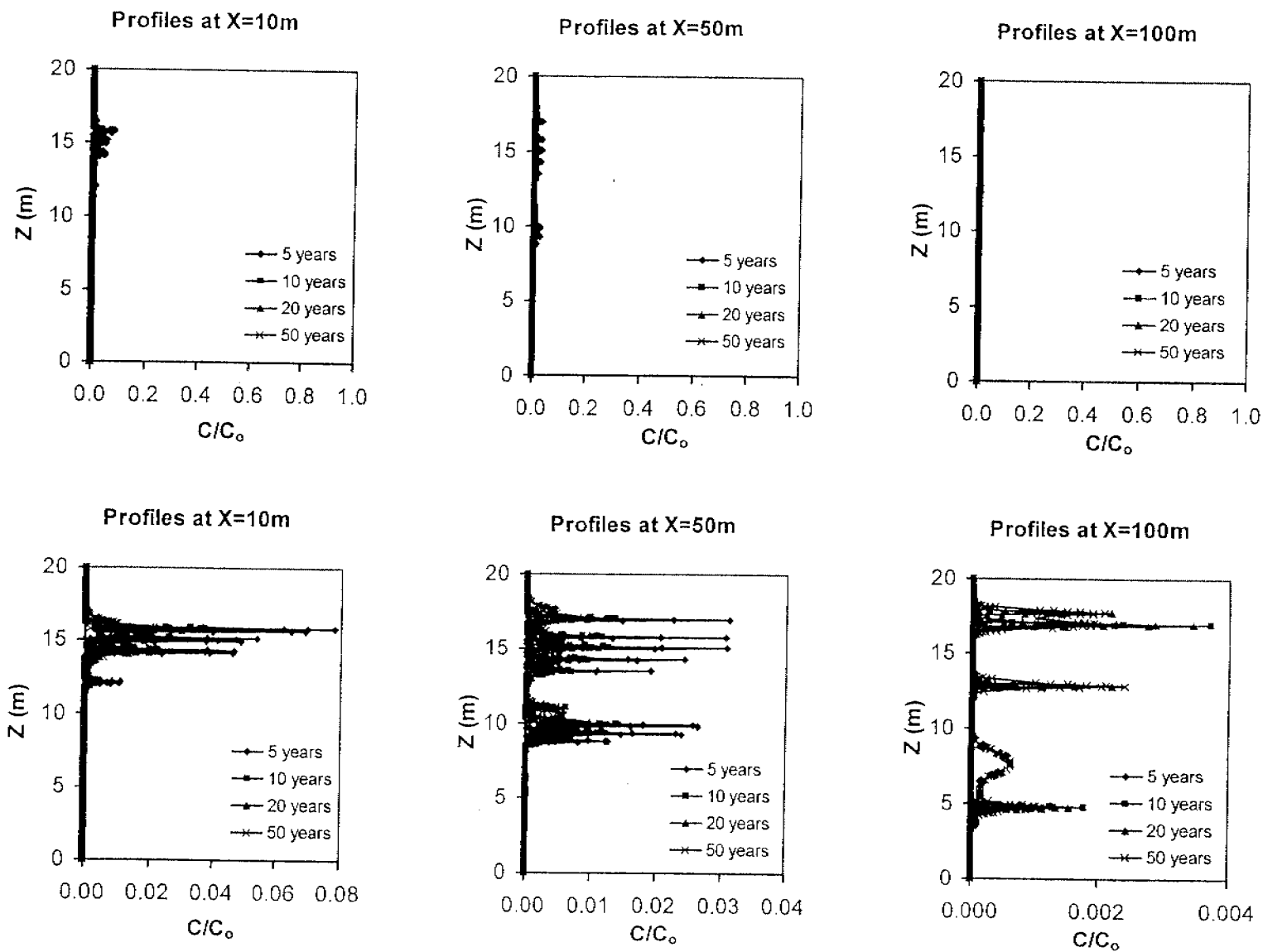
Figure 9

Figure 12

Case (d): 5 Year Source; $R_m=3.0$



Case (e): Residual DNAPL Source; $R_m=3.0$



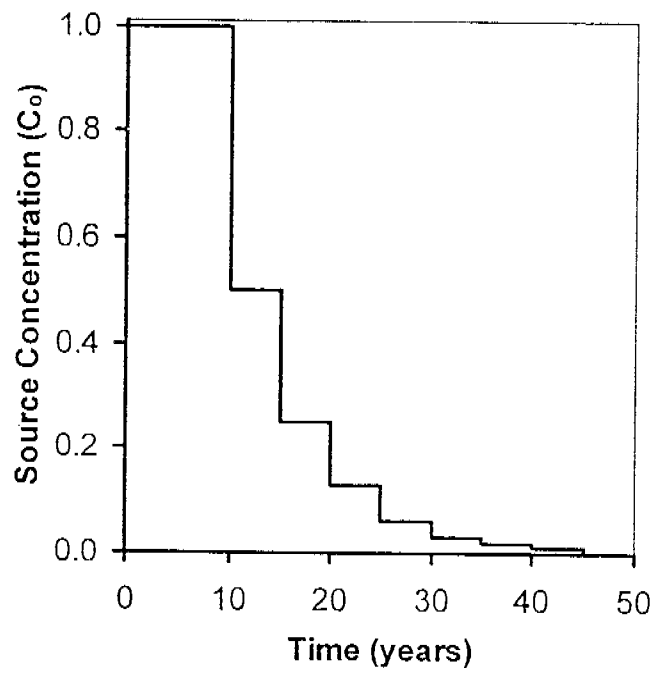


Figure 14

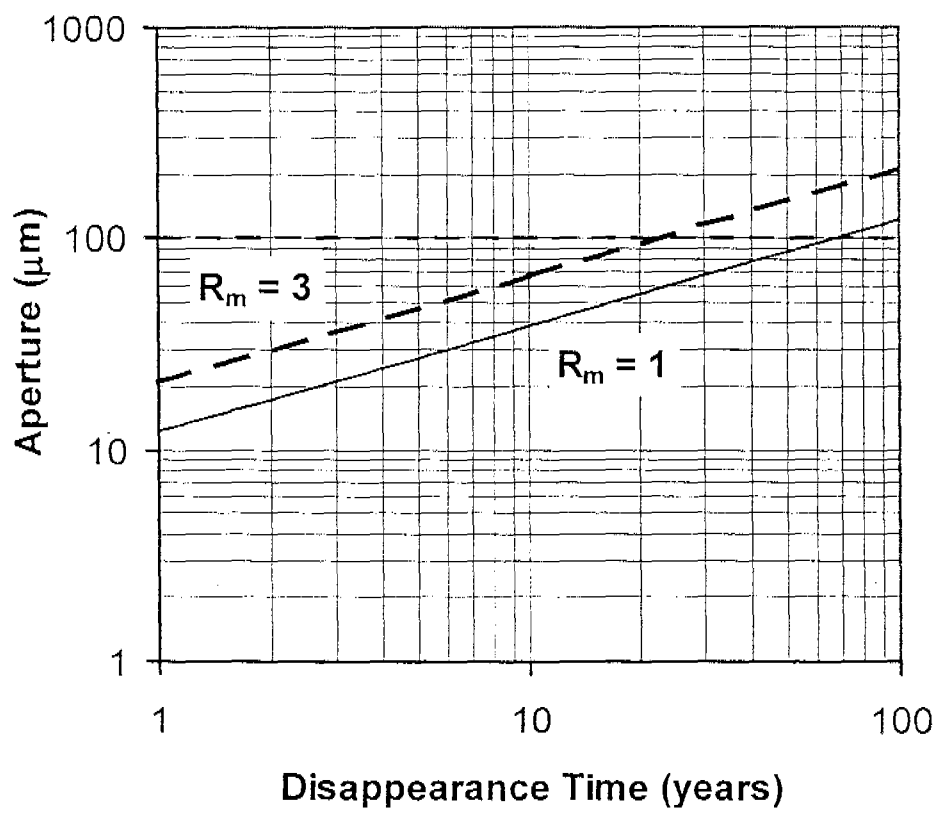


Figure 15

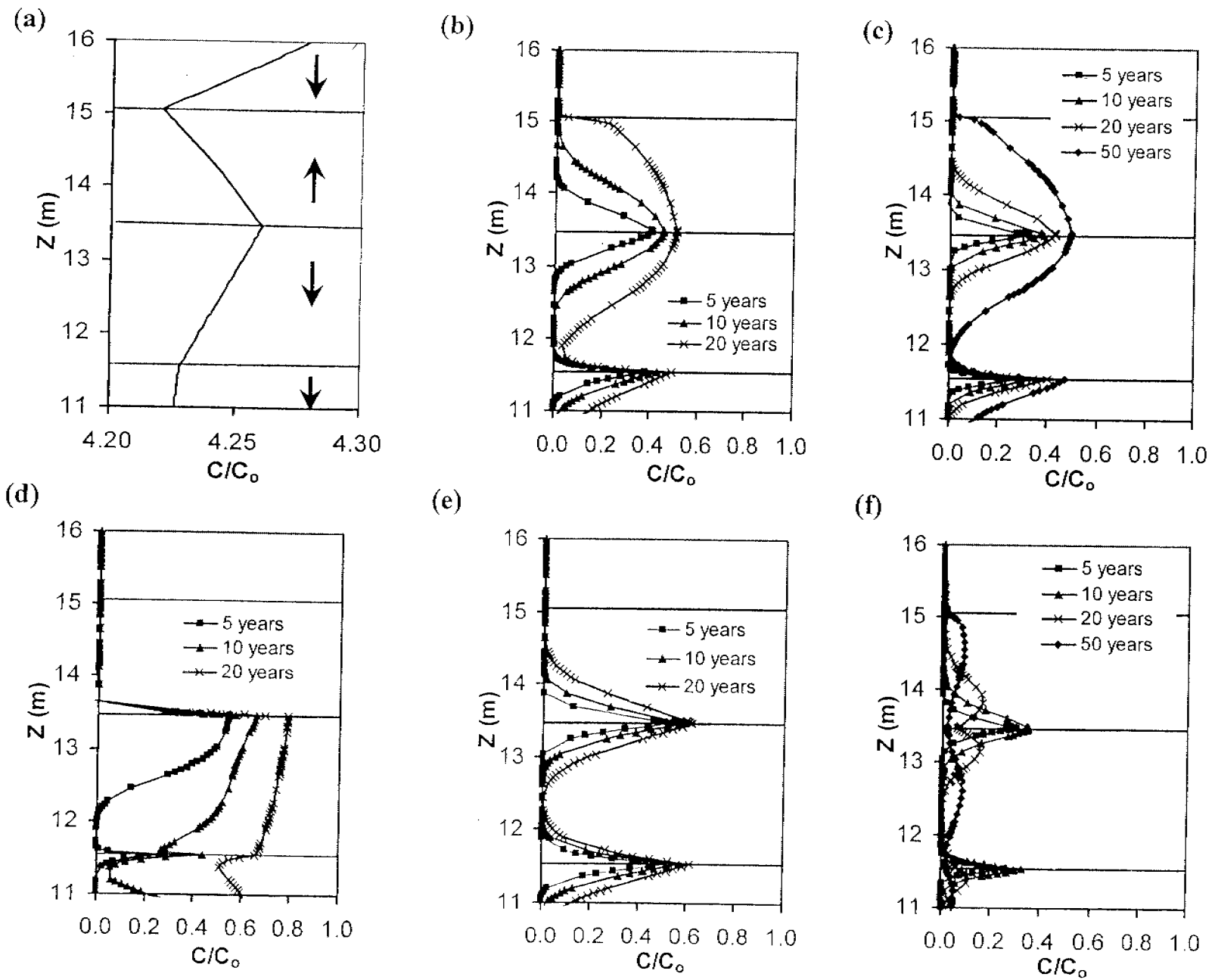


Figure 16

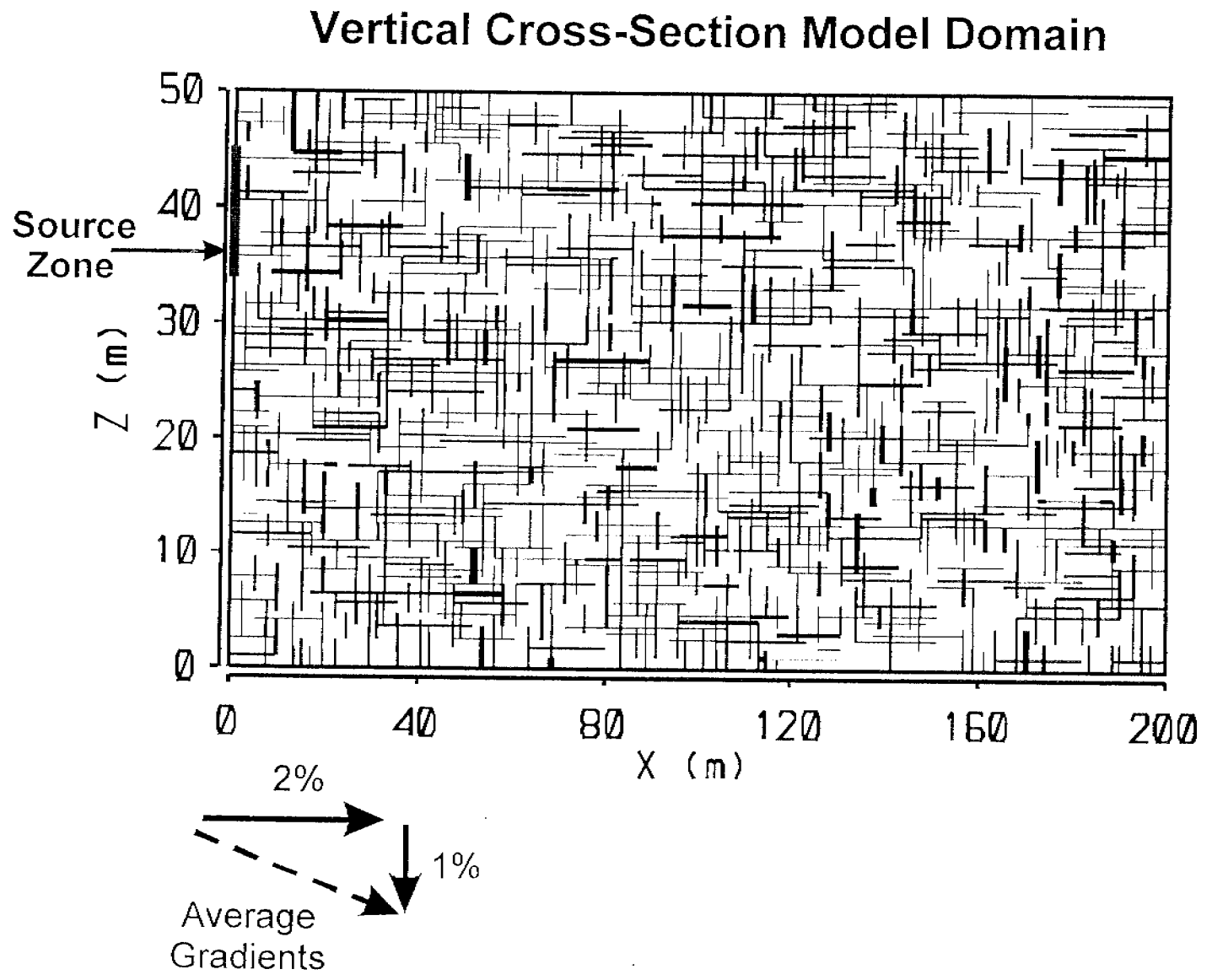


Figure 17

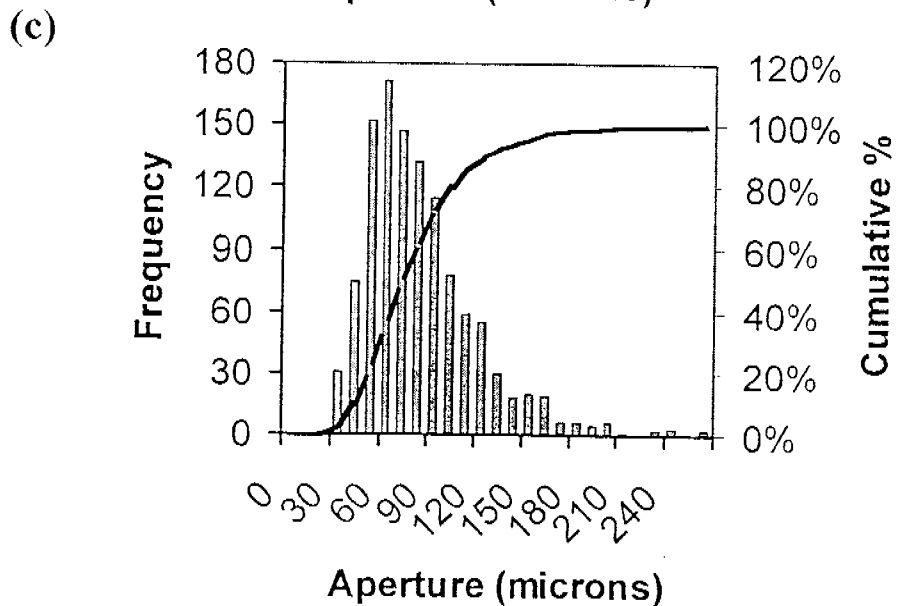
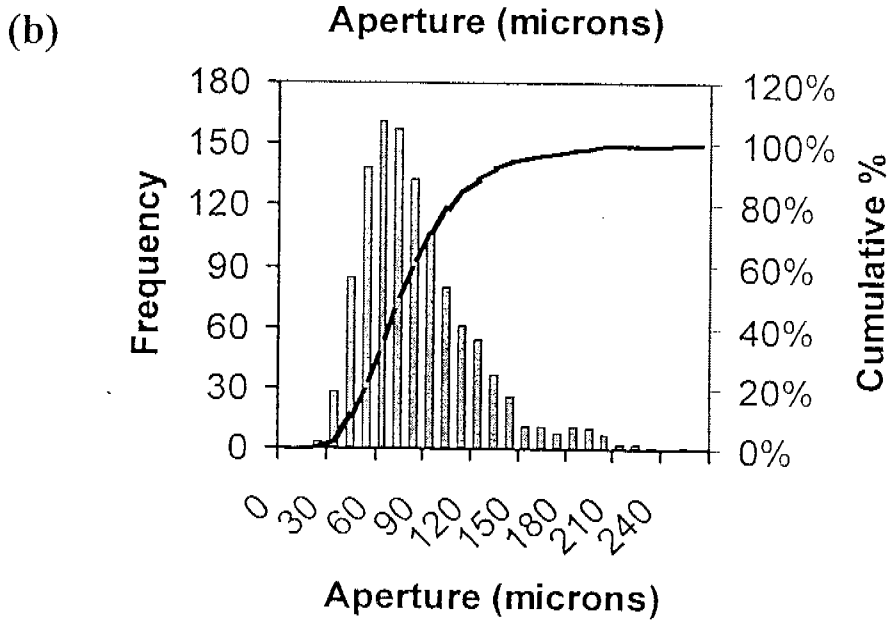
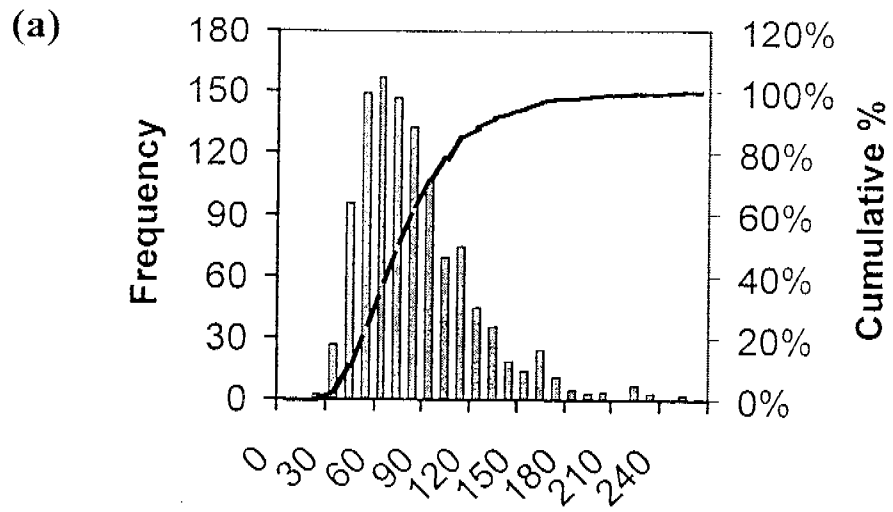
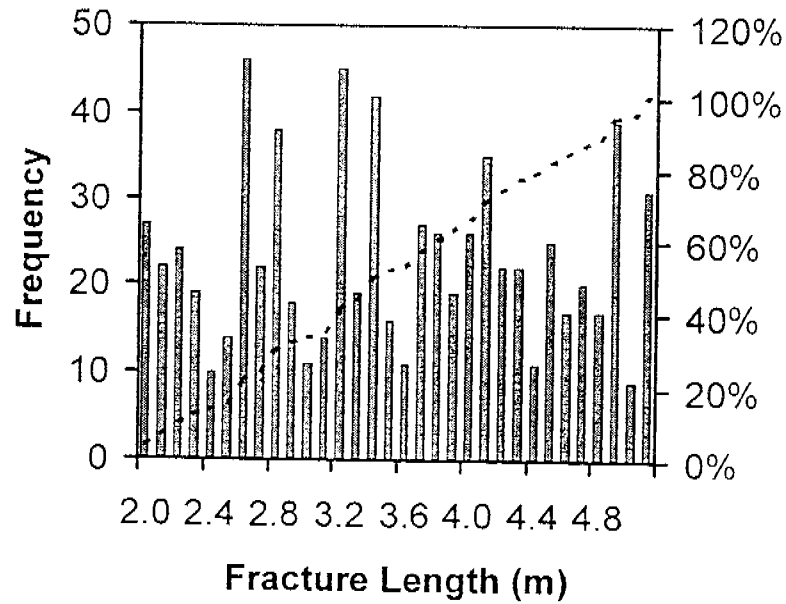


Figure 18

(a)

Vertical Fractures



(b)

Horizontal Fractures

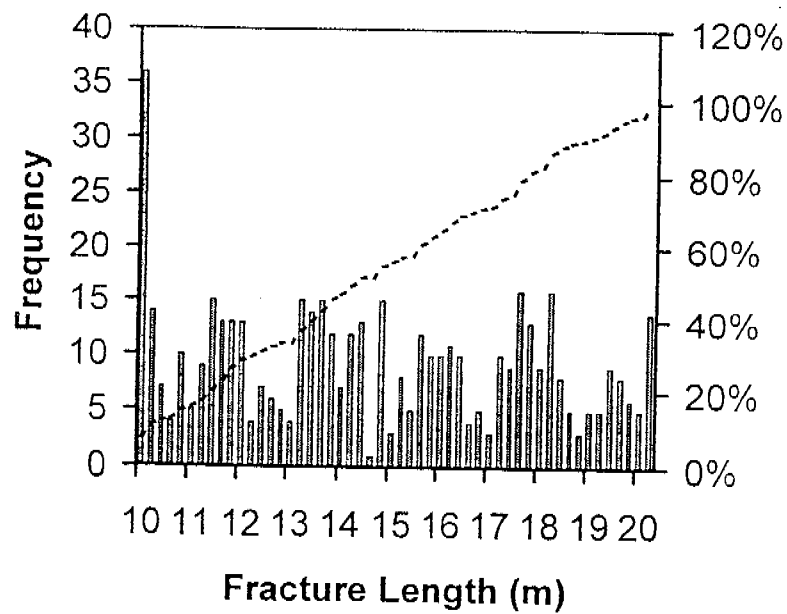


Figure 19

Function: Hydraulic Head
Set : Heads at steady-state
Data set: vert12o

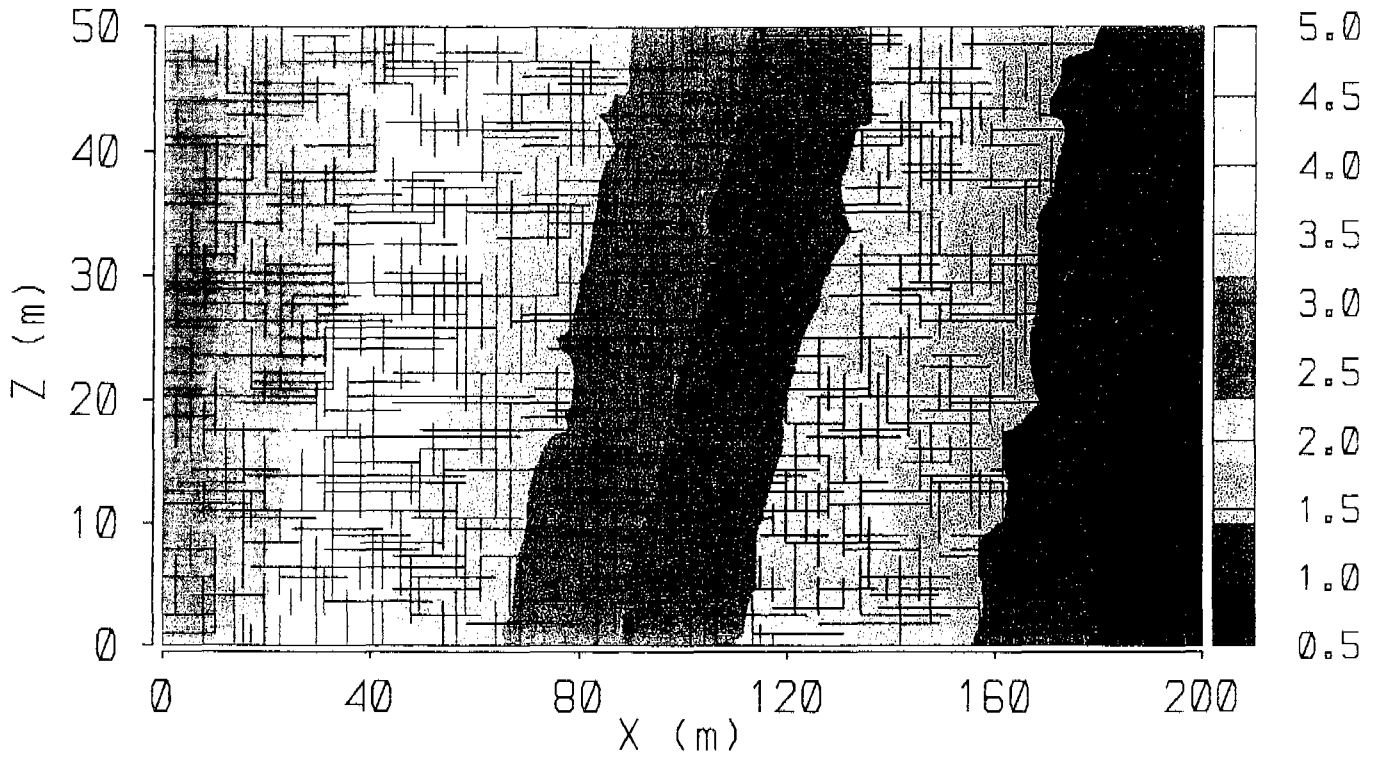


Figure 20

Function: Hydraulic Head
Set : Heads at steady-state
Data set: vert13o

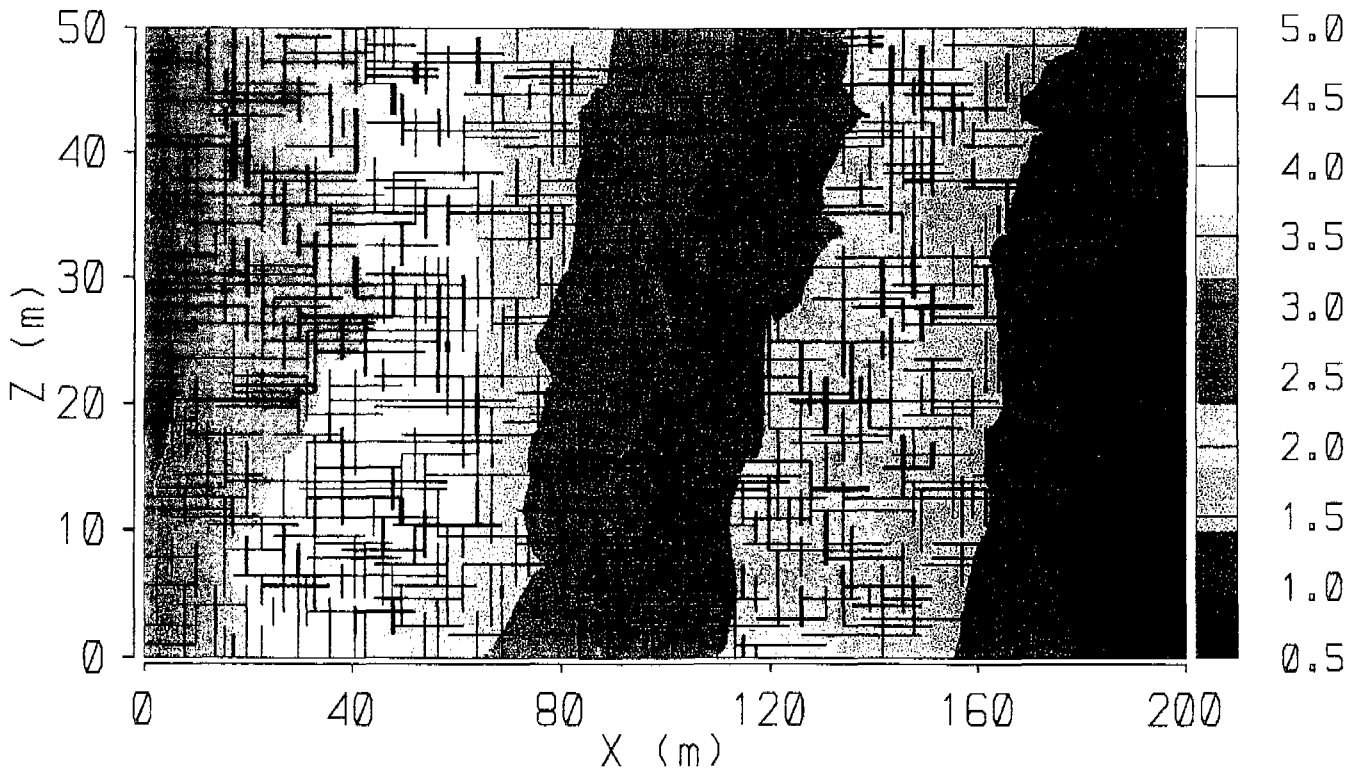


Figure 21

Function: Hydraulic Head
Set : Heads at steady-state
Data set: vert14a

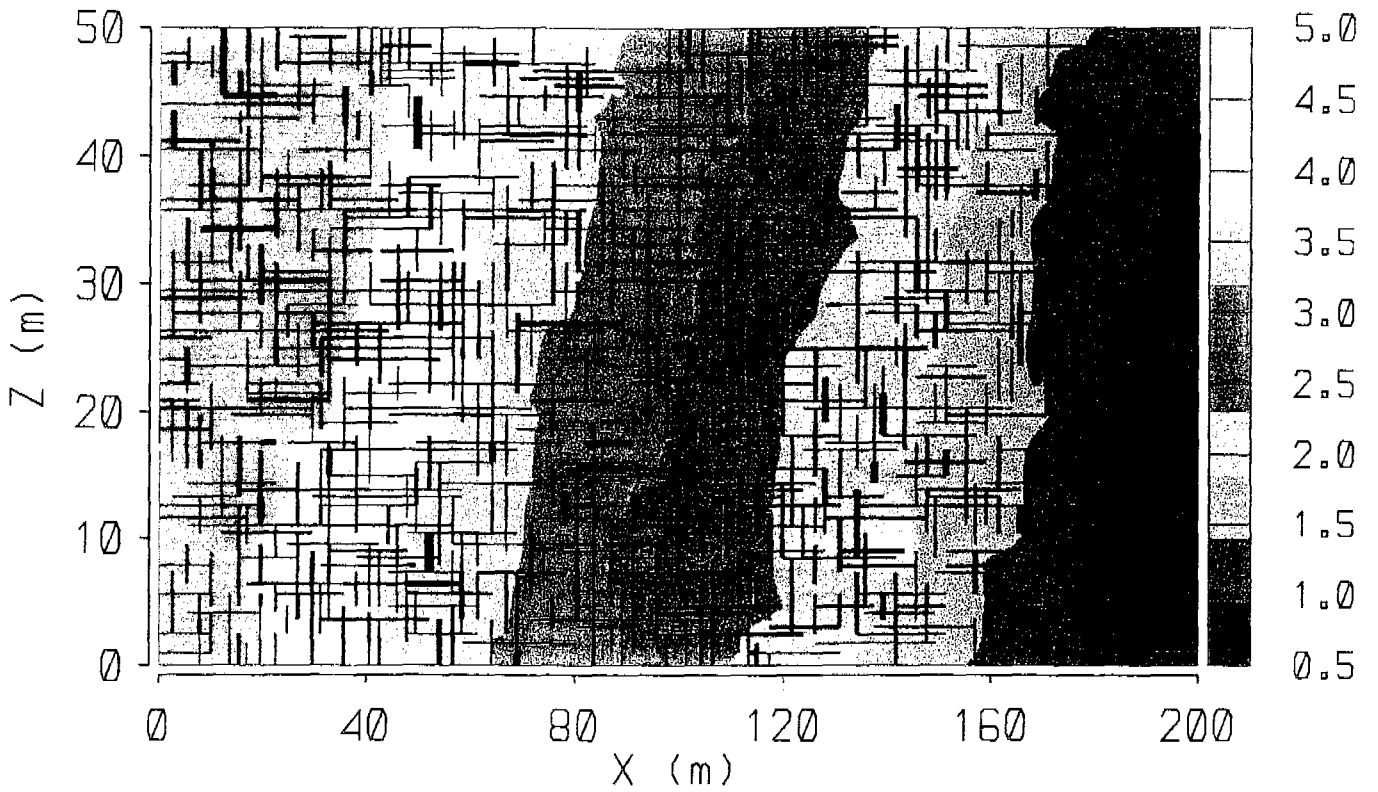


Figure 22

Function: Hydraulic Head
Set : Heads at steady-state
Data set: vert15a

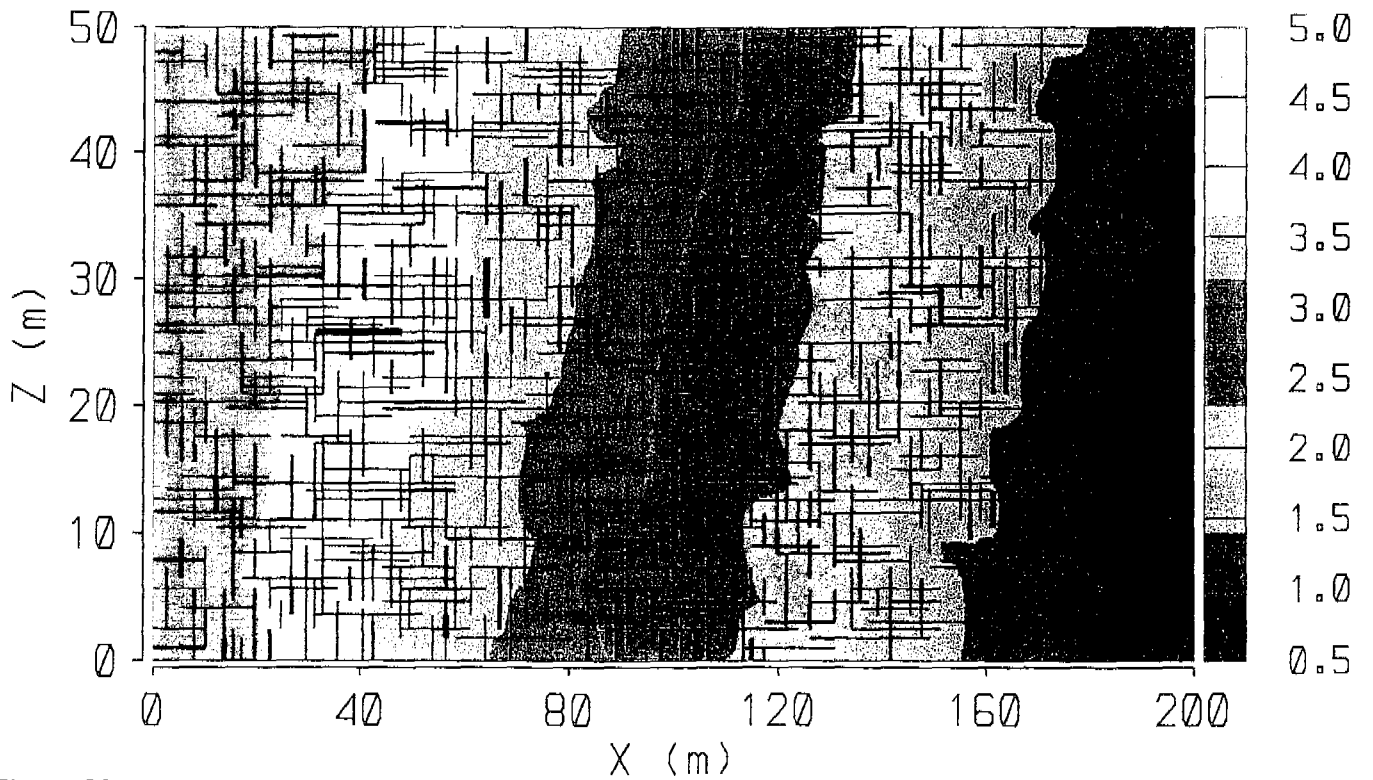


Figure 23

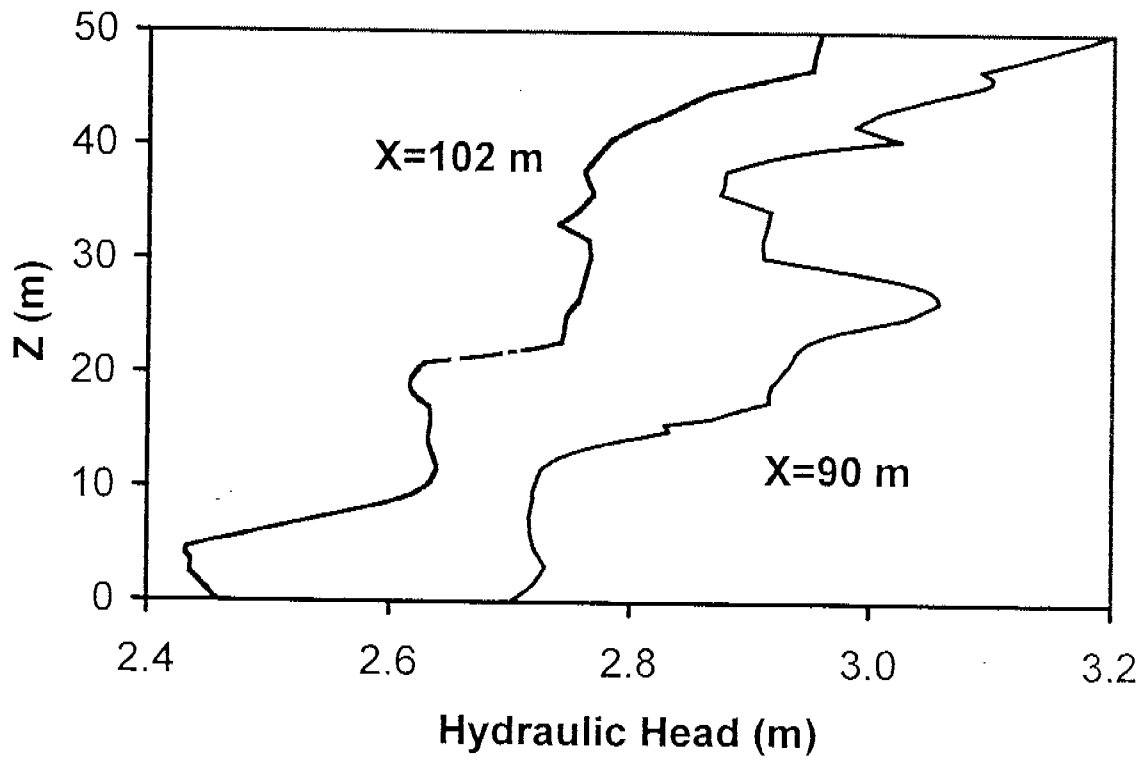


Figure 24

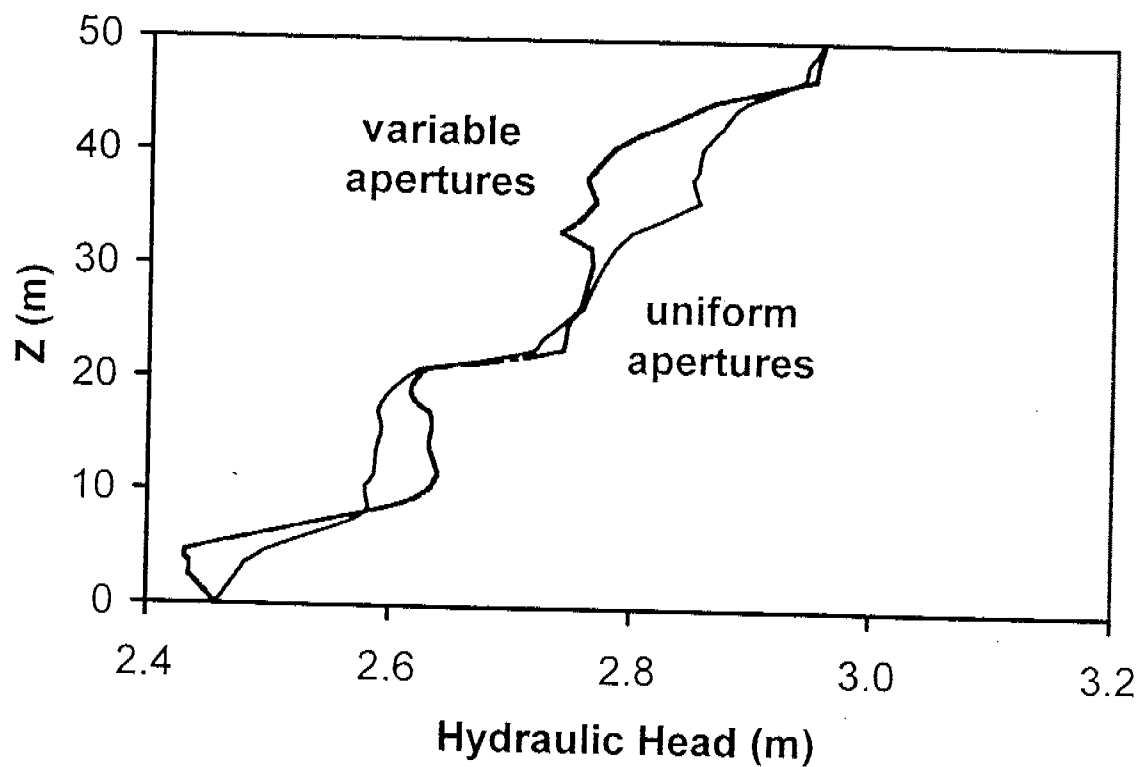
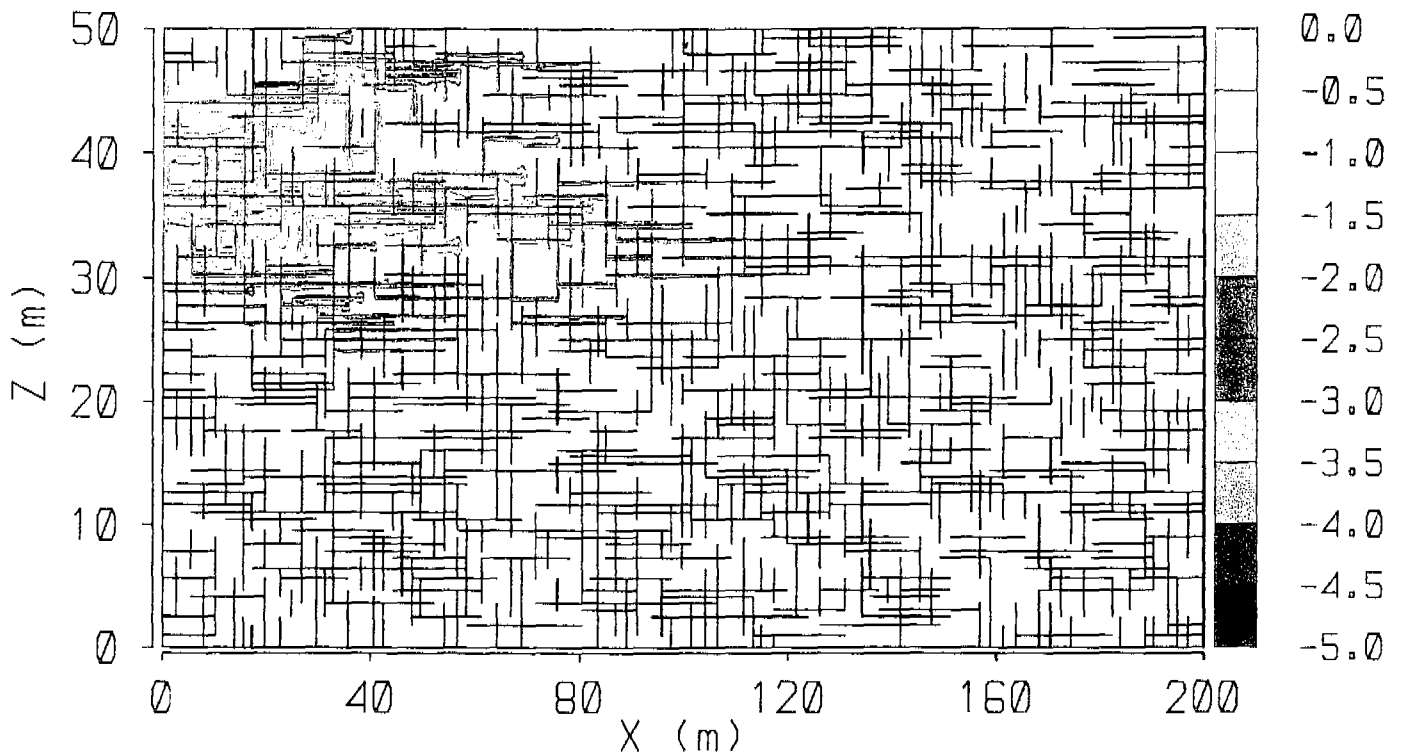


Figure 25

(a)

Function: Concentration
Set : Concentration at 20.0
Data set: vert12a



(b)

Function: Concentration
Set : Concentration at 50.0
Data set: vert12a

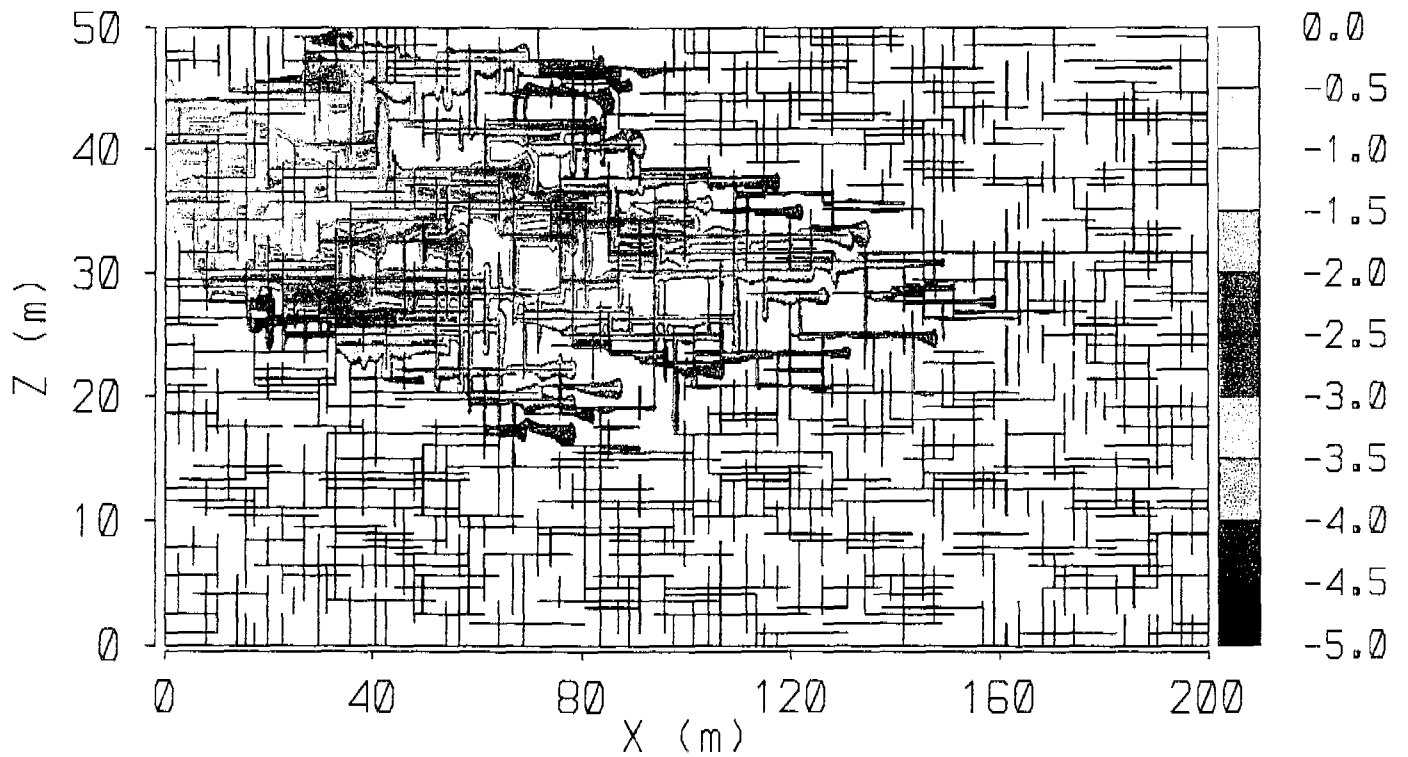
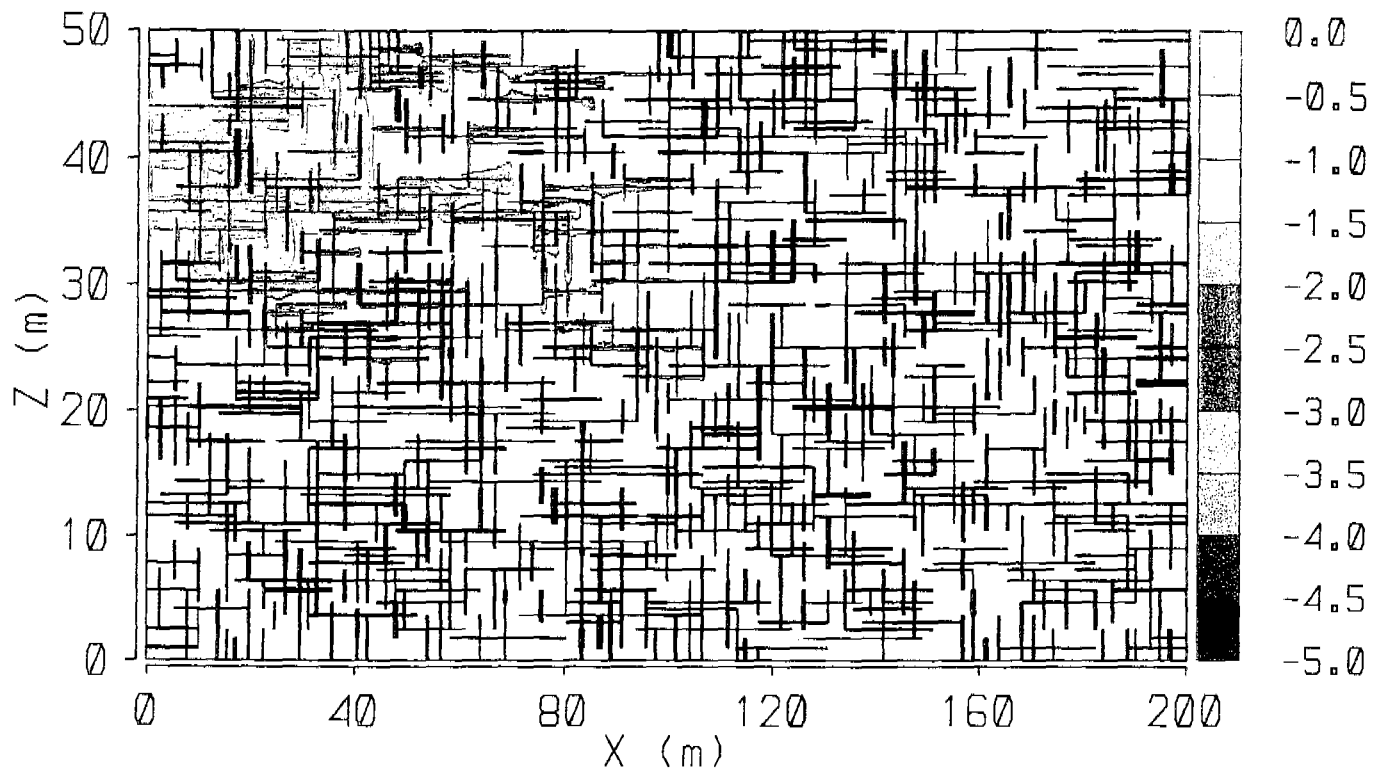


Figure 26

(a)

Function: Concentration
Set : Concentration at 20.0
Data set: vert13o



(b)

Function: Concentration
Set : Concentration at 50.0
Data set: vert13o

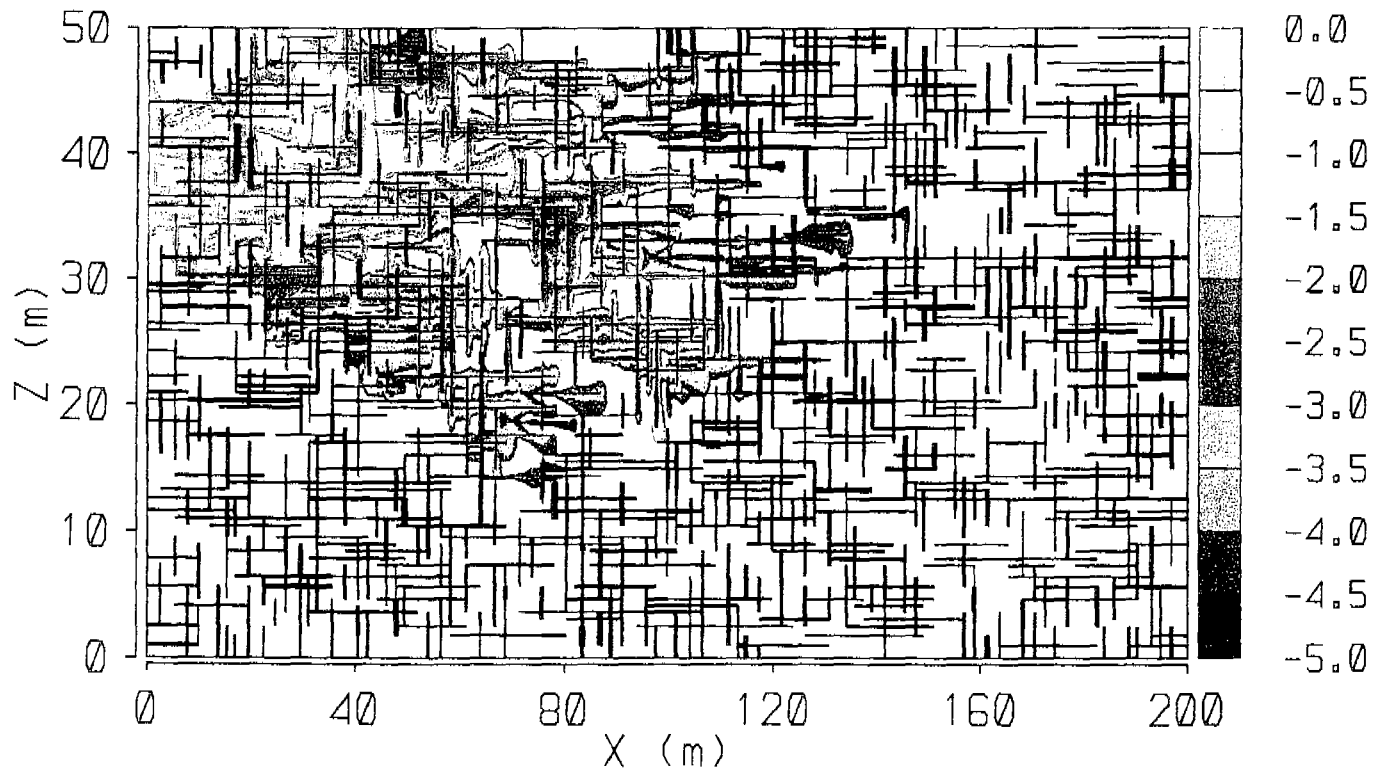
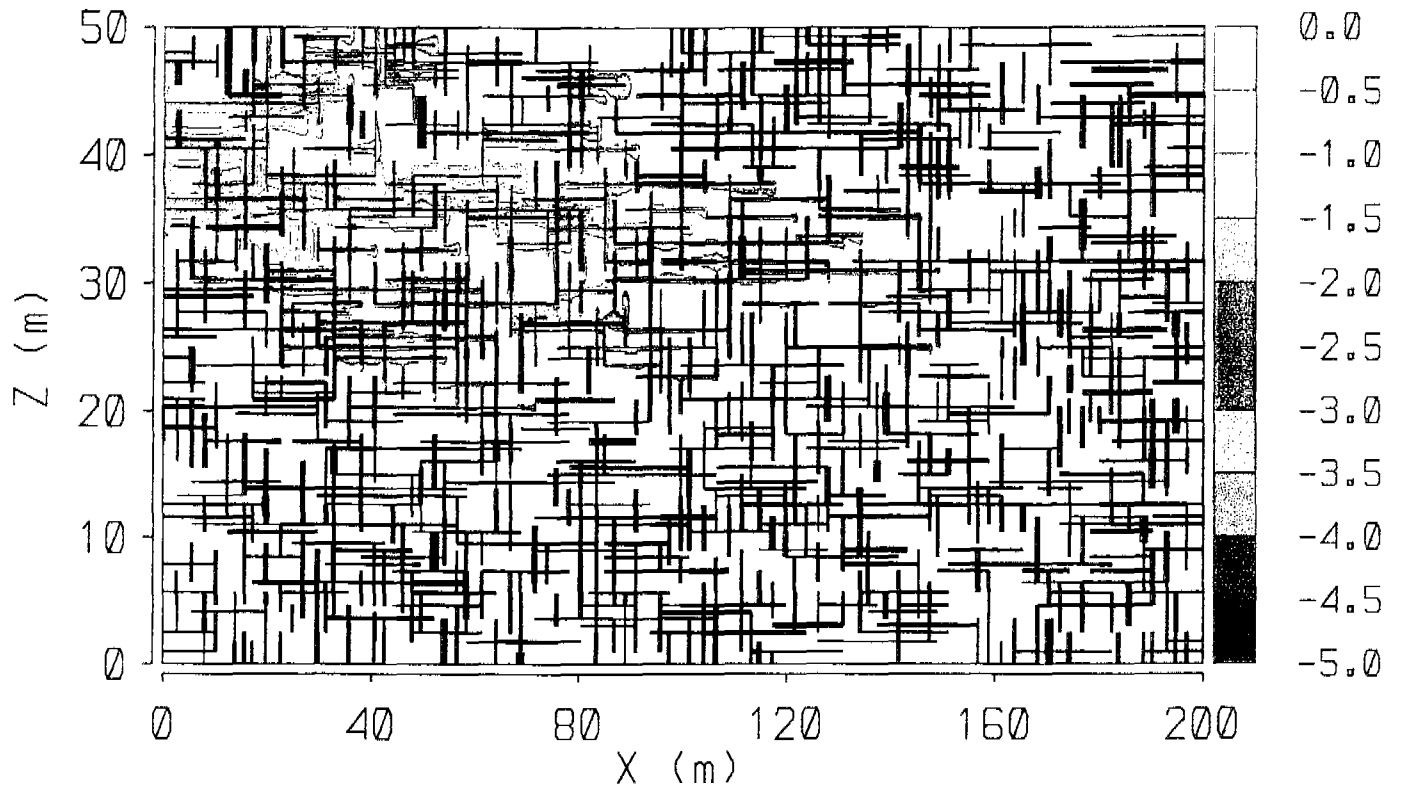


Figure 27

(a)

Function: Concentration
Set : Concentration at 20.0
Data set: vert14a



(b)

Function: Concentration
Set : Concentration at 50.0
Data set: vert14a

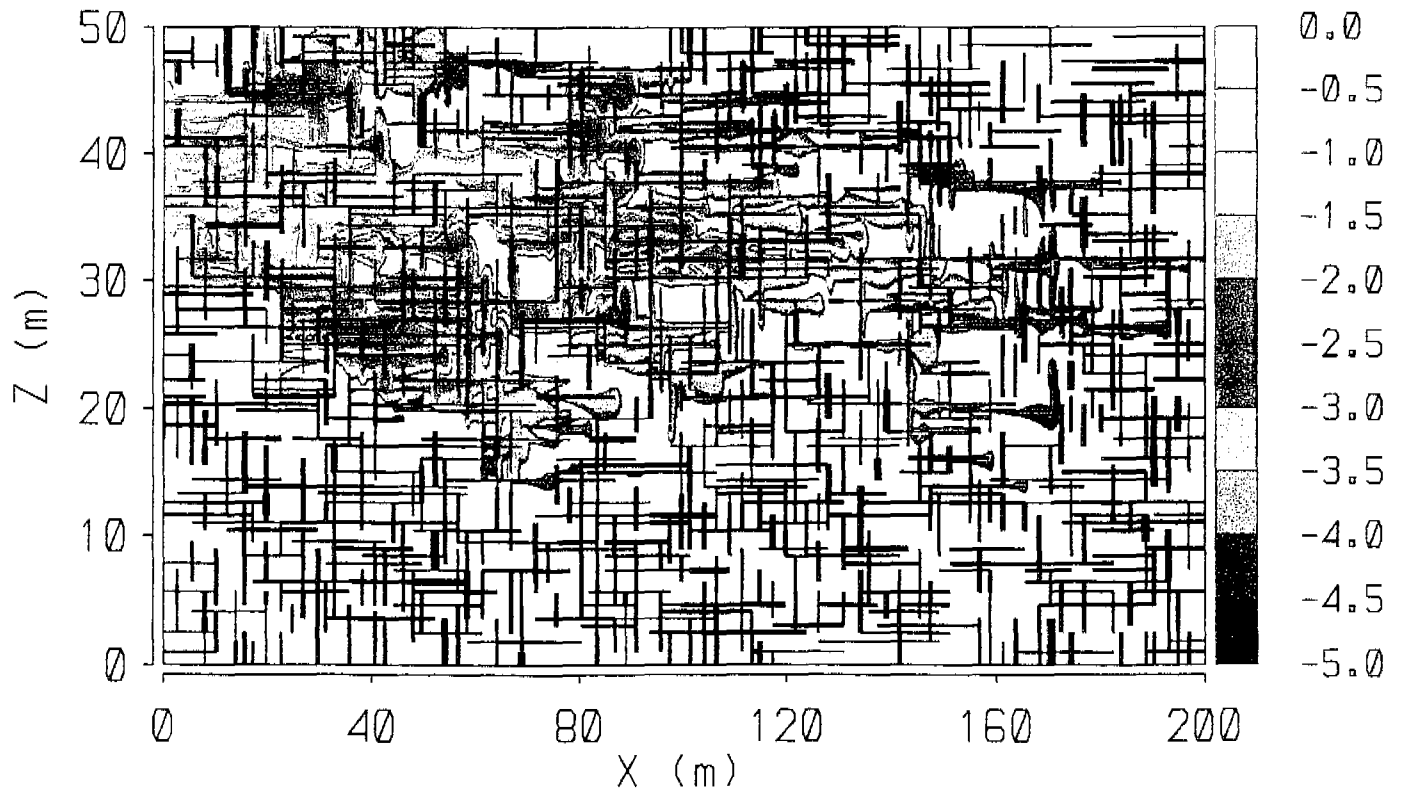
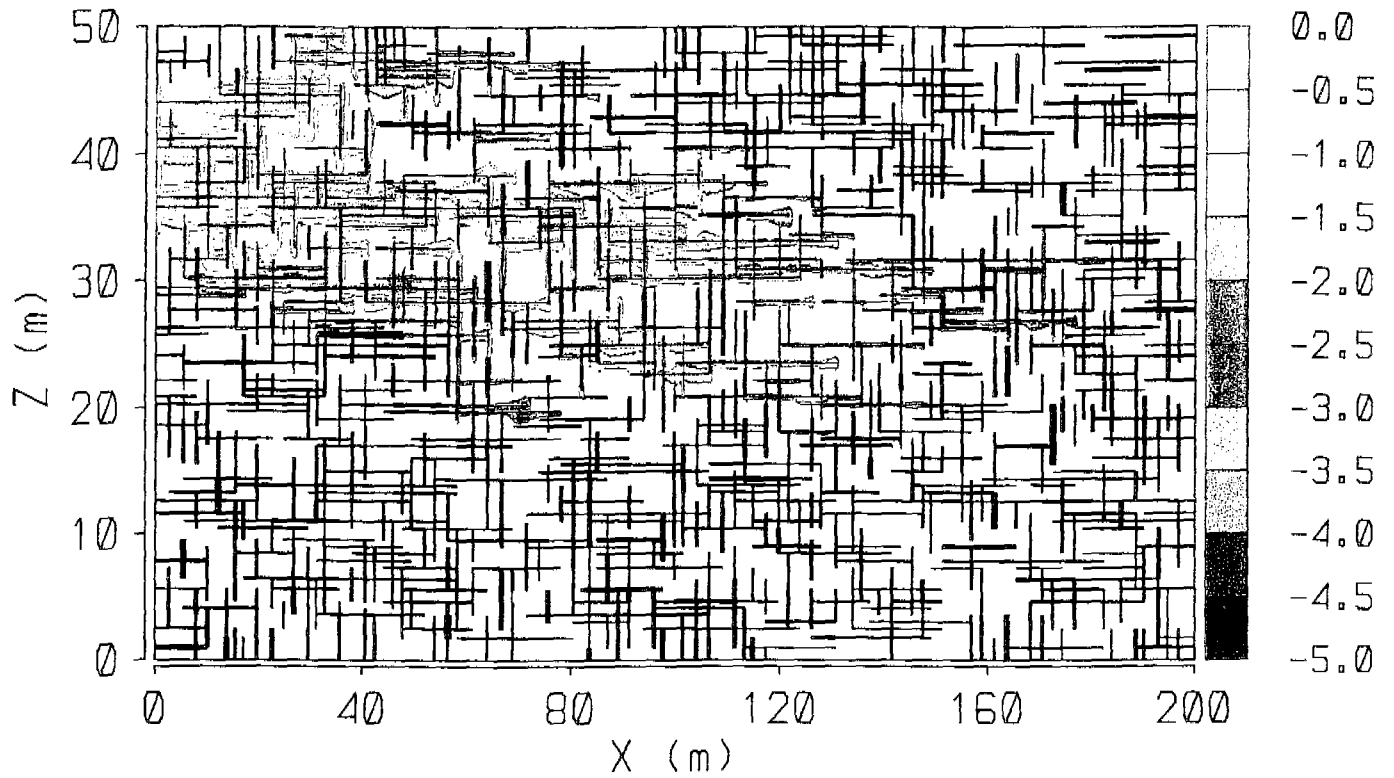


Figure 28

(a)

Function: Concentration
Set : Concentration at 20.0
Data set: vert15o



(b)

Function: Concentration
Set : Concentration at 50.0
Data set: vert15o

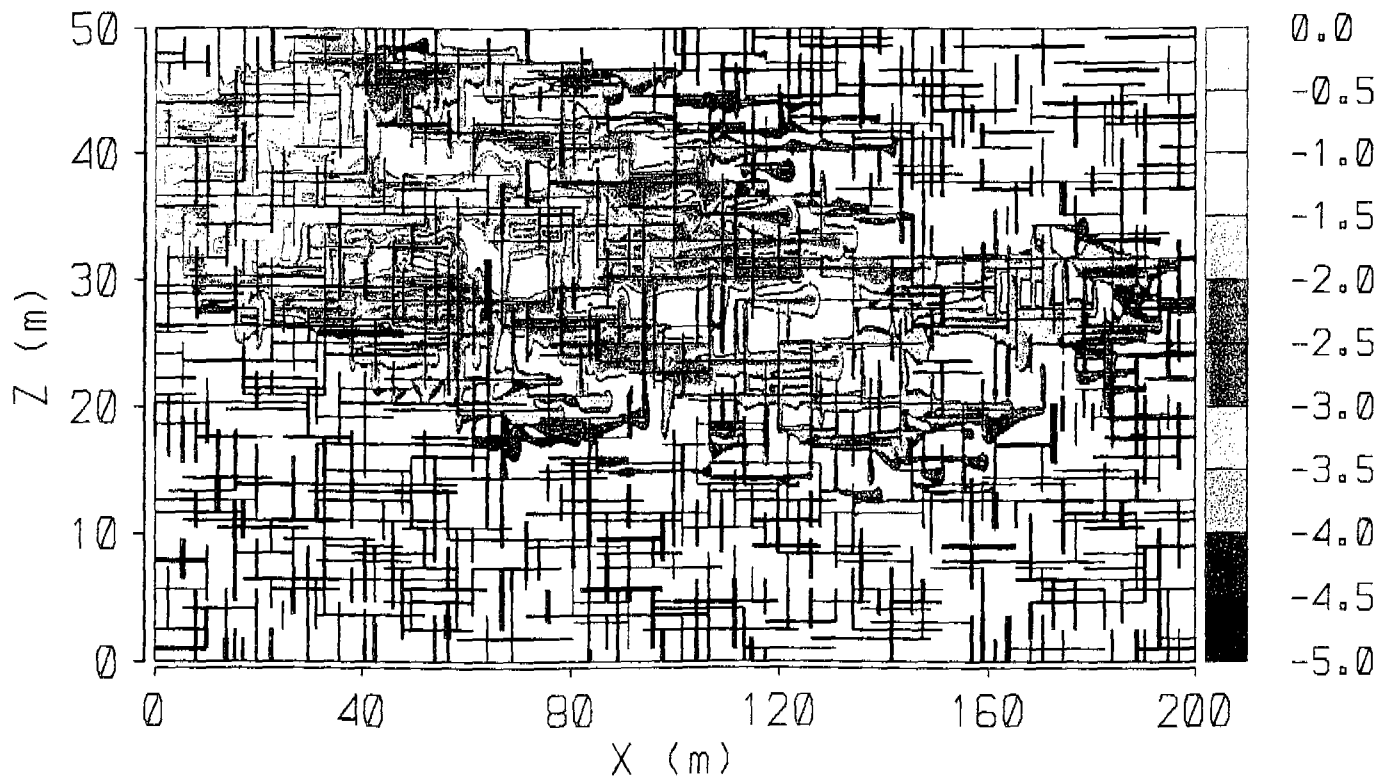
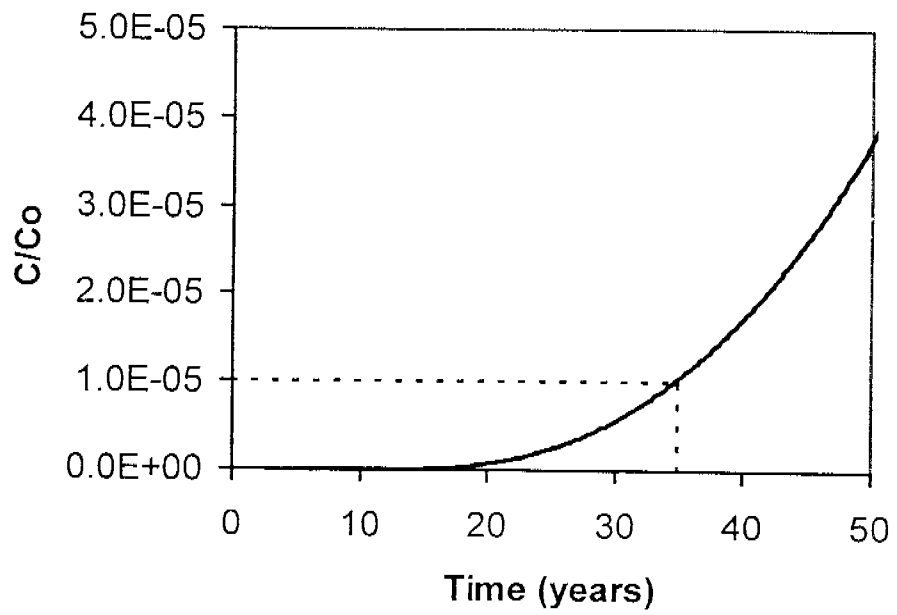


Figure 29

(a)



(b)

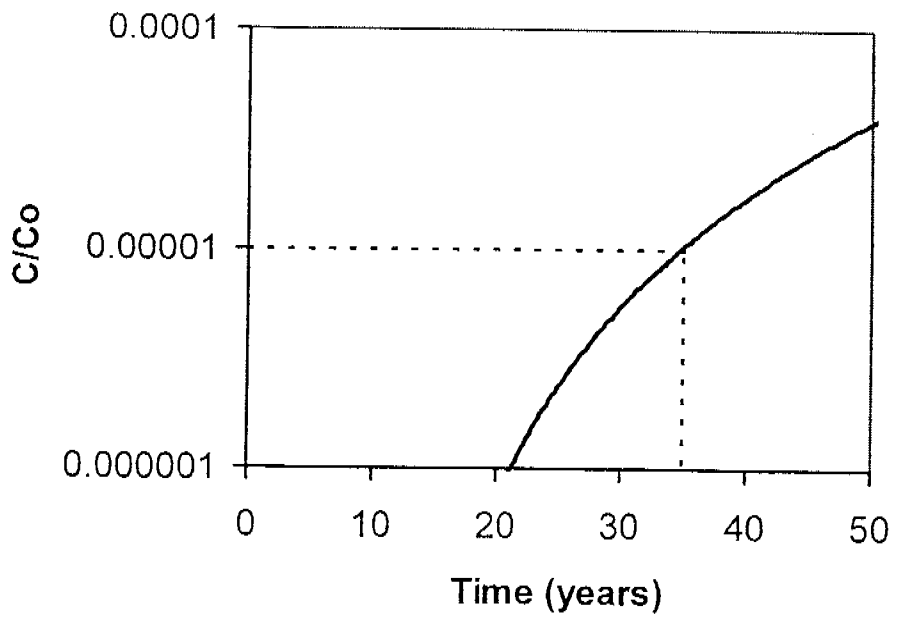


Figure 30

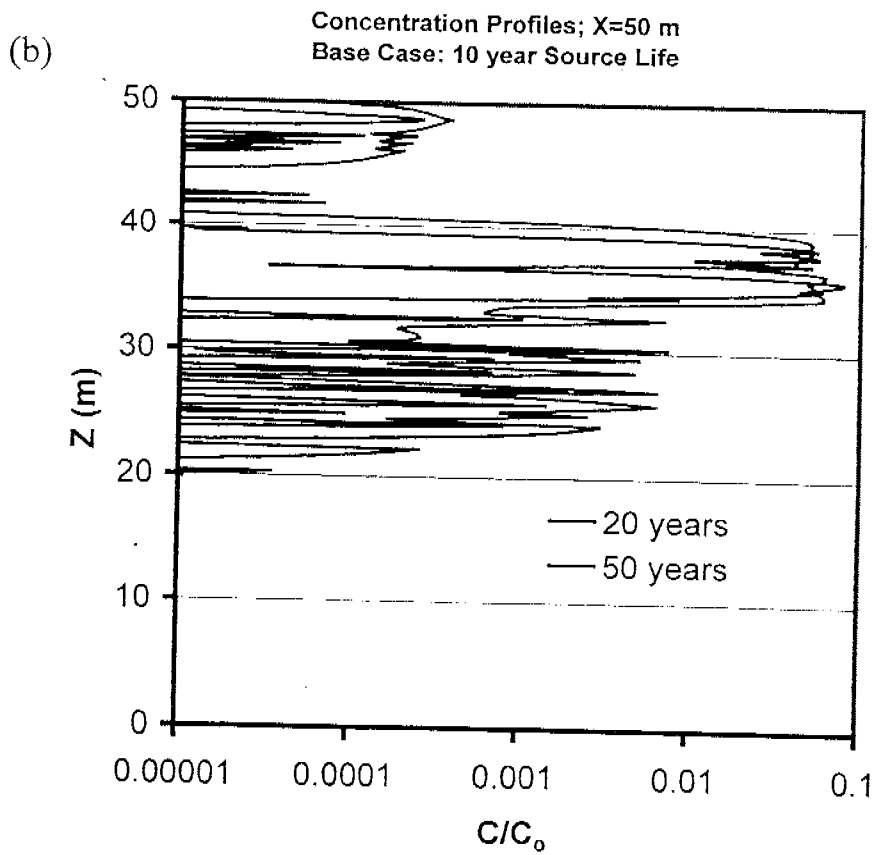
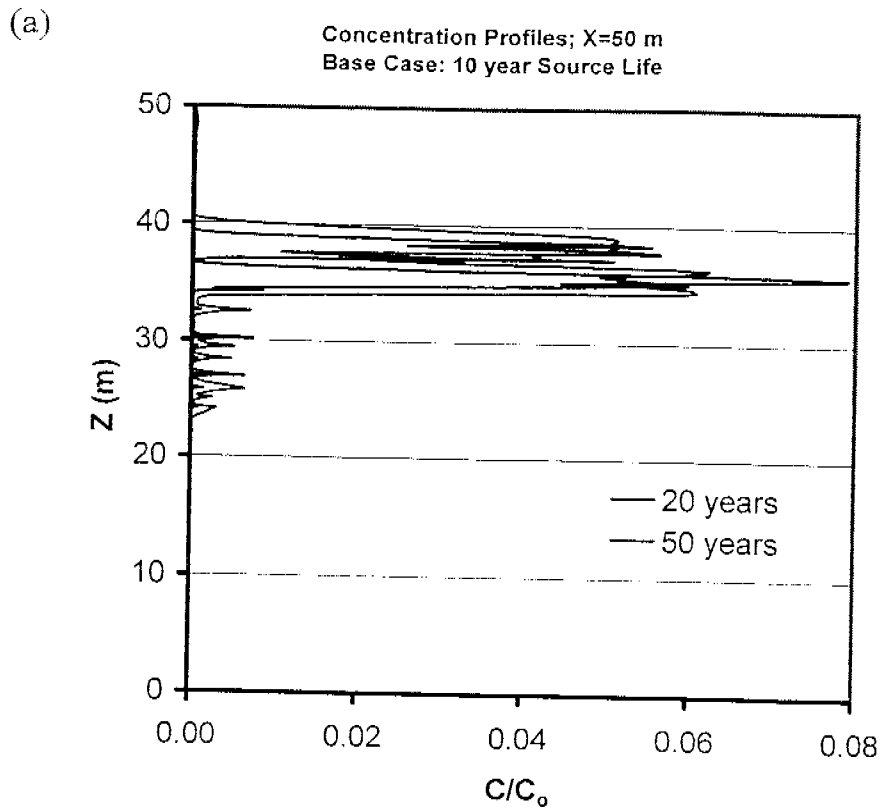


Figure 31

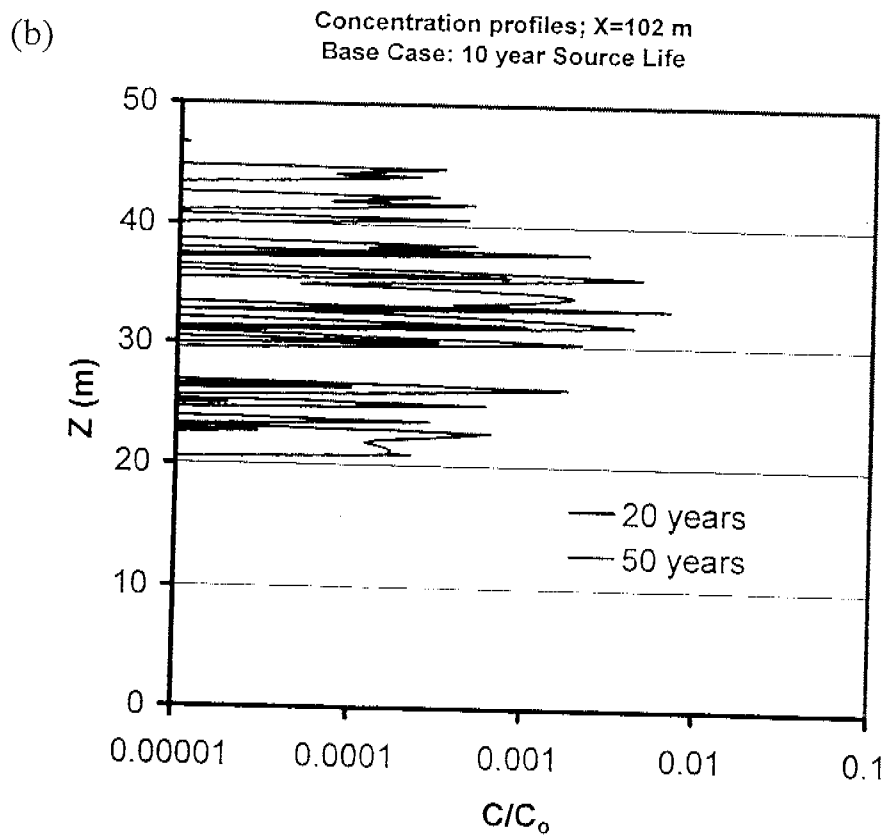
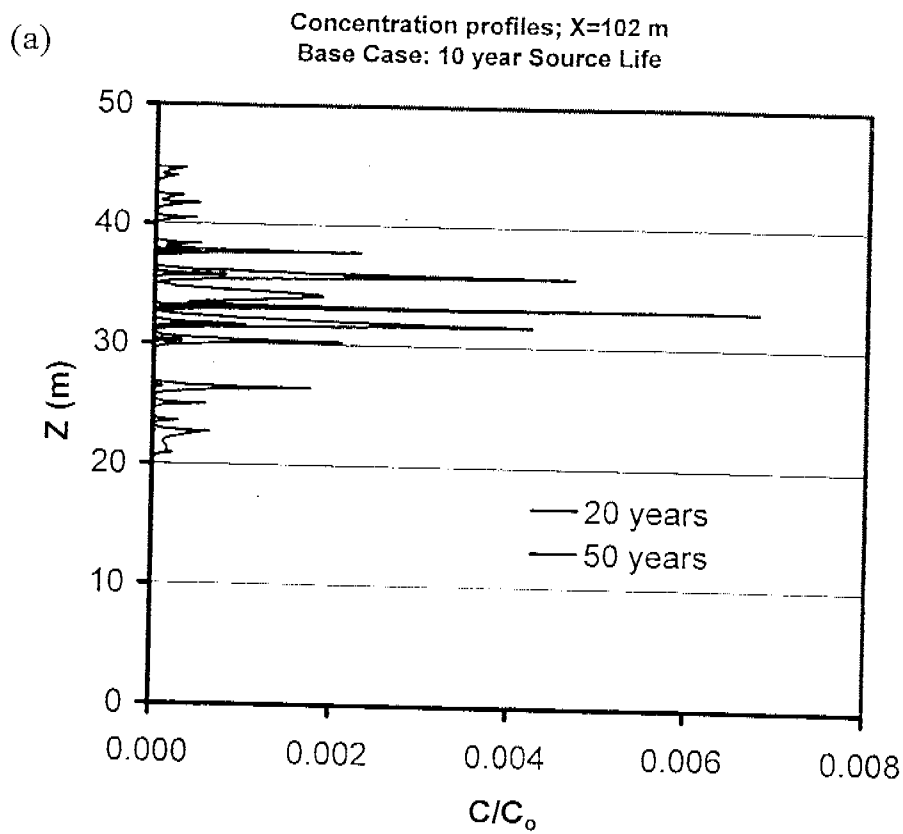
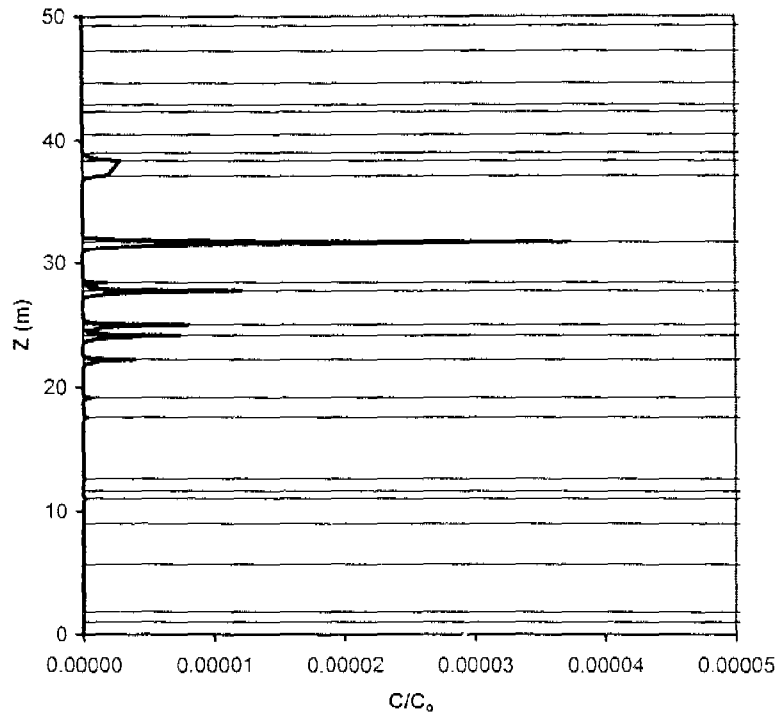


Figure 32

(a)

Concentration Profiles; X=200m; 50 years
Base Case: 10 year Source Life



(b)

Concentration Profiles; X=200m; 50 years
Base Case: 10 year Source Life

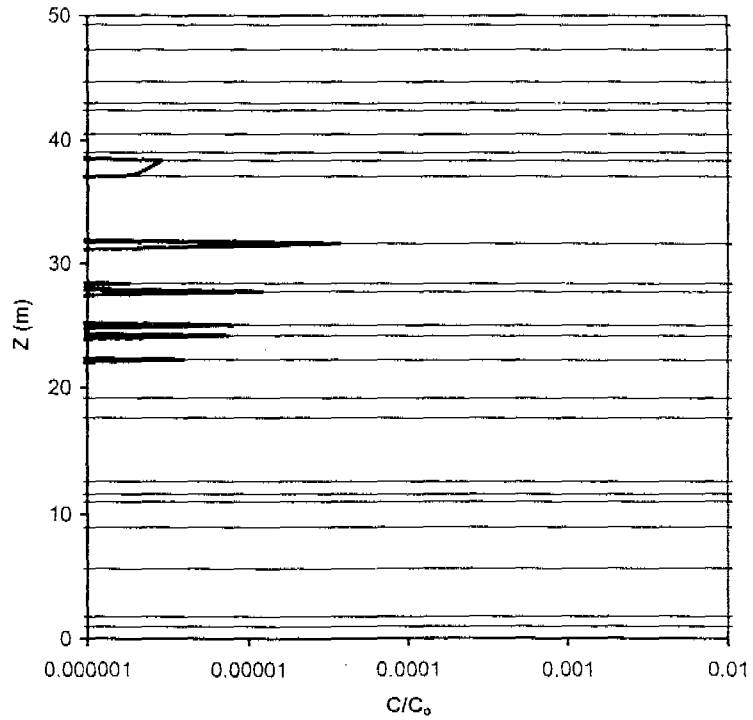


Figure 33

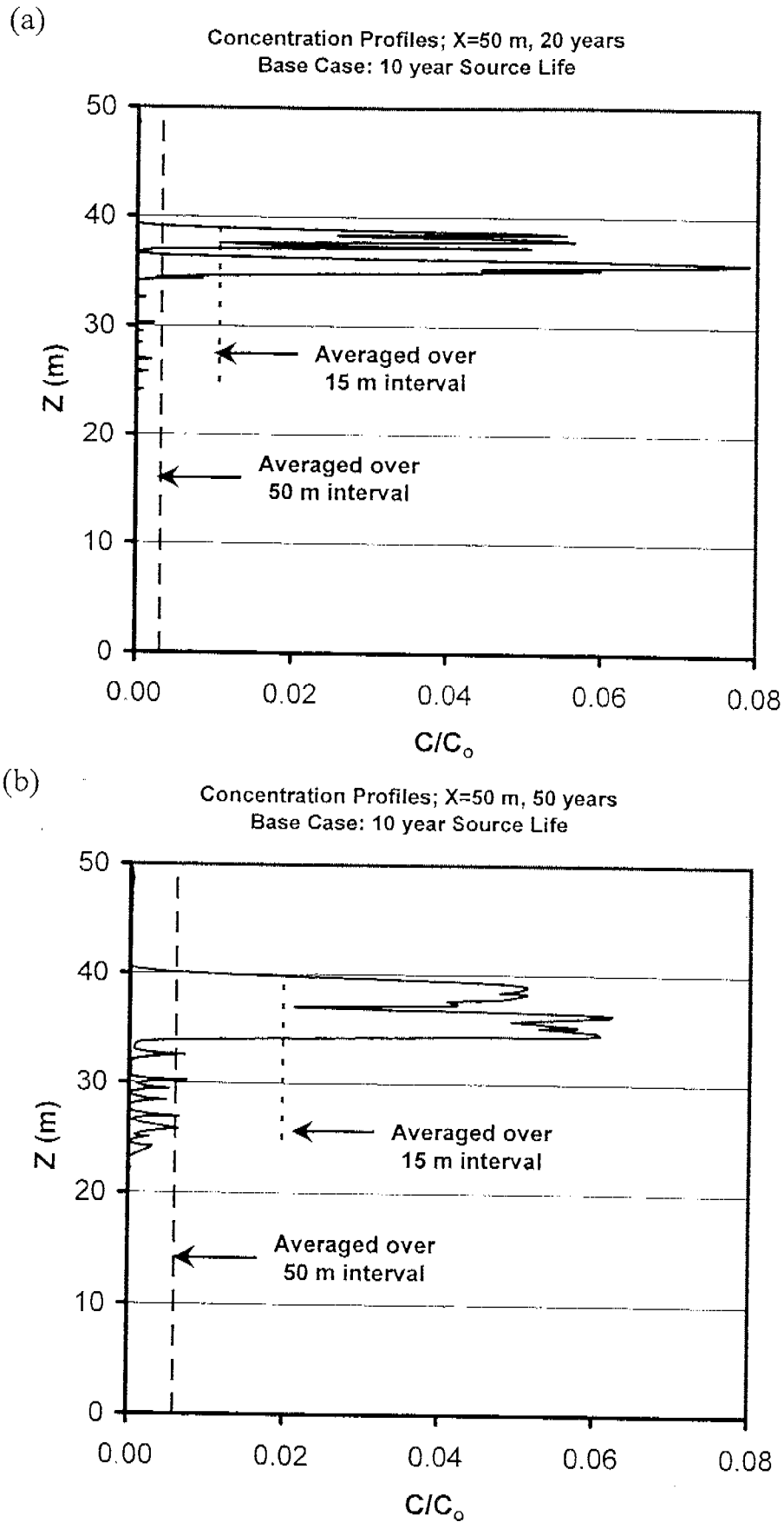


Figure 34

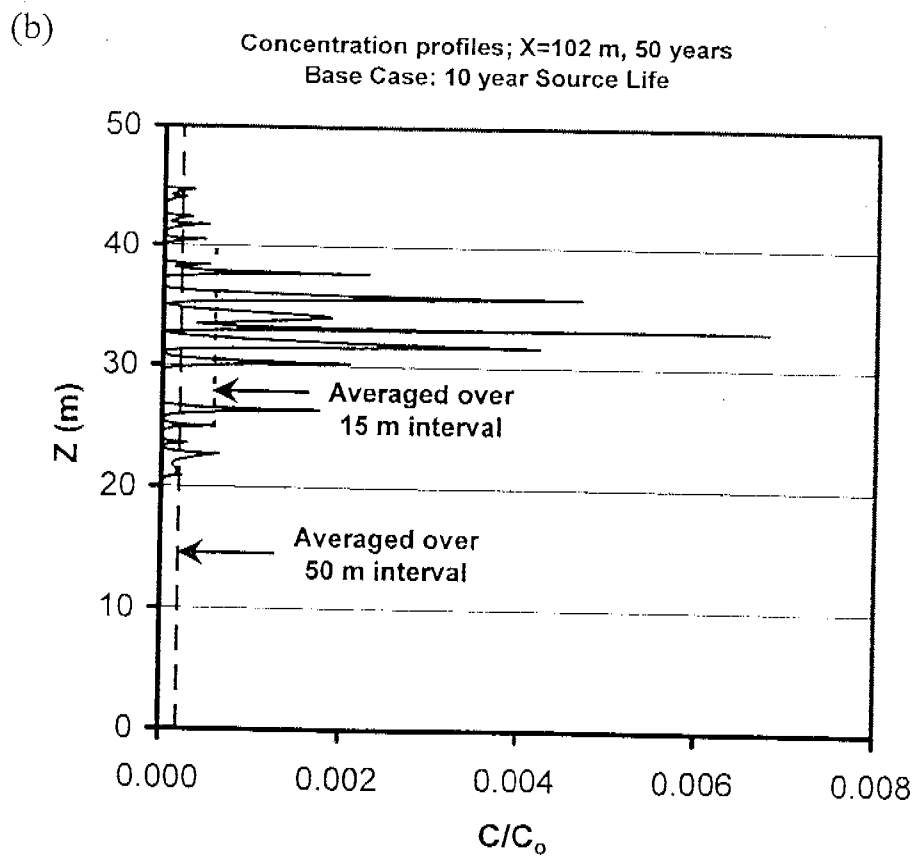
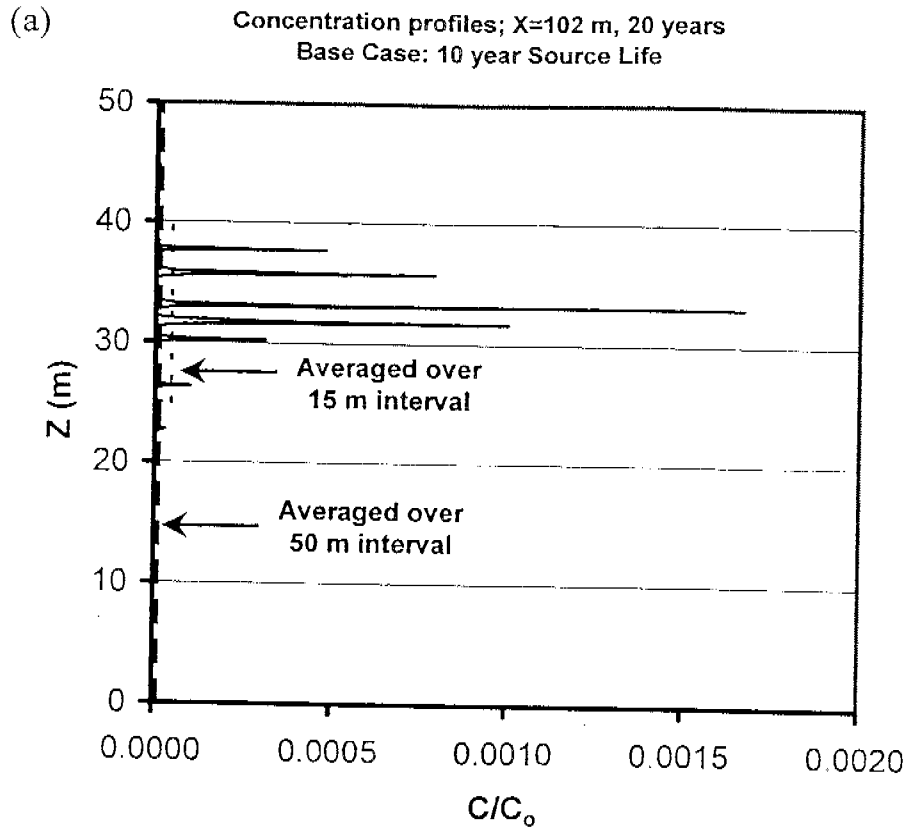


Figure 35

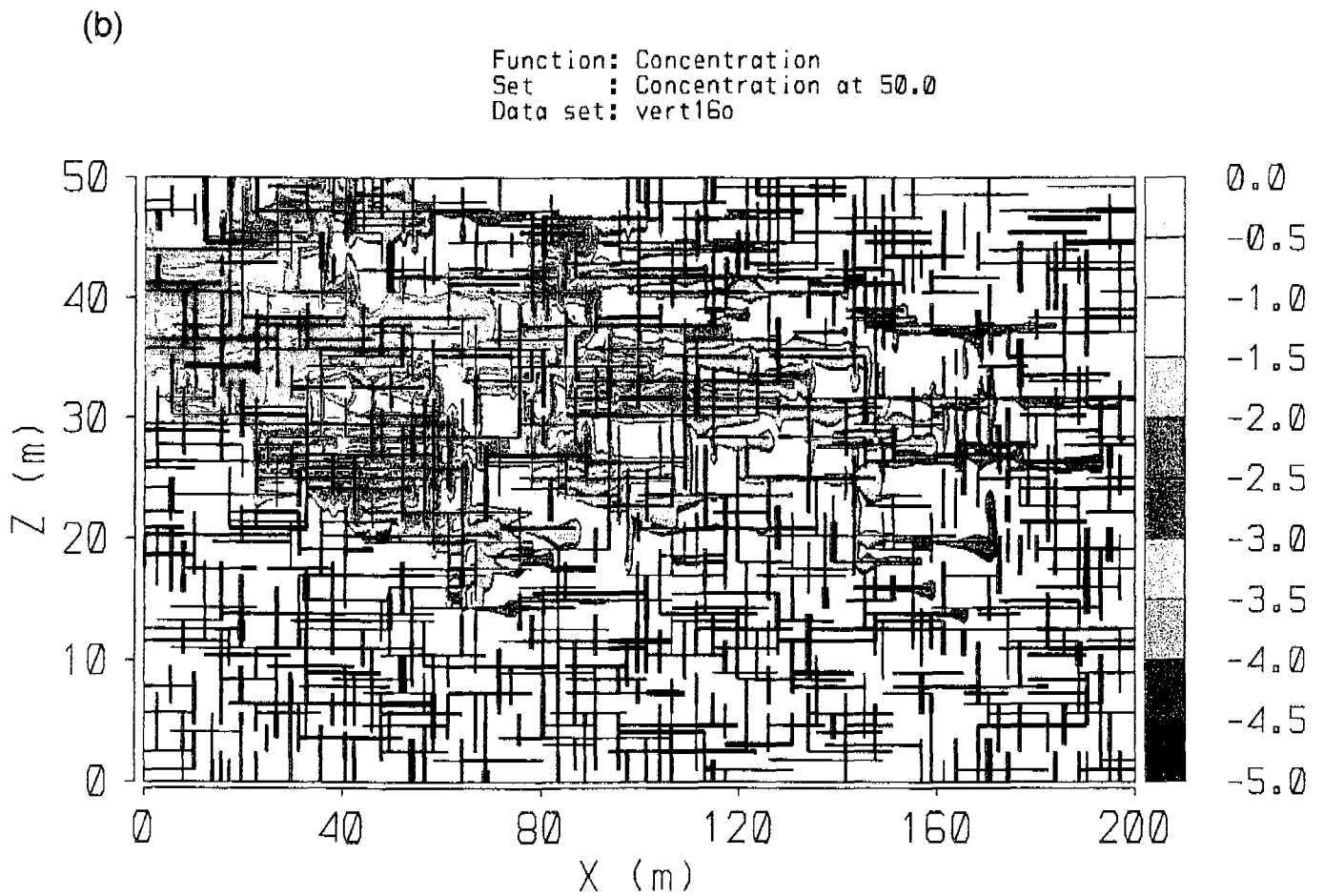
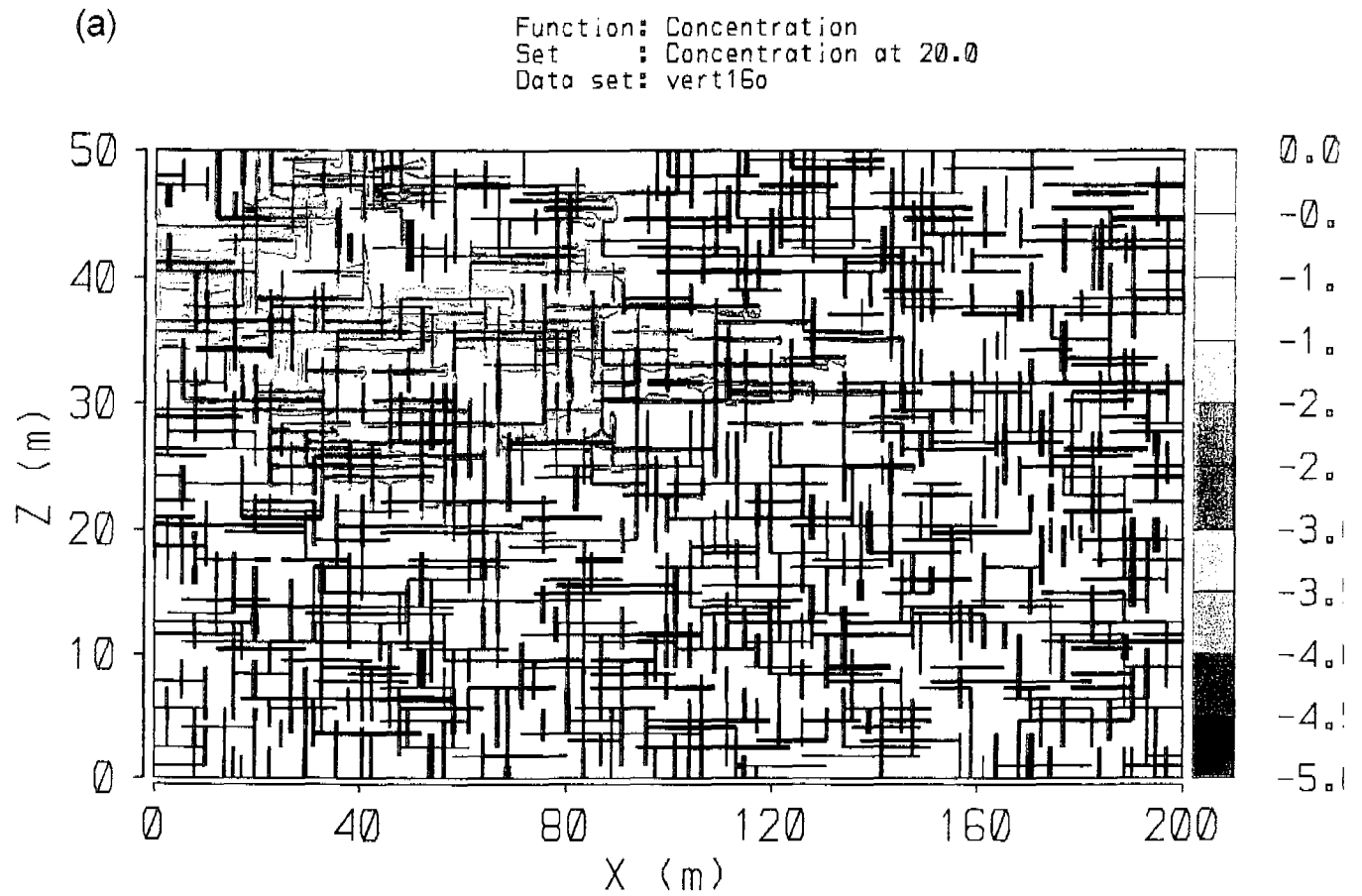
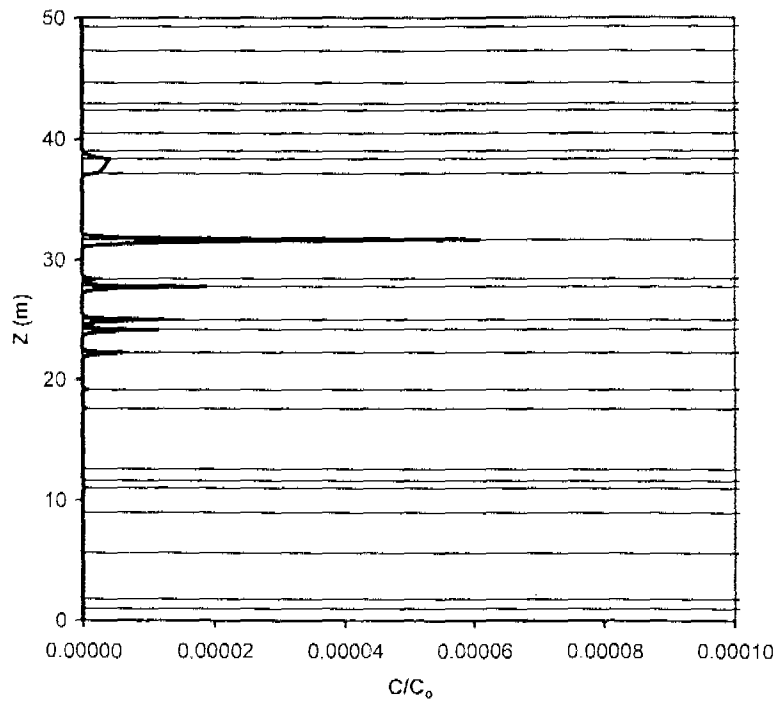


Figure 36

(a)

Concentration Profiles: X=200m; 50 years
Constant Source



(b)

Concentration Profiles: X=200m; 50 years
Constant Source

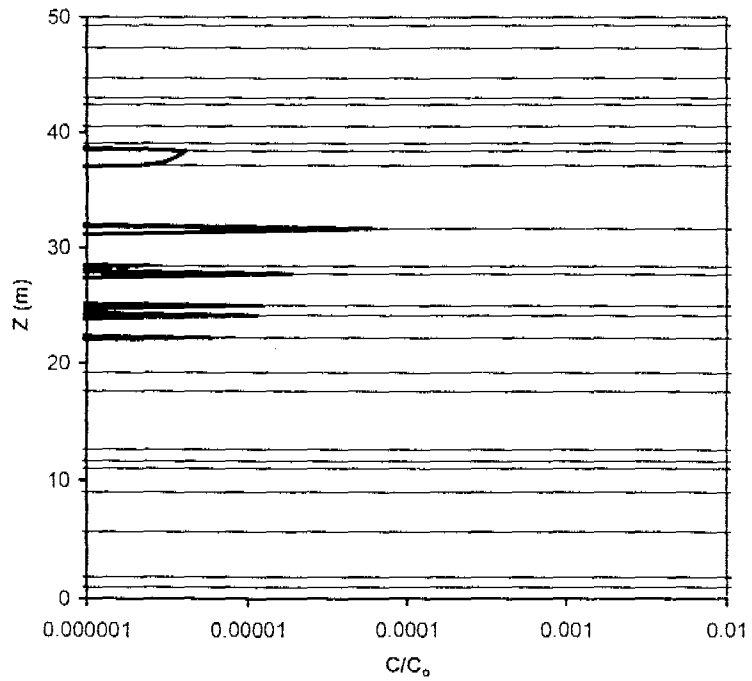


Figure 37

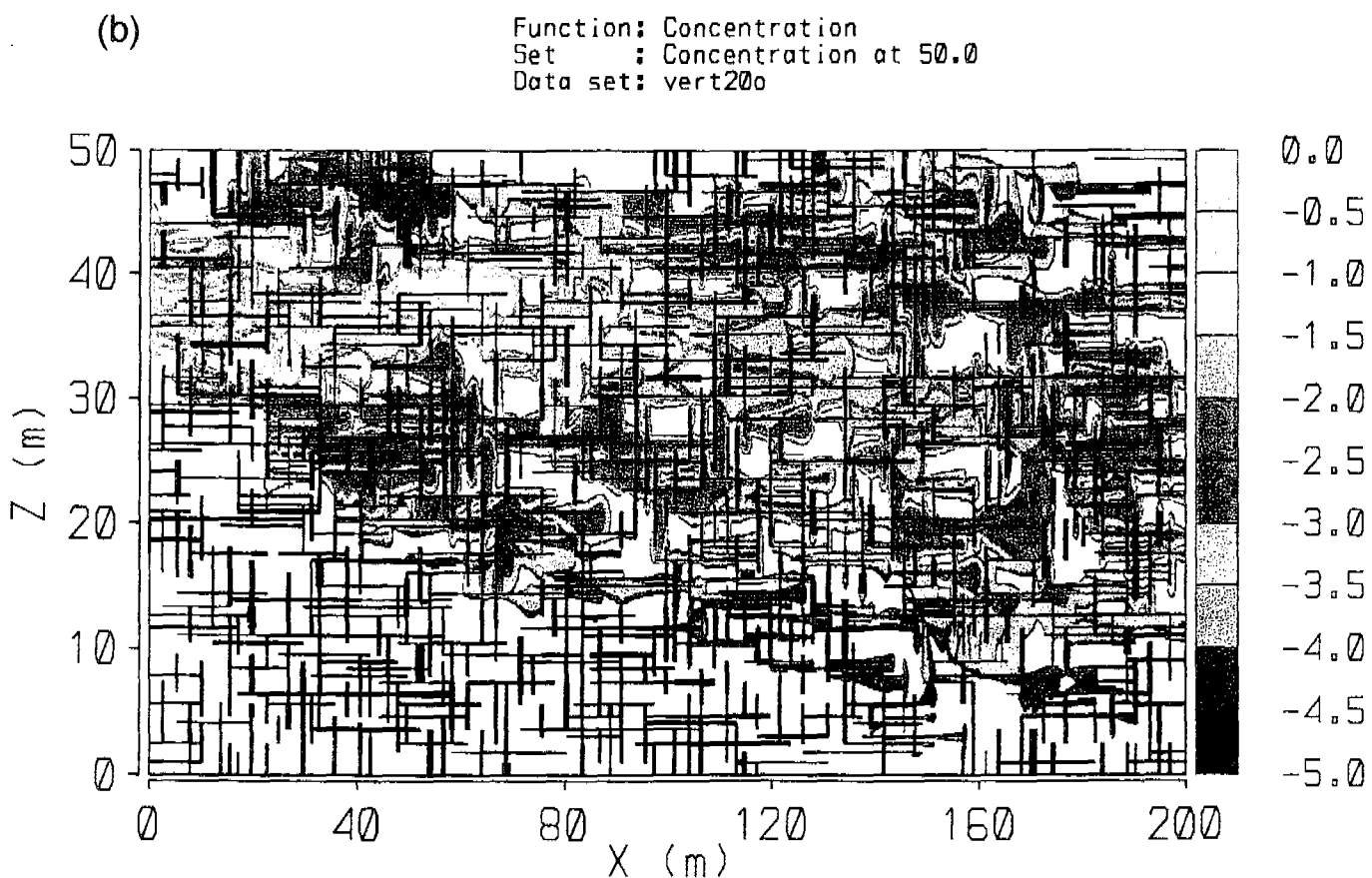
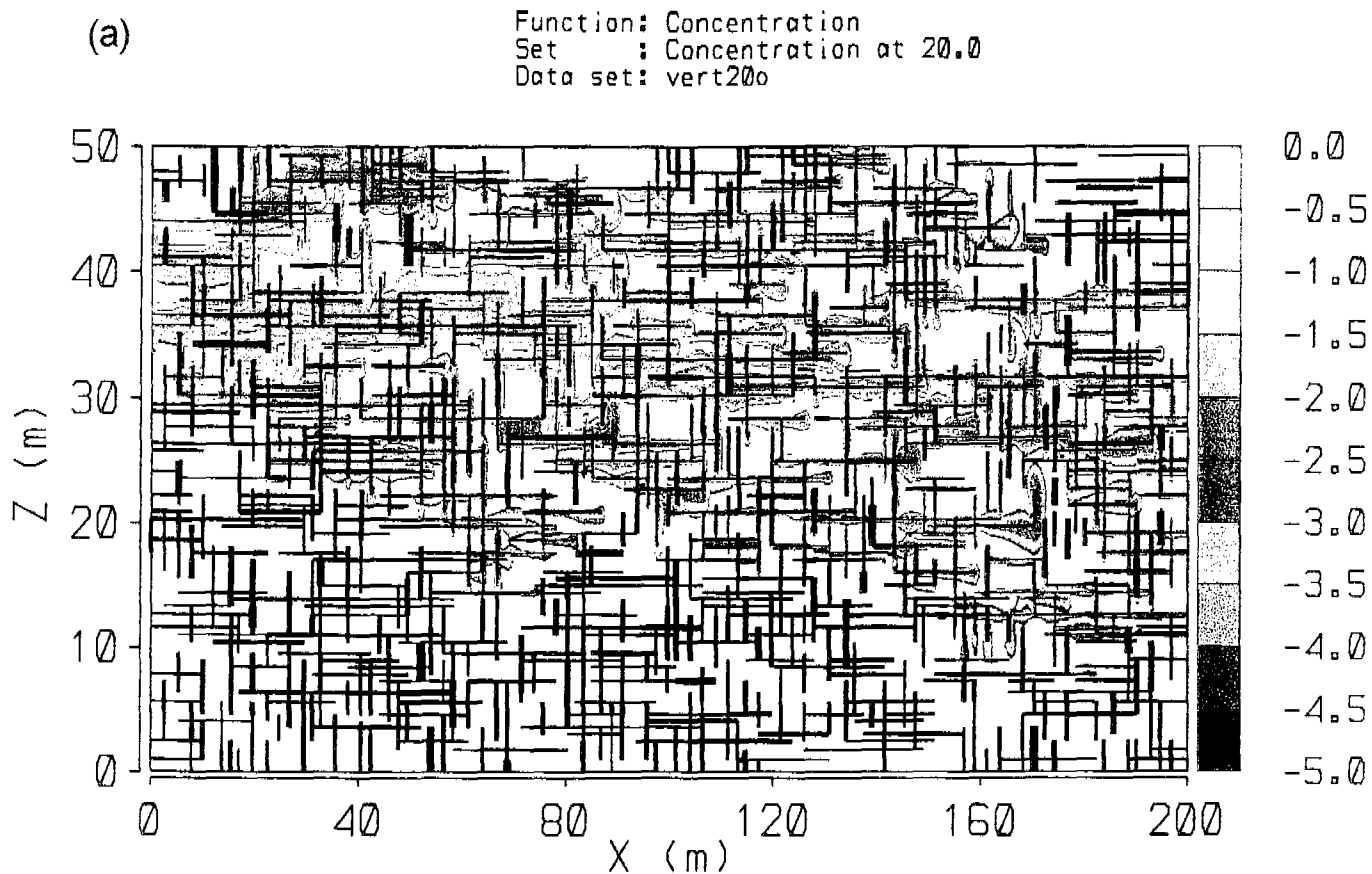


Figure 38

APPENDIX G

GROUNDWATER MONITORING IN FRACTURED SANDSTONE AND IMPLICATIONS FOR Santa Susana Field Laboratory Ventura County, CA

Prepared by:

John A. Cherry and Beth L. Parker
Department of Earth Sciences
University of Waterloo

Prepared for:

Montgomery Watson
1340 Treat Boulevard
Suite 300
Walnut Creek, CA 94596

and

Rocketdyne Propulsion and Power
The Boeing Company
6633 Canoga Avenue
Canoga Park, CA 91309-7922

CONTENTS

INTRODUCTION.....	1
SIMULATIONS USING A TWO DIMENSIONAL MODEL.....	3
DISPERSION.....	6
The Junction Effect.....	6
Dispersion In Each Fracture Plane.....	7
APPROACHES FOR MONITORING AT SSFL.....	8
Conventional Monitoring Wells.....	8
Monitoring By Rock Core Analyses.....	11
Removable Multilevel Systems.....	12
TEMPORAL VERSUS SPATIAL MONITORING.....	14
SUMMARY OF CONCLUSIONS.....	15
REFERENCES.....	17

INTRODUCTION

It is believed that the Chatsworth Formation can be monitored reliably to determine the spatial distribution of solutes such as TCE and other chemical constituents that may impact groundwater and also to determine the evolution of the solute distributions over time. This belief is based on five main factors:

- 1) The interconnected nature of the fracture network.
- 2) The strong influence of matrix diffusion on solute behaviour .
- 3) The distributory influence of dispersion on solute behaviour.
- 4) Results of modeling simulations of TCE in fractured sandstone.
- 5) Recent advances in monitoring methods.

The evidence for the first two factors is considered in other appendices. The other three factors are the focus of this appendix. The belief that monitoring can determine solute distribution does not imply that complete delineation of the solute zones is necessary, but rather that the determination of solute distribution can be accomplished to verify the conceptual site model at appropriate locations and for delineation where appropriate.

The term 'plume' derives from studies of air pollution in which the term has long been used to refer to zones of smoke or other contamination transported by air downwind of emission points such as smoke stacks. A plume in a hydrogeological context is an entity (continuum) of mobile dissolved contaminant mass that moves with the groundwater. It has a beginning at a source such as a landfill, mine tailing impoundment and/or NAPL zone that continuously supplies contaminant mass to the moving groundwater. As that plume migrates from the source the plume body has an interior and a front. The plume front is the leading edge of the dissolved contaminant zone defined by a specified concentration such as the detection limit, MCL or other value. Plumes are common in granular porous media, fractured media and fractured porous media. The ease of characterizing or delineating a plume in geologic media is a function of the complexity or heterogeneity of the system. Heterogeneity is affected by bedding/strata as well as the orderliness and interconnectedness of fracture networks. However, in all cases the plume is definable conceptually and advances along pathways that are necessarily connected. The plume serves as a tracer of the groundwater flow paths.

In this appendix, plumes are examined in the context of TCE in the Chatsworth Formation. This examination uses a discrete-fracture mathematical model for simulations of plumes in idealized fractured rock and an integration of concepts and experimental results of solute behaviour in single fractures and fracture networks.

SIMULATIONS USING A TWO DIMENSIONAL MODEL

A two dimensional model (FRACTRAN) developed by Sudicky and McLaren (1992) was used to simulate patterns of dissolved-phase transport in a network of discrete uniform fractures in which the fractures have variable length and are oriented either parallel or orthogonal to the general groundwater flow direction. This model has been used previously to study solute behaviour in several types of porous media with discrete fracture networks (e.g. Harrison et al. 1992). The model simulates steady groundwater flow through the model domain from left to right. The flow occurs exclusively through the fractures because the hydraulic conductivity assigned to the rock matrix is relatively small. The solute is transported in the fractures by groundwater flow (advection). As the solute front moves forward, dispersion occurs in the direction of flow in each fracture (longitudinal dispersion). The magnitude of the longitudinal dispersivity is constrained to being negligible in the simulations. The model is two-dimensional and therefore it does not include transverse dispersion in each fracture plane. At each fracture junction, the model produces complete instantaneous mixing of all solute molecules that enter the junction from different fractures.

Figure 3 shows the model domain, with a constant solute input to an area of fracture network 200m x 200m. The model domain is set up to represent a horizontal plane through a solute transport zone. Table 1 lists the geometric properties of the fracture network. Figure 4a shows the steady-state hydraulic head distribution. Figure 4b shows the pattern of solute transport in the fracture network for the case in which the rock matrix has negligible porosity. The bulk average linear velocity across the model domain (Darcy discharge based on the hydraulic conductivity times the hydraulic gradient divided by the bulk fracture porosity) is 1 mile per year (1.6 km per year). Thus, the front of the solute zone reaches the right-hand side of the model domain in less than three months and then the pattern of solute occurrence in the fracture domain shown in Figure 4b remains steady with time. The front of the zone moves quickly through the model domain because there is no retardation caused by matrix diffusion (i.e. zero matrix porosity). The front of the simulated solute zone described above would be very difficult to monitor

factor of five (i.e. anisotropy ratio of 5). This results in the solute plume moving nearly horizontally across the rectangular domain (Figure 8b).

Figure 9 represents the solute transport plume after 20 and 50 years. The plume is caused by the solute source near the upper left side of the model domain. Similar to Figure 5, the dashed line encompasses the area in which fractures contain solute at a relative concentration above 10^{-4} . The source contributes solute at a constant concentration for 10 years, which represents DNAPL occurrence causing solute saturation levels for 10 years. After 10 years, the DNAPL has disappeared from all of the fractures in the source zone by mass transfer to the rock matrix and the solute mass in the source zone begins to be depleted as groundwater flows through the source zone. Therefore, there is no addition of solute mass to the model domain after the end of the 10 year period. Figure 10 shows the solute distribution along a vertical line through the modeled domain at a distance of 50m downgradient of the source. C/C_0 represents the measured concentration relative to the initial concentration (i.e. TCE solubility). This 'sampling' of the modeled plume is analogous to the results of closely-spaced rock core analyses from a continuously cored hole. This figure also shows, for comparison, depth-averaged solute concentrations over vertical 'sampling intervals' of 15m (48 ft.) and 50m (160 ft.). These comparisons show that the concentration obtained from a monitoring location depends on the scale of sampling. The pattern of solute distribution in Figures 9a and 9b for the vertical domain are generally similar to the patterns in Figure 5 for the horizontal domain. This illustrates the expectation that, when considered in three dimensions, an interconnected fracture network with many fractures will produce a solute plume in which the solute occurs in many fractures of different orientation (e.g., vertical and horizontal fractures).

The simulations described above represent contaminant distributions in two-dimensional horizontal and vertical planes in which the fracture pattern represents the pattern of vertical or sub-vertical joints on the plane. This is analogous to taking a planar slice through the three-dimensional representation of the plume shown in Figure 2. In a real three-dimensional plume in sedimentary rock, contaminant migration also occurs along the bedding plane fractures. Therefore, a vertical borehole or well through the three-dimensional contaminant domain has enhanced probability of encountering solute. Also each two-dimensional horizontal planar domain through the plume shown in Figure 2 represents a pattern of vertical joints that has offsets from the patterns on horizontal planes above and below. At sites such as SSFL, this

The fracture information from boreholes and outcrops at SSFL are consistent with this conceptualization of the fracture network. (See Appendices A, B, and E).

Dispersion In Each Fracture Plane

In addition to the dispersion that occurs at junctions, longitudinal (in the flow direction) and transverse (orthogonal to flow) dispersion of the solute also takes place in each fracture plane. This dispersion is caused by the large variability of aperture along each fracture as illustrated by Figure 12. Aperture variability along each fracture causes the solute molecules to follow irregular pathways of preferential groundwater flow. The phenomenon of preferential flow, commonly described as channeling, has been invoked to explain dispersion in many laboratory and field studies of solute transport in fractured rock. The channeling effect due to aperture variability along each fracture causes each solute molecule transported by the flowing groundwater in the fracture, to follow a very irregular path (Figure 13a). This effect insures that solute occurrence is not restricted to narrow enclosures as it moves from fracture to fracture. This spreading effect makes the solute easier to find and thus monitor due to its transverse spread. The consideration of many solute molecules transported by groundwater in the single fracture provides a vision of many small plumes spreading laterally as they advance along the fracture (Figure 13b). The individual 'plumes', or more correctly 'plume segments', are caused by channeled flow in the fracture. Varying rates of groundwater flow from channel to channel impose lateral concentration gradients on the plume segments. The lateral concentration gradients result in transverse dispersion within the fracture plane. This process of lateral dispersion occurs in each fracture plane where solute transport occurs.

The most detailed field experiment to demonstrate the effects of transverse (orthogonal to flow) and longitudinal dispersion (in the flow direction) in a single horizontal fracture was conducted by Lapcevic et al. (1999) in a bedded shale and limestone rock sequence near Toronto, Ontario (Table 3). This experiment, which was initiated by injecting a small volume of tracer into the fracture plane, involved monitoring tracer movement in 27 boreholes in a 35 x 40 m area (Figure 14). Test data revealed a tracer plume that spread both longitudinally and transversely in the direction of mean groundwater flow (Figure 15).

The tracer arrival curves were simulated using a two-dimensional numerical model for solute transport that incorporated both transverse and longitudinal dispersion, diffusion into the rock matrix and constant fracture aperture. The mean aperture obtained from this modeling was close

- removable multilevel monitoring systems

Figures 17,18 and 19 illustrate these three approaches. Figure 20 shows the locations of the monitoring wells and Figure 21 shows the two locations (RD-35 and RD-46) where removable multilevel systems were used. In addition to these three methods of sampling groundwater from boreholes, rock core analyses were used at the two locations of the removable multilevel systems (RD-35 and RD-46) to determine VOC concentrations in the rock matrix.

In response to changes in general practice in the hydrogeological profession and to adapt to new information provided by monitoring results, there has been an evolution in the approach to bedrock monitoring since monitoring began in 1983. The purpose of this Appendix is to comment on each of the methods in light of the most recent advances in monitoring technologies and approaches. Long open boreholes were the preferred monitoring method in the 1980's because they were believed to be the most cost-effective means of locating plumes. Although the long open boreholes did locate several plumes, they produced blended values of water level and solute concentration. These concentrations are generally not representative of actual concentrations in the plume at the borehole location. In cases where no VOC's are detected, the long open boreholes also provide the possibility that actual VOC's at the location are diluted to levels below detection by mixing in the borehole. Therefore, long open boreholes are no longer a preferred method of monitoring.

Long open boreholes present another disadvantage. In some cases, cross connection in the borehole causes shallow water to flow downward in the borehole and then outward into deeper fractures. This type of borehole cross connection was observed in RD-35B, as described in the M.Sc. thesis by Sterling (1999). Sterling (1999) shows a comparison of the hydraulic head profiles obtained using a removable multilevel system (Solinst system) at RD-46B and the blended head from this hole measured after the multilevel system was removed from the hole. When removed, the hole behaved as a long open well bore. The blended head was dominated by one fracture zone in the hole that had a high head and a relatively large hydraulic conductivity. This blended head was much different than the mean head calculated from the discrete-level head measurements in the hole. In other cases cross connection in the borehole causes upward flow, as occurred in RD-46B (Sterling 1999).

water containing TCE originating from at least several fractures at various distances from the well. Thus, the TCE concentration measured in the sample is a blended value dependant on the local details of fracture network. The fact that each well samples a domain that is local but has appreciable size, provides confidence that the plume, if it exists in the vicinity of the well, will be detected by the sampling. Additional insight into the distribution of TCE in the vicinity of a monitoring well can be obtained by analysis of a series of samples collected from the pumped water over a time starting soon after purging begins. Each subsequent sample is drawn to the well from a zone farther from the well bore.

Monitoring By Rock Core Analyses

Another approach for monitoring plumes in fractured sandstone involves the analysis of rock samples obtained from continuous cores. For volatile organic investigations in rock this approach was first used in North America by B.L. Parker at a fractured sandstone site, in Rochester, N.Y. in 1989. It has also been applied to determine PCE occurrence in the Chalk Aquifer in England (Lawrence et al. 1990), where this "rock" is soft so that cores were taken using the push-tube method rather than the rotary drilling method necessary in most sedimentary rocks. The core sampling approach to identify contaminant migration pathways is shown schematically in Figures 22 and 23.

This rock core method was used at two locations at SSFL (RD-35B and RD-46B) where continuously cored holes were drilled in 1998. The core holes were drilled by standard diamond-bit drilling with water mist circulation. Soon after arrival of the core at surface many small pieces of core were removed for the VOC analyses. The field procedure for obtaining and then preserving the rock pieces for analyses was developed to minimize loss of volatile organics from the samples. Figure 21 illustrates the approach used for sampling the core and sample processing. The rock samples for VOC analyses were collected from the continuous core (5 foot segments) at a rate that did not slow the drilling operations. The sample analyses were done in an offsite laboratory using standard methods. Sterling (1999) describes the procedure, and the results summarized by Figure 25. He provides evidence indicating that minimal TCE loss occurred during coring and sample processing. Rock core analyses provide detailed information on the vertical distribution of TCE at each core hole location. Unlike monitoring well data, rock core VOC profiles can be used to determine the VOC mass storage depth at each location and to identify specific VOC migration pathways. The analysis of core samples from many depths in each hole avoids possibilities of not identifying all major VOC pathways within the vertical span

Another design for multilevel monitoring in boreholes was developed by Cherry and Johnson (1982) which later became available commercially (The Waterloo System) from Solinst Canada Limited in 1988. These systems have many monitoring intervals (ports) in each hole; each open interval has a specified vertical length with inflated packers above and below to prevent vertical leakage. The systems provide both hydraulic head data and water samples from each monitoring port. The Westbay System and the Waterloo System have been used at many fractured rock contaminated sites around the world, however they have the disadvantage of being very difficult to remove or decommission once the need for monitoring ends or when failure of downhole components occurs. In 1998 two new multilevel systems became available, one from Solinst Canada Limited and one from Flexible Liner Underground Technologies Limited of Santa Fe, New Mexico. These two systems are designed to be easily removed from boreholes once the need for monitoring ends or to reconfigure or repair the systems for continued use in the holes. The removable Solinst System is an adaptation of the earlier permanent system for groundwater monitoring in rock. A prototype version of the removable Solinst System was used in RD-35B and RD-46B in 1998. The new system uses water inflated packers that are easy to inflate and deflate (Figure 18). The installation of the two removable systems at SSFL in 1998 was the first field use of this device. The two Solinst systems performed successfully. Two minor design problems have been corrected by changes in the current version of the system.

The FLUTE system has been used in many holes in the vadose zone since it was developed in 1990, however, use below the water table only began in 1998. Both the FLUTE and Solinst systems have the same design goals: to acquire head data and groundwater samples from several different depths in each borehole for a set period of time after which the system can be removed from the hole. The successful use of the Solinst System in RD-35 and RD-46, and successful uses of the FLUTE system at other fractured rock sites since 1998 indicate that these two systems are now proven alternatives to the use of cluster wells for groundwater monitoring. These systems are well suited for acquisition of vertical profiles of hydraulic head. Such profiles are needed to develop a clear understanding of the groundwater flow systems and the migration of TCE solute. The monitoring systems can also be used for groundwater sampling for VOC and other chemical analyses. However, as demonstrated by the cross connection effects observed in RD-35B, it is necessary to minimize open-hole time prior to installing the multi-level system in order for the system to produce chemical results representative of the in situ conditions. The FLUTE and Solinst systems are rugged so that they can be left in place for long periods of

location. These data sets can accomplish plume characterization and conceptual model verification. In the first step in the data acquisition process, a cored hole is drilled and samples for rock core VOC analyses are collected as drilling proceeds. Borehole geophysics are then conducted to provide geological information and to identify the most active hydraulic flow zones. At SSFL, the bulk hydraulic conductivity and fractures are small so that the detection limits for flow zone identification are higher than all but the most active flow zones. Based on the rock core log and rock core VOC analyses, a removable multilevel system is then installed to measure the hydraulic head profile for a period of time and in some cases to sample groundwater. Between these stages of borehole use, the hole should be plugged with a flexible liner to prevent cross connection. A period of a few months to a year may be needed to complete all of the stages. After completion of the above steps, the borehole can be permanently decommissioned by grouting, or temporarily decommissioned using a flexible liner plug. It may also be decided that a permanent monitoring well should be placed in the hole to monitor a critical depth interval identified from the comprehensive data set.

SUMMARY OF CONCLUSIONS

The hydrogeological conditions of the Chatsworth Formation at SSFL are very favourable for monitoring to determine source zone and plume characteristics and to verify the site conceptual model. The conditions are favourable for several reasons:

- 1) The overall structural geology and stratigraphy is not unduly complex,
- 2) The fracture network is comprised of many interconnected fractures,
- 3) Matrix diffusion combined with matrix sorption and small fracture apertures causes very slow TCE migration,
- 4) Dispersion and other factors cause the TCE impacted zones to spread transverse to the main directions of groundwater flow, which increases the target size for locating plumes by monitoring,
- 5) The rock characteristics are such that rock core analyses can be used to locate VOC mass, and
- 6) The boreholes generally have sufficient stability to allow for multiple entries with monitoring devices such as geophysical tools and removable multilevel monitoring systems.

REFERENCES

- Castillo, E., R.J. Krizek and G.M. Karadi, 1972. Comparison of dispersion characteristics of fissured rock. Proc. Sec. Symp. Fundamentals of Transport Phenomena in Porous Media, Vol. II, pp. 778-797.
- Chernyshev, S.N. and W.R. Dearman, 1991. Rock Fractures. Butterworth-Heinmann, Reed Book Services Ltd., Northants, England, 272 pp.
- Cherry, J.A. and P.E. Johnson, 1982. A multilevel device for monitoring in fractured rock, Ground Water Monitoring Review, Vol. 2, no. 3, pp. 41-44.
- Freeze, R.A. and Cherry, J.A., 1979. "Groundwater" (a textbook), Prentice-Hall Inc., Englewood Cliffs, N.J. 604 pp.
- Harrison, B., E.A. Sudicky and J.A. Cherry, 1992. Numerical analysis of solute migration through fractured clayey deposits into underlying aquifers. Water Resources Research, Vol. 28, pp. 515-526.
- Krizek, R.J., G.M. Karadi and Enrique Socias, 1972. Dispersion of a contaminant in fissured rock. Proc. Symp. Percolation Through Fissured Rock, Stuttgart, T3-C, 1-15.
- Lapcevic, P.A., K.S. Novakowski and E.A. Sudicky, 1999. The interpretation of a tracer experiment conducted in a single fracture under conditions of natural groundwater flow. Water Resources Research, Vol. 35, No. 8, pp. 2301-2312.
- Lawrence, AR., P.J. Chilton, R.J. Barron and U.M. Thomas, 1990. A method for determining volatile organic solvents in chalk pore waters (Southern and Eastern England) and its relevance to groundwater contamination. J. Contaminant Hydrology, Vol. 6, pp.377-386.
- Sterling, S.N., B.L. Parker, and J.A. Cherry, 2000. Comparison of new and conventional field methods for characterizing trichloroethene distribution in a fractured sandstone. Submitted to Groundwater 2000 International Conference on Groundwater Research, June 6-8, Copenhagen, Denmark.
- Sudicky, E.A. and R.G. McLaren, 1992. The Laplace Transform Galerkin Technique for large-scale simulation of mass transport in discretely fractured porous formations. Water Resources Research, Vol. 28, No. 2, pp. 499-514.

Table 1: Fracture Network Properties Plan View Domain; Uniform 100 μm Fractures

Fracture connection density = 0.033 connections/m²

	Parallel Fractures	Transverse Fractures
minimum fracture spacing (m)	2.0	2.0
fracture density (fractures/m ²)	0.015	0.015
minimum fracture length (m)	10	10
maximum fracture length (m)	20	20
average fracture frequency (fractures/m)	0.15	0.15
average fracture spacing (m)	6.7	6.7

Note: fracture frequency and density were estimated by counting the # of fractures along 3 profiles in each direction and averaging the results.

Table 3: Fracture Network Properties: Vertical Cross-Section Domain; Uniform 100 μm Fractures

Fracture connection density = 0.141 connections/m²

	Horizontal Fractures	Vertical Fractures
minimum fracture spacing (m)	0.5	1.5
fracture density (fractures/m ²)	0.050	0.075
minimum fracture length (m)	10	2
maximum fracture length (m)	20	5
average fracture frequency (fractures/m)	0.58	0.19
average fracture spacing (m)	1.7	5.4

Note: fracture frequency and density were estimated by counting the # of fractures along 3 profiles in each direction and averaging the results.

APPENDIX: Groundwater Monitoring In Fractured Sandstone And Implications For SSFL

FIGURES / CAPTIONS

1. Contrasts in features between two types of contaminant impacted groundwater zones (a) difficult to monitor, (b) favorable to monitor.
2. Three dimensional conceptual view of a plume in fractured sandstone with an orderly network of interconnected fractures.
3. Boundary conditions and internal characteristics of the planar model domain of the discrete fracture network modeling using FRACTRAN (a) schematic of model view, (b) plan view model domain.
4. Model results: (a) steady-state hydraulic head distribution showing gradient from left to right, (b) pattern of solute distribution showing transport pathways for the case with no matrix diffusion.
5. Horizontal plane model results for the case with matrix diffusion and sorption: the dashed line encompasses all fractures containing solute. The area inside this dashed line represents the plume. (a) the solute distribution after 20 years (b) the solute distribution after 50 years.
6. Schematic illustration of the vertical groundwater flow domain used in the planar cross section FRACTRAN modeling.
7. Characteristics of the variable-aperture fracture network used in the planar cross section FRACTRAN modeling (a) fracture network, (b) statistical features of the network.
8. Hydraulic features of the modeled domain: (a) hydraulic conductivity and velocity, and (b) steady-state hydraulic head distribution.
9. Vertical plane model results for the case of matrix diffusion with sorption: (a) solute distribution after 20 years, (b) solute distribution after 50 years.
10. Vertical profile of solute distribution in fractures and the rock matrix at 50 m from the input location after 50 years of solute transport: (a) arithmetic plot of concentration profile with vertically averaged zones, (b) log scale plot of the high concentration zone.
11. Schematic illustration of the effects of solute mixing at fracture intersections (junctions): (a) detailed view of three junctions, each receiving clean and contaminated water, (b) the transverse dispersion effect caused by junction mixing.

(a)

**Source
Zone**

**Source
Zone**

Plume

(b)

Figure 1: Contrasts in features between two types of contaminant impacted groundwater zones (a) difficult to monitor, (b) conducive to monitoring.

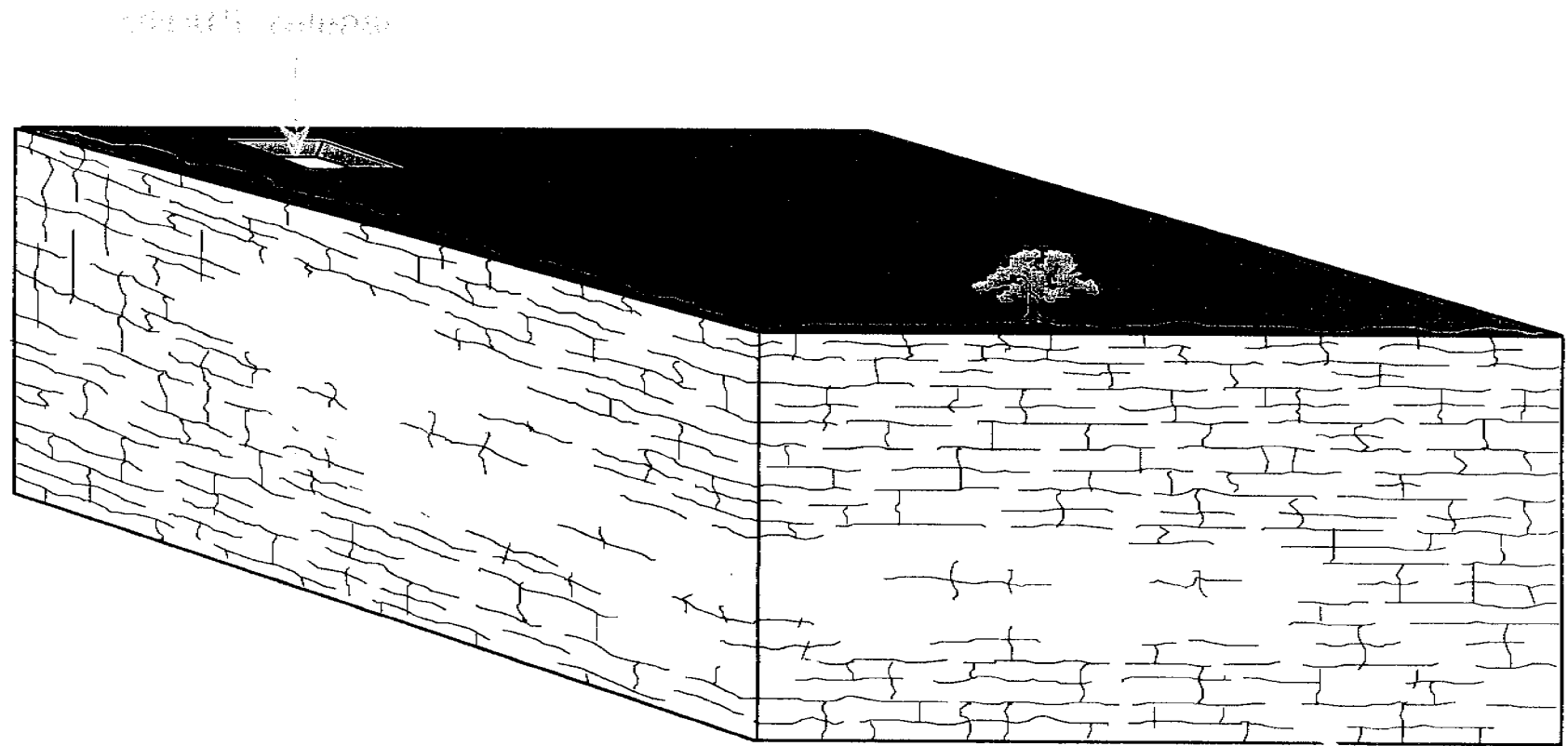


Figure 2: Three dimensional conceptual view of a plume in fractured sandstone with an orderly network of interconnected fractures.

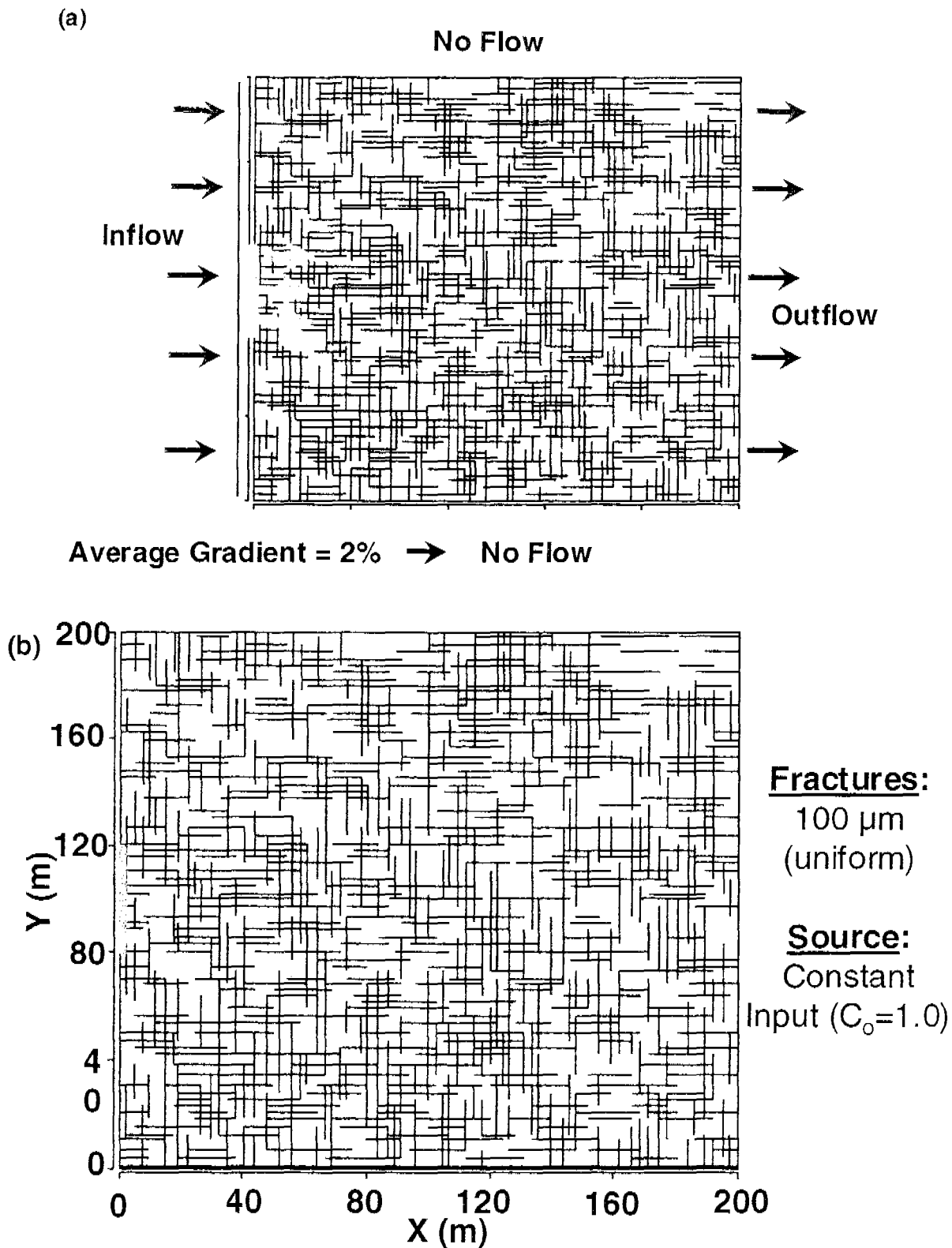


Figure 3: Boundary conditions and internal characteristics of the planar model domain of the discrete fracture network modeling using FRACTRAN (a) Schematic of model view; (b) Plan view model domain.

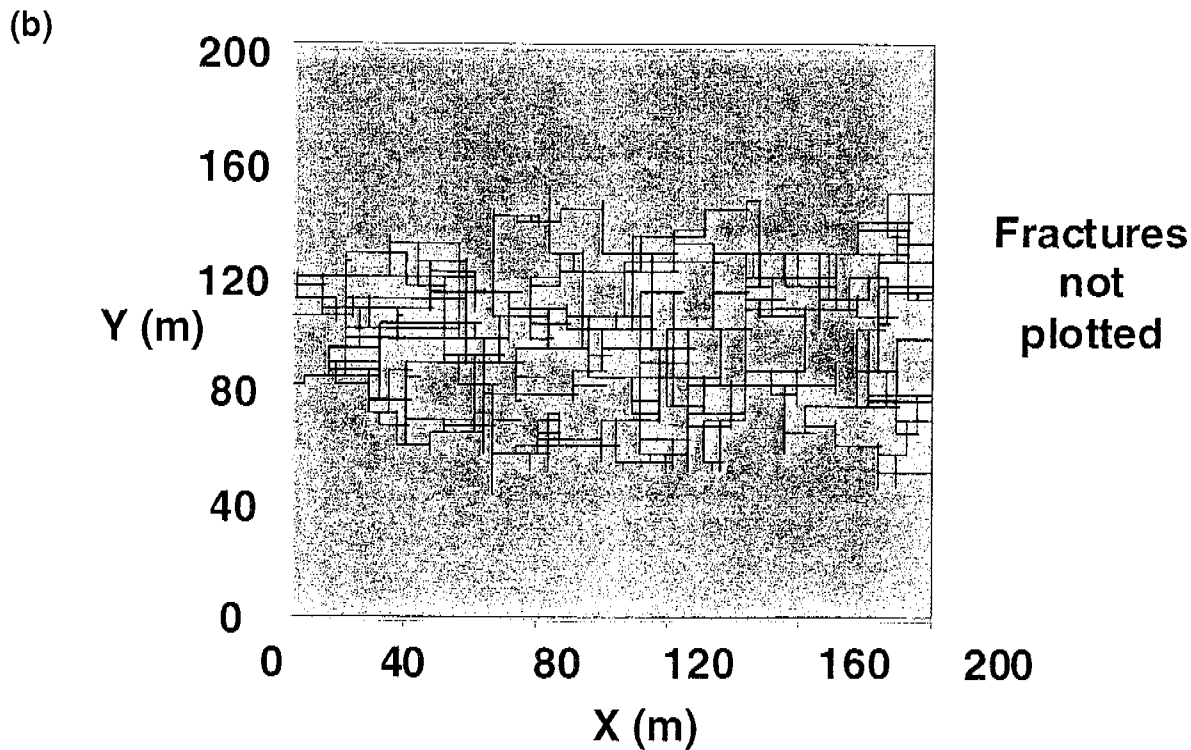
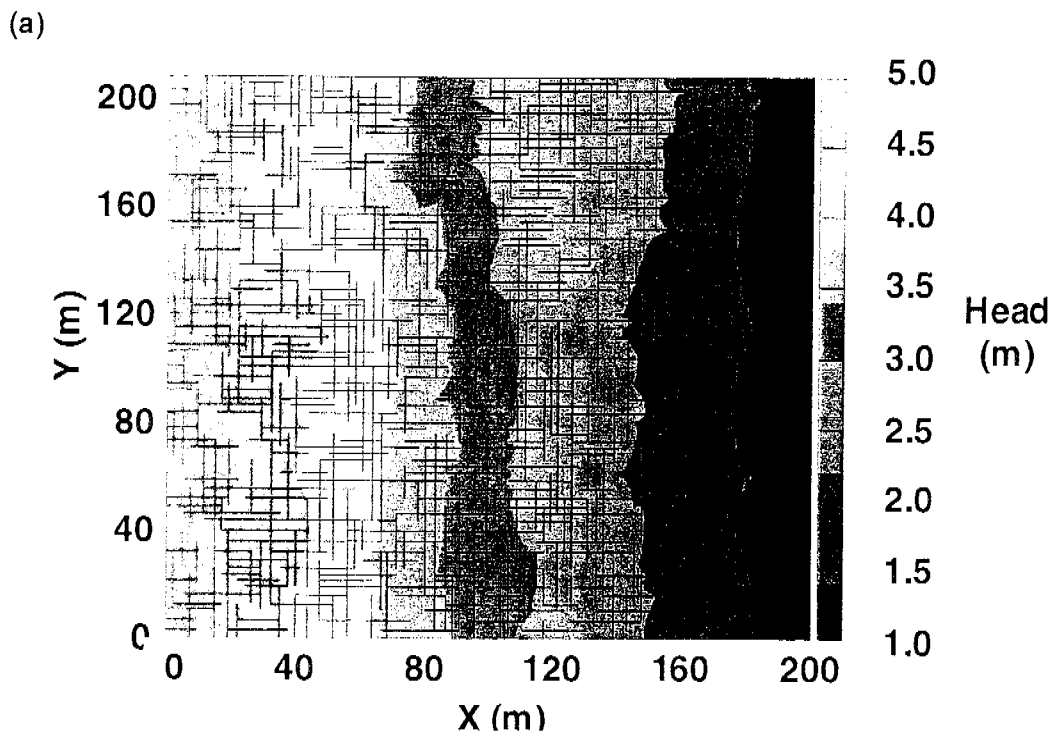


Figure 4: Model results: (a) steady-state hydraulic head distribution showing gradient from left to right, (b) pattern of solute distribution showing transport pathways for the case with no matrix diffusion.

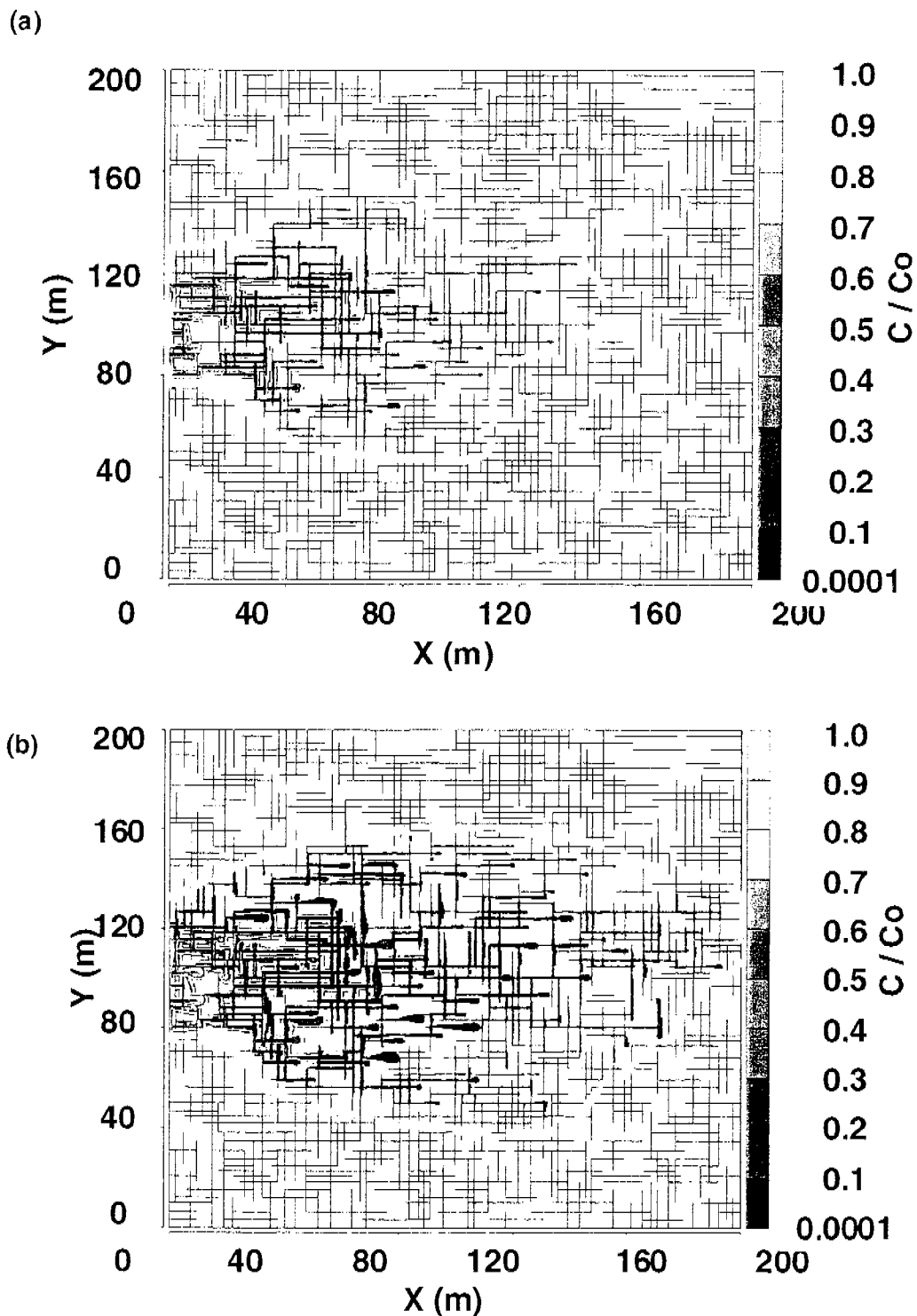


Figure 5: Horizontal plane model results for the case with matrix diffusion and sorption: the dashed line encompasses all fractures containing solute. The area inside this dashed line represents the plume. (a) the solute distribution after 20 years; (b) the solute distribution after 50 years.

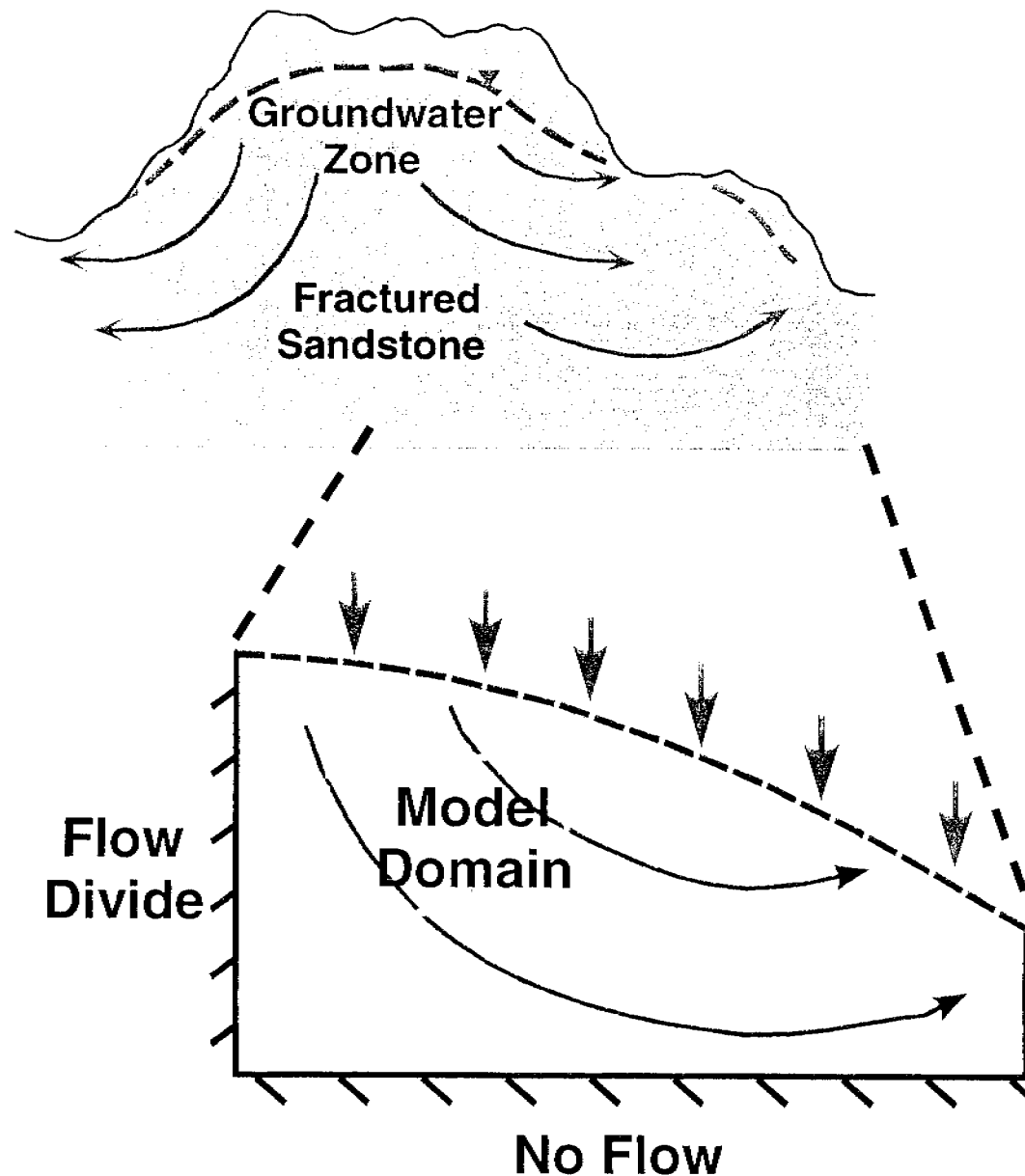


Figure 6: Schematic illustration of the vertical groundwater flow domain used in the planar cross section FRACTRAN modeling.

(a)

Mean Aperture $70 \mu\text{m}$

Bulk Hydraulic Conductivity (K):

$$\left. \begin{array}{l} K_x = 1.5 \times 10^{-5} \text{ cm/sec} \\ K_z = 3.0 \times 10^{-6} \text{ cm/sec} \\ \phi_f = 5.9 \times 10^{-5} \end{array} \right\} \begin{array}{l} K_x = \text{horizontal} \\ K_z = \text{vertical} \\ \text{Anisotropy Ratio} \sim 5 \end{array}$$

Estimated Average GW Velocity (2% gradient):

$$V_f = \frac{K_b i}{\phi_f} \sim 1.6 \text{ km/yr} \quad (1 \text{ mile/yr})$$

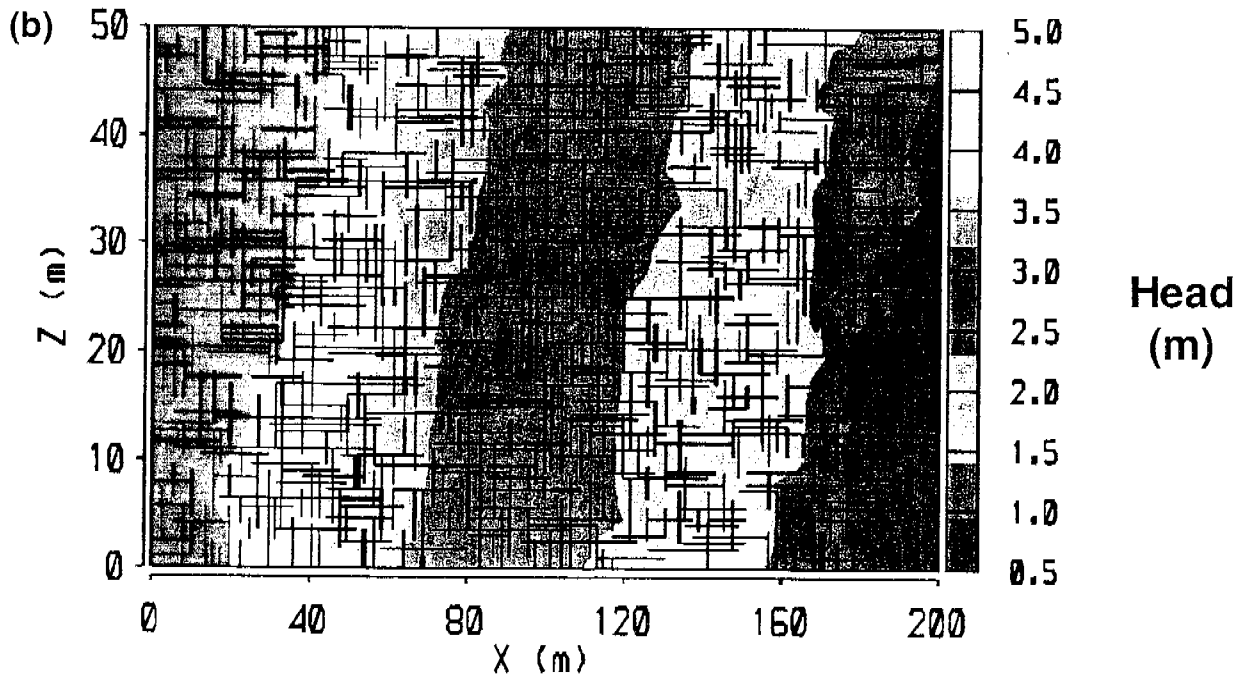


Figure 8: Hydraulic features of the modeled domain: (a) hydraulic conductivity and velocity, and (b) steady-state hydraulic head distribution.

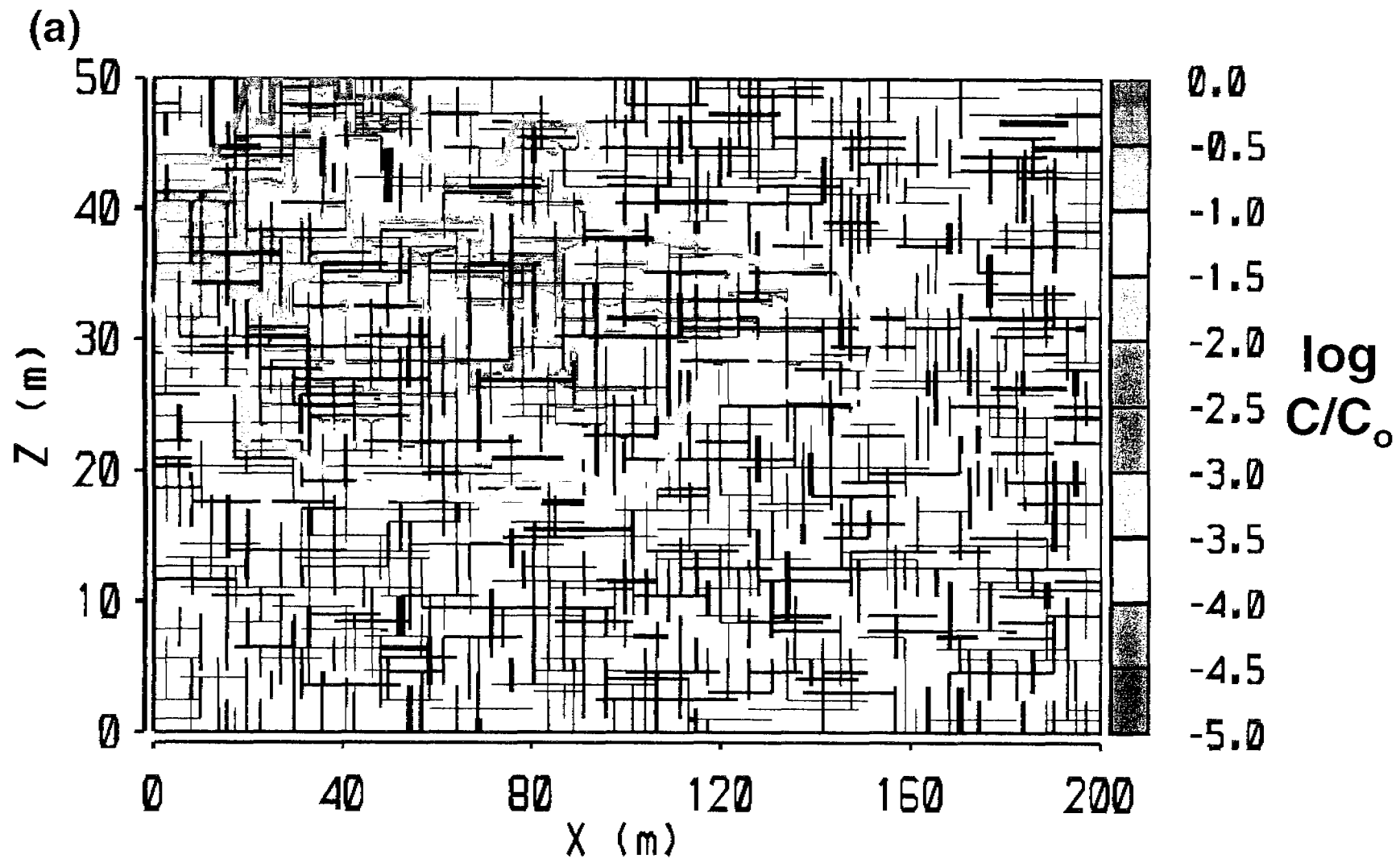


Figure 9: Vertical plane model results for the case of matrix diffusion with sorption:
(a) solute distribution after 20 years.

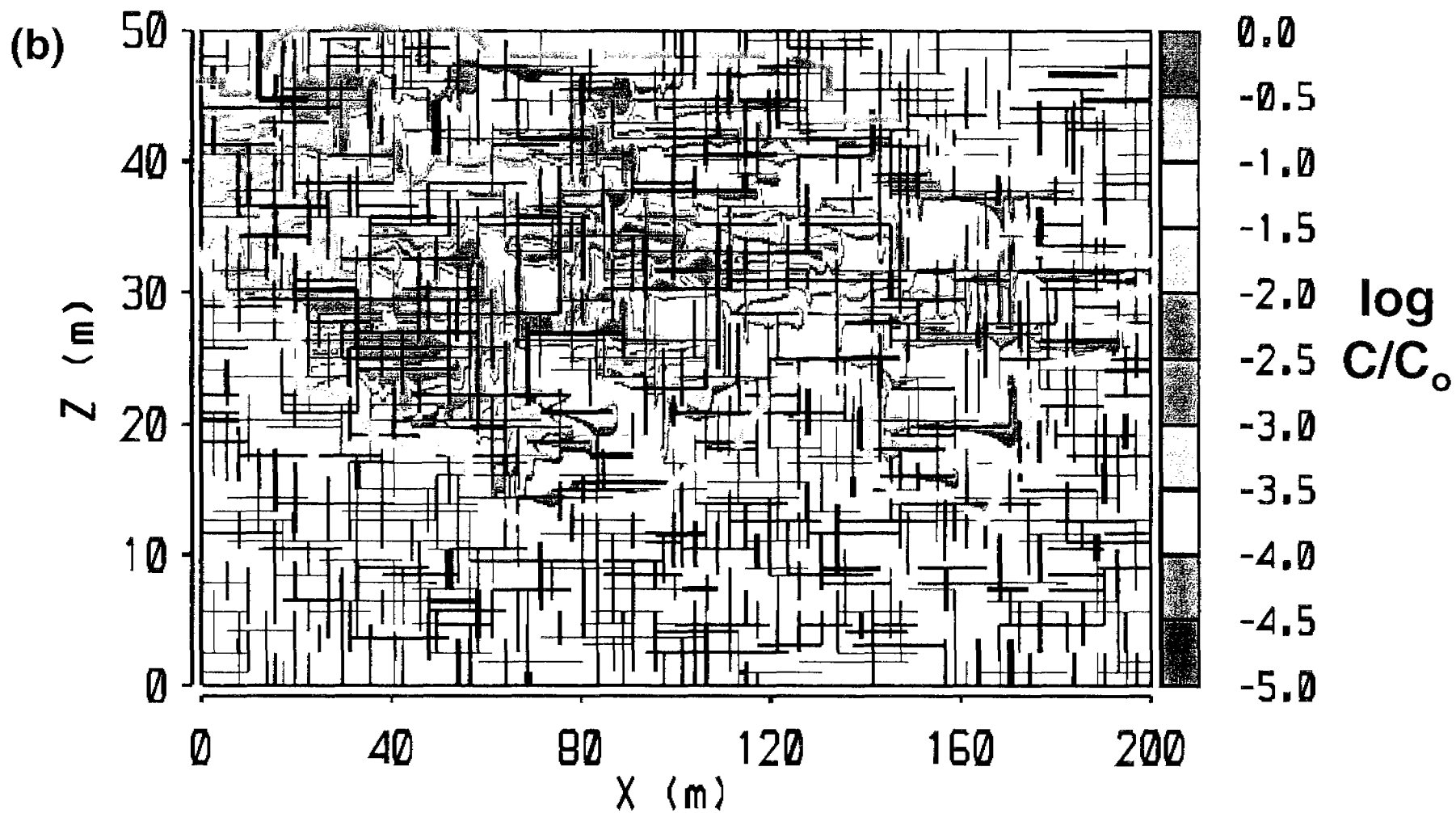
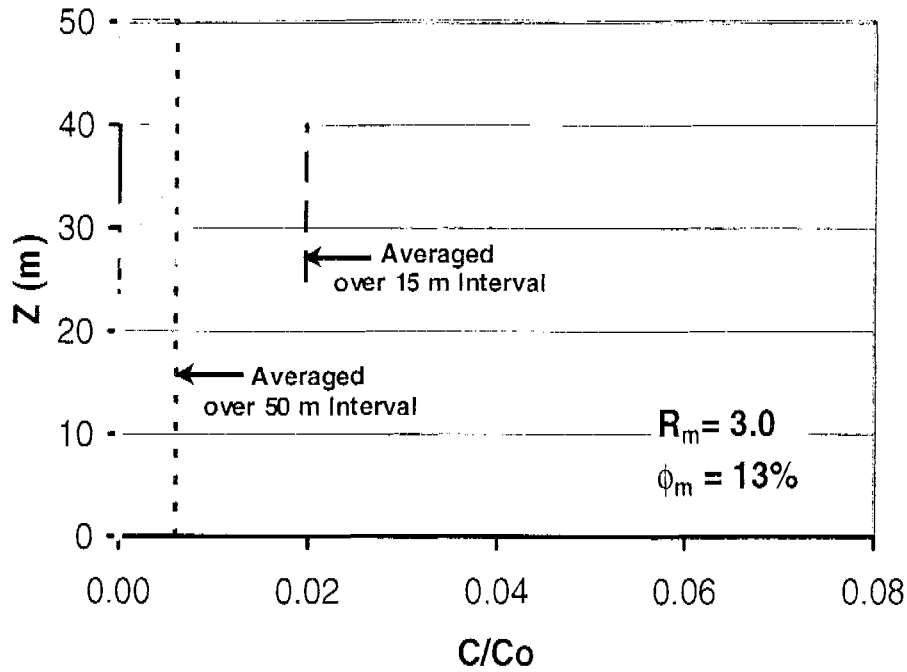


Figure 9: Vertical plane model results for the case of matrix diffusion with sorption: (b) solute distribution after 50 years.

(a)



(b)

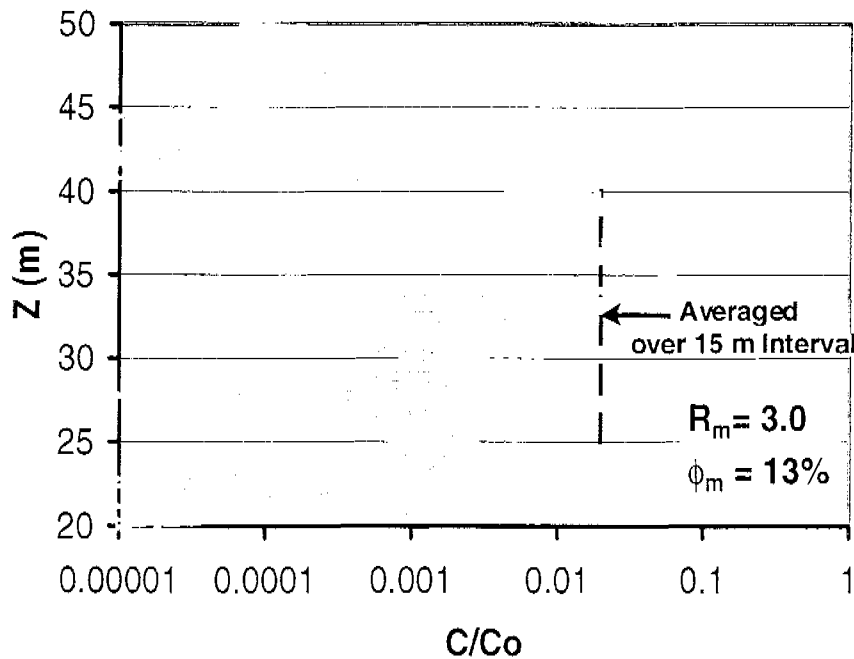


Figure 10: Vertical profile of solute distribution in fractures and the rock matrix at 50 m from the input location after 50 years of solute transport: (a) arithmetic plot of concentration profile with vertically averaged zones, (b) log scale plot of the high concentration zone.

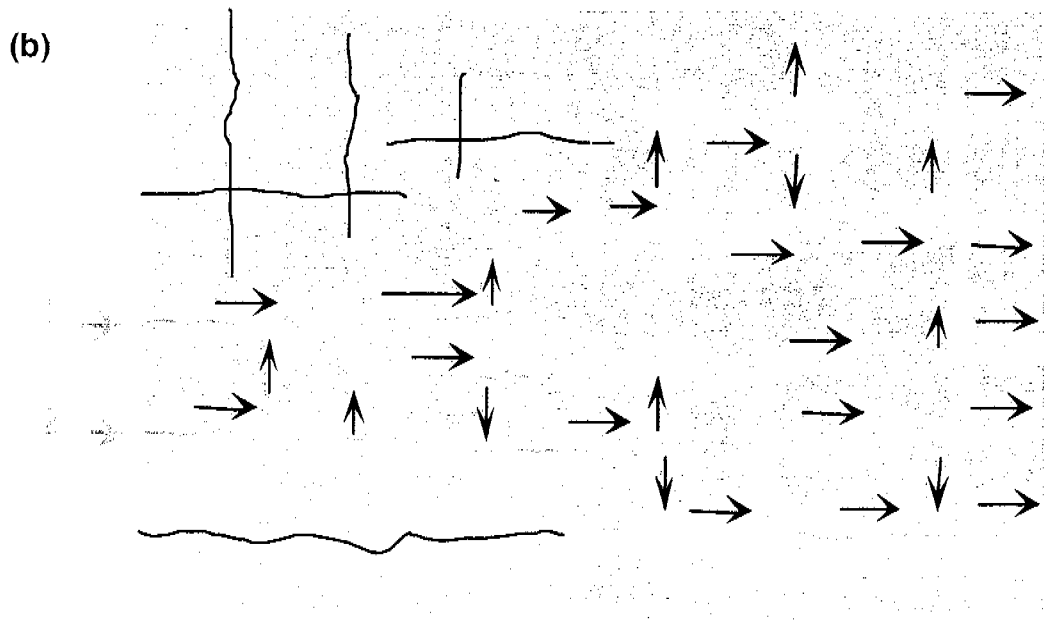
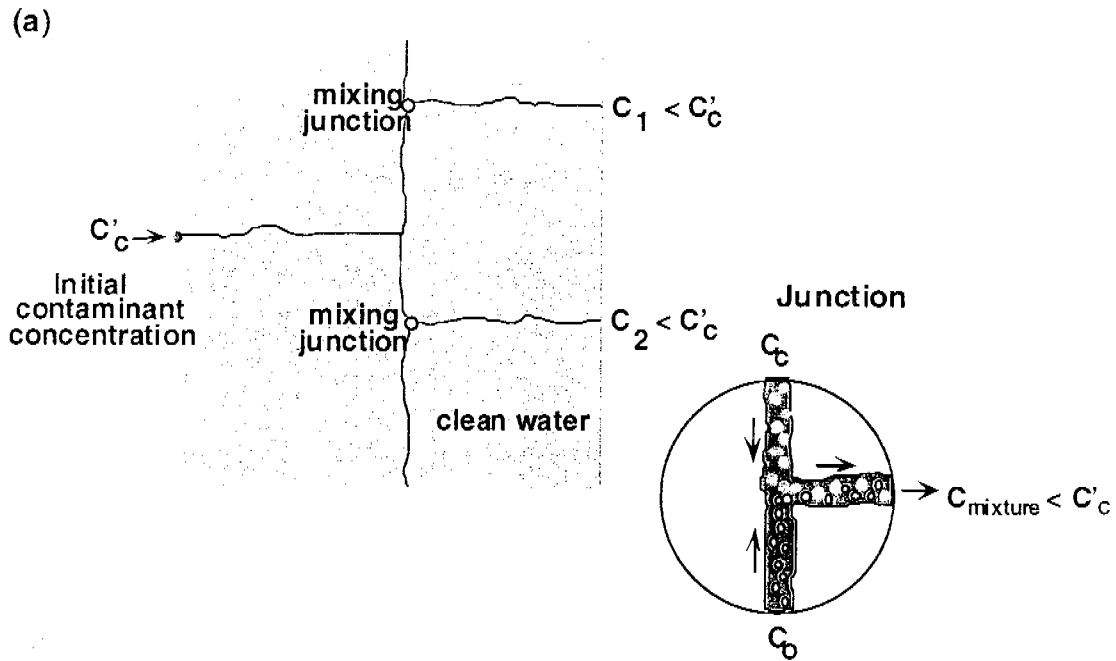
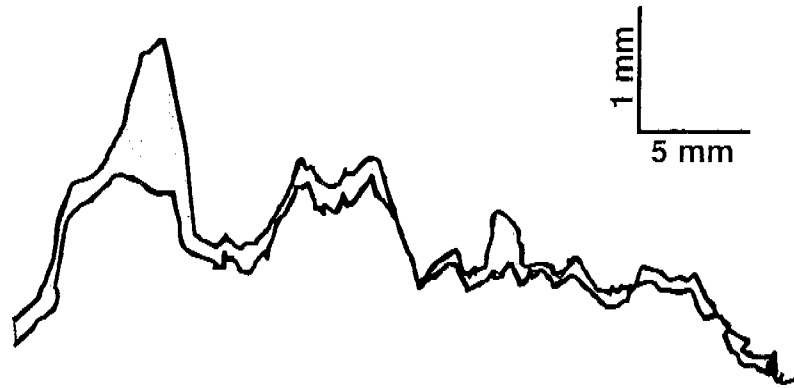


Figure 11: Schematic illustration of the effects of solute mixing at fracture intersections (junctions): (a) detailed view of three junctions, each receiving clean and contaminated water, (b) the transverse dispersion effect caused by junction mixing.

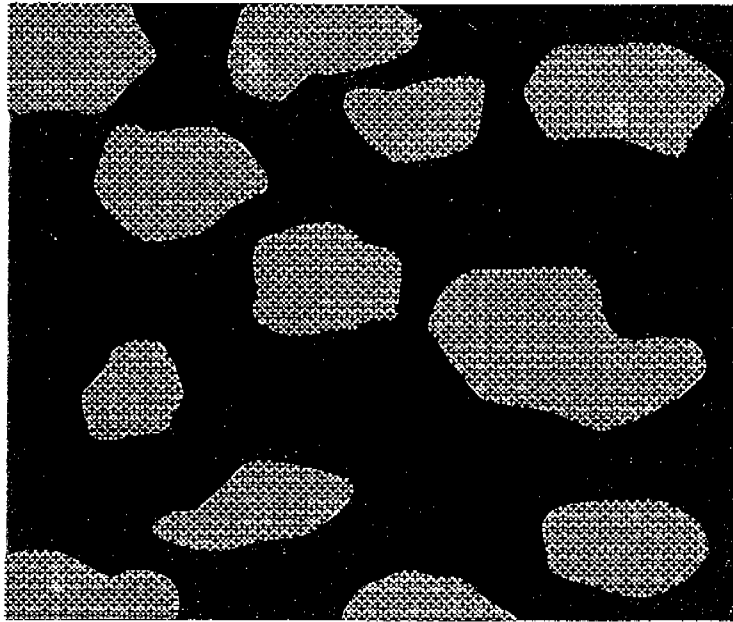
(a)



Source: NRC, 1996

Open and closed domains

(b)



area of closed fracture

Figure 12: Aperture variability in a single natural fracture: (a) cross section, (b) plan view showing areas where the fracture is closed due to stress or geochemical infilling.

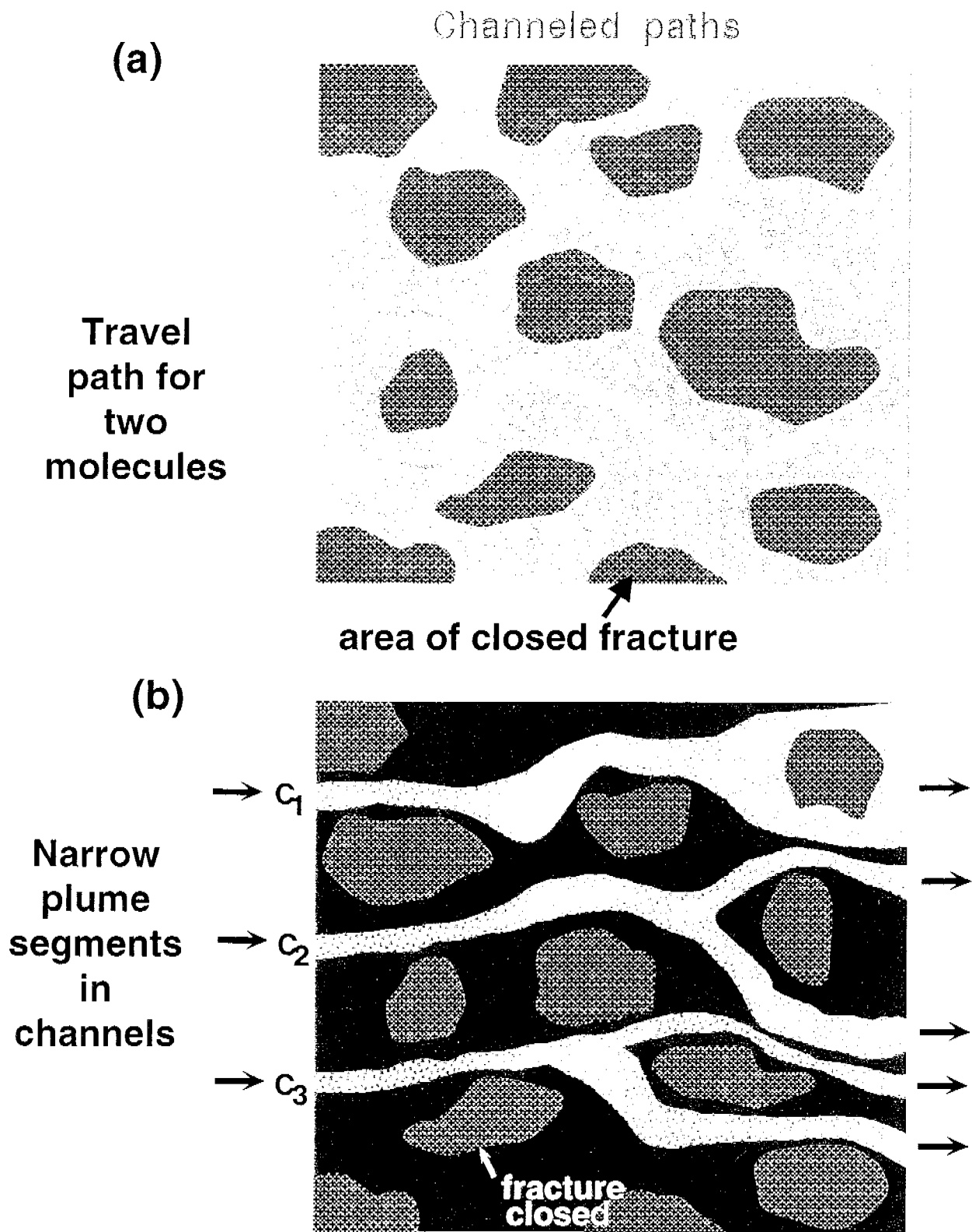
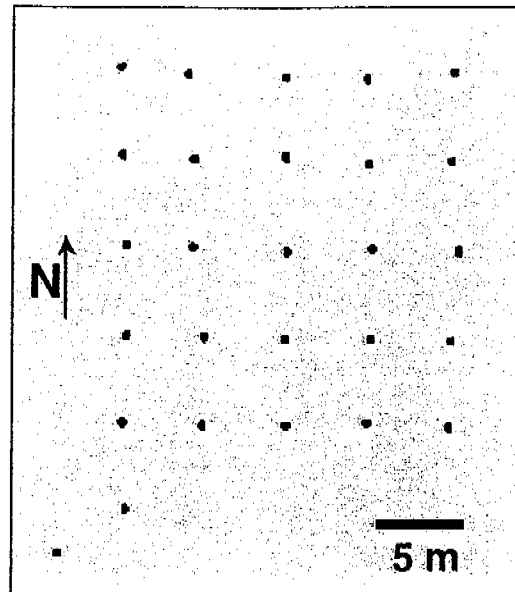


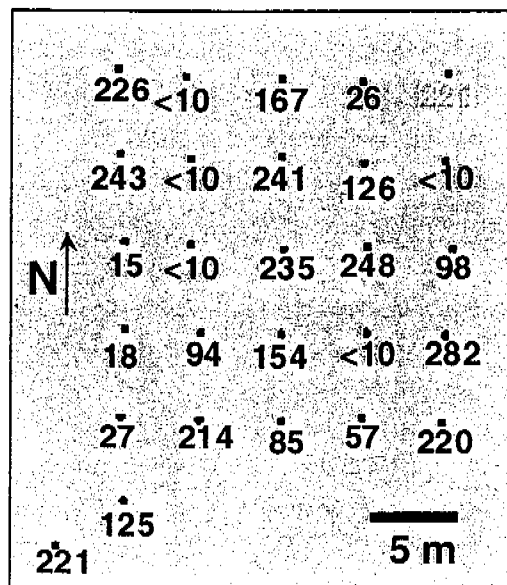
Figure 13: Effects of aperture variability along single fractures: (a) molecule transport paths, (b) dispersion due to channeling.

(a)



Lapcevic et al. (1999)

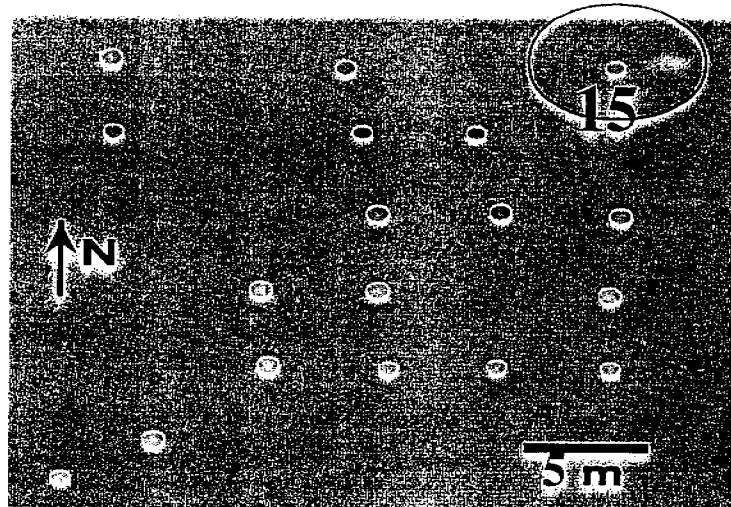
(b)



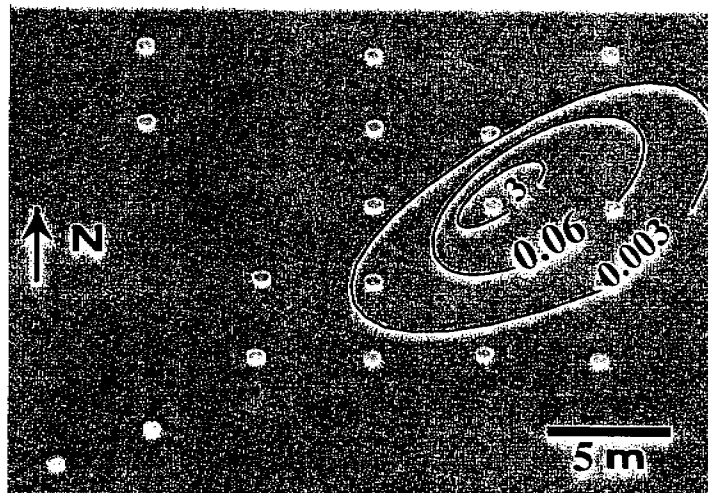
Legend
235 Aperture (μm)

Lapcevic et al. (1999)

Figure 14: Monitoring boreholes used in the tracer test area: (a) borehole locations, (b) hydraulic apertures obtained by straddle packer tests, (adapted from Lapcevic et al. 1999).

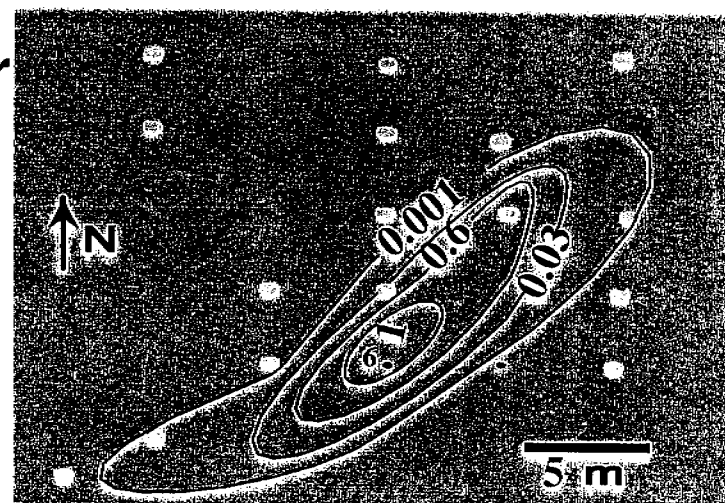


t = 0



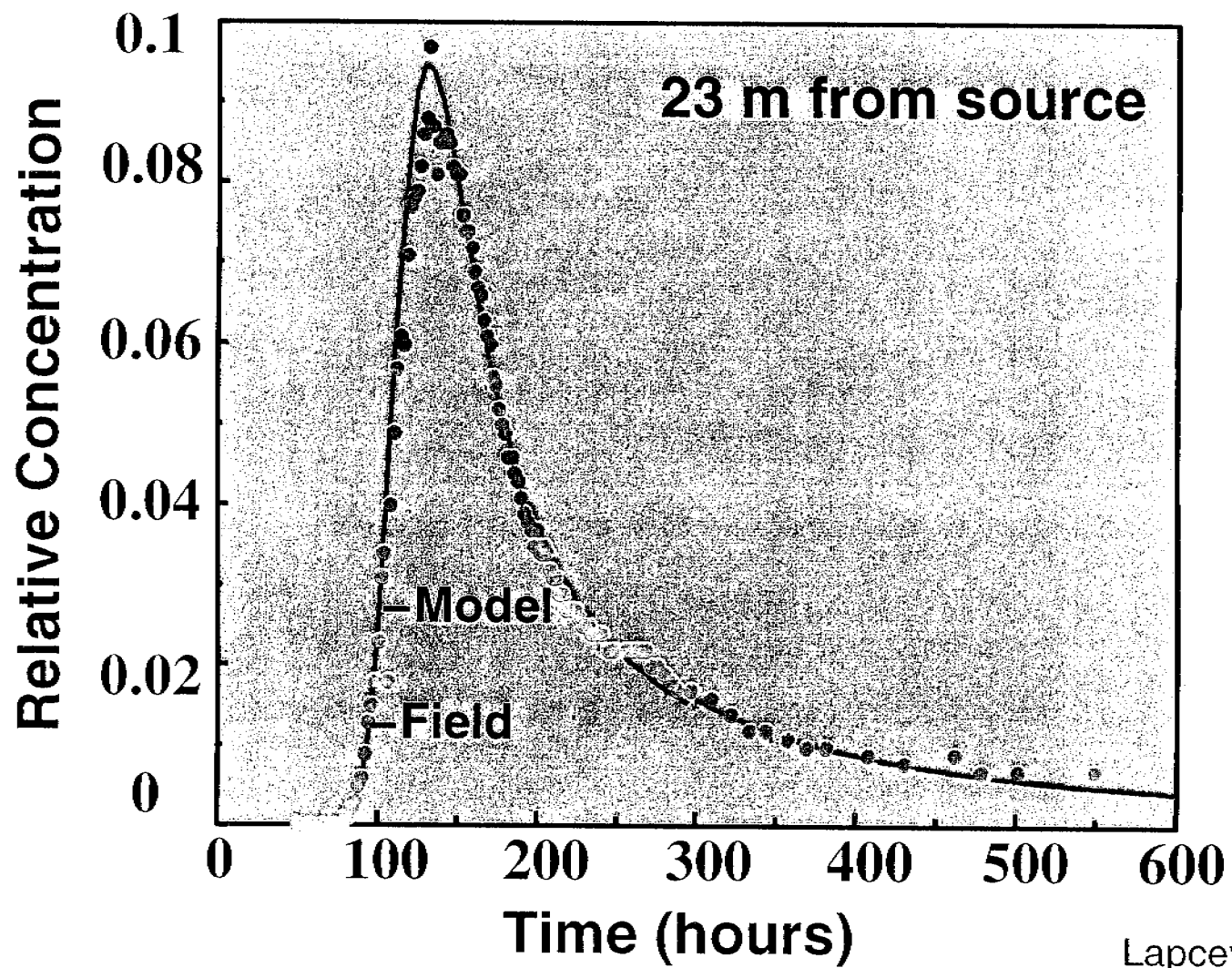
t = 72 hr

t = 135 hr



Lapcevic et al. (1999)

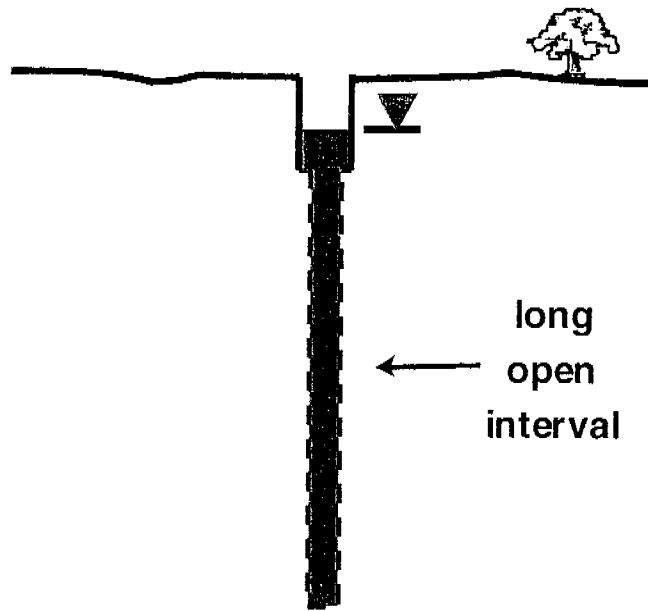
Figure 15: Tracer zone (mg/L) delineated at three times after injection (adapted from Lapcevic et al. 1999).



Lapcevic et al. (1999)

Figure 16: Tracer concentration versus time at 23 m downgradient of the injection point (adapted from Lapcevic et al. 1999).

(a)



(b)

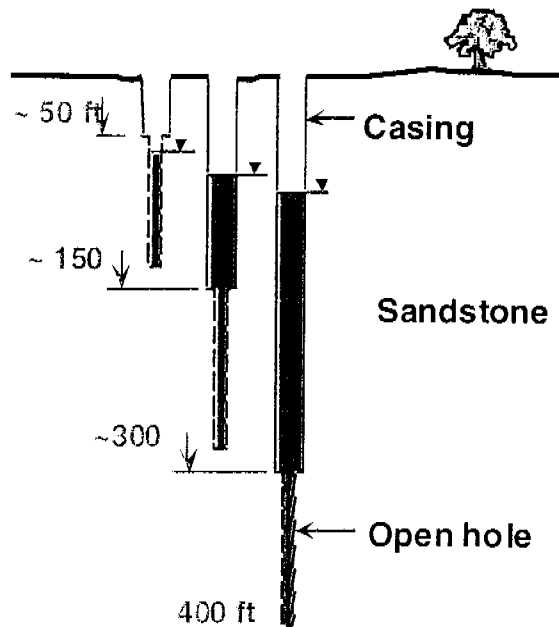


Figure 17: Schematic illustrations of two of the groundwater monitoring well approaches in boreholes at SSFL: (a) single well with long open intake interval, (b) cluster wells, each well with a short intake interval.

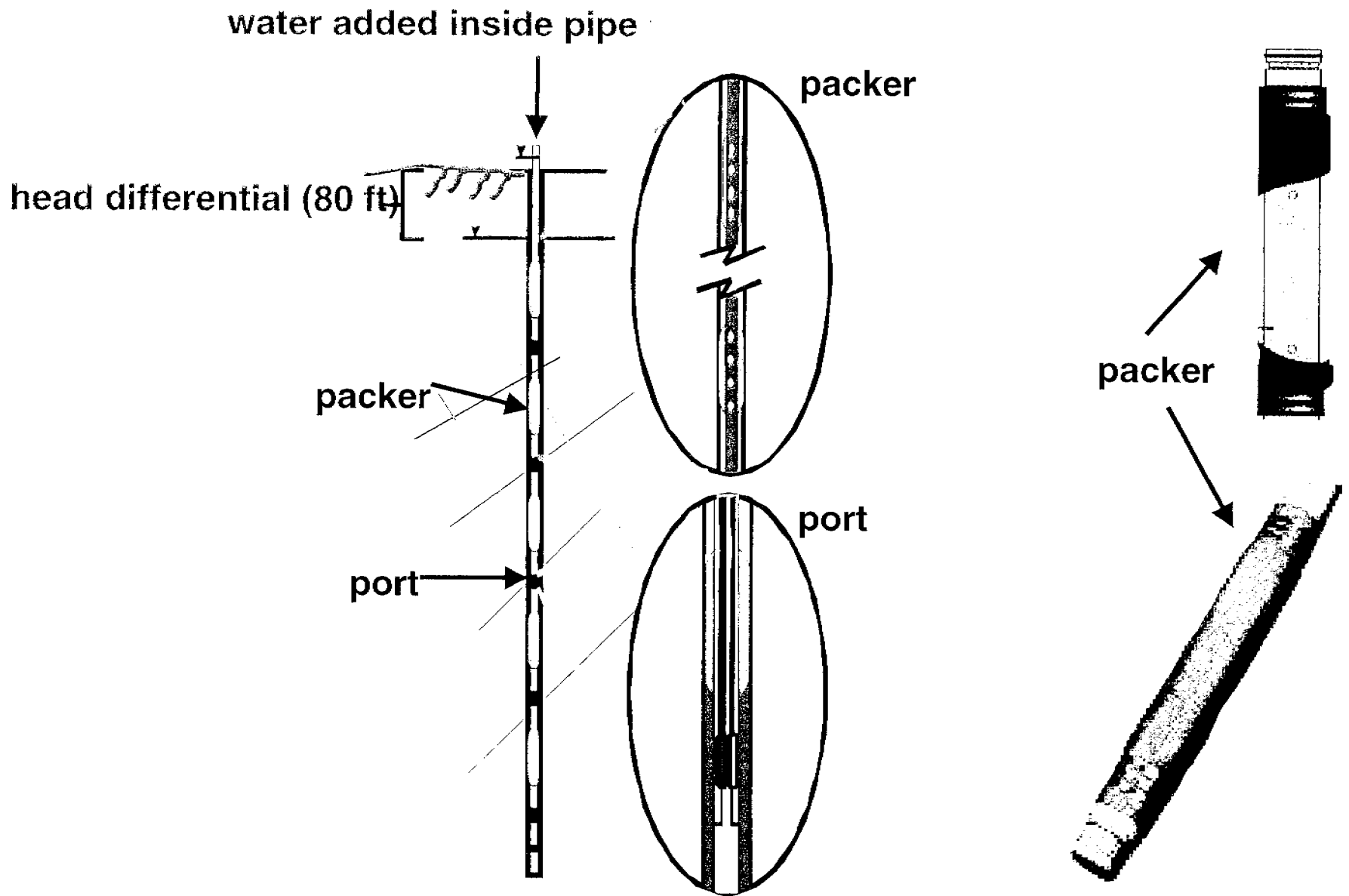


Figure 18: The Solinst removable multilevel monitoring system used in RD-35B and RD-46B.

(a)



(b)

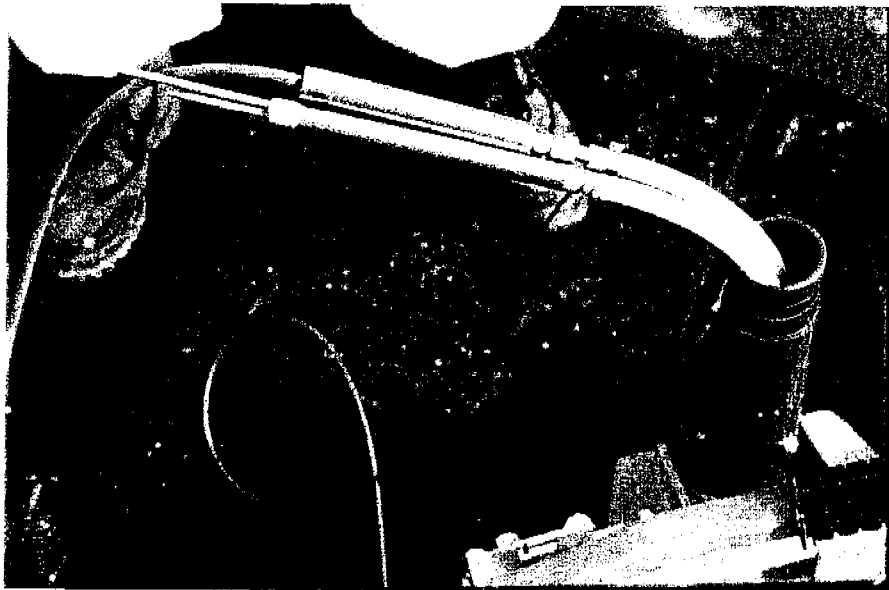


Figure 19: Installation of the Solinst removal multilevel monitoring system (a) ; VWP transducer and double valve pump (b).

- Cluster
- Single Well

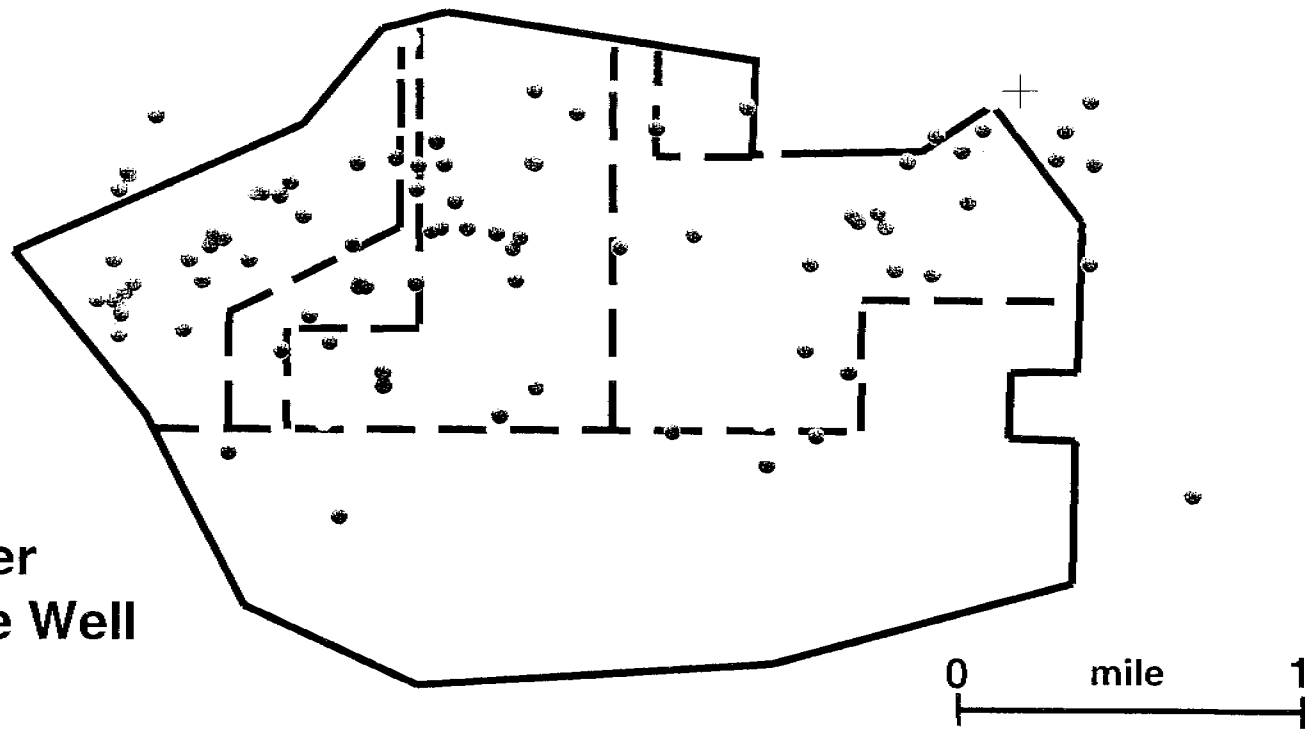


Figure 20: Locations of monitoring wells in the Chatsworth Formation

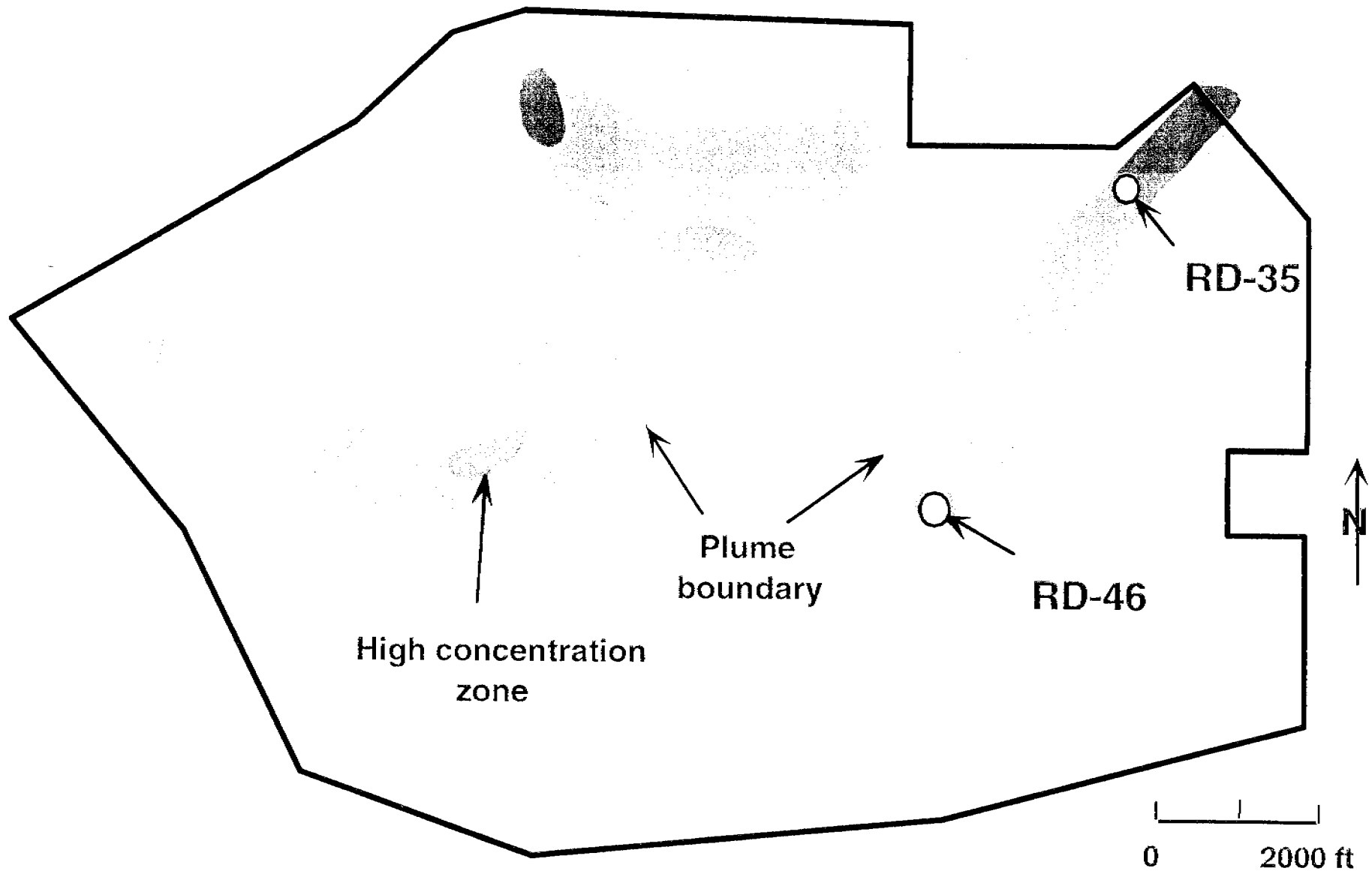


Figure 21: Locations of monitoring wells in the Chatsworth Formation: RD-35B and RD-46B.

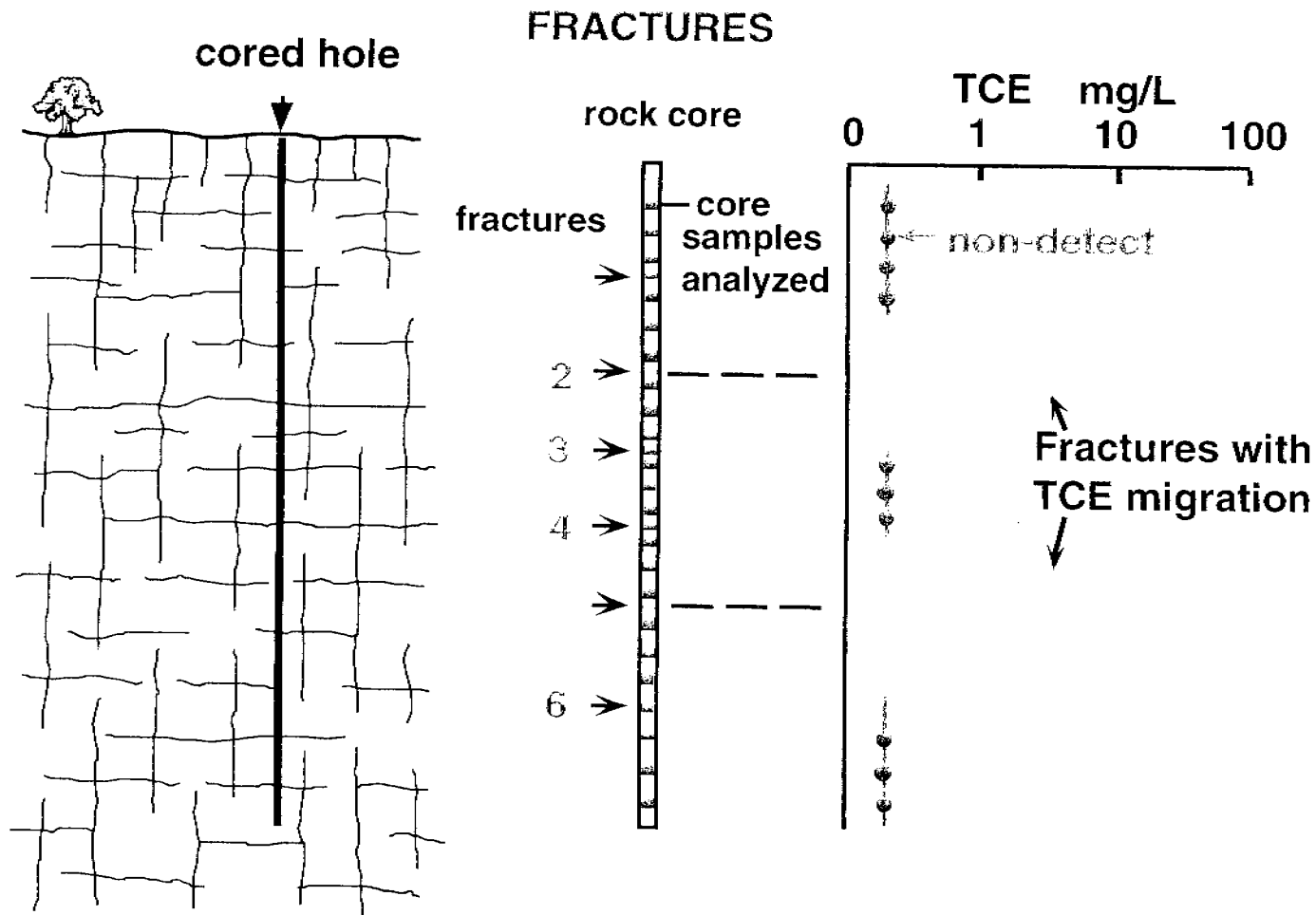


Figure 22: Schematic illustration of the use of rock core analyses to identify TCE pathways

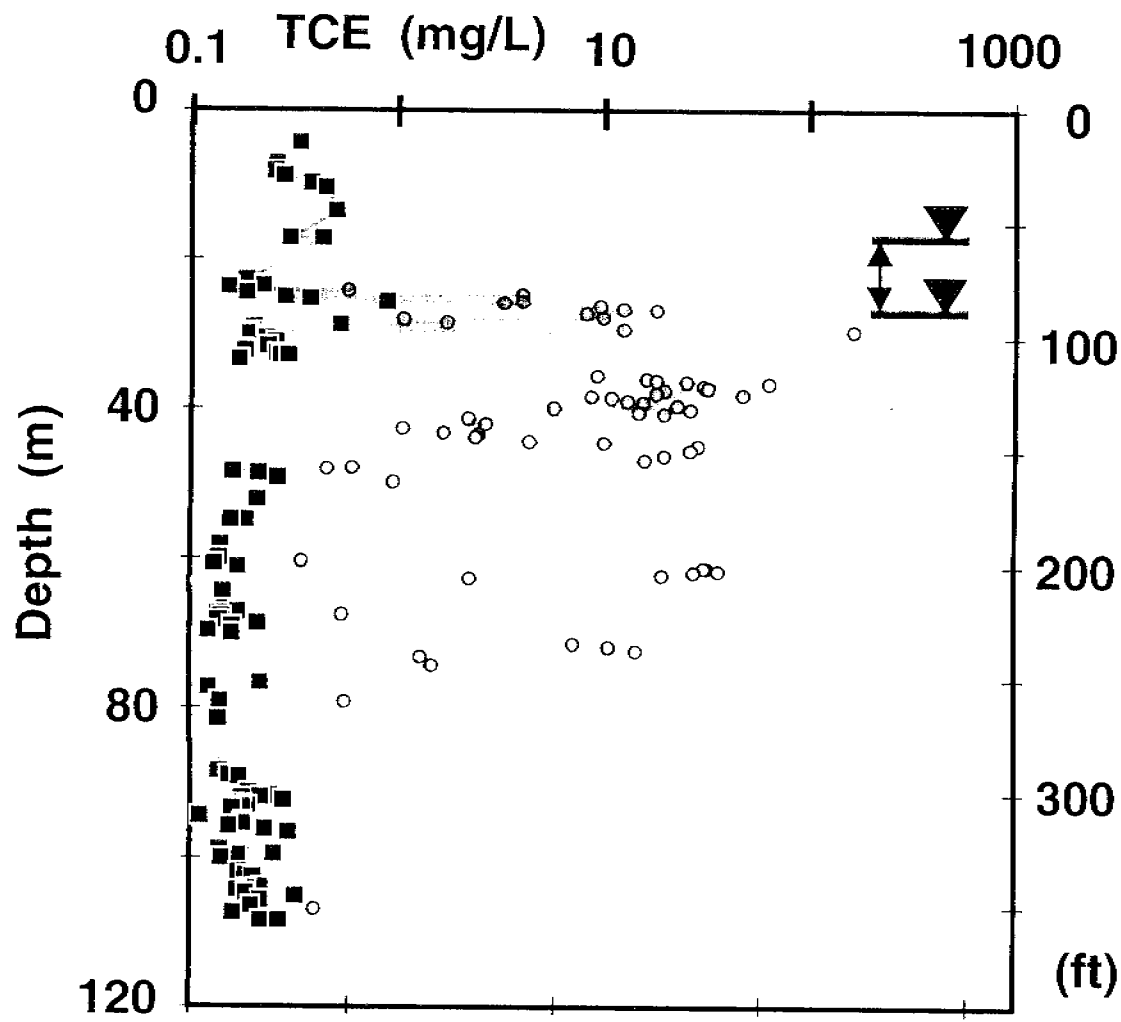
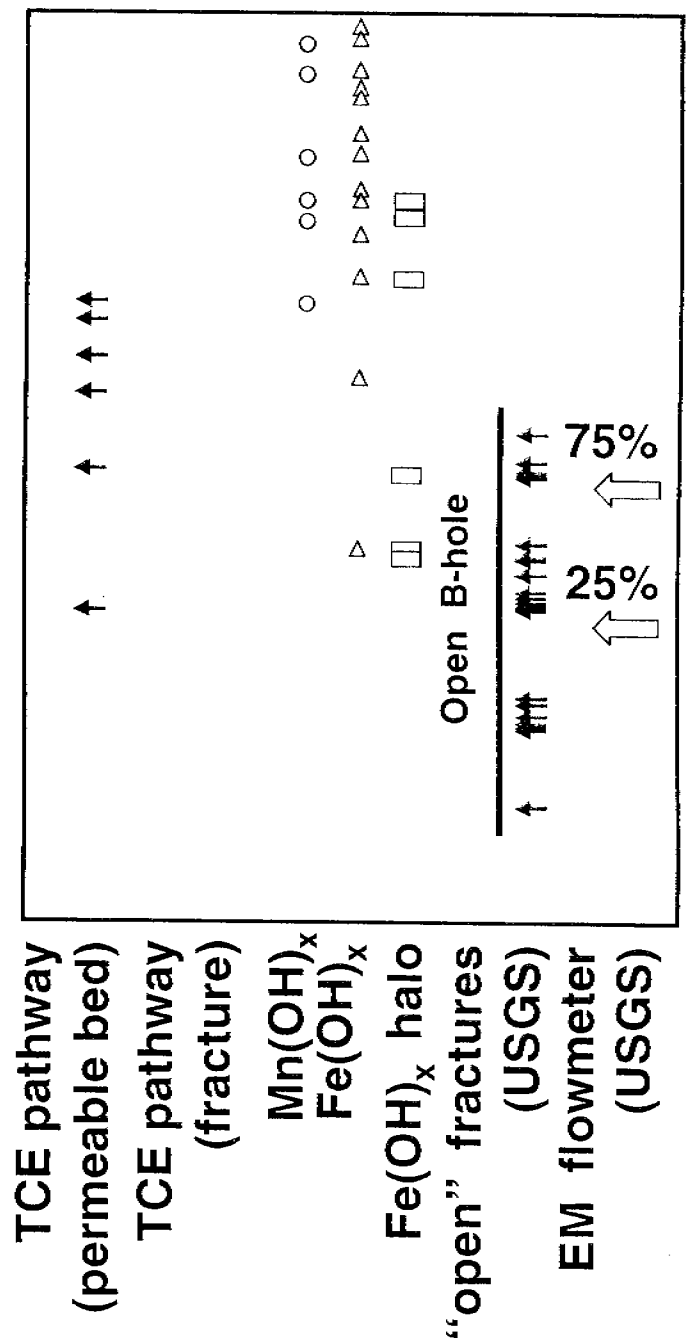
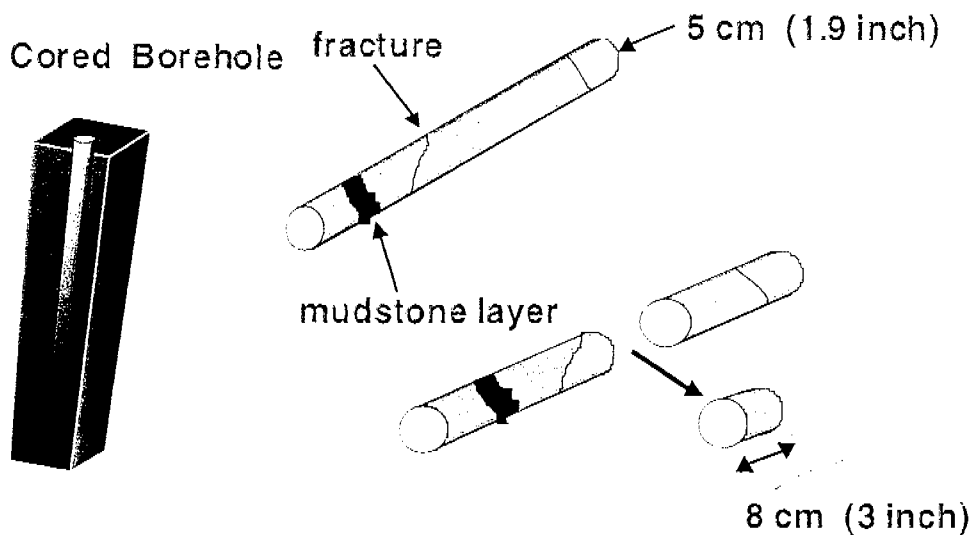


Figure 25: Results of rock core TCE analyses from RD-35B. No other VOC's were found at significant concentrations. The analytical results as ug/g of total TCE in the sample were converted to equivalent groundwater concentrations using information on rock matrix porosity and organic carbon content (adapted from Sterling 1999).

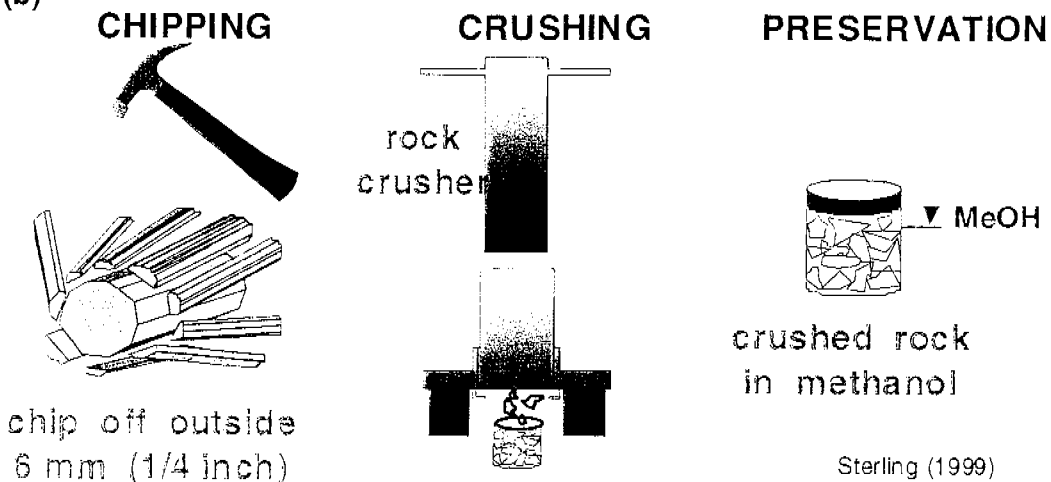


(a)



Sterling (1999)

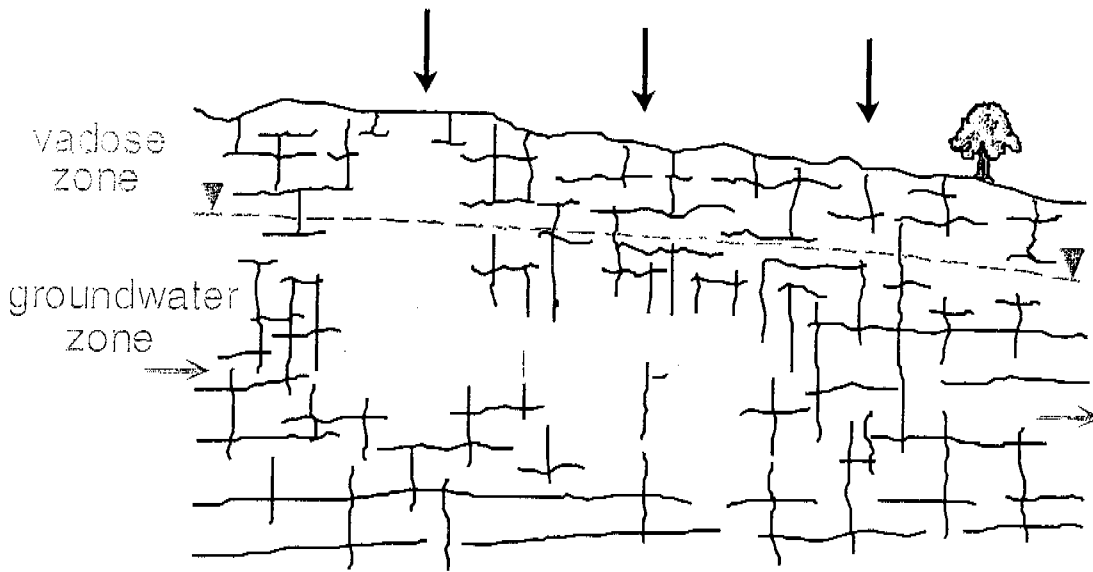
(b)



Sterling (1999)

Figure 24: Stages in the sampling and preservation of rock core samples for VOC analyses (a) Stage 1: Coring and sample collection; (b) Stage 2: Rock Crushing

(a)



(b)

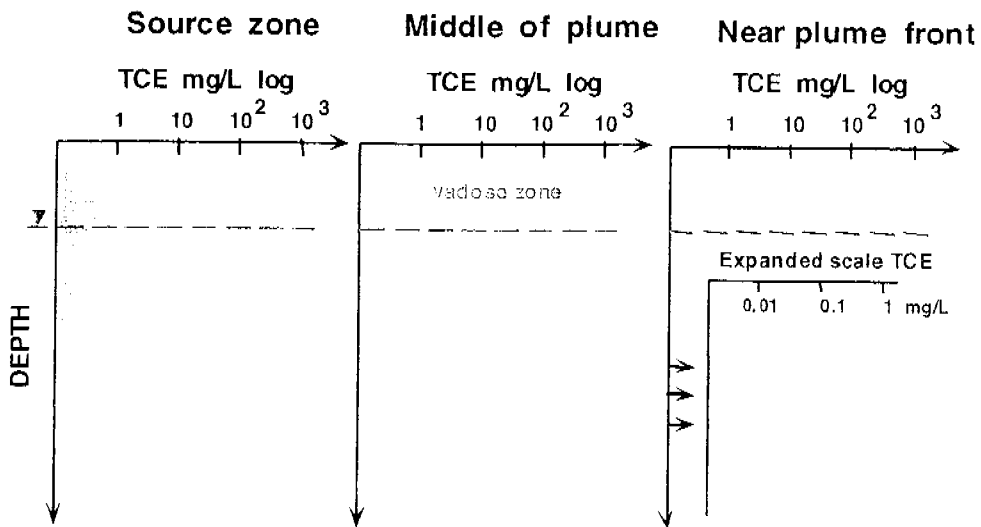


Figure 23: Schematic examples of (a) cross-section of plume and source zone and (b) rock core VOC profiles from source zone to plume fronts.

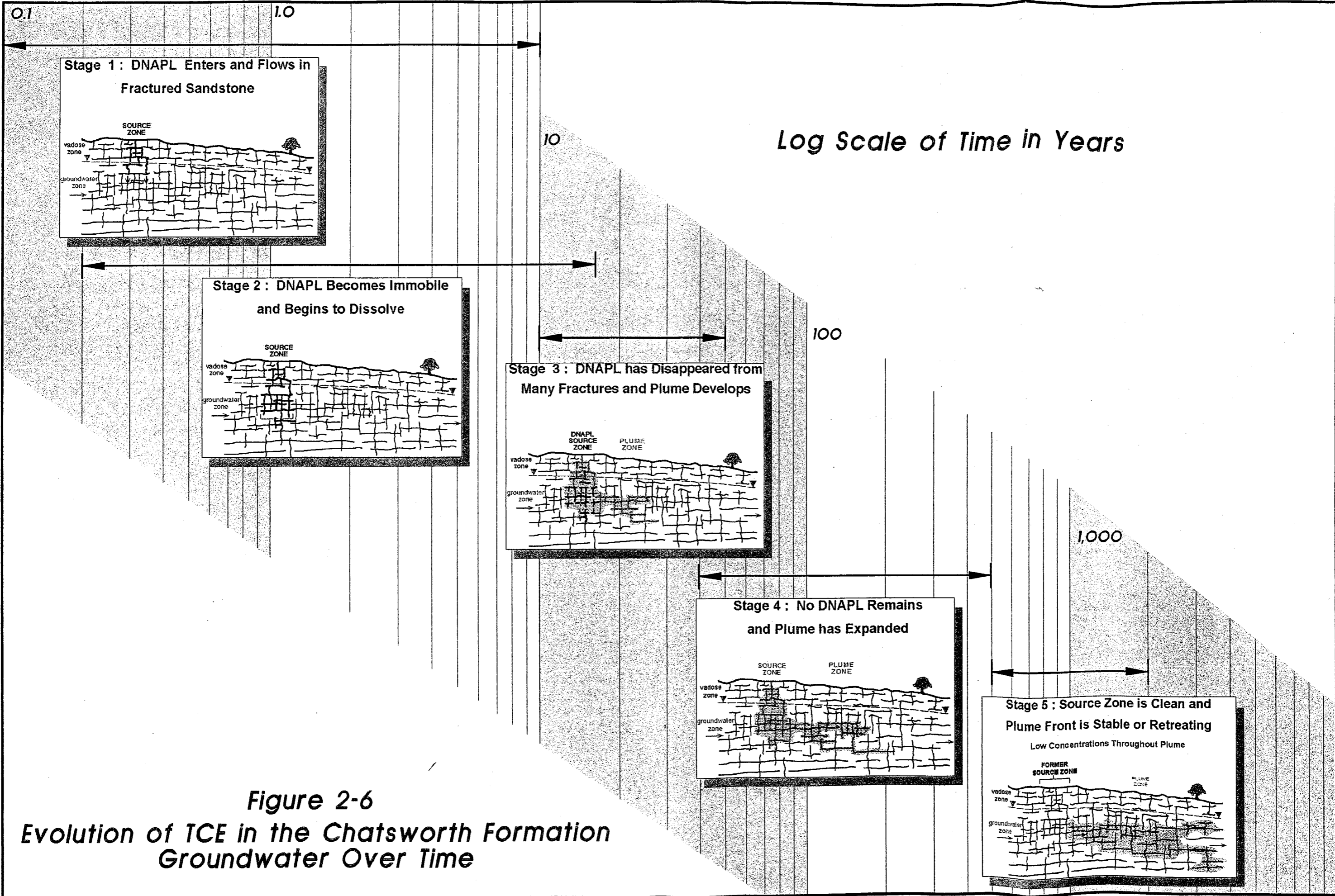


Figure 2-6
Evolution of TCE in the Chatsworth Formation
Groundwater Over Time